

THE VIBRATIONS OF ICE I AND SOME
CLATHRATE-HYDRATES BELOW 200°K

by

Arvid Holger Hardin

B.Sc.(Hons.), The University of British Columbia, 1963

A THESIS SUBMITTED IN PARTIAL FULFILMENT OF
THE REQUIREMENTS FOR THE DEGREE OF

DOCTOR OF PHILOSOPHY

in the Department

of

Chemistry

We accept this thesis as conforming to
the required standard

THE UNIVERSITY OF BRITISH COLUMBIA

July, 1970

In presenting this thesis in partial fulfilment of the requirements for an advanced degree at the University of British Columbia, I agree that the Library shall make it freely available for reference and Study.

I further agree that permission for extensive copying of this thesis for scholarly purposes may be granted by the Head of my Department or by his representatives. It is understood that copying or publication of this thesis for financial gain shall not be allowed without my written permission.

Department of Chemistry

The University of British Columbia
Vancouver 8, Canada

Date Aug. 12, 1970

ABSTRACT

The vibrations of H_2O , HDO and D_2O molecules participating in the hydrogen bonding of vitreous and crystalline solids, and some alkyl halides and halogens encaged in these solids, were studied by infrared spectroscopy between 4.2 and 200°K over the 4000 to 160 cm^{-1} frequency range. Four kinds of $\text{O}-\text{H}\cdots\text{O}$ hydrogen bonding lattices were investigated, vitreous and annealed (cubic) ice I and vitreous and annealed clathrate-hydrate mixtures.

In vitreous ice I the effects on the molecular and lattice vibrations were observed in detail for H_2O between 77 and 180°K during the phase transformation to cubic ice I, and the results of the transformation for HDO and D_2O were recorded. As well, the effects on the molecular and lattice vibrations of H_2O , D_2O , H_2O (5.94% HDO), and D_2O (4.00% HDO) cubic ices I were studied during warming from 4.2 to 200°K.

Similar studies were made for the vibrations of H_2O , HDO , D_2O and guest molecules, during the vitreous-crystalline phase transformation of seven clathrate-hydrate mixtures and during warming of the resulting annealed mixtures.

For ice I the method involved condensation of the vapour at 77°K, observation of the spectra during warming in stages to $185 \pm 5^\circ\text{K}$, cooling to 4.2°K, and observation of the cubic sample spectra during warming to 200°K. The results were plotted as a function of temperature and were correlated to calculated $\text{O}\cdots\text{O}$ distances and RMS amplitudes of translation. As well four models for molecular libration were investigated.

Three approaches were taken to the clathrate-hydrate problem. In parallel to the ice I method gaseous stoichiometric mixtures were con-

densed, observed during transformation, cooled to 4.2°K and observed during warm-up. Other gaseous clathrate mixtures were condensed in an isolated sample chamber, to prevent sample fractionation, and treated as before. Finally, low temperature mulls of solid clathrate-hydrate mixtures were prepared and observed at $83 \pm 3^{\circ}\text{K}$.

The results show that on warming the ice I phase transformation occurred between 120 ± 5 and $135 \pm 5^{\circ}\text{K}$ and required less than 18 minutes at $135 \pm 3^{\circ}\text{K}$. Weak peaks due to oligomeric H_2O and D_2O units disappeared during annealing, while all hydrogen bonded H_2O molecular modes shifted to lower frequency and all lattice modes shifted to higher frequency. The half-height widths of the composite H_2O band ($\nu_2/2\nu_R$) appeared to increase upon annealing and to decrease upon warming while the ($\nu_R, \nu_R + \nu_T$) and ($\nu_1, \nu_3, \nu_1 + \nu_T$) bands had the opposite behaviour. This was interpreted as indicating a weak $2\nu_R$ band underlying the stronger ν_2 absorption near 1600 cm^{-1} .

The frequency-temperature dependences of all cubic ice I bands were interpreted on a bilinear, high and low temperature basis (the lattice modes shifted to lower frequency and the molecular modes to higher frequency with increasing temperature). For HDO above 80°K $\Delta\nu_{\text{OH}}/\Delta T$ was $0.200 \pm 0.005 \text{ cm}^{-1}/^{\circ}\text{K}$, $\Delta\nu_{\text{OD}}/\Delta T$ was $0.123 \pm 0.005 \text{ cm}^{-1}/^{\circ}\text{K}$, the frequencies were "frozen-in" at $80 \pm 5^{\circ}\text{K}$ and $65 \pm 5^{\circ}\text{K}$ and had irregular behaviours between 50 and 70°K . The low temperature dependences were $0.047 \pm 0.005 \text{ cm}^{-1}/^{\circ}\text{K}$ in both modes. An explanation is given for the apparent displacement of the HDO stretching frequencies from the H_2O and D_2O frequencies.

The HDO results also permitted the accurate determination of $\Delta\nu_{\text{OH}}/\Delta R(0 \cdots 0)$ as $1921 \text{ cm}^{-1}/\text{\AA}$ and $\Delta\nu_{\text{OD}}/\Delta R$ as $1281 \text{ cm}^{-1}/\text{\AA}$ above 150°K and

as $8202\text{ cm}^{-1}/\text{\AA}$ and $6629\text{ cm}^{-1}/\text{\AA}$ below 100°K . As well, the HDO stretching frequencies gave an anharmonicity which increased from 4.2 to 80°K and then decreased between 80 and 200°K .

The clathrate-hydrate mixtures transformed on warming in the temperature range 125 ± 5 to $145 \pm 5^{\circ}\text{K}$ and required less than 18 minutes at 135°K as for ice I. Similarly, the weak oligomeric and guest absorptions disappeared upon annealing. From the comparison of the three sets of "clathrate" results and the behaviour of annealed sample peaks we concluded that cubic ice I and not clathrate-hydrate was probably formed.

TABLE OF CONTENTS

	PAGE
Abstract	ii
Table of Contents.	v
List of Tables	ix
List of Figures.	xi
Acknowledgements	xiv
INTRODUCTION	1
Hydrogen Bonding.	1
A. Theories of Hydrogen Bonding	2
B. Spectroscopic Manifestations of Hydrogen Bonding	6
Clathrate-Hydrates.	12
A. The Clathrate-Hydrate Problem.	12
B. The Structures of the Clathrate-Hydrates	12
C. Formation of Clathrate-Hydrates.	17
D. Previous Investigations of the Clathrate-Hydrates.	18
E. The Present Approach to the Clathrate-Hydrate Problem.	19
Ice	20
A. The Ice Problem.	20
B. Non-Spectroscopic Investigations of Ice.	20
C. Spectroscopic Investigations of Ice.	27
D. The Present Approach to the Ice Problem.	37
CHAPTER ONE: APPARATUS.	38
1.1 The Perkin-Elmer 112-G Spectrophotometer	38
1.2 The Perkin-Elmer 421 Spectrophotometer	40
1.3 The Perkin-Elmer 301 Spectrophotometer	42
1.4 The Hornig-Wagner Liquid Nitrogen Cell	42
1.5 The Duerig-Mador Liquid Helium Cell.	45
1.6 The Metal Liquid Nitrogen Cell	45

CHAPTER TWO: METHODS AND MATERIALS.	47
2.1 Water Samples and Clathration Materials.	47
2.2 Infrared Windows and Sample Mounts	48
2.3 Preparation of Clathrate-hydrates.	49
A. Preparation of Solid Samples	49
B. Preparation of Stoichiometric Gaseous Mixtures	50
2.4 Preparation of Infrared Specimens.	52
A. Low Temperature Mulling.	52
B. Isolated Chamber Condensation.	53
C. Open Chamber Condensation.	54
2.5 Devitrification.	55
2.6 Temperature Variation Methods.	56
CHAPTER THREE: ICE I: EXPERIMENTAL AND RESULTS	58
3.1 The Vitreous-Cubic Ice Phase Transformation.	58
A. Experimental	58
B. Results of Devitrification	59
3.2 Temperature Dependence of Cubic Ice I Absorptions.	69
A. Temperature Dependence of HDO Absorptions.	69
B. Temperature Dependence of H ₂ O and D ₂ O Absorptions. . .	79
3.3 The H ₂ O, D ₂ O and HDO Ice I Absorptions at 83°K	95
A. Experimental	95
B. Results at 83°K.	95
3.4 Summary of Ice I Results	101
A. Vitreous-Cubic Ice I Transformation.	101
B. HDO in Cubic Ice I	102
C. H ₂ O and D ₂ O in Cubic Ice I	102

CHAPTER FOUR: DISCUSSION OF ICE I	103
4.1 The Ice I Vitreous-Cubic Phase Transformation.	103
A. General Discussion	104
B. Fundamental Lattice Mode Transformations	107
C. Fundamental Molecular Mode Transformations	111
D. Combination and Overtone Mode Transformation	117
E. Confidence in the Cubic Ice I Samples.	118
4.2 Temperature Dependence of Cubic Ice I Absorptions.	120
A. Dependence of HDO Bands on Temperature	121
B. Dependence of H ₂ O and D ₂ O Bands on Temperature	159
4.3 Assignments of the Cubic Ice I Absorption Bands.	175
A. The Fundamental Lattice Modes.	175
B. The Fundamental Molecular Modes.	177
C. The Overtone and Combination Modes	186
4.4 The Libration of HDO, H ₂ O and D ₂ O.	187
A. The Moments-of-Inertia Models	187
B. The H ₂ O ₃ Model of Ice.	198
C. A Summary of H ₂ O, HDO and D ₂ O Librations	211
CHAPTER FIVE: CLATHRATE-HYDRATE EXPERIMENTAL DETAILS AND RESULTS	214
5.1 The Vitreous-Crystalline Clathrate-Mixture Phase Transformation	214
A. Experimental	214
B. Results of Devitrification	216
5.2 Clathrate Mixture Guest Absorptions.	228
A. Condensation in an Open Chamber.	229
B. Condensation in an Isolated Chamber.	233
C. Low Temperature Mulls.	233
5.3 Temperature Dependence of the Crystalline Clathrate Mixture Absorptions.	234
A. Temperature Dependence of the HDO Absorptions.	234
B. Temperature Dependence of the H ₂ O and D ₂ O Absorptions.	239

CHAPTER SIX: DISCUSSION OF THE CLATHRATE MIXTURES	247
6.1 The Clathrate Mixture Vitreous-Crystalline Phase Transformation	247
A. General Discussion	247
B. Annealing $\text{Cl}_2 \cdot 7.67\text{H}_2\text{O}$ on CsI	248
C. Oligomeric H_2O Absorptions	251
D. Unannealed Sample Guest Absorptions.	251
6.2 Guest Species Absorptions.	255
A. Isolated Chamber Condensation.	256
B. Low Temperature Mulls.	257
C. Summary.	258
6.3 The Temperature Dependences of Crystalline Clathrate Mixture Absorptions.	259
A. HDO in Clathrate Mixtures.	259
B. H_2O and D_2O in Clathrate Mixtures.	261
CHAPTER SEVEN: SUMMARY.	264
7.1 Suggestions for Further Work	264
A. Clathrate Mixtures	264
B. Ice Systems.	265
C. Other Chemical Systems	267
7.2 Conclusions.	268
A. Annealing Ice I_V	268
B. HDO Studies.	268
C. The H_2O and D_2O Studies.	270
D. Clathrate Mixture Annealing.	272
REFERENCES	273

LIST OF TABLES

TABLE		PAGE
0.1	Typical clathrate-hydrates and their properties.	14
0.2	Clathrate-hydrate unit cell dimensions, guest sizes and filled cavities.	16
0.3	Stable temperature ranges of vitreous, cubic and hexagonal ice I.	23
0.4	Some physical properties of the ices	25
0.5	H ₂ O vapour, liquid and ice I frequencies and assignments .	29
III.I	Cubic and vitreous ice I frequencies at 82°K	62
III.II	Vitreous ice I oligomeric absorptions.	65
III.III	H ₂ O composite band half-height widths.	68
III.IV	The behaviour of HDO stretching modes in cubic ice I . . .	72
III.V	The behaviour of HDO librational modes in cubic ice I. . .	74
III.VI	HDO stretching modes half-height widths.	76
III.VII	HDO stretching modes peak heights.	77
III.VIII	Ice I sample histories	80
III.IX	Cubic ice I H ₂ O and D ₂ O absorptions.	83
III.X	Cubic ice I $\nu_T(\text{H}_2\text{O})$ absorptions.	91
III.XI	(a) Present and previous H ₂ O assignments for cubic ice I .	96
	(b) Present and previous frequencies for $\nu_T(\text{H}_2\text{O})$	97
III.XII	Present and previous HDO frequencies for cubic ice I . . .	98
III.XIII	Present and previous D ₂ O assignments for cubic ice I . . .	99
IV.I	Calculated and observed RMS amplitudes of translation for H ₂ O and D ₂ O.	149
IV.II	H ₂ O, HDO and D ₂ O moments-of-inertia.	190
IV.III	Symmetric G-matrix elements for H ₂ O ₃	201

TABLE	PAGE
IV.IV	H_2O_3 and D_2O_3 force constants for ice I. 208
V.I	The clathrate-mixture sample histories 215
V.II	H_2O frequencies in unannealed and annealed $CH_3Cl \cdot 7.67H_2O$. 221
V.III	Oligomeric frequencies at 83°K in unannealed clathrate-mixtures 223
V.IV	Temperature dependences of oligomeric frequencies in unannealed clathrate mixtures. 224
V.V	The stable temperature ranges of the oligomer peaks. . . . 225
V.VI	The alkyl halide guest absorptions in unannealed clathrate mixtures at 83°K 230
V.VII	The temperature dependence of the guest frequencies during annealing 231
V.VIII	The stable temperature ranges for the guest absorptions. . 232
V.IX	The behaviour of HDO stretching modes for annealed clathrate mixtures 237
V.X	HDO librations for three annealed clathrate mixtures . . . 241
V.XI	Average H_2O and D_2O frequency-temperature data for annealed clathrate mixtures. 244
V.XII	Data for $Cl_2 \cdot 7.67H_2O$ and $Br_2 \cdot 8.6H_2O$ on CsI and AgCl. . . . 245
VI.I	H_2O frequencies for hydrated alkali halide salts. 250
VI.II	Oligomeric H_2O and D_2O peaks in clathrate mixtures and rare gas matrices. 252
VI.III	Alkyl halide frequencies in pure solids and clathrate mixtures 254

LIST OF FIGURES

FIGURE		PAGE
1.1	The stainless steel deposition tube.	44
1.2	The isolated sample chamber.	46
3.1	Representative spectra of vitreous and cubic ices.	60
3.2	Frequency shifts during phase transformation	61
3.3	Oligomeric H ₂ O and D ₂ O absorptions in vitreous ice I	64
3.4	Half-height width shifts for (ν_R , $\nu_R + \nu_T$) and (ν_1 , ν_3 , $\nu_1 + \nu_T$).	66
3.5	Half-height width shifts for (ν_2 , $2\nu_R$)	67
3.6	HDO stretching frequency shifts for cubic ice I.	71
3.7	HDO librational frequency shifts for cubic ice I	73
3.8	HDO stretching mode half-height width shifts for cubic ice I.	75
3.9	HDO stretching mode peak height shifts for cubic ice I	78
3.10	The shifts of cubic ice I ν_3	82
3.11	The shifts of cubic ice I ν_1	85
3.12	The shifts of cubic ice I ν_2	86
3.13	The shifts of cubic ice I ν_R	88
3.14	The cubic ice I ν_T (H ₂ O) band at 83°K	89
3.15	The shifts of cubic ice I ν_T	90
3.16	The shifts of cubic ice I ($\nu_1 + \nu_T$).	92
3.17	The shifts of cubic ice I $3\nu_R$	93
3.18	The shifts of cubic ice I ($\nu_R + \nu_T$).	94

FIGURE

PAGE

4.1	The calculated linear thermal expansion coefficient of cubic ice I	128
4.2	The calculated cubic ice I lattice parameter as a function of temperature	129
4.3	The calculated O····O distance for cubic ice I as a function of temperature	131
4.4	Cubic ice I HDO stretching frequencies as a function of $R(O····O)$	132
4.5	Comparison of observed and predicted $\nu_{OH}^{(HDO)} - R(O····O)$ dependence.	137
4.6	The calculated cubic ice I harmonic HDO frequency as a function of temperature	143
4.7	The calculated HDO anharmonicity.	144
4.8	A plot of HDO anharmonicity against $R(O····O)$	145
4.9	Calculated RMS amplitudes of translation $\langle \Delta r^2 \rangle^{\frac{1}{2}}$	150
4.10	A plot of $\langle \Delta r^2 \rangle^{\frac{1}{2}}$ against $R(O····O)$	151
4.11	A plot of $\nu_{OH}^{(HDO)}$ and $\nu_{OD}^{(HDO)}$ against $\langle \Delta r^2 \rangle^{\frac{1}{2}}$	152
4.12	The cubic ice I ν_3 dependences on $R(O····O)$	165
4.13	The calculated hexagonal ice I ν_3 dependence on $R(O····O)$	166
4.14	The calculated hexagonal ice I $\nu_{OH}^{(HDO)}$ and $\nu_{OD}^{(HDO)}$ dependences on $R(O····O)$	167
4.15	H ₂ O, HDO and D ₂ O vapour and cubic ice I phase frequencies	180
4.16	The effects of uncoupling on the HDO stretching frequencies	184
4.17	The principal axes of H ₂ O, HDO and D ₂ O.	189
4.18	The H ₂ O ₃ model of H ₂ O in ice.	199
4.19	The internal coordinates of H ₂ O ₃	202
4.20	The symmetry coordinates of H ₂ O ₃	203

FIGURE		PAGE
5.1	Clathrate-mixture frequency shifts during transformation .	217
5.2	Typical annealing spectra for CH_3Cl , CH_3Br and CH_3I clathrate-mixtures	218
5.3	Typical annealing spectra for CHCl_3 and $\text{C}_2\text{H}_5\text{Br}$ clathrate-mixtures	219
5.4	Typical annealing spectra for Br_2 and Cl_2 clathrate- mixtures	220
5.5	Consecutive spectra for annealing $\text{Cl}_2 \cdot 7.67\text{H}_2\text{O}$ on CsI . . .	227
5.6	Frequency shifts for $\nu_{\text{OH}}(\text{HDO})$ of annealed $\text{CH}_3\text{Br} \cdot 7.67\text{D}_2\text{O}$ (4.00% HDO).	235
5.7	Frequency shifts for $\nu_{\text{OD}}(\text{HDO})$ of annealed $\text{CH}_3\text{Br} \cdot 7.67\text{H}_2\text{O}$ (5.94% HDO).	236
5.8	The half-height width shifts for ν_{OH} and ν_{OD} of several clathrate-mixtures	238
5.9	The shift of $\nu_{\text{R}}(\text{HDO})$ in annealed $\text{CH}_3\text{Br} \cdot 7.67\text{D}_2\text{O}$ (4.00% HDO).	240
5.10	Shifts of $\nu_1(\text{D}_2\text{O})$ for annealed $\text{CH}_3\text{Br} \cdot 7.67\text{D}_2\text{O}$	242
5.11	Shifts of $\nu_3(\text{D}_2\text{O})$ for annealed $\text{CH}_3\text{Br} \cdot 7.67\text{D}_2\text{O}$	243

ACKNOWLEDGEMENTS

To Professor K.B. Harvey who has the assured faith in graduate students to allow them to choose and pursue a range of interests in vibrational spectroscopy, and who instills a beneficial but often frustrating independence of thought and action.

To Professors R.F. Snider and A. Bree who as members of my committee were also willing to discuss problems related to this work.

To the members of the mechanical, glass blowing and electronics workshops for their excellent craftsmanship and cheerful aid.

To Raymond Green and other students and faculty for the many opportunities to discuss diverse problems and for the ready mutual exchange of ideas.

And to my wife and family for their special help and the joy they provide.

DEDICATION:

To my parents

Karl Johan Frithiof Hardin

and

Beatrice Mary (Trojanoski) Hardin

INTRODUCTION

The phenomenon of hydrogen bonding has played an increasingly important role in the theories of certain chemical and bio-chemical systems for more than three decades. Several models, depending on the physical property investigated, have been proposed to explain the experimental results. However, for crystals a unified hydrogen bond model has not yet developed which is consistent with all the chemical and physical properties of the solid state.

The present work is a spectroscopic investigation of solid state hydrogen bonding in vitreous and cubic ice I and in vitreous and crystalline clathrate-hydrate mixtures; the nature of the clathrate-hydrate solids formed by vapour condensation is uncertain. A detailed study of the large changes (relative to non-hydrogen-bonded solids) in the infrared (ir) absorptions as a function of temperature provides information on changes in hydrogen bonding as a function of the oxygen-oxygen nearest-neighbour distance ($R(O\cdots O)$) both for individual molecules and for the collective solid arrays. These data help to describe precisely changes in one solid's molecular potential and should aid in the development of a unified hydrogen bond model.

Hydrogen Bonding

The main effects manifested by the hydrogen bond ($A-X-H\cdots Y-B$) on the ir spectra are: 1) large frequency shifts, 2) alterations in intensity, 3) increased band width, and 4) the appearance of new bands associated with the deformation of the hydrogen bond. The general phenomenon of hydrogen bonding has been reviewed by Pimentel and McClellan (1), Sokolov and

Tschulanovski (2), and by Hadzi and Thompson (3). Recently Hamilton and Ibers (4) discussed the roles of hydrogen bonding in chemical structures. The specific effects of hydrogen bonds on the chemical and physical properties of ice are treated in books by Eizenberg and Kaufmann (5) and by Riehl, Bullemer and Engelhardt (6).

A. Theories of Hydrogen Bonding

Hydrogen bonding theories fall into two classes--classical and quantum mechanical; the latter includes three separate approaches--valence bond (VB), charge transfer (CT) and molecular orbital (MO) representations. The conclusions drawn from all the theories are that both electrostatic, charge migration and short range repulsion give concerted effects and both are concurrently important (7).

(i) Classical Theories

The classical electrostatic theories are based on Pauling's (8) description which assumed the H atom could form a single covalent bond only.

(a) Point charge models. In the early work (1933-1957) the charge distribution was approximated by a set of point charges (9-12). For the ice and clathrate-hydrate systems with O-H...O bonds, 4 electrons (2 in the O-H bond and 2 in the O lone pair) were considered and the remaining electrons and protons were assumed to form the molecular core. The charges were located so that the correct O-H and lone pair dipole moments were obtained. The interaction energy of the hydrogen bond, calculated by assuming a simple Coulomb potential, was then 6 kcal/mole. The theories have successfully explained the lengthening of the X-H bond ($r(X-H)$) and the X-H stretching frequency (ν_{XH}) red shift.

Two conclusions have been drawn from the simple electrostatic model. First, electrostatic energy is important in hydrogen bonding as is indicated by the decreasing bond strength with decreasing electronegativity of the proton acceptor and proton donor. Secondly, electrostatic energy causes at least part of $\Delta R(X \cdots Y)$ and Δv_{XH} .

(b) Continuous charge distribution model. This model was presented in 1964 by Bader (13) for the $O-H \cdots O$ system typical of ice and clathrate-hydrates. He considered all the electrons, by methods developed for hydrides and binary hydrides (14,15), in spherical charge distributions and calculated the electrostatic force by classical electrostatic methods. The conclusions and interpretation of Bader's model are the same as for the point charge model.

(c) Summary of the classical theories. The electrostatic theories ignore four important facts about hydrogen bonding. For example, hydrogen bonds may not be completely ionic since there is no correlation between dipole moments and hydrogen bond strengths in the hydroxides. As well, both the point and continuous charge distribution models assume the electronic charge distributions are undistorted by the formation of a hydrogen bond. Another point to consider is that the $X \cdots Y$ distances are much less than the covalent van der Waal's radii suggesting that forces other than repulsion are important. Finally, the electrostatic theories cannot explain the increase of intensity of the X-H stretching mode.

(ii) Quantum Mechanical Theories

The first quantum mechanical theory of the hydrogen bond was published in 1952 by Sokolov (16), although such methods have become practical only recently. Since the results of this thesis are not interpreted in detail by the quantum theories, they will only be outlined and their results will be stated.

(a) Valence bond theories. The VB calculations (16,17) did not give exact physical solutions since the method has a largely empirical origin. As in the elementary electrostatic models only four electrons were considered. Later Tsubomura (18) showed that four effects contribute to the hydrogen bond and that the agreement of the electrostatic model with experiment may be fortuitous since the three non-electrostatic effects may cancel each other. The four energies contributing to the hydrogen bond energy are: 1) the electrostatic energy, 2) the short-range repulsion energy, 3) the dispersion energy, and 4) the delocalization energy due to CT. Tsubomura characterized effects 2, 3 and 4 explicitly. He assumed there were 5 contributing resonant structures:

ψ_1	$X \text{---} H$	Y	covalent X-H
ψ_2	$X^- \quad H^+$	Y	pure ionic
ψ_3	$X^+ \quad H^-$	Y	pure ionic
ψ_4	$X^- \quad H \text{---} Y^+$		covalent H-Y CT
ψ_5	$X \text{---} H^- \quad Y^+$		covalent X-Y CT

Tsubomura's calculation showed that the delocalization energy amounts to 8.1 kcal/mole---about 1.5 times larger than the electrostatic energy. The repulsion energy and dispersion energy are of opposite sign to the delocalization energy and appear to cancel it.

The VB method has received more recent treatments (19,20). Hasegawa, Daiyasu and Yomosa (20) reported a four electron VB calculation of the hydrogen bond potential energy. They used Tsubomura's (18) 5 resonant structures and constructed the contributing ψ -functions from trigonal or tetrahedral Slater atomic orbitals. The proton potential was calculated as a function of $R(O \cdots O)$ and $r(O-H)$. As well, the shifts in $r(O-H)$ and ν_{OH}

upon hydrogen bonding were studied.

The calculations of Hasegawa et al. ignored the contributions of the CT structures, ψ_4 and ψ_5 , and resulted in an asymmetric, single minimum potential. They deduced that to account for $\Delta r(\text{O-H})$ and $\Delta \nu_{\text{OH}}$ the polarization of the surroundings must be considered, i.e. ψ_4 and ψ_5 must be included. When that was done a double minimum potential resulted.

One can summarize the VB theories by stating the following conclusions:

1) in addition to electrostatic forces other forces are important--dispersion, exchange repulsion and delocalization, 2) CT from Y to X is not negligible for short bonds but may be for long bonds, 3) the amount of CT changes very rapidly as a function of $r(\text{X-H})$ and $r(\text{X-Y})$ (the contribution of ψ_4 rises much faster (10 times) than the contributions of ψ_2 , ψ_3 and ψ_5).

(b) Charge transfer theories. Since a well developed theory for CT exists, several workers applied these techniques to the hydrogen bond (21, 22, 23). Bratoz (22) applied the CT theory to $\text{O-H}\cdots\text{O}$ with four electrons in three orbitals, the OH bonding and antibonding orbitals and the O lone pair orbital.

The conclusions Bratoz (7) reached from these CT theories are:

1) the VB picture of the hydrogen bond is valid, 2) since the H atom is small, the short range repulsive forces are small and the H atom has a special role for this kind of intermolecular interaction, 3) a fraction of an electron exists in the OH antibonding orbital, reducing the bond strength and allowing longer $r(\text{X-Y})$ and weaker X-H force constants, 4) CT theories predict an increased polarity in the $\text{O-H}\cdots\text{O}$ complex and therefore an increased infrared ν_{OH} intensity.

(c) Molecular orbital theories. The FHF anion has been examined in detail since it is relatively small with respect to physical size, bond length and number of electrons. Larger systems such as $(\text{H}_2\text{O})_2$, $(\text{HF})_2$, and $(\text{H}_2\text{S})_2$ cannot be treated exactly since drastic approximations must be made.

For $\text{O}-\text{H}\cdots\text{O}$ Weissmann and Cohen (24) found a very asymmetric single minimum potential, in contrast to the empirical double minimum result of Lippincott and Schroeder (25). Weissmann's results predicted an H_2O dipole moment of 2.40 D in ice, in good agreement with the experimental value of Eisenberg (5), 2.40-2.87 D, however, the method was less successful in predicting the $r(\text{X}-\text{H})$ and $r(\text{X}-\text{Y})$ distances. More recently, Rein, Clarke and Harris (26) studied the hydrogen bond of water by MO methods. The important point of this work is that the atomic charges and overlap populations indicate a substantial CT across the hydrogen bond.

Molecular orbital theories so far indicate 2 properties of hydrogen bonds: 1) formation of a hydrogen bond induces electron charge migration from the molecular core to the external region and 2) the $\text{H } 2p_\pi$ atomic orbital contribution to the ground state is not negligible--there is a small amount of π character in the hydrogen bond.

B. Spectroscopic Manifestations of Hydrogen

Bonding

As early as 1933 Bernal and Fowler (9) recognized in H_2O the large shift in ν_{OH} ($\Delta\nu_{\text{OH}} = \nu_{\text{OH}}(\text{vapour}) - \nu_{\text{OH}}(\text{hydrogen bonded})$) caused by hydrogen bonding. Infrared techniques still remain the most versatile tool to investigate the hydrogen bonds in vapours, liquids and solids. However, the relatively large electron migrations induced by hydrogen bonds give large

changes in nuclear shielding and shifts in the nmr transitions. The present work is concerned only with the ir manifestations of hydrogen bonding in the $O-H\cdots O$ system ice I and in clathrate-hydrates.

(i) The General Effects of Hydrogen Bonding

The four main spectroscopic effects in hydrogen bonded solids are often large in contrast to the small effects found between the vapour and solid phases of molecules incapable of hydrogen bonding. The first correlation made from the experimental data was the relationship between $R(X\cdots Y)$ and the ν_{XH} shifts from the monomer frequency in the bonded complex. Generally it is found that the shift, breadth and intensity of ν_{XH} depends on the strength of the hydrogen bond.

Those properties are largest for the strong hydrogen bonding system FHF^- , but are much smaller in the weak $NH\cdots N$ systems since the N van der Waal's radii are larger. The four effects will now be considered in detail.

(a) Frequency shifts. Not all of the molecular vibration frequencies are strongly affected by hydrogen bonding. The X-H stretching frequency is shifted to lower frequency by 10-50% of the vapour phase frequency and the R-X-H bending vibration experiences a relatively smaller shift to higher frequency. The novelty of the large stretching mode shifts can be grasped by comparing non-hydrogen bonding and hydrogen bonding molecules.

	(b)	Vapour	Solid	$\Delta\nu$
(a) no hydrogen bonding	CO_2	1285 cm^{-1}	1285 cm^{-1}	0 cm^{-1}
	CH_4	2914 cm^{-1}	2906 cm^{-1}	8 cm^{-1}
(b) hydrogen bonding				
i) FHF		HF vapour	(a) $(HF)_2$	(a) KHF_2
	ν_{HF}	4140 cm^{-1}	3440 cm^{-1}	1450 cm^{-1}
	$\Delta\nu$		-700 cm^{-1}	-2690 cm^{-1}
	$R(F\cdots F)$		2.55 Å	2.26 Å

(a) Nakamoto et al., Ref. 27. (b) CO_2 bonding mode.

Tables and plots of ν_{XH} as a function of $R(\text{X} \cdots \text{Y})$ were compiled by Nakamoto, Margoshes and Rundle (27) for the FHF, OHF, NHF, OHN, NHO, NHN, OHCl and NHCl families of hydrogen bonding compounds. For small $R(\text{X} \cdots \text{Y})$ the ν vs. R relationships are linear as Pimentel and Sederholm (28) proposed. For large $R(\text{X} \cdots \text{Y})$ the ν vs. R relationship is non-linear: the behaviour over all $R(\text{X} \cdots \text{Y})$ suggested an asymptotic relationship.

(b) Band broadening. An increased half-height width ($\Delta\nu^{\frac{1}{2}}$) is found for ν_{XH} and its overtones in hydrogen bonded systems (29). In contrast the effect is much smaller on the width of the R-X-H bending modes.

In the early work the explanation for broadening was thought to lie in the form of the intermolecular potential perturbation. Such an explanation is sufficient only for weak or moderate strength hydrogen bonds, but not for strong hydrogen bonds. Strong hydrogen bonds give broad bands in the vapour phase as well as in the liquid and solid phases. Hence the breadth is independent of the non-hydrogen bond intermolecular forces to the first order.

Bratoz and Hadzi (30) and Reid (31) suggested that the breadth arises from the anharmonicity perturbations and changes or differences in the anharmonicity over many molecules. Generalizing the discussions of ice they suggested that in all X-H...Y systems the breadth of the ν_{XH} absorption arises from a group of closely spaced bands.

(c) Band intensity. The integrated intensity coefficients often increase many-fold upon hydrogen bond formation. Also the overtones of ν_{XH} decrease in intensity. The apparent relationships among $\Delta\nu$, $\Delta\nu^{\frac{1}{2}}$ and intensity (large shift, broad band, large intensity) do not necessarily hold for all types of hydrogen bonding complexes.

There is little reliable data on integrated intensities due to experimental difficulties, however, early work by Huggins and Pimentel (29) established that hydrogen bonded complexes which show no increase in the intensity of ν_{XH} appeared to have non-linear hydrogen bonds.

The increased intensity of ν_{XH} and the unaffected intensity of ν_{R} cannot be explained by electrostatic theories of the hydrogen bond: Electrostatics requires that both ν_{XH} and ν_{R} increase in intensity. However, CT theories predict that only ν_{XH} increases in intensity.

(d) New absorptions. For $\text{X-H}\cdots\text{Y}$ systems new bands appear in the spectra associated with the deformation of the hydrogen bond. In ice the hydrogen bond stretch and hydrogen bond bend correspond to molecular translation (ν_{T}) and molecular libration (ν_{R}) modes, the so-called lattice modes.

(ii) The O-H \cdots O Hydrogen Bond Effects

The discussions here have so far been concerned with correlations among different hydrogen bonding families. However, there is a very big problem involved in such comparisons, the different $\text{X-H}\cdots\text{Y}$ systems have differences in molecular polarizability, van der Waal's radii, sizes of orbitals, dispersion forces, etc. Therefore one must expect different relationships among $\Delta\nu_{\text{XH}}$, $\Delta\nu_{\text{XH}}^{1/2}$, intensity and $R(\text{X}\cdots\text{Y})$. These parameters in cubic ice I and the clathrate-hydrates can best be compared to other O-H \cdots O systems and preferably to other H_2O allotropes, i.e., the high pressure ices.

In order to study ν_{XH} as a function of $R(\text{O}\cdots\text{O})$, Nakamoto et al. (27) compiled $\Delta\nu_{\text{OH}}$ and $R(\text{O}\cdots\text{O})$ data for 26 compounds. As well, they correlated $R(\text{O}\cdots\text{O})$ to $r(\text{O-H})$ from neutron diffraction data. The results indicate

that as $R(O\cdots O)$ decreases then $r(O-H)$ increases linearly for long hydrogen bonds and exponentially for strong (short) hydrogen bonds. They felt that inclusion of covalency in the hydrogen bond was important, as in Tsubomura's (18) work.

In order to understand the potential energy of the proton as a function of $R(O\cdots O)$, Lippincott and Schroeder (25) constructed a one dimensional model of the hydrogen bond. By applying the conditions of equilibrium, they obtained relations for $\Delta\nu_{OH}$, $r(O-H)$, hydrogen bond energy and force constants as a function of $R(O\cdots O)$. Their results agree well with experiment: for ice, where $R(O\cdots O) = 2.76 \pm 0.1 \overset{\circ}{\text{A}}$, their relationship between ν_{OH} and $R(O\cdots O)$ is linear. Unfortunately their formulas are not good for predicting the ν_{OH} of ice over a small range of $R(O\cdots O)$ since there is some arbitrariness in defining the hydrogen bond dissociation energy.

Reid (31) constructed the potential surface for simultaneous H and O motion in $O-H\cdots O$ hydrogen bonds over a wide range of $R(O\cdots O)$ and $r(O-H)$. He modified the Lippincott-Schroeder potential by changing the hydrogen bond dissociation energy from molecule to molecule, i.e., with changing $R(O\cdots O)$. Reid used his potential functions to interpret the changes in ir results with changes in crystalline lattice dimensions.

He proposed that the breadth of ν_{OH} was due to its strong dependence on $R(O\cdots O)$. During any ν_T vibration many $R(O\cdots O)$ distances occur and many ν_{OH} 's are observed.

Recently Bellamy and Pace (32) reviewed the relations among $\Delta\nu_{XH}$ and $R(X\cdots Y)$. They deduced that X and Y can approach only to the combined van der Waal's radii, further approach of X and Y is permitted only if

hydrogen bonding occurs. For example in the $\text{O}-\text{H}\cdots\text{O}$ system the van der Waal's radii give an $\text{O}\cdots\text{O}$ closest approach distance of $3.6 \overset{\circ}{\text{\AA}}$. The weakest hydrogen bond has an $R(\text{O}\cdots\text{O})$ of $3.36 \overset{\circ}{\text{\AA}}$, therefore $R(\text{O}\cdots\text{O})$ contracts upon formation of the hydrogen bond. Extrapolations of the X-Y plots of Nakamoto et al. indicated that the limiting $R(\text{X}\cdots\text{Y})$ is the sum of X and Y van der Waal's radii but not including H:

$$\text{FHF}^- \text{ intercept } 2.7 \overset{\circ}{\text{\AA}} \text{ (calc. } 2.7 \overset{\circ}{\text{\AA}})$$

$$\text{OH}\cdots\text{O} \text{ intercept } 2.84 \overset{\circ}{\text{\AA}} \text{ (calc. } 2.8 \overset{\circ}{\text{\AA}})$$

This suggested that in hydrogen bonds the H orbital disappears or is completely overlapped and that there is no repulsion due to it.

Bellamy and Owen (33) extended this idea and proposed that the rate of increase of repulsion is proportional to the rate of increase in lone pair - lone pair repulsions. They adopted the 6-12 potential to describe the repulsive terms from lone pairs in X and Y and finally obtained an expression relating $\Delta\nu_{\text{XH}}$ and $R(\text{X}\cdots\text{Y})$. For $\text{O}-\text{H}\cdots\text{O}$ this has the form

$$\Delta\nu_{\text{OH}} = .50 \left[\left(\frac{3.35}{R} \right)^{12} - \left(\frac{3.35}{R} \right)^6 \right].$$

This relationship gives good agreement with the work of Nakamoto et al.

However by inspection of Nakamoto's work one sees that no unique $\nu_{\text{OH}} - R(\text{O}\cdots\text{O})$ relation exists for the $\text{O}-\text{H}\cdots\text{O}$ family. There are too many variables. It seems more reasonable to study one molecular system like H_2O in a variety of crystal habits and to attempt to vary only $R(\text{O}\cdots\text{O})$ in some way. For example, a study of H_2O in all 9 ice phases and in clathrate-hydrates as a function of temperature may provide useful results.

Clathrate-Hydrates

A. The Clathrate-Hydrate Problem

Quantized rotation or libration of trapped (guest) molecules in the (host) lattice cavities has been suggested by previous ir (34,35) and nmr (36,37) studies. Now detailed ir assignments of the guest rotations and their behaviour in the host cavity are required to determine the form of the potential well surrounding the guest molecules. In order to determine the changes in the interactions of the guest molecules with the host lattice and the height of the barrier to guest rotations, it is necessary to know precisely how the guest molecule absorptions and host lattice absorptions vary as a function of temperature.

B. The Structures of the Clathrate-Hydrates

Clathrates are a type of inclusion compound in which one stable molecule forms a union with 2 or more other stable molecules, atoms or molecular elements without the existence of chemical bonds between the components. (The enclosing lattice which contains the cavities is called the host and the enclosed molecule is called the guest.) A common property of some important clathrate compounds is hydrogen bonding. Some examples of clathrates are:

- 1) β -quinol clathrates, $0.74 \text{ Kr} \cdot 3 \text{ C}_6\text{H}_4(\text{OH})_2$
- 2) gas hydrates, $\text{Ar} \cdot 7.67 \text{ H}_2\text{O}$
- 3) tetraalkylammonium clathrates, salt hydrates

$$[(n - \text{C}_4\text{H}_9)_4\text{N}] \text{C}_6\text{H}_5\text{CO}_2 \cdot 39.5 \text{ H}_2\text{O}$$
- 4) $\text{Ni}(\text{CN})_2 \cdot \text{NH}_3 \cdot \text{C}_6\text{H}_6$

A clathrate-hydrate is a clathrate compound formed with an H_2O host lattice in which a variety of small atoms and covalent molecules are trapped. The clathrate-hydrates can be separated into two classes: The gas hydrates are clathrates formed between H_2O (host) and small, covalent gases (guests, G) and liquid hydrates are clathrates formed between H_2O (host) and molecules of volatile liquids (guests, G).

Three crystal structures have been found for the clathrate-hydrates. The so-called gas hydrate clathrates, Type I, are cubic and have maximum ideal stoichiometries of $8\text{G} \cdot 46\text{H}_2\text{O}$ or $6\text{G} \cdot 46\text{H}_2\text{O}$. The so-called liquid clathrate-hydrates, Type II, are also cubic and have maximum ideal stoichiometries of $8\text{G} \cdot 136\text{H}_2\text{O}$ or $16\text{G} \cdot 8\text{G} \cdot 136\text{H}_2\text{O}$. Bromine liquid clathrate-hydrate, Type III, is tetragonal and has a maximum ideal stoichiometry of $20\text{G} \cdot 172\text{H}_2\text{O}$.

(i) Type I Clathrate-Hydrates

These compounds form a cubic crystal of $\text{Pm}\bar{3}\text{n}$ symmetry (38,39) with a 12 \AA unit cell edge and 46 H_2O molecules in a unit cell. Two pentagonal dodecahedrons are formed by 20 H_2O molecules each. Those two cavities are linked by the remaining 6 H_2O molecules to form 6 tetrakaidecahedra, giving a total of 8 cavities per unit cell.

In Type I clathrate-hydrates the nearly spherical pentagonal dodecahedra have free diameters of 3.95 \AA and the spheroidal tetrakaidecahedra have free diameters of 5.8 \AA (for a 12.0 \AA unit cell). Molecules and atoms whose maximum dimensions are less than 5.1 \AA can fill all 8 cavities and would have an ideal clathrate stoichiometry of $8\text{G} \cdot 46\text{H}_2\text{O}$ (i.e. $\text{G} = \text{Ar}, \text{CH}_4, \text{H}_2\text{S}$). Molecules and atoms whose maximum dimensions are less than 5.8 \AA but are larger than 5.1 \AA will fill only the 6 tetrakaidecahedra and would have

Table 0.1 Some typical clathrates and their properties.

P_{diss} gives the clathrate decomposition pressure at 0°C ,

T_{max} gives the maximum stable temperature of the clathrate and

T_{b} gives boiling temperature of pure guest.*

Type	Clathrate	a_{o} c_{o}	P_{diss} at 0°C	T_{max}	T_{b} G
	$8\text{G}\cdot 46\text{H}_2\text{O}$	$\overset{\circ}{\text{A}}$		$^{\circ}\text{C}$	$^{\circ}\text{K}$
	Ar	--	95.5 atm	--	83
	Kr	--	14.5	--	121
	Xe	11.97	1.15	--	166
I	H_2S	12.00	698 Torr	29.5	213
(cubic)	$6\text{G}\cdot 46\text{H}_2\text{O}$				
	Cl_2	12.03	252	28.7	239
	CH_3Cl	12.00	311	2.1	249
	CH_3Br	12.09	187	14.5	277
	SO_2	11.94	297	12.1	263
	$8\text{G}\cdot 136\text{H}_2\text{O}$				
	CH_3I	17.14	74	4.3	316
	CHCl_3	17.30	50	1.6	334
II	$\text{C}_2\text{H}_5\text{Br}$	17.26	155	--	311
(cubic)	CH_2Cl_2	17.31	116	1.7	315
	C_3H_8	17.40	(1.74 atm)	5.69	228
	$\text{C}_2\text{H}_5\text{Cl}$	17.30	201	4.8	286
	$20\text{G}\cdot 172\text{H}_2\text{O}$				
III	Br_2	a_{o} 23.8	43.90	5.81	332
(tetrag)		c_{o} 12.2			

* Reference 40

$6G \cdot 46H_2O$ stoichiometry (Cl_2 , SO_2 , C_2H_6). Some properties of the clathrates formed in these two ratios are given in Table 0.1. One may also form a mixed hydrate of the form $2G \cdot 6G' \cdot 46H_2O$, i.e. $2H_2S \cdot 6C_2H_6 \cdot 46H_2O$.

In the practical situation the unit cell dimension varies according to the size of the guest species, Table 0.2.

(ii) Type II Clathrate-Hydrates

These compounds form a cubic crystal of $Fd3m$ (38) symmetry with a 17 \AA unit cell edge and 136 H_2O molecules in a unit cell (i.e. $G = CH_3I$, $CHCl_3$, C_2H_5Br). There are 16 pentagonal dodecahedral cavities and 8 hexakaidecahedral cavities in one unit cell. The free diameters are 5.0 and 6.7 \AA respectively (for a 17.4 \AA unit cell).

Molecules which have a maximum dimension greater than 5.8 \AA and less than 6.7 \AA cannot form Type I clathrates, but do form Type II clathrates. That implies they occupy only the hexakaidecahedra with an ideal stoichiometry of $8G \cdot 136H_2O$. Some Type II clathrates, the guest sizes, and the unit cell dimensions are given in Tables 0.1 and 0.2.

(iii) Type III Clathrate-Hydrates

The clathrate-hydrate of Br_2 was originally thought to be of Type II. However, work by Allen and Jeffrey (41) has shown that it forms a tetragonal crystal of symmetry $4/mmm$ with $a = 23.8$ and $c = 12.2 \text{ \AA}$ unit cell edges and 172 H_2O molecules in a unit cell. They reported 20 polyhedral cavities large enough to accommodate Br_2 molecules, 10 small pentagonal dodecahedra, 16 tetrakaidecahedral and 4 pentakaidecahedral. The ideal stoichiometry is then $20Br_2 \cdot 172H_2O$. Some data are given in Tables 0.1 and 0.2.

Table 0.2 The types of cavities, the maximum allowed occupancy, guest sizes and unit cell dimensions of typical clathrate-hydrates.

Type	Clathrate	a_o c_o	Guest size	Allowed V_{12}	occupancy of cavities V_{14}	V_{15}	V_{16}
I (cubic)	$8G \cdot 46H_2O$	$\overset{o}{A}$	$\overset{o}{A}$				
	Ar	--	3.76	2(2)*	6(6)		
	Kr	--	4.04	2	6		
	Xe	a_o 11.97	4.40	2	6		
	H_2S	12.00	4.40	2	6		
	$6G \cdot 46H_2O$						
	Cl_2	12.03	5.17	0(2)	6		
	CH_3Cl	12.00	5.06	0	6		
	CH_3Br	12.09	5.33	0	6		
	SO_2	11.94	5.00	0	6		
II (cubic)	$8G \cdot 136H_2O$						
	CH_3I	17.14	5.70	0(16)			8(8)
	$CHCl_3$	17.30	6.44	0			8
	C_2H_5Br	17.26	6.47	0			8
	CH_2Cl_2	17.31	6.08	0			8
	C_3H_8	17.40	6.28	0			8
	C_2H_5Cl	17.30	6.20	0			8
III (tetrag)	$20G \cdot 172H_2O$						
	Br_2	a_o 23.8 c_o 12.2	5.68	0(10)	16(16)	4(4)	

V_{12} -- pentagonal dodecahedron, $V_{14,15,16}$ - tetrakai, pentakai, hexakaidodecahedrons.

* - numbers in brackets show maximum number of cavities per unit cell.

Since the present experiments attempt to accurately correlate ν_{OH} and $R(O\cdots O)$ for seven Type I, II, and III clathrate-hydrates, the $R(O\cdots O)$ distances are required. However, the structures were determined by assuming constant $R(O\cdots O)$ throughout the unit cell, e.g. $2.81 \overset{\circ}{\text{\AA}}$ for a Type I clathrate ($12.0 \overset{\circ}{\text{\AA}}$ unit cell) and $2.78 \overset{\circ}{\text{\AA}}$ for a Type II clathrate ($17.3 \overset{\circ}{\text{\AA}}$ unit cell). In order to accomodate the pentagonal dodecahedra and other polyhedra in the unit cell, the O-O-O angles were distorted from tetrahedral. Von Stackelberg (38) reported angles from 100.0° to 124.6° . It seems likely that in reality the $O\cdots O$ distances are also irregular and a range of $R(O\cdots O)$ exist for each clathrate-hydrate. That will unfortunately broaden the ir results even more than in ice I.

Indeed for Type I clathrate-hydrates (cubic, $Pm3n$) the H_2O oxygen atoms lie on 3 unit cell sites (k, i, and c). Consequently, there are 4 types of hydrogen bonds; k-k, k-i, k-c, i-i. It seems reasonable that these may not be identical in the real crystal.

C. Formation of Clathrate-Hydrates

A general phase diagram was proposed by Roozeboom and is shown in von Stackelberg's work (38). At constant temperature there are 2 boundary conditions to permit formation of clathrate-hydrates, raising the pressure of G to form either guest G(gas) or G(liquid) plus hydrate. If the partial pressure of guest applied to the sample is less than the equilibrium dissociation partial pressure then the clathrate dissociates.

In a recent review Byk and Fomina (42) discussed the conditions for formation and the thermodynamics of formation. As well, Barrer and Ruzicka (43) studied the kinetics of rare gas clathrate formation at low temperatures.

Specifically, they investigated the formation of clathrate-hydrate from ice and Ar, Kr and Xe gases at 90°K and 195°K.

Their technique involved depositing a thin layer of H_2O in a glass bulb at 77°K. The sample was warmed to 195°K and either Ar, Kr or Xe (190 Torr) was admitted. The gas uptake as a function of time was measured. They found that Kr and Xe, but not Ar, reacted with ice at 195°K. Ar was found to react slowly at 90°K at 190 Torr. Their results suggested the ready formation of clathrate-hydrates at low temperatures with a critical formation pressure of less than 190 Torr.

D. Previous Investigations of the Clathrate-Hydrates

Contemporary interest in clathrates has been centered on the motion of the guest molecules in the host lattices. Thus the methods of dielectric relaxation (44-46), x-ray diffraction (38,47), nmr (48-51), thermodynamics (38), and ir spectroscopy (52-57, 34) have been applied to quinol clathrates and clathrate-hydrates to discover whether guest rotations are free or restricted, how fast they rotate, and what are the barriers to free rotation. Similarly, deductions with respect to hindered translations (rattling) of the guest have been made (48-51).

The first work on clathrate-hydrates in the ir was reported by McCourt (56). He studied the three Type I clathrate-hydrates of Ar, Kr, and SO_2 . The main points of his thesis were: 1) there was an H_2O host band at 2425 cm^{-1} in addition to the well known ice absorptions, 2) the ν_R band was shifted -50 cm^{-1} from ice I, 3) the 1600 cm^{-1} and 2210 cm^{-1} absorptions of the host were ν_2 (HOH bending) and $\nu_2 + \nu_R$ respectively, 4) SO_2 absorbed at 2455 cm^{-1} and 3570 cm^{-1} (a weak shoulder on ν_1 and ν_3 , the symmetric and

assymmetric stretches, of H_2O) in the clathrate-hydrate.

Shurvell (57) followed up the above work by observing SO_2 , H_2S , and Kr Type I clathrate hydrates ($8\text{G}\cdot46\text{H}_2\text{O}$). For $\text{SO}_2\cdot7.67\text{H}_2\text{O}$ Shurvell reported: 1) that $\nu_{\text{R}}(\text{H}_2\text{O})$ was 40 cm^{-1} less than that of ice, 2) that the 1600 cm^{-1} band of ice was at 1640 cm^{-1} in the clathrate and was therefore ν_2 rather than $2\nu_{\text{R}}$, 3) that the 2230 cm^{-1} was $\nu_2 + \nu_{\text{R}}$, and 4) that H_2O in clathrates had a new feature at 2410 cm^{-1} in addition to the ice bands. As well, he found that the $\nu_3(\text{SO}_2)$ had a central peak and 2 wings, 1336, 1342 and 1348 cm^{-1} . There was no splitting of $\nu_3(\text{SO}_2)$ as in the pure SO_2 solid and the clathrated SO_2 bands were broadened by "rattling" and rotational fine structure. The wings were thought to be due to combinations with librations (hindered rotations) and translations.

Both McCourt (56) and Shurvell (57) formed the clathrate-hydrates by condensation of stoichiometric gas mixtures on CsI windows at 77°K . Shurvell reported his samples were annealed to devitrify the condensed phase. The results of these preliminary investigations on Type I clathrate-hydrates were summarized by Harvey, McCourt and Shurvell (34).

E. The Present Approach to the Clathrate-Hydrate Problem

Three facets of the clathrate-hydrate ir absorptions were studied in this work. First, in order to analyze previous work (56,57), the forms of the clathrate-hydrate absorptions were determined from low temperature mulls of solid clathrate samples. Secondly, the vitreous-crystalline phase transformation was observed by ir spectroscopy as a function of temperature for clathrate-hydrates (types I, II and III) condensed from gaseous stoichiometric

mixtures. Thirdly, the temperature dependences were determined for the ir absorption of devitrified "clathrate" samples.

Ice

A. The Ice Problem

Many theories have been proposed to explain the origins of the frequency shifts, the large band widths and the large intensities in ice. Now data are required which will either support an existing theory or which will suggest some modifications to the theory. Specifically, the correlations of absorption band frequencies, widths and heights to $\Delta R(0 \cdots 0)$ are required for ice I.

B. Non-Spectroscopic Investigations of Ice

(i) Structural Studies

Ice exists in at least twelve^{*} structural allotropes above 77°K and at pressures of up to 25,000 atmospheres. The ice phases stable at 1 atmosphere are all called ice I. In fact, there are three allotropes of ice I, the vitreous or amorphous, the cubic and the hexagonal phases (Iv, Ic and Ih). The ice I structural results up to 1958 were summarized by Lonsdale (58) and Owston (59). Recently, Brille and Tippe (60) measured by x-ray diffraction the ice Ih lattice parameters between 15° and 200°K. As well, Arnold, Finch, Rabideau and Wenzel (61) reported a neutron diffraction study of ice Ic.

(a) Hexagonal ice I. The ordinary phase of ice at S.T.P. is hexagonal ice I (Ih) in which the oxygen atoms form a $P6_3/mmc$ unit cell with 4 molecules.

* Assuming solid polywater is a unique solid of H_2O .

The unit cell dimensions are (62);

	a_0	c_0
H_2O (163°K)	4.493 Å	7.337 Å
D_2O (143°K)	4.495	7.335

The oxygen-oxygen nearest-neighbour distances ($R(O \cdots O)$) in H_2O are 2.76 Å at 163°K. The molecules are hydrogen bonded to 4 nearest-neighbours in layers of hexagonal, puckered rings. The open structure has channels parallel and perpendicular to the c_0 axis.

There is still some uncertainty about the unit cell dimensions of ice Ih. The disagreement between Lonsdale's (58) expansion coefficients and the direct dilatometric measurements seems to arise from differences in crystallinity among the worker's samples. The x-ray diffraction work of La Placa and Post (63) agrees well with Dantl's (64) direct thermal expansion measurements: La Placa and Post's (63) work was confirmed by Brille and Tippe (60). The latter found that the c/a ratio is temperature independent, not reaching 1.633 even at 15°K; they found $c/a = 1.6280 \pm 0.0002$.

(b) Amorphous ice I. This phase is formed by the slow condensation of vapour onto a cold surface. Beaumont, Chihara and Morrison (65) found that amorphous ice I was formed when the deposition rate at 135°K was less than 0.04 g/cm²/hour. The x-ray and electron diffraction patterns are diffuse and the samples are clear, transparent films. The samples have consequently been variously described as vitreous, amorphous or microcrystalline. Virtually nothing is known about the structure of amorphous ice I.

(c) Cubic ice I. Ice Ic can be formed by the irreversible transformation of amorphous ice I or from the high pressure ices. The vitreous-cubic ice I transformation has been reported to start as low as 110°K and as high

as 153°K by various authors, Table 0.3. The high pressure ice-cubic ice transformations have been studied by Bertie, Calvert and Whalley (66) at 77°K by release of pressure. Cubic ice I can also be formed by vapour condensation between 133° and 153°K. When warmed above 210°K cubic ice I transforms irreversibly to hexagonal ice I with a small enthalpy change, i.e. <1.5 cal/gm (65).

The crystal structure of the oxygen atoms in cubic ice I is the "diamond" structure, $Fd\bar{3}m$ with 8 molecules per unit cell. The oxygens are arranged in a similar fashion to that of hexagonal ice in layers of puckered hexagonal rings. However, the six O atoms adjoining 2 nearest-neighbours are eclipsed in cubic ice I and staggered in hexagonal ice I. The lattice parameters (62) at 143°K are $a_o(H_2O) = 6.350 \overset{\circ}{\text{Å}}$ and $a_o(D_2O) = 6.351 \overset{\circ}{\text{Å}}$.

(d) Disorder in Ice I. The neutron diffraction work of Peterson and Levy (quoted in Lonsdale (58)) showed that each oxygen was surrounded by four 1/2 hydrogens at $1.01 \overset{\circ}{\text{Å}}$. They asserted that the DOD angle = 000 angle and, therefore, that the hydrogen bonds are linear. Their results were the same at 123° and 223°K, indicating no ordering of the lattice down to 123°K. Pauling predicted a residual entropy at 0°K of $R \ln 3/2$ or 0.805 e.u. However, Onsager and Dupuis (67) showed that Pauling's result is only the lower bound to the true calculated value. Nagle (68) found by lattice statistics that the theoretical value is 0.8145 ± 0.0002 e.u., compared to an experimental value of 0.82 ± 0.15 e.u. Disorder in cubic ice I was confirmed by electron diffraction(69).

Pitzer and Polissar (70) discussed the order-disorder problem in ice I and concluded that the ordered structure is more stable at low temperatures. However, they estimated that the transformation time may exceed a day. They

Table 0.3 Temperature ranges of stability at 1 atmosphere of vitreous, cubic and hexagonal ice I by several experimental methods.

Technique	Low Temperature Phase and Range °K	Cubic Phase Range °K	Hexagonal Phase Range °K	Workers
heat capacity	77 - 144 amorphous	crystalline 144 --	273	Pryde <u>et al.</u> (a)
elect.diffraction	77 - 107	107 - 190	190 - 273	Honjo <u>et al.</u> (b)
calorimetry	77 -(150 ± 10) amorphous	crystalline 150 --	273	de Nordwall <u>et al.</u> (c)
elect.diffraction	77 - 151 amorphous	151 - 173	173 - 273	Blackman <u>et al.</u> (d)
x-ray diffraction	77 - 110 amorphous	113 - 143	143 - 273	Dowell <u>et al.</u> (e)
diff.therm. anal.	77 - 149 glass	149 - 186	186 - 273	McMillan <u>et al.</u> (f)
x-ray diffraction	77 -(148 ± 8) amorphous	(148 ± 8) - (220±20)	220±20 - 273	Beaumont <u>et al.</u> (g)
thermal analysis	77 - 154 amorphous	154 - 208	208 - 273	Ghormley (h)
calorimetry	77 - 135 amorphous	135 - 160	160 - 273	Sugisaki <u>et al.</u> (i)

(a) Ref. 71, (b) Ref. 69, (c) Ref. 72, (d) Ref. 73, (e) Ref. 74, (f) Ref. 75, (g) Ref. 65,
(h) Ref. 76, (i) page 329, Ref. 6.

also estimated the Curie point to be near 60°K.

(e) High pressure ices. The allotropes of ices II through IX may not constitute all possibilities. More allotropes may exist below 77°K and at higher pressures. Some of the crystallographic properties and structural parameters of the ice allotropes are given in Table 0.4. Phases II, VIII and IX are ordered and all others are disordered with respect to proton position. The higher densities of the high pressure ices derive not from shorter R(O....)) but from distorted hydrogen bonds. The distortions result in much closer (3.2 Å) next-nearest-neighbours compared to ice Ih(4.5 Å). There is considerable distortion of the HOH angles: Ice II has 18 HOH angles between 80° and 128°.

(ii) Electrical Properties of Ice

Recently dielectric constant work was reported by Wilson et al. (77) and by Whalley and Heath (78). In general, they found that ice I has a large reciprocal dielectric relaxation constant (about 10^5 reorientations per second), and that the disordered high pressure ices have even larger τ_d^{-1} 's. The τ_d^{-1} 's of ordered ices, however, are small (no reorientations). The τ_d^{-1} of ice I increases very rapidly with decreasing temperature due to the increasing electric field of the approaching neighbouring molecules: τ_d^{-1} is 2000 times larger at 208°K than at 273°K. An accepted mechanism of reorientation invokes the migration of Bjerrum (79) D- and L- defects.

(iii) Thermodynamic Properties of Ice

There is support for some ordering in ice Ih from heat capacity (C_p) and electricity measurements. Helmreich and Riehl (80) deduced from electricity measurements that the proton disorder is partially removed as

Table 0.4 Physical properties of the ices.*

ICE	Ih	Ic	II	III	IV	V	VI	VII	VIII	IX
Crystal System	Hexag.	Cub.	Rhomb.	Tetrag.	Monocl.	Monocl.	Tetrag.	Cub.	Cub.	Tetrag.
Space Group	$P6_3/mmc$	$Fd3m$	$R\bar{3}$	$P4_1 2_1 2$	$A2/a$	$A2/a$	$P4_2/mmc$	$Im3n$	$Im3m$	$P4_1 2_1 2$
Z	4	8	12	12	28	28	0	2	2	12
Density g/cm ³	0.94	--	1.17	1.14		1.23	1.31	--	1.50	
No.n-neighbours	4	4	4	4	4	4	4	8	8	4
R n-neighbours	2.74	2.75	2.75	2.76		2.76	2.81	2.86	2.86	
R n.n-neighbours $\begin{smallmatrix} \circ \\ \text{A} \end{smallmatrix}$			-2.84	-2.80		-2.87				
R n.n-neighbours $\begin{smallmatrix} \circ \\ \text{A} \end{smallmatrix}$	4.49	4.50	3.24	3.47		3.28 3.46	3.51	2.86	2.86	
O.....O.....O angle deg	109.5	109.5	80 -128	87 -141		84 -135	76 -128	100.5	109.5	
4 positions	disord.	disord.	ord.	disord.	ord.	disord.	disord.	disord.	ord.	ord.

* Table from ref. (5).

temperature decreases. The effects found were small and they therefore deduced a small fraction of the sample was ordered: A finite number of ordered domains in a disordered continuum. Pick (81) also suggested that regions of short-range ordering are formed as the temperature of ice I is lowered. However, he pointed out that the D- and L- defects responsible for reorientation (ordering) decrease in number exponentially with decreasing temperature. Hence the time for establishing an ordered crystal increases exponentially as temperature decreases.

The heat capacity of ice Ih above 15°K was first investigated by Giauque and Stout (82). They found that the samples attained thermodynamic equilibrium in the range 85° to 115°K only slowly. The reason is not understood.

Recently Flubacher et al. (83) studied the ice Ih Cp below 15°K. They found Cp extrapolates to zero at 0°K and is consistent with a continuous decrease. As well they pointed out that the translational, librational and internal energies are separable and that the librational contribution to Cp is explained well by an average frequency for H₂O of 620 cm⁻¹.

Leadbetter (84), in a comprehensive interpretation of the ice I thermodynamics, explained Cp in terms of the excitation of translational (ν_T) and librational (ν_R) vibrations. Below 80°K, Cp was derived entirely from excitations of ν_T , while above 150°K ν_R gave a significant contribution. He also predicted that between 0° and 273°K the ν_T frequency shifts by $8 \pm 2\%$ and that ν_R shifts by $6 \pm 2\%$ for H₂O (for D₂O $10 \pm 2\%$ and $8 \pm 2\%$ respectively).

Blue's (85) elementary treatment of Cp gave a surprisingly good value for the librational average frequency, 660 cm⁻¹. He also gave a convenient formula for deducing the set of ir librational frequencies:

$$\nu_{R_n} = \frac{1}{2\pi c I_n} \left[\frac{1}{2} \sum_i k_{in} r_{in}^2 \right]^{\frac{1}{2}} \quad [1]$$

where I_n is the moment of inertia about axis n in gm/cm^2 ,

k_{in} is the force constant restraining atom i from rotation about axis n in dynes/cm,

r_{in} is the normal distance of atom i to axis n in cm,

c is the velocity of light cm/sec.

C. Spectroscopic Investigations of Ice

The effects of hydrogen bonding have been observed in 3 fields of spectroscopy; electronic, nmr and vibrational. For example, both red and blue shifts (from the non-hydrogen bonded frequency) are observed depending on whether the hydrogen bond is stronger in the ground electronic state or in the excited state. In nmr spectra the proton signals of (H atoms in) hydrogen bonded molecules are shifted to a lower field than for the non-hydrogen bonded molecule. In ice, nmr has been used to find proton separations and to determine charge redistributions.

Vibrational studies of ice have been made by neutron inelastic scattering, Raman, and infrared spectroscopy. The previous work will be considered in two sections, modes occurring below and above 1000 cm^{-1} (the fundamental lattice and molecular mode regions). The results of previous works are tabulated in Chapter 3 for comparison to the results of the present work.

The H_2O molecule has 3 molecular vibrations; a symmetric and an asymmetric stretch and a symmetric HOH bend ($\nu_1(a_1)$, $\nu_3(b_1)$ and $\nu_2(a_1)$ respectively). In cubic ice I ($\text{Fd}3\text{m}$) with 2 molecules per primitive unit cell ($Z = 2$) there are $(3n)Z$ (where n is the number of atoms/molecule) or

18 crystal vibrations. Of those, $(3n-6)Z$ or 6 of these are molecular vibrations, $3Z$ or 6 are rotatory in nature, $3(Z-1)$ or 3 are translatory vibrations and 3 are simple translations of the complete unit cell. Hence in a mole (N) of unit cells there are $6N$ molecular vibrations, $6N$ rotatory vibrations, $3N$ optical translations and $3N$ acoustical translations.

Ice spectra are characterized by 5 very broad bands. Two bands occur below 1000 cm^{-1} in the H_2O ices. A band with at least 6 features and centred near 230 cm^{-1} is attributed to hydrogen bond stretching modes, the lattice translational modes ν_T . A band with from 3 to 16 features and centered near 830 cm^{-1} is attributed to hydrogen bond bending modes, the lattice hindered rotational modes, ν_R .

Between 1000 and 4000 cm^{-1} 3 bands are observed. The band near 1630 cm^{-1} has been attributed to $2\nu_R$, ν_2 or to overlapping $2\nu_R/\nu_2$. The band near 2200 cm^{-1} has been assigned to $\nu_2 + \nu_R$ or $3\nu_R$. The features of the 3200 cm^{-1} band have been assigned by various authors to: 1) $2\nu_2$, ν_3 , ν_1 (105), 2) ν_1 , ν_3 , $\nu_3 + \nu_T$ (108), and 3) all as $\nu_{\text{OH}}(\text{H}_2\text{O})$ (95). The vapour, liquid and ice I frequencies, with the various assignments are given in Table 0.5.

The analysis of the vibrations of crystalline materials usually begins with a factor group analysis based on the known diffraction symmetry, i.e. based on oxygen atoms and $\frac{1}{2}\text{H}$ atoms. Now the disordered H positions are averaged in the time of a diffraction experiment, while in vibration spectroscopy the instantaneous symmetry of the unit cell is important.

(i) The Lattice Modes

(a) Translations. For ices Ih and Ic the factor group analysis, based on symmetric $\frac{1}{2}\text{H}$ positions and the above diffraction symmetries, pre-

Table 0.5 H₂O vapour, liquid and ice Ih infrared absorption frequencies, half-height widths and intensities and the divergent assignments made to the bands of ice.

	(a) Vapour	(b) Liquid	(c) Ice I	(d) Ice $\Delta\nu^{1/2}$	(d) Ice Peak Height	(c) Ockman 1957	(e) Hornig 1958	(f) Pimentel 1959	(g) Whalley 1964
H ₂ O	cm ⁻¹	cm ⁻¹	cm ⁻¹	cm ⁻¹					
(D ₂ O)		160	232		weak	ν_T		ν_T	ν_T
		(170)	(218)						
		650	800	200	strong	ν_R	ν_R	ν_R	ν_R
		(500)	(590)						
1595	1570,1645	1640	250	med.	ν_2	ν_2	ν_2	ν_2	$\nu_2, 2\nu_R$
(1178)	(1160,1210)	(1210)	(150)						
	2130	2225	200	weak	$\nu_2 + \nu_R$	$3\nu_R$	$3\nu_R$	$3\nu_R$	$3\nu_R, \nu_2 + \nu_R$
	(1620)	(1620)	(180)						
3657	3219	3142			ν_1	$2\nu_2$			$\nu_{OH}(H_2O)$
(2671)	(-)	(2347)		very					
3756	3445	3252	300	strong	ν_3	ν_3			$\nu_{OH}(H_2O)$
(2788)	(2500)	(2440)	(250)						
		3352			$\nu_3 + \nu_T$	ν_1			
		(2514)							
HDO		810 ^d			weak		ν_R		ν_R
		(600) ^d					ν_R		ν_R
3707	3405	3275	80	very		ν_{OH}			ν_{OH}
(2727)	(2520)	(2416)	(2)	strong		ν_{OD}			ν_{OD}

(a) Ref. 116, (b) Ref. 98, (c) Ref. 108, (d) Ref. 106, (e) Ref. 105, (f) Ref. 97, (g) Ref. 95.

dicts 9 optical modes for Ih (A_{1g} , B_{1g} , B_{2u} , E_{1g} , E_{2g} , and E_{2u}) and 3 optical modes for Ic (F_{1g}). The normal $k = 0$ selection rules predict that all these modes are ir inactive and that all g modes are Raman active. However, ir translational absorption (ν_T) is observed (86) for both Ih and Ic ices. In fact the absorptions are nearly identical. The factor group analysis fails for ν_T of hexagonal and cubic ices, as well as for the other disordered ices, V and VI (86).

In contrast, the factor group analysis works well for ν_T of ices II and VIII, the ordered H atom ices (86).

The H atoms in ice Ic are not symmetrically placed along $R(0 \cdots 0)$ in the unit cell. Even if the H atoms were perfectly ordered, with 2 near and 2 away from each O atom, the crystal symmetry of ice Ic could not be $Fd3m$ since the T_d symmetry would be destroyed. One might expect ice Ic to order itself in a sub-group of $Fd3m$ or similar to one of the structures in ices II, VIII or IX ($R\bar{3}$, $Im3n$ or $P_{41}2_12$). Then the ν_T modes may not be all inactive in the ir. If short range ordering is present (as suggested before) then the effective crystal symmetry may be a subgroup of S_6 , O_h or D_4 , since the nearest molecules determine the effective potential at the central molecule.

(b) Disorder theory. Whalley and Bertie (87) proposed a theory to explain the activity of lattice modes in orientationally disordered crystals. They considered ice Ic to have (near) positional symmetry (order) of the O atoms but orientational disorder of the H atoms. They suggested that the result is a small effect on the mechanical form of the translational vibrations, therefore the translational modes are mechanically regular. However, since in the course of a vibration $\Delta\mu$ varies according to the local molecular orientations, then the crystal translational vibrations are electrically irregular.

Whalley and Bertie (87) assumed that the dipole derivative could be split into a symmetric part, M' , (corresponding to diffraction symmetry part) and an asymmetric, irregular part, M'' , due to the H atom disorder. Then they showed that the molecular intensity of absorption has a part for zero wave vector ($\underline{k} = 0$) transitions, which are the normal symmetry allowed transitions, and a finite intensity for all $\underline{k} \neq 0$ transitions due to M'' . Therefore they deduced that all translational vibrations are ir active.

In a subsequent paper Bertie and Whalley (88) used the above theory to describe the density of states in ν_T of ices Ih and Ic. They assigned the 229.2 cm^{-1} peak to degenerate longitudinal and transverse optical modes at the zone center, the 160 cm^{-1} peak to the longitudinal acoustical mode of a zone boundary, and the 190 cm^{-1} shoulder to the longitudinal optical mode at the same zone boundary. They showed a density of states curve for ices Ih and Ic.

As well, Bertie and Whalley (88) found that $\nu_T(\text{H}_2\text{O})$ shifted by 7 cm^{-1} to lower frequency upon raising the temperature from 100° to 168°K . They attributed the red shift to excitation of hot bands.

The results of $\nu_T(\text{H}_2\text{O})$ for vitreous ice I are conflicting (88,89). Giguere and Arraudeau (89) indicated considerable band structure.

(c) Raman spectra. Scattering from $\nu_T(\text{H}_2\text{O})$ was reported by Val'kov and Maslenskova (90) with a medium intensity peak at 230 cm^{-1} and weak features at 291 and 310 cm^{-1} . As well, Taylor and Whalley (91) reported the Raman spectra of ices Ih, Ic, II, III and II. They reported a peak at 225 cm^{-1} in ices Ic and Ih and at 151 cm^{-1} in ice II.

(d) Neutron inelastic scattering. Spectra were reported by Prask and Boutin (92) for ice Ih and Trevino (93) and Renker and Blanckenhagen

(94) calculated the ν_T spectra of ice I. The frequency distributions calculated and observed in neutron work agree quite well with Bertie and Whalley's (88) predictions from the ir.

(e) Libration. Hydrogen bonding also gives rise to hindered rotational transitions in the ices. For H_2O this absorption is seen from $1000 - 400\text{ cm}^{-1}$ and for D_2O from 750 cm^{-1} to 350 cm^{-1} . The ratio of ν_R for H_2O and D_2O would ideally be 1.41 for purely rotational motion and 1.05 for purely translational motion: The observed values lie closer to 1.35.

Blue's (85) treatment of H_2O libration was based on the assumption of three ν_R uncoupled, degenerate librators. The hydrogen bond bending force constant was assumed to be symmetric about the $O-H\cdots O$ axis and only nearest-neighbour interactions were considered. In such an approximation the libration about the C_{2v} axis is ir inactive.

Bertie and Whalley (95), in contrast, pointed out that the very existence of the ν_R bands is due to the strong coupling of the $3N$ librations of N molecules in a mole of unit cells. The crystal field and hydrogen-bond coupling yield a broad band of crystal frequencies. Since ice Ic is disordered and has only symmetry E , all the crystal frequencies are ir active. However, the distribution of ir intensities across the band of crystal frequencies is unknown, and the shape of the ir absorption band is not necessarily the shape of the crystalline vibration band.

Bertie and Whalley (95) reported that the ν_R absorptions of ices Ic and Ih are identical. For H_2O they observed 5 features on ν_R between 900 and 555 cm^{-1} ; for D_2O they observed 3 features between 675 and 425 cm^{-1} . (However, the mulling agent used obscured the results in some areas.) Similar bands were observed in the high pressure ices (96).

The ordered ice II appears to obey the factor group splitting predictions with respect to ν_R . Bertie (86) suggested 12 ν_R ir active modes. In fact, 16(9) features were observed between 475 and 1066 cm^{-1} with a band center at 800 (593) cm^{-1} . As well, Bertie and Whalley (96) suggested that a mode $\nu_R + \nu_T$ may be active in ice II.

The librational absorptions of vitreous, hexagonal and cubic ice I were reported also by Giguere and Arraudeau (89). For vitreous ice they reported features at 800(600), 840(635) and 900 (675) cm^{-1} . In cubic and hexagonal ice I they observed only two features, 835(625) and 890(673) cm^{-1} . The two crystalline modes were assigned to ν_R and $\nu_R + \nu_T$. For vitreous ice they suggested the C_{2v} libration was active due to the asymmetric electric field. The observed frequency of 800(600) cm^{-1} is in good agreement with the predictions of Blue's equation, 802(604) cm^{-1} .

Zimmermann and Pimentel (97) studied the temperature dependence of ν_R and ν_T between 93° and 273°K. From a normal coordinate analysis based on an H_2O_3 model they deduced that the hydrogen bond bending force constant varies from 0.095 to 0.085×10^5 dynes/cm between 93° and 273°K. This agrees with the concept of a weakening hydrogen bond as $R(\text{O} \cdots \text{O})$ increases.

(ii) Modes Above 1200 cm^{-1}

(a) Temperature dependences of the modes. Temperature dependences of the ice absorptions have been observed previously by at least 5 groups. Giguere and Harvey (98) reported frequencies for ν_R , ν_2 and ν_3 at 103°, 217° and 268°K for H_2O and D_2O . They observed solids formed by condensing the liquid or vapour phase.

Ice Ih (H_2O and D_2O) single crystal Raman spectra were reported by Val'kov and Maslenkova (99) for several temperatures above 77°K. On the

basis of intense α_1 Raman scattering and the similarity to vapour phase scattering, they assigned individual ν_1 and ν_3 ice frequencies. That is in direct contrast to more recent work (95) which strongly coupled ν_1 and ν_3 into two separate but equally mixed bands. Val'kov and Maslenkova suggested that the ratio ν_3/ν_1 for H_2O in the solid should be the same as for the vapour, as well as for D_2O . They also observed other lines in the stretching region which may have arisen from combinations with lattice modes.

Zimmermann and Pimentel (97) also reported the temperature dependences of ν_2 and $3\nu_R$ above 93°K . As the temperature was increased from 93° to 273°K they found that ν_R and $3\nu_R$ decreased and ν_2 increased in frequency. Thus the 1600 cm^{-1} ice band could not be $2\nu_R$. As well, they found that at 93°K $\nu_2(\text{solid}) < \nu_2(\text{vapour})$.

The most accurate study of temperature dependences in ice was recently reported by Ford and Falk (100) for the $\nu_{\text{OH}}(\text{HDO})$ and $\nu_{\text{OD}}(\text{HDO})$ modes. By preparing a dilute concentration of HDO in H_2O or D_2O one maintains a constant crystal field, but removes the dynamical intermolecular coupling of one HDO mode to the surrounding lattice (101, 102). Consequently, Ford and Falk observed relatively sharp HDO bands, the half-height width ($\Delta\nu^{\frac{1}{2}}$) was about 18 cm^{-1} for $\nu_{\text{OH}}(\text{HDO})$ at 97°K . That is still much wider than for ice II, $\Delta\nu^{\frac{1}{2}} = 5\text{ cm}^{-1}$, where the H atoms are ordered.

The widths of HDO bands in ice II are due to hot bands, overtones, and sum and difference bands. (Hot and difference bands should be removed near 10°K .) The widths of the HDO bands in ice Ih are due to the above effects plus H atom disorder (irregular Hydrogen bond potentials).

The problem of forming hydrated salt windows and not ice I was discovered by Mutter, Mecke and Lutke (103) and was clarified by Schiffer (104). Hydrated salt window absorptions are readily distinguished from those of ice.

(b) Infrared absorption spectra. The spectra of H_2O , HDO and D_2O were studied in detail by Hornig, White and Reding (105), Table 0.5. The fundamentals ν_1 and ν_3 were assumed to have reversed order in energy from the vapour phase order because of the stretch-stretch interaction constant. They also estimated that the barrier to proton jumping was 27 kcal/mole.

Unfortunately, it now appears their samples were of amorphous and not crystalline ice. (Many of their conclusions are still valid however.) Zimmermann and Pimentel (97) pointed out the need to anneal solid samples formed by vapour condensation. They demonstrated the ir effects of annealing amorphous ice, but did not study the phase transformation in detail.

Ice Ih spectra of H_2O , D_2O and HDO were obtained by Haas and Hornig (106) at 83°K. They observed $2\nu_{\text{OH}}(\text{HDO})$ and suggested that the barrier to proton transfer exceeded 23 kcal/mole. However, they suggested that proton tunneling may occur, leading to broad HDO bands. On the other hand, they used very high concentrations (8-10%) of HDO in H_2O and D_2O . The resulting HDO-HDO coupling (neighbours) gave wider bands as well as a pair of shoulders one on either side of the main HDO stretching band.

Their results showed that the width of hydrogen bonded O-H stretching bands was not a characteristic of the $\text{O-H}\cdots\text{O}$ bond but arose from extensive molecule-molecule coupling of O-H motions.

The work of Bertie and Whalley (95) is the most comprehensive study of cubic and hexagonal (H_2O , HDO and D_2O) ice I. Their results were obtained at 110°K by the low temperature mulling techniques developed by them (107). The cubic or hexagonal crystallinities of their samples were confirmed by x-ray diffraction.

Bertie and Whalley reported that the ir spectra of ice Ih and Ic were identical. As well, they obtained much sharper spectra than the previous workers (97, 105, 106, 108) due to the absence of amorphous ice. They rejected the interpretation of the bands in terms of ν_1 , ν_2 , ν_3 and ν_R on the basis of strong intermolecular coupling. For example, in ice crystals the neighbouring ν_1 vibrations were assumed to couple with each other to form one broad, symmetric ν_1 band. Similarly a broad symmetric ν_3 band formed. Finally they suggested the ν_1 coupled-band could interact with the physically and energetically adjacent ν_3 coupled-band to give two broad bands which were equal admixtures of ν_1 and ν_3 ; two hybrid ν_1 - ν_3 bands. Bertie and Whalley suggested that different portions of these coupled, broad bands were ir and Raman active, accounting for the differences between the ir and Raman results.

With respect to the widths of the ice I absorptions, they suggested that H atom disorder leads to local variations in O atom positions and variations in the local potential, as earlier suggested by Reid (31). Three other causes of the broad bands were also reviewed (96). These were:

- 1) the occurrence of sum, difference and hot bands with lattice modes,
- 2) the occurrence of proton tunnelling and the resulting increase in the width of the energy level by a decreased lifetime, and 3) Fermi resonance between the fundamental modes and overtones or combinations.

Bertie and Whalley (95) discussed the 1650 cm^{-1} absorption as arising from combined $2\nu_R$ and ν_2 vibrations, but they pointed out that discussion in terms of a unimolecular ν_2 mode is not meaningful. One must consider the $N\nu_2$ modes/mole of crystal.

D. The Present Approach to the Ice Problem

Three facets of the ice problem were studied in this work. First, to help clarify the discrepancies among ir and Raman results for ice I samples condensed from the vapour or crystallized from the liquid, the temperature dependences of vitreous ice absorptions were observed and the vitreous-cubic phase transformation was characterized. Secondly, the temperature dependences of cubic ice I absorptions were observed in order to make specific correlations of ν_{STR} to $R(O\cdots O)$ and to discover the contributions of hot bands to the band widths. Thirdly, data from the two above methods were used to confirm previous ice I band assignments.

CHAPTER ONE

APPARATUS

1.1 The Perkin-Elmer 112-G Spectrophotometer

The Perkin-Elmer 112-G instrument is a high resolution single beam spectrophotometer based on a double pass (model 99) grating monochromator. The monochromator employs a 75 lines/mm replica echelette grating which is blazed to reflect maximum intensity at 12μ in the first diffraction order and has a grating-ghost between 1000 and 1070 cm^{-1} . Unwanted orders are eliminated by a fore-prism monochromator situated between a glober source and the grating monochromator. The fore-prism filter monochromator consists of a 60° KBr prism mounted in Littrow configuration. This monochromator arrangement gives an instrument resolving power of 0.5 cm^{-1} or better. Spectral slit widths [calculated by Siegler's method (109)], are indicated on the appropriate spectra.

Thermal radiation is detected by a thermocouple or PbS sensor. However, only 2nd pass radiation is chopped at 13 cps and amplified in a standard model 107 amplifier. The 13 cps electrical signal is mechanically rectified synchronously with the optical chopper. This d.c. signal is applied to a conventional 10 mv Speedomax-G recorder.

In the experiments to be described, the P.E. 112-G was used from 5000 to 550 cm^{-1} with thermocouple detection in all regions. The instrument was calibrated at each use with atmospheric H_2O and CO_2 or with $\text{NH}_3(\text{g})$.

Low temperature experiments on ice are hampered in the P.E. 112-G by the small sampling area and severe atmospheric absorption. The spectrophotometer was modified considerably to eliminate or reduce these and other difficulties. At the PbS detector mount a simple ellipsoidal-plane mirror system is placed which produces a monochromatic source image in free space 50.5 cm from the exit slits. A second detection unit (thermocouple, focussing optics and pre-amplifier) is mounted in series with the added optical system. These modifications offer several advantages over standard P.E. 112-G sampling facilities. For example, beam vignetting losses may be reduced and smaller samples may be used by placing the sample at the source image in the new sample area. Also, concurrent calibration and sample observation is possible when a calibration gas is placed at the standard sample mount and the sample is placed at the new sampling area. In addition, there is 15 cm of optical path length and ample surrounding free space for mounting bulky accessories, i.e. low temperature cells. A more important advantage is the decreased range of thermal radiation striking samples mounted in the monochromatorexit beam. Tests indicate a 5% energy loss between the standard and modified detector configurations.

The complete instrument, excluding the new thermocouple detector unit, is placed in a metal-plexiglass drybox to reduce background atmospheric attenuation from H_2O and CO_2 . The new detector unit has its own chamber, and sampling accessories are used to couple the two chambers. Spectrophotometer controls are easily operated outside the drybox by simple mechanical extensions. However, the grating drive and transmission are now located at the front of the instrument outside the drybox. A standard drybox air lock and rubber gloves permit the introduction and manipulation of conventional ir accessories in the primary sample mount. The $N_2(g)$ drybox

atmosphere is circulated through one of two parallel molecular sieve columns (Linde 13X 1/16 in. pellets) to remove residual H_2O and CO_2 . When the circulating system is in use one column is on-line while the other is regenerated by combined evacuation and heating. This system eliminates absorption from atmospheric H_2O but is less effective in reducing atmospheric CO_2 absorption.

To achieve maximum performance for fore-prism/grating monochromator assemblies of the P.E. 112-G type the two monochromators must transmit the identical frequencies. Normally, the fore-prism monochromator slits are set at the maximum widths which just separate the various grating orders. This allows the grating monochromator to be scanned with reasonable performance over varying, limited frequency ranges which depend on the region of the spectrum. A mechanical servo system was designed to link the two monochromators permitting them to be scanned in near resonance. Lengths of certain scans (at acceptable energy levels) can be doubled by this arrangement. The design uses a variable ratio, ball and disc gearbox, reduction gears, and linking driveshafts. A more powerful motor replaces the standard grating drive motor to compensate for the added load. Despite the difficulty in maintaining exact fore-prism/grating monochromator resonance, because of non-linear prism dispersion, the modification improves the scanning characteristics.

1.2 The Perkin-Elmer 421 Spectrophotometer

The Perkin-Elmer 421 instrument is a moderate resolution (1 cm^{-1}), double beam, null recording grating spectrophotometer of conventional design. A Nernst glower source and thermocouple detector are used in conjunction with interference filters (which eliminate unwanted orders) and a

single pass grating monochromator. Two removable, self-contained monochromators are readily interchanged, permitting rapid conversion of the scanned frequency range. Each interchange comprises the appropriate interference filters and a pair of gratings mounted back-to-back on a cosecant drive: One interchange is used from $4000 - 530 \text{ cm}^{-1}$ and the other from $2000 - 220 \text{ cm}^{-1}$. Grating and filter operations are automated by pre-programmed mechanical and electrical servo systems. Spectral slit widths [calculated by the method of Roche (110)] are indicated on the appropriate spectra.

Some minor up-dating modifications have been made, i.e. installation of a larger (0.8 amp) Nernst glower and alteration of the grating switching mechanism to prevent arcing. A local modification is the provision of inlet and exhaust ports, in the monochromator and source housings respectively, permitting the use of a circulating dryer (manufactured by P.E. Bodenseewerk for the P.E. 225 spectrophotometer). This drying unit is remarkably effective in reducing atmospheric H_2O absorptions but is less effective with respect to CO_2 .

The P.E. 421 was operated under the normal, recommended conditions. Specific conditions of operation are listed with the results. General conditions of operation are listed below.

The automatic slit program was set at 2×10.00 which gave spectral slit widths of 3.86 and 2.22 cm^{-1} at 3300 and 800 cm^{-1} respectively. Spectra were recorded on U.B.C. Chemistry Department charts, which were printed on Rolland Colonial Bond rag content paper. The charts have an inaccurate frequency scale but frequency markers were applied with the absorbance scale expansion switch to coincide with the frequency readout drum. The drum was read to $\pm 0.05 \text{ cm}^{-1}$ and the marker was applied to within $\pm 0.1 \text{ cm}^{-1}$ but could be read from the charts to $\pm 1.0 \text{ cm}^{-1}$ for $100 \text{ cm}^{-1}/\text{in.}$ recording.

1.3 The Perkin-Elmer 301 Spectrophotometer

The Perkin-Elmer 301 grating instrument is a far-infrared, double beam, recording spectrophotometer of the Halford-Savitsky type. Two complementary, readily exchangeable sources (a globar and a high pressure mercury lamp) are used to cover the instrument range from 650 cm^{-1} to 14 cm^{-1} . Combinations of interference filters, scatter plates and crystal choppers (CsI or BaF_2) are used to reduce scattered radiation and to eliminate the energy of unwanted diffraction orders. A standard, single pass model 210 grating monochromator is used with 3 pairs of complementary, readily exchangeable gratings which are mounted back-to-back on kinematic mounts. The P.E. 301 optical design produces a large image at the detector and necessitates a detector with a large target. A golay sensor is suitable and is used over the full instrument range. Signal to noise ratios may be doubled if the instrument is operated in the single beam mode by replacing a split aperture (1/2 image) I-Io mirror with a full aperture I or Io mirror. An advantage of the P.E. 301 is the chopping of source radiation before it enters the sample chamber. Therefore radiation originating at the sample is not amplified.

The P.E. 301 was modified by installing inlet and exhaust ports for the P.E. Bodenseewerk dryer. Severe background atmospheric water problems can be almost completely eliminated by using this dryer.

1.4 The Hornig-Wagner Liquid Nitrogen Cell

The low temperature cell which proved most useful for obtaining spectra above 80°K was constructed from a design originally given by Wagner and Hornig (111). Our cell, which has been described previously

(112, 57) has a glass body and reservoir, a brass sample block, and CsI or AgCl windows. Thermal contact between the sample window and sample block was improved with layers of silver conductive paint on contact surfaces. Temperature was measured with a fused Cu-constantan thermocouple soldered to the brass sample holder base. Thermocouple wires and cell windows were sealed to the cell with Cenco soft-seal Tackiwax. This wax is slightly plastic at room temperature, flows well and is ideal for vacuum sealing when extremely low pressure is not required.

Although liquid nitrogen coolant comes into direct contact with the brass sample block, the spectrophotometer source beam radiation raised the block temperature to $83 \pm 3^\circ\text{K}$. Because of non-ideal thermal contact and low sample window thermal conductivity, sample temperature was considerably above that of the block. From melting point observations the sample window temperature was estimated to be 10°K higher than that of the sample block. Unless otherwise stated, all temperatures quoted in this work are not corrected for source heating.

Two sample deposition tubes were used with this cell, one of all-glass and the other of metal construction. Both were mounted with their tips 7mm from the sample window surface. At such a distance there are large heat losses (from the sample tube tip to the window and cooling block) permitting sample condensation at the cold tips. Dangers of selective H_2O condensation or fractionation of clathrate mixtures at the tube tips were avoided by using external heating on the stainless steel tube, Fig. 1.1.

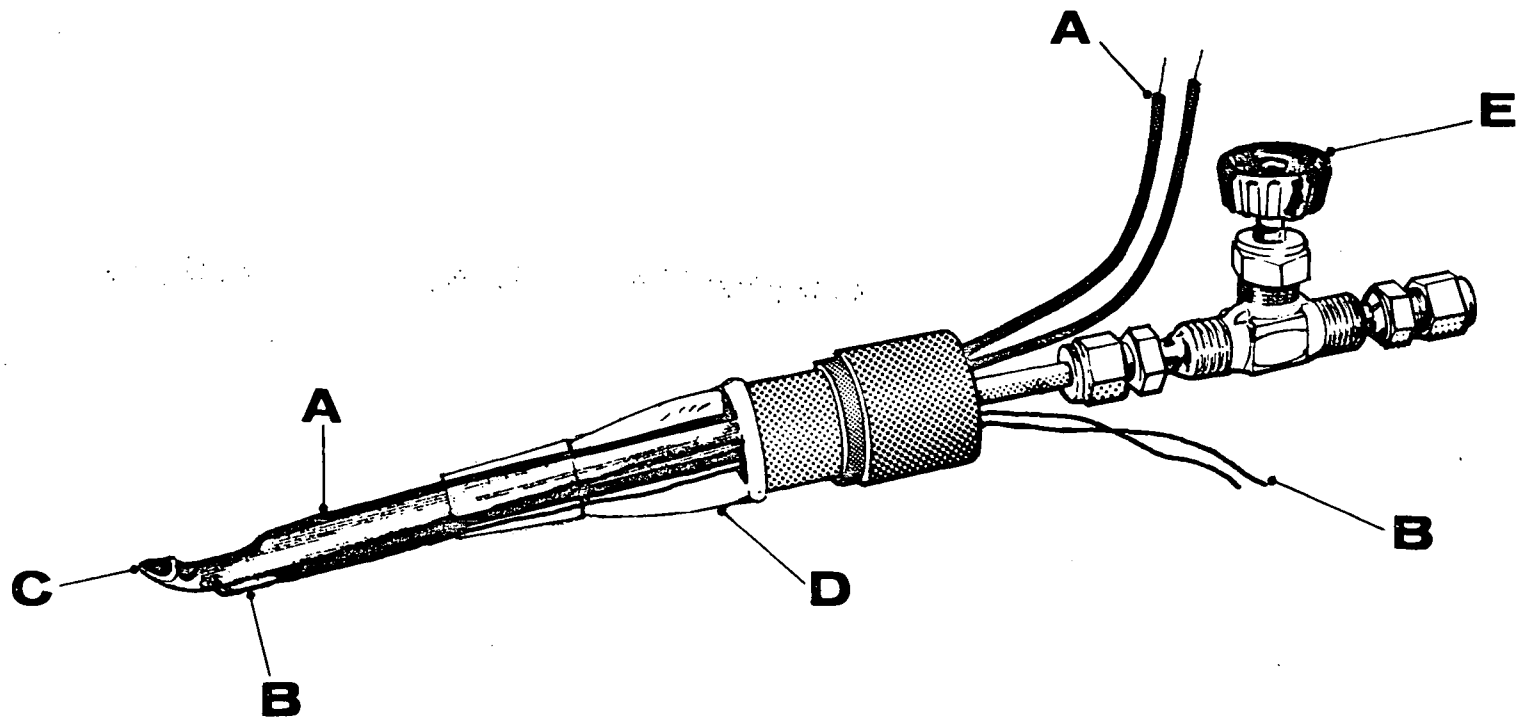


Fig. 1.1 The stainless steel sample deposition tube: A - pyrotenax heater, B - Cu-Constantan thermocouple, C - deposition tube tip, D - B-19^a conical glass joint, a Kovar metal glass joint, and a brass cap, E - needle valve and "swage-lok" fittings.

1.5 The Duerig-Mador Liquid Helium Cell

Spectra of samples below 83°K were observed through a liquid helium cell which is described elsewhere (112, 57) and is similar in design to that of Duerig and Mador (113). A principal modification incorporated in our cell is the use of a vacuum seal/bearing which permits the helium container and sample holder to be rotated through 90° for sample deposition. Thermal contact between sample windows (CsI or polyethylene) and the Cu sample block was improved by painting the contact surfaces with silver conductive paint. Sample block temperature was measured with a Au-Co/Ag-Au thermocouple. The thermocouple was calibrated at 4.2°K and with 9 boiling liquids or slushes from 77° to 273°K. Actual sample window temperature was estimated to be 10°K higher than the temperature indicated with the thermocouple.

1.6 The Metal Liquid Nitrogen Cell

To prepare clathrate-hydrates by deposition from the gas phase one must first ensure that the guest and host components condense in the proper stoichiometries. In an attempt to achieve the ideal clathrate condensation a liquid nitrogen cell was constructed containing an evacuable sample chamber, Fig. 1.2.

To help prevent fractionation in the sample chamber, one window is embedded in the cold block and the other is thermally insulated from the first by a stainless steel spacer ring (which provided the chamber body) and two teflon gaskets. Only one window is cooled to refrigerant temperature during the cell operation. The sample chamber body and sample tube were heated by a Pyrotenax wire heater. Sample block temperatures were monitored with a fused Cu-Constantan thermocouple soldered to the sample block.

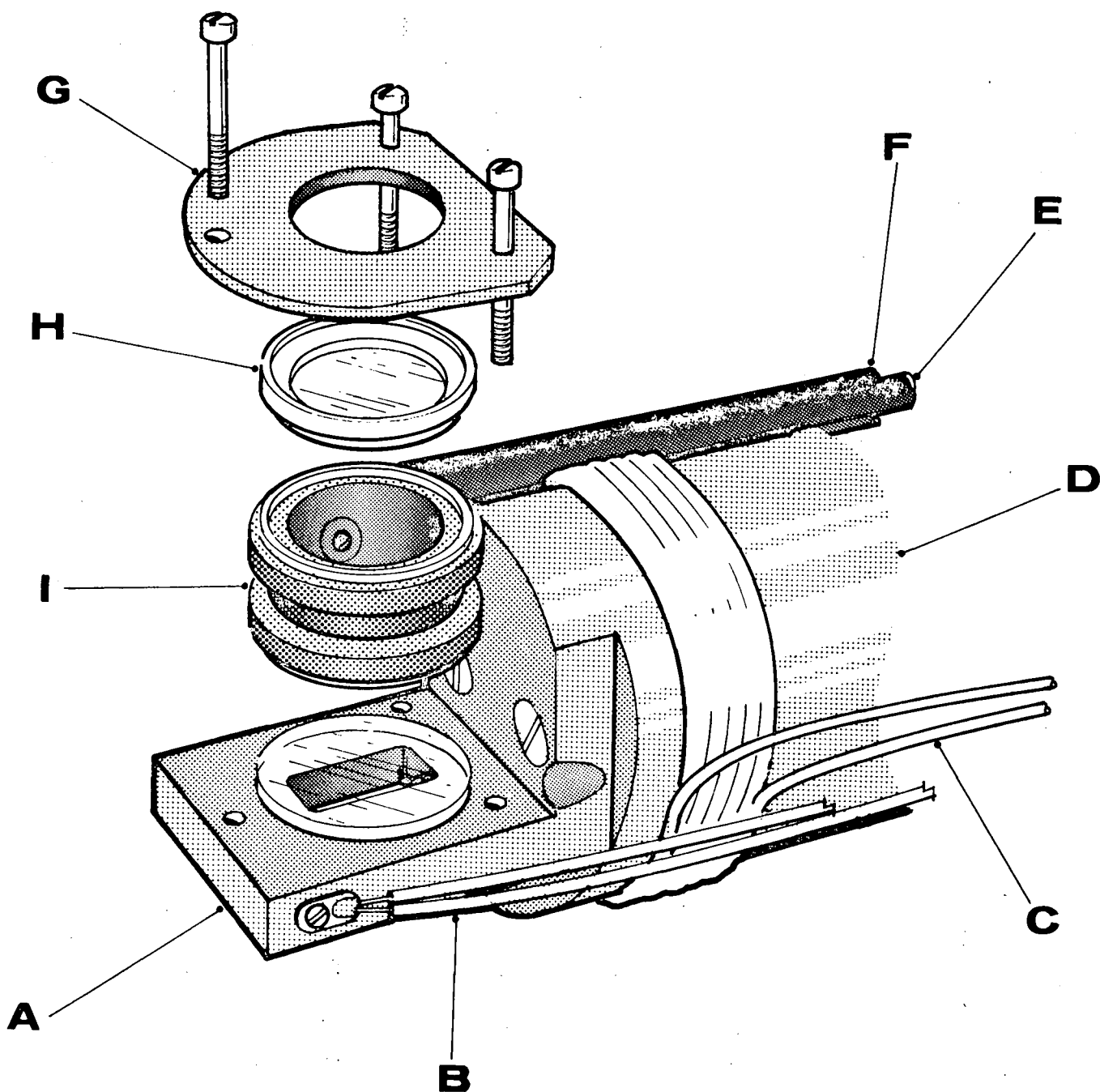


Fig. 1.2 The isolated sample chamber: A - Cu cooling block and "cold" window, B - Cu-Constantan thermocouple, C - pyrotenax heater, D - coolant reservoir, E - deposition and evacuation tube, F - pyrotenax heater, G - pressure plate and stainless steel screws, H - sample window and holder, I - sample chamber, sample port and teflon gaskets.

CHAPTER TWO

METHODS AND MATERIALS

2.1 Water Samples and Clathration Materials

Clathrate-hydrate guest molecules were either Matheson compressed gases, Fisher certified reagents, or British Drug House analar reagents.

Bromomethane (99.5% pure), trichlorofluoromethane (99%), dichlorodifluoromethane (99.0%), chlorotrifluoromethane (99.0%) and chlorine (99.9%) were used directly from their lecture bottles. Chloromethane (99.5%) was supplied in a No. 4 cylinder and was used without purification. Trichloromethane (Certified Reagent, 99.9% purity), iodomethane (C.R. 99.9%), and bromoethane (C.R. 99.9%) were partially repurified before each use by freezing and pumping off non-condensable impurities. Bromine liquid (Analar Reagent, 99.0%) was also partially purified by freezing and pumping. Guest compound purity was checked by ir vapour phase absorption spectra.

Clathrate-hydrate host and ice I compounds used were H_2O , D_2O , H_2O (5.9% HDO), and D_2O (4.0% HDO). Before use the H_2O water was distilled, de-ionized and finally degassed by several cycles of freezing and pumping. D_2O was supplied by Merck, Sharpe and Dohme in 100g lots and had a stated purity of 99.7%; D_2O was degassed in the usual way. Mixtures of D_2O or H_2O with HDO were made by mixing 49.0 ml D_2O with 1.0 ml H_2O and 49.0 ml H_2O with 1.5 ml D_2O . In both cases the isotopic impurity was almost all present as HDO at equilibrium. Residual H_2O (or D_2O) was spectroscopically undetected. No quantitative analyses of the isotopic mixtures were undertaken.

2.2 Infrared Windows and Sample Mounts

Choice of window material is tempered by the necessary application of thermal stress and essential non-reactivity with applied samples. The latter property is important in studies of water containing compounds since, as Mecke (103) found and Schiffer (104) proved, thin hydrated layers may form on alkali halide crystals. CsI is suitable for all cryostats used here since it is relatively soft and ductile and accepts the considerable thermal shock. Only $\text{Cl}_2 \cdot 7.67\text{H}_2\text{O}$ samples reacted detectably with CsI windows. That experiment was repeated using an AgCl sample mount. Silver chloride does not transmit as widely as cesium iodide over our range of interest, however AgCl is soft and easily withstands thermal shocks. Also, it is apparently non-reactive to chlorine and bromine.

Cell windows and a sample support used in the P.E. 301 v_T experiment were cut directly from commercial high density polyethylene (A powdered polyethylene was also available). The windows were only used from 650 cm^{-1} to 160 cm^{-1} and through the temperature range 5°K to 200°K . The polyethylene was apparently non-reactive to the clathrate-hydrate mixtures investigated.

Polyethylene is not an entirely satisfactory sample support since its thermal conductivity is low and source heating may be high. To counteract source heating, sample supports were pressed from powdered polyethylene embedded with a brass or copper grid. The method consisted of placing a wire grid between two lightly pressed (7000 psi, unheated) 0.20 g discs, heating to the polyethylene flow temperature ($130 \pm 5^\circ\text{K}$) under light pressure (1000 psi) and pressing to 15,000 psi while cooling to less than 35°C . The result was a low scattering pellet with 58% transmission at 361 cm^{-1} .

and 171 cm^{-1} . Energy transmission could be improved by reducing the effective reflecting surface area of the metal with finer gauge wire.

2.3 Preparation of Clathrate-hydrates

A. Preparation of Solid Samples

Clathrate-hydrates with stoichiometries $1M \cdot 17\text{ H}_2\text{O}$, and whose guest molecules formed liquids at room temperature, were prepared by repeated cycles of cooling and warming stoichiometric liquid mixtures between 77°K and 265°K . To $3\text{g H}_2\text{O}$ (0.17 moles) in a 10 cm by 1.2 cm test tube was added 0.01 moles of liquid guest compound. The mixture was agitated and successively immersed for about 30 sec in an ice-water-sodium chloride bath (265°K) and 30 sec in a liquid nitrogen bath. The sample was then warmed to a viscous state. The procedure was repeated until a uniform, white solid formed--about 5 repetitions for each sample. Samples were stored over dry ice for a short time before use.

Clathrate-hydrate samples were prepared by two other methods, but such samples were not investigated spectroscopically. For clathrates whose guest molecules are ordinarily gases, the method of Allen (114) was used with some modification: a preparation cell similar to Allen's was constructed. For clathrates whose guest molecules are ordinarily liquids, the basic method of Allen (114) was used but with major modifications. A preparation cell of similar dimensions to the one above, but with provision for mechanical stirring and liquid guest addition, was constructed. Samples prepared by these two methods were also stored over dry ice and were analyzed with a gas burette.

B. Preparation of Stoichiometric Gaseous Mixtures

There are a number of criteria which must be satisfied in forming a stable, suitable sample. For example, the clathrate-hydrate or ice phase must form a stable thermodynamic system in the region 4.2° to 200°K . Also, the method must maintain the clathrate stoichiometry, avoiding guest molecule loss by diffusion and dissociation--the equilibrium dissociation pressure of guest molecules must remain negligible. As well, since ice has very large O-H extinction coefficients (~ 140) the samples must be thin--3 microns or less.

Deposition of water vapour or a gaseous stoichiometric clathrate mixture on a cold sample mount gives samples which satisfy some of these criteria (43).

The quantity of a stoichiometric gas mixture which can be prepared in a vacuum system is clearly limited by the saturation vapour pressure of H_2O at the given temperature and the mixing bulb volume. The calibrated mixing bulb (including a side bulb) had a volume of 3.853 l and contained 2.76 millimoles of H_2O at 293°K and 17.53 Torr H_2O . If uniformly deposited on a typical window with a surface area of 7 cm^2 , 2.76 m moles of H_2O would form a layer approximately 70μ thick. A 3.853 l mixing bulb obviously supplies enough sample for several deposits.

The molar ratios for the 12 \AA cubic structure are 1 guest: $5.75\text{ H}_2\text{O}$ and 1 guest: $7.67\text{ H}_2\text{O}$, while the corresponding ratios for the tetragonal and 17 \AA cubic structures are 1 guest: $8.6\text{ H}_2\text{O}$ and 1 guest: $17\text{ H}_2\text{O}$. Clearly the numbers of guest mmoles required to combine with 2.76 m moles of H_2O are very small. Measurement of at best one-fifth of 2.76 (0.48) mmoles of gas in 3.853 l at 20°C is impractical due to the large error in measuring

small pressure differences. Gaseous guest aliquots were first isolated in a 0.1039 liter bulb and then expanded into the 3.853 liter mixing bulb. The numbers of guest mmols and their pressures in the 2 bulbs are shown below for four clathrate structures.

Clathrate	mmole X		Partial Pressure of Guest X	
	2.76mm H ₂ O	3.853 l bulb	0.1039 l bulb	
1 X · 5.75 H ₂ O	0.48	3.05 Torr	117.10 Torr	
1 X · 7.67 H ₂ O	0.36	2.28	87.54	
1 X · 8.60 H ₂ O	0.32	2.04	78.32	
1 X · 17.0 H ₂ O	0.16	1.03	39.55	

After the guest sample was expanded into the mixing bulb at 20°C, the chamber was saturated with H₂O vapour from liquid previously isolated and degassed in a side bulb. The system was equilibrated in that state for ten minutes before the liquid H₂O was again isolated from the mixing chamber. Since the densities of the gases in the bulb varied over the range from $17.3 \times 10^{-6} \text{ g/cm}^3$ for H₂O to $13.3 \times 10^{-6} \text{ g/cm}^3$ for Br₂ and $6.30 \times 10^{-6} \text{ g/cm}^3$ for CH₃Cl, the mixing was forced by heating the lower hemisphere of the chamber with an electric heating tape. Such convection mixing was maintained for a minimum of 30 minutes before sample deposition. Suitably mixed gases were used either directly from the mixing chamber, for deposition in the isolated chamber of the metal liquid nitrogen cryostat, or were transferred to a portable 3.0 liter bulb and attached to a Duerig-Mador or Hornig-Wagner cryostat.

2.4 Preparation of Infrared Specimens

A. Low Temperature Mulling

Clathrate-hydrates decompose if mounted at 293°K by the usual spectroscopic means, but they are metastable at 77°K. Low temperature mulls of the clathrate-hydrates were prepared by an adaptation of the method Bertie and Whalley (107) used for the high pressure ices.

Preparation of a suitable spectroscopic sample required approximately 0.5h. A few grams of solid clathrate were placed in liquid nitrogen in a mortar at 77°K and ground manually for 10 minutes. A small portion of the sample was placed in the center of a mounted window and enough condensed liquid mulling agent was dropped on the sample to prepare a uniform suspension. A second window was placed over the sample and secured in place by a retaining ring. The window assembly was placed in the sample block of a standard Wagner-Hornig nitrogen cryostat. The assembled cryostat was immediately evacuated.

Contamination of the sample by condensed atmospheric CO₂ and H₂O is most likely to occur during cryostat assembly. Blank runs, and runs with mulling agent only, made it clear that little impurity absorption was found even for the most intense H₂O stretching band [see also Whalley (107)].

Recalling that the transmission spectrum of a mulled sample can be distorted from the idealized absorption spectrum, one can have confidence in the low temperature mull spectra only if distortion is minimized by attention to the particle size of the sample and the refractive index of the mulling agent. Whalley (107) found that even for the most intense H₂O stretching frequencies, where reflectivity is greatest, the spectra of mulls were in good agreement with those of thin films.

B. Isolated Chamber Condensation

The sample chamber designed for approximate comparison of absorption intensities of clathrate-hydrates was described in detail in section 1.6 (page 45). A typical run with this isolated sample chamber involved degassing the metal surfaces, depositing the sample, annealing, and observing the absorption. Those metal surfaces exposed to the sample were degassed by heating to 393°K while evacuating to 2.0×10^{-5} Torr for two hours. Sample block temperatures from 300°K to a maximum of 393°K could be maintained with the coolant reservoir empty. Several blank spectroscopic runs were made to ensure that no impurities were being deposited. The sample tube heater was left on but the sample cooling block heater was shut off, while liquid nitrogen coolant was added to the reservoir. Twenty minutes after the collector plate window had recooled to 83°K, the background spectra were recorded from 550 cm^{-1} to 4000 cm^{-1} . No impurity absorptions were observed.

For deposition the gaseous sample was expended in short bursts down the heated sample tube into the sample chamber which was held at 83°K after the method of Barrer and Ruzicka (43). With the sample tube at 343°K and the sample tube heaters on, some heating of the stainless steel spacer occurred which aided the thermal insulation of the second, "hot" window. The CsI sample mounts are poor thermal conductors and too rapid a sample condensation may produce sufficient localized heating to permit self-devitrification--diffusion of the guest molecules into clusters or diffusion out of the lattice completely.

Subsequently, samples were annealed to temperatures between 160 - 180°K for 5 to 10 minutes. The sample chamber was not subject to pumping

and the sample tube was warmed to 343°K prior to annealing. The sample block heater was used only in the initial stages of annealing, i.e. up to 100°K . The warming was completed by passing a stream of dry, room temperature N_2 gas through the coolant reservoir. The rates of warming and re-cooling are described in section 2.5. After recooling the sample block to 83°K , the sample tube heaters were shut off and the spectra were observed in the desired range. The specific instrument conditions are listed with the results.

C. Open Chamber Condensation

Deposition of gaseous samples on a cold substrate, which was exposed to the cryostat cell body, was used for both the Wagner-Hornig cryostat and the Duerig-Mador cryostat for observation on either the P.E. 421 or P.E. 301 spectrophotometers. Gases used were either vapours evaporated directly from liquid H_2O , D_2O or $\text{H}_2\text{O}/\text{D}_2\text{O}$ mixtures or were water/guest mixtures prepared as described in section 2.3. Cryostats were degassed by evacuation for a minimum of 10 hours before cooling with liquid nitrogen to 83°K . To ensure a minimum collector plate temperature, the source beam was blocked and the cryostat was allowed to equilibrate for 15 to 20 minutes.

Typically, samples were deposited as follows. Ten ml of sample (at a pressure at 8.7 Torr), were isolated in the sample deposition tube. Several of these aliquots were passed in bursts onto the collector plate at 83°K . The cryostat vacuum jacket was isolated from the pumping station during sample deposition to minimize distortion of the sample gas stream. The H_2O ν_{OH} stretching region was monitored briefly after each burst to

determine the intensity of absorption. We estimated that the sample thicknesses ranged from 0.6μ for very thin samples to several microns for thick samples. The rates of deposition were estimated as $0.04 \text{ g/cm}^2\text{-h}$. Such deposits were subsequently annealed by the standard procedure.

2.5 Devitrification

As was discussed in the introduction, deposition of water vapour on alkali halide substrates held near 80°K has led to doubts of sample crystallinity and confusion in the interpretation of the various ir results. The situation was clarified by Beaumont, Chihara and Morrison (65) through correlated heat capacity/x-ray diffraction studies. Their work accentuated the differences in sample crystallinity among the ir ice spectra of various authors (105, 106, 95, 97) and clearly demonstrated the processes of devitrification and transition linking the ice I allotropes.

In order to make comparative ir studies of ice I and clathrate-hydrates as a function of temperature in this work, one had to reproducibly form the ice I allotropes. However, no attempt was made to restrict self-annealing by limiting deposition rates to that recommended by Beaumont et al. -- 0.04 g/h-cm^2 . That the samples did not undergo a high degree of self-annealing was demonstrated by the broad, featureless ir absorption bands observed immediately after deposition.

Attention was initially directed to annealing condensed, vitreous samples to the common ice phase, hexagonal ice I, whose transition temperature from cubic ice I lies between 200 and 250°K . The vitreous sample was warmed to the hexagonal transition at 5.0 to 12.5 deg/min from 83°K to $205 \pm 5^\circ\text{K}$ (with the sample source beam off and no pumping in the sample chamber). It was recooled to 83°K at 50 deg/min after being held for

2 to 3 min at the maximum annealing temperature. Unfortunately, the samples were unstable above 195°K with respect to this procedure.

In view of the great difficulty with sample stability and the low rate of transition from cubic to hexagonal ice, further attempts to devitrify at $205 \pm 5^\circ\text{K}$ were abandoned.

Further extensive tests showed that thin films of H_2O could be annealed under vacuum to $185 \pm 5^\circ\text{K}$ from $83 \pm 5^\circ\text{K}$ (at between 5 and 12.5 deg/min with no pumping and the source beam off), and maintained stable at 185°K for up to 5 minutes. The samples were successfully recooled at 50°K/min with little loss of sample as detected by slightly diminished absorption. According to the data of Beaumont et al. (65) this should give a well developed polycrystalline cubic ice sample, since the transition temperature was well exceeded and the rate of transition is fast, i.e. a few minutes. Samples observed spent a minimum of 9 minutes at (or above) the transition temperature, 150°K. Before spectroscopic investigations began, the thin films were thermally equilibrated for 20 minutes with the sample source beam on.

Discussion of the nature of samples formed by condensing and annealing stoichiometric gaseous mixtures is left until Chapter 6.

2.6 Temperature Variation Methods

The purposes of this work are to study the variations of ice and clathrate spectra as a function of temperature and to show that gas condensation and devitrification gives legitimate crystalline samples. The same sample heating and ir observation techniques were used for both vitreous and crystalline sample studies.

All the samples studied as a function of temperature were formed in either the glass liquid nitrogen cell or the liquid helium cell by the methods of section 2.4(c). The nitrogen cell was mounted only in the P.E. 421 and was used for preliminary observations between 83° and 200°K. The helium cell was mounted either in the P.E. 301 or in the P.E. 421 spectrophotometer, and was used for the detailed studies between 4.2° and 200°K.

Two methods of warming these cryostats were used: 1) natural, unforced warming due to radiative and conductive heating, and 2) warming with a stream of $N_2(g)$. The helium cell was allowed to warm from 4° to 83°K by the natural heat influx after evaporation of the liquid helium. Above 83°K the helium cell was warmed with $N_2(g)$ (293°K) passing slowly through the reservoir. The nitrogen cell was held at 4 to 8 constant temperatures ($\pm 3^\circ K$) for devitrification studies (at 83°K $N_2(liq)$ was used and at higher temperatures 1-2 ml of $N_2(l)$ were added to the empty reservoir at appropriate intervals).

Sets of spectra were obtained by continuously recycling the spectrometers over the spectral range desired as the cell warmed continuously, or spectra were recorded at certain successively higher constant ($\pm 3^\circ K$) temperatures. Some sets of spectra were also recorded at successively cooler constant temperatures ($\pm 3^\circ K$) from $190 \pm 10^\circ K$ to 83°K after devitrification as a check on the reversibility of absorption maxima shifts.

CHAPTER THREE

ICE I: EXPERIMENTAL AND RESULTS

This chapter is comprised of four main sections. The first section contains the results from temperature variation studies of vitreous ice I-- observations of the vitreous-cubic phase transformation. The second section contains the results from temperature variation studies of cubic ice I-- observations of $\Delta v/\Delta R$ for crystalline ice. The third section uses the results of sections one and two as an aid in assigning the ice absorptions. The fourth section is a brief summary of the results.

3.1 The Vitreous-Cubic Ice Phase Transformation

The spectra recorded during vitreous-cubic phase transformations exhibited diminishing oligomeric peak heights (I) and irreversible peak frequency and half-height width shifts.

A. Experimental

Two vitreous ice I (H_2O) samples were prepared (by the method of section 2.4(c)) and observed in the glass liquid nitrogen cell (section 1.4). Sample A was deposited on CsI at $82 \pm 3^\circ K$, warmed from 82° to $169^\circ K$ in five stages over 105 min and was annealed to a maximum temperature of $185 \pm 3^\circ K$. Sample B was deposited on CsI at $81 \pm 3^\circ K$, warmed from 81° to $161^\circ K$ in four stages over 120 min and was annealed to a maximum temperature of $182 \pm 3^\circ K$. Seven spectra were recorded for each of samples A and B during devitrification.

The basic spectrophotometer conditions were described previously (section 1.2). For these samples (A and B) P.E. 421 spectra were recorded at $100\text{ cm}^{-1}/\text{in.}$ No reference cell compensation was used, but the instrument was purged with dry $\text{N}_2(\text{g})$. The liquid nitrogen cell and the spectrophotometer sample compartment were masked so that the sample compartment was also purged.

B. Results of Devitrification

Infrared absorption spectra representative of samples A and B are shown in Fig. 3.1 (top). Frequency and half-height width ($\Delta\nu^{1/2}$) data were derived independently, but by the same methods, for the two sets of spectra. Peak absorptions were determined (to within $\pm 10\text{ cm}^{-1}$) at the intersection of lines along the band sides, while shoulders were determined (to within $\pm 14\text{ cm}^{-1}$) at the point of minimum slope. Band heights were measured on the absorbance scale (I) from the baseline and $\Delta\nu^{1/2}$ was measured at ($I/2$).

(i) The Effect of Devitrification on the Peak Maxima

The vitreous H_2O ice I absorption maxima are plotted in Fig. 3.2 as a function of increasing temperatures. Important parameters derived from these graphs are given in Table III.I. Although devitrifications of D_2O ice and HDO bearing ice were not observed in detail, data from such samples, immediately before and after devitrification, are included in Table III.I for comparison to H_2O data. In Fig. 3.2, the transformation temperature ranges are indicated for ν_1 , ν_3 and $\nu_1 + \nu_T$. Transformation was assumed to have begun at the onset of peak shift and was assumed to have finished upon reversal of peak shift direction.

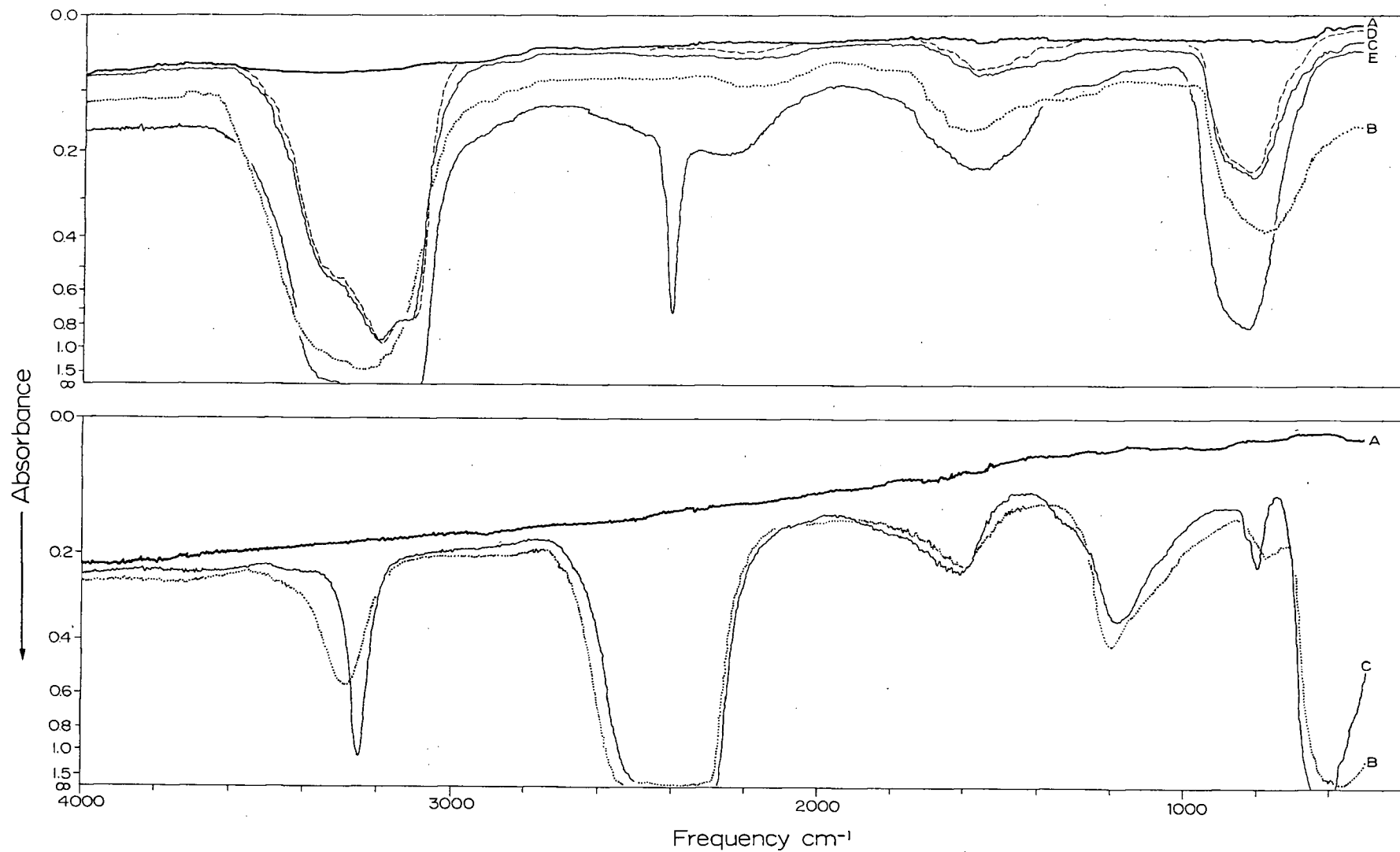


Fig. 3.1 Representative spectra of vitreous and cubic ices at various temperatures. Top: A - cryostat background at 83°K (compensated), B - H₂O ice I_v at 83°, C - sample B annealed to 185°K and recooled to 83°K (cubic ice), D - sample C at 7°K, and E - cubic ice (H₂O(5.94% HDO)) at 83°K. Bottom: A - cryostat background, B - D₂O(4.0% HDO) vitreous ice at 83°K, C - sample B annealed to 185°K, cubic ice at 83°K.

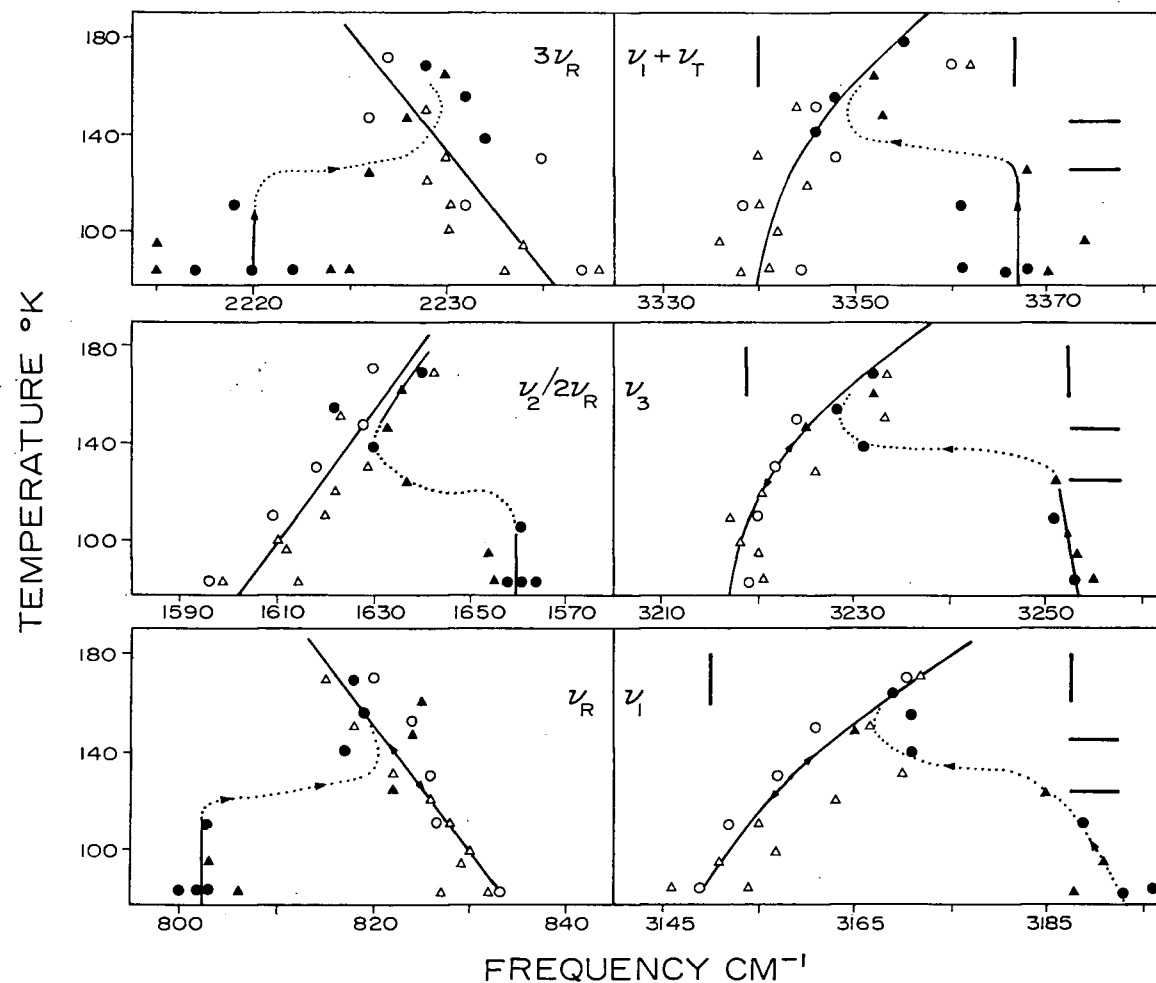


Fig. 3.2 Shifts of H₂O frequencies during the vitreous-cubic ice phase transformation and subsequent behaviour of cubic ice. The full circles and triangles are from spectra recorded during warm-up from 83°K to 185°K. The open circles and triangles give the behaviour after annealing.

Table III.I The frequencies of cubic and vitreous ice I at 82°K, their differences, the transformation range and the cubic ice absorptions temperature dependences.

H ₂ O (D ₂ O)	Ice I _v 82°K	Ice I _c 82°K	$\Delta\nu$ I _c -I _v 82°K	Transformation Temperature Range	Ice I _c $\Delta\nu/\Delta T$
	cm ⁻¹	cm ⁻¹	cm ⁻¹	± 5°K	cm ⁻¹ /°K
$\nu_1 + \nu_T$	3367 ± 7 (2499)	3340 ± 7 (2465)	-27 (-34)	130 - 145	0.26 ± 0.05 (0.16)
ν_3	3253 ± 5 (2436)	3217 ± 5 (2413)	-36 (-23)	125 - 145	0.20 (0.13)
ν_1	3191 ± 7 (2372)	3149 ± 7 (2321)	-42 (-51)	120 - 145	0.25 (0.18)
3 ν_R	2220 ± 5 (1617)	2235 ± 5 (1635)	+15 (+18)	115 - 130	-0.11 (-0.11)
	1660 ± 5	1604 ± 5	-56	115 - 130	0.36
ν_2	1570 (1212)	1570 (1194)	(-18)		(0.14)
ν_R'	846 ± 7 (--)	881 ± 7 (661)	+35 (--)	115 - 130	-0.19 (-0.16)
ν_R	802 ± 5 (600)	833 ± 5 (627)	+31 (+27)	115 - 130	-0.18 (-0.12)
	--	780 ± 7			
	675 ± 7	690 ± 7	+15		
	535 ± 7	570 ± 7	+35		
ν_T	212.8 ± 1	227.8 ± 5	+15		
HDO					
ν_{OH}	3304 ± 1 (2437)	3266 ± 1 (2442) (2416) (2392)	-38 (-21)		0.20 ± 0.005 (0.123 ± 0.005)
ν_R'	--	854 ± 1.5	--		-0.154 ± 0.022
ν_R	792 ± 1	819 ± 0.5	+27		-0.147 ± 0.012

There are five important effects to notice: 1) between 115° and 145°K the molecular modes shift towards lower frequencies while the lattice modes shift towards higher frequencies, 2) the reversal of peak shift direction, 3) the irreversibility of the devitrification transitions, 4) the large frequency displacements between the same bands in cubic and vitreous ice I at 82°K, and 5) the reversibility of peak shifts in cubic ice I.

These effects can be seen in Fig. 3.2 for the $\nu_3(\text{H}_2\text{O})$ data. The frequency was constant up to $125 \pm 5^\circ\text{K}$, and shifted irreversibly by $36 \pm 2 \text{ cm}^{-1}$ to lower frequency between 125 ± 5 and $142 \pm 5^\circ\text{K}$. The frequency attained a positive, reversible temperature dependence of $+0.23 \text{ cm}^{-1}/^\circ\text{K}$ above 142°K . Subsequent warming and cooling cycles revealed a sample with an approximately linear frequency-temperature dependence between 82°K and 180°K . The remaining absorptions of ice I behaved similarly during devitrification. However, all internal modes exhibited positive, and all librational modes exhibited negative temperature dependences after devitrification.

(ii) Oligomeric H_2O Absorptions

In addition to all the expected vitreous ice I absorptions, weak absorptions were observed near the frequencies previously reported (115) for oligomeric H_2O and D_2O . Weak peaks (0.01 abs units) were found near 3690 cm^{-1} in H_2O and 2720 cm^{-1} in D_2O and H_2O shoulders near 3647 cm^{-1} (Fig. 3.3). They persisted only up to $125 \pm 5^\circ\text{K}$ and did not reappear upon recooling the sample. Half-height widths were between 15 and 20 cm^{-1} . No detailed study was made for oligomers, but data from several samples are compiled in Table III.II.

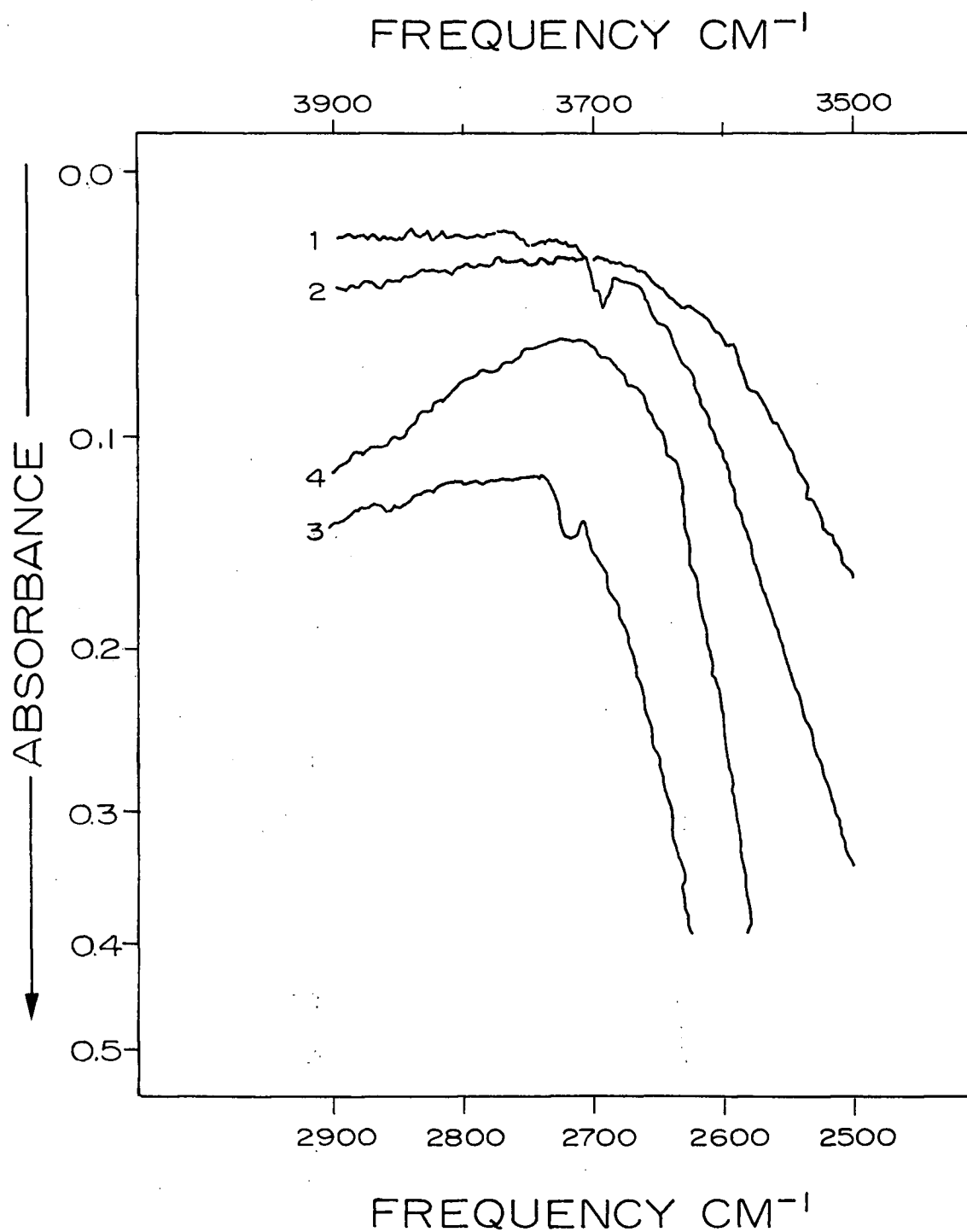


Fig. 3.3 Oligomeric H_2O and D_2O absorptions in vitreous ice I at 83°K : 1) vitreous H_2O ice, 2) cubic H_2O ice, 3) vitreous D_2O ice, 4) cubic D_2O ice. The features were more or less accentuated depending on the deposition rate.

Table III.II Oligomeric $\text{H}_2\text{O}(\text{D}_2\text{O})$ ν_1 and ν_3 ir absorptions seen for vitreous ice I samples before and during warm-up. The $\nu_3(\text{H}_2\text{O})$ absorptions were weak peaks and the $\nu_1(\text{H}_2\text{O})$ and $\nu_3(\text{D}_2\text{O})$ absorptions were weak shoulders. One $\nu_3(\text{D}_2\text{O})$ absorption is given in brackets.

H_2O (D_2O)	Temperature of Observation, $^{\circ}\text{K}$					
	82	85	94	110	125	140
	cm^{-1}	cm^{-1}	cm^{-1}	cm^{-1}	cm^{-1}	cm^{-1}
ν_3	3692	3687(2724)	3689	3690	3690	--
	3677	3658	3674			
ν_1	--	3637	3650	3647	--	--
	--	--	3640			

(iii) The Effect of Devitrification on H_2O Half-height Widths

A comparison of H_2O spectra B and C in Fig. 3.1 (top) shows that the composite bands (ν_1 , ν_3 , $\nu_1 + \nu_T$), (ν_2 , $2\nu_R$) and (ν_R , $\nu_R + \nu_T$) are sharper in cubic ice I than in vitreous ice I. Half-height widths for these composite bands from the sets of H_2O spectra (samples A and B) were measured as a function of temperature, Figs. 3.4 and 3.5. [The large scatter in the data arises from several sources: 1) the choice of baseline ($\pm 2 \text{ cm}^{-1}$), 2) the error in assessing I and $\frac{1}{2}$ I for intense peaks ($\pm 5 \text{ cm}^{-1}$), and 3) atmospheric attenuation or distortion of the ν_2 band.] The parameters are compiled in Table III.III.

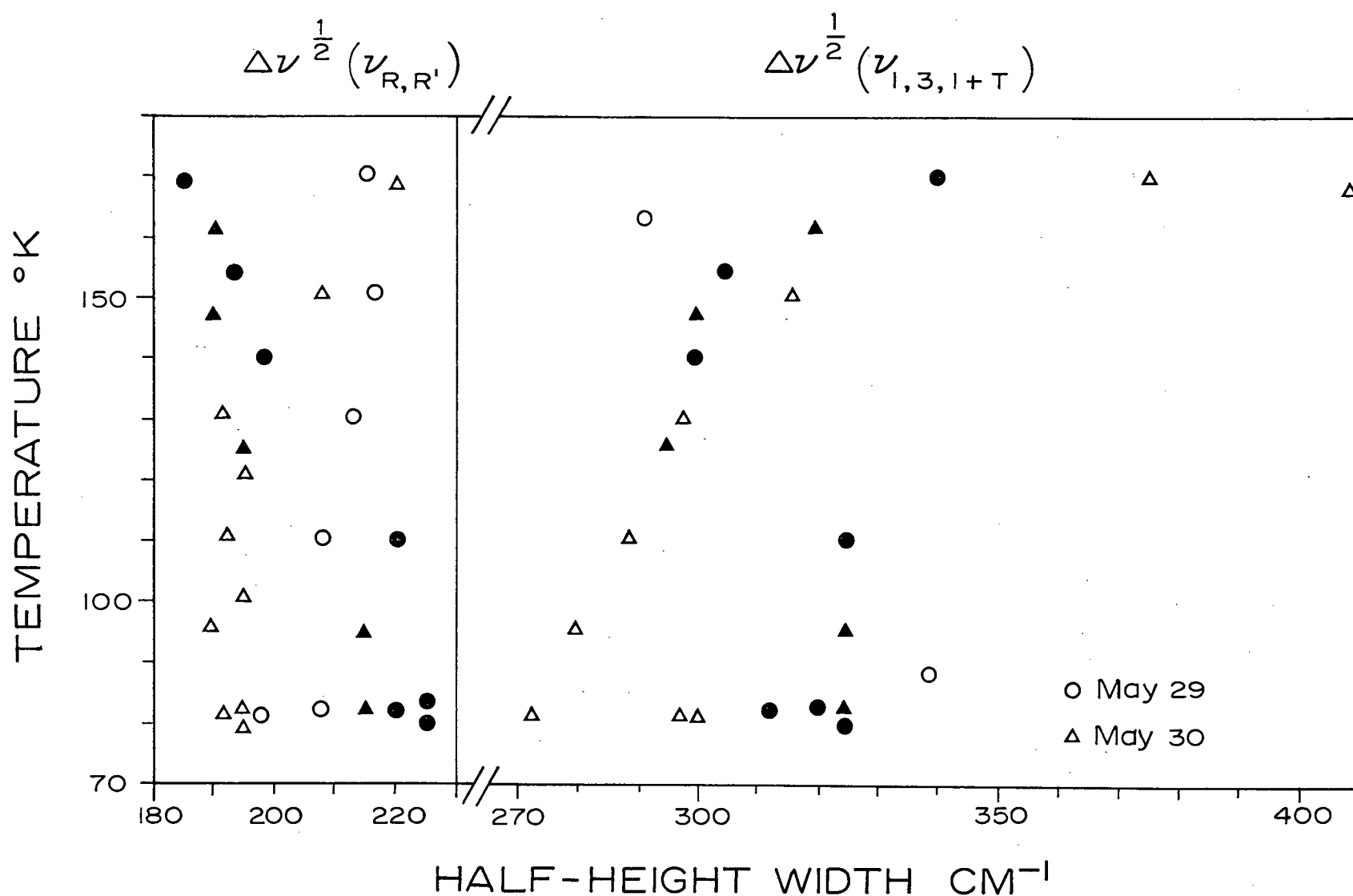


Fig. 3.4 The shifts of H₂O half-height widths for the composite H₂O bands (ν_R , $\nu_R+\nu_T$) and (ν_1 , ν_3 , $\nu_1+\nu_T$) during the vitreous-cubic ice transformation and subsequent to annealing. Solid circles and triangles are for the unannealed sample warm-up. Open circles and triangles are for the annealed sample warm-up.

$$\Delta \nu^{\frac{1}{2}} (\nu_2 / 2\nu_R)$$

67

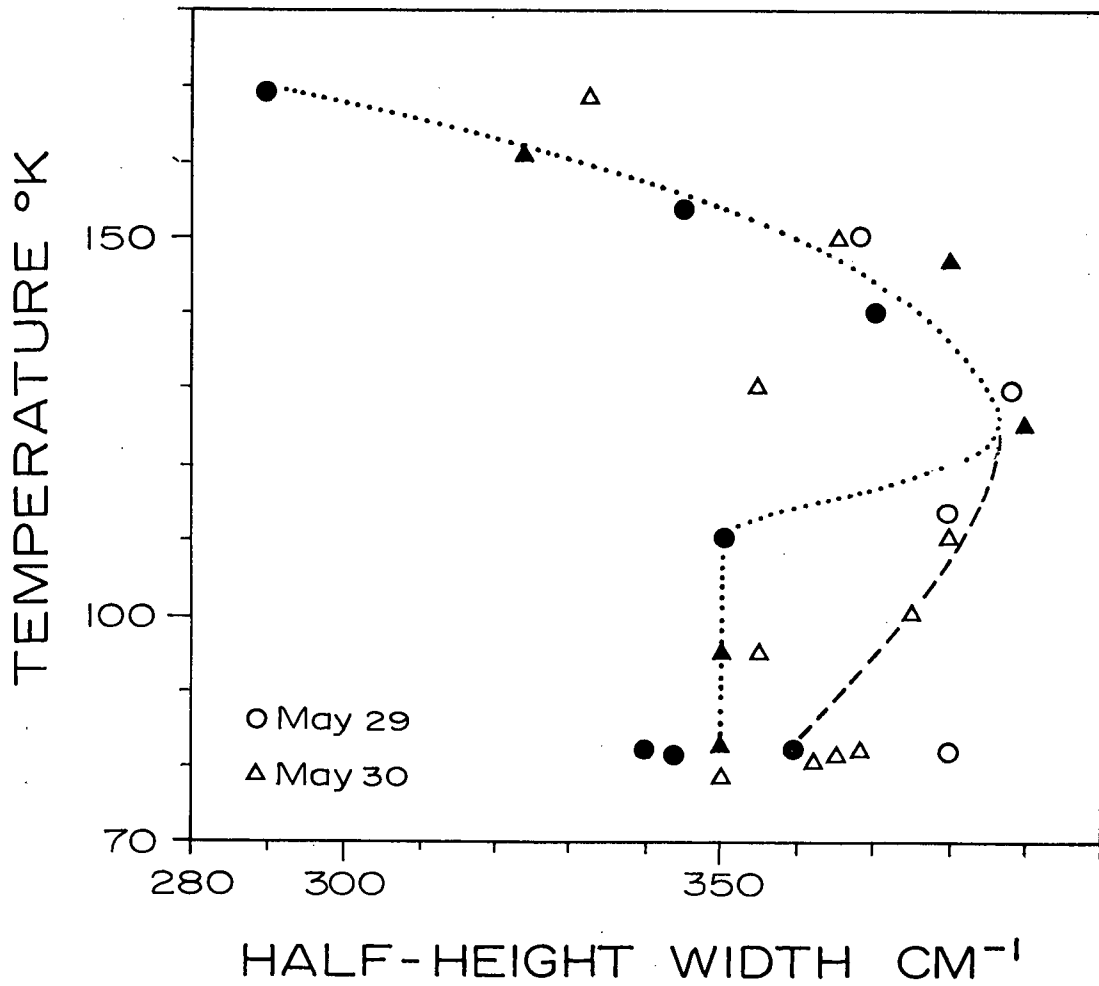


Fig. 3.5 The shifts of half-height width for the composite H₂O ($\nu_2, 2\nu_R$) band during the vitreous-cubic phase transformation and subsequently for cubic ice I. Solid points were obtained during vitreous sample warm-up from 83° to 185°K. Open points were obtained from annealed samples.

Table III.III The half-height widths of the vitreous and cubic H₂O ice composite bands at 82°K and their temperature dependences for cubic ice I.

Composite Band	Vitreous $\Delta v^{1/2}$ 82°K	Cubic $\Delta v^{1/2}$ 82°K	Difference $\Delta v^{1/2}$ 82°K	Transition Temperature Range
H ₂ O	cm ⁻¹	cm ⁻¹	cm ⁻¹	°K
($v_1, v_3, v_1 + v_T$)	322 ± 7	287 ± 5	-35	115 ± 5 - 130 ± 5
($v_2, 2v_R$)	350 ± 10	365 ± 10	+15	115 ± 5 - 140 ± 5
($v_R, v_R + v_T$)	220 ± 5	195 ± 3	-25	115 ± 5 - 150 ± 5

During warming from 82°K the half-height widths of vitreous ice spectra shifted irreversibly over the transformation temperature range. Subsequent warming-cooling cycles showed that the cubic ice spectra half-widths shifted reversibly and that the vitreous and cubic data agreed above 150°K.

There are specific differences among the three sets of composite bands (see Figs. 3.4 and 3.5). These are as follows: 1) the stretching band $\Delta v^{1/2}$ increased, 2) the bending band $\Delta v^{1/2}$ decreased and 3) the librational band $\Delta v^{1/2}$ appeared to increase with increasing temperature. Also, the v_2 half-height width initially increased during devitrification, although it was expected to decrease.

Annealing effects on v_T (H₂O) were not observed in detail, but the differences between vitreous and cubic ice at 83°K were measured. The data are 62.8 cm⁻¹ and 23.2 cm⁻¹ for vitreous and cubic ice. Also, the

absorbance of $\nu_T(\text{cubic})$, $I = 1.285$, was almost exactly double that of $\nu_T(\text{vit.})$. The vitreous $\nu_T(\text{H}_2\text{O})$ absorption features were: a peak at $212.8 \pm 0.5 \text{ cm}^{-1}$ and faint shoulders centered at 301 ± 3 and $271 \pm 3 \text{ cm}^{-1}$.

3.2 Temperature Dependence of Cubic Ice I Absorptions

A. Temperature Dependence of HDO Absorptions

The four observed HDO absorptions provided the best measurements of band parameters as a function of increasing temperature in cubic ice I.

(i) Experimental

Three samples of D_2O (4.00% HDO) and two samples of H_2O (5.94% HDO) were prepared (section 2.4(c)) and observed in the liquid helium cell (section 1.5). Samples C(1,2,3) were deposited at $85 \pm 3^\circ\text{K}$ on CsI, warmed from 85° to 187°K in 9 minutes, annealed at $187 \pm 3^\circ\text{K}$ for 2 minutes and were recooled to 84°K in 4 minutes. The resulting cubic C samples were then cooled to 4.2°K and observed for 3 hours before warming began: Warming from 4.2°K to 200°K required 6-8 hours. Samples D(1,2) (5.94% HDO in H_2O) were deposited at $83 \pm 3^\circ\text{K}$ on CsI, warmed to $188 \pm 3^\circ\text{K}$ in 8 minutes, annealed at $188 \pm 3^\circ\text{K}$ for 4 minutes and rapidly recooled to 83°K . Samples D1 and D2 were then treated as in C above.

During warming sets of P.E. 421 spectra were recorded for each sample under identical spectrophotometer conditions. The basic spectrometer conditions were the same as those for samples A and B (section 3.1 a) with small variations. For example, HDO peaks were recorded at $20 \text{ cm}^{-1}/\text{in}$ or $2 \text{ cm}^{-1}/\text{div}$, and a 10 cm path gas cell (in the reference beam) was used with the Bodenseewerk unit for effective instrument purging. Among the three

sets of C sample spectra, frequencies were reproduced to within $\pm 2 \text{ cm}^{-1}$ at 170°K and $\pm 1 \text{ cm}^{-1}$ at 4°K , while among the two sets of D sample spectra frequency reproducibility was only $\pm 3 \text{ cm}^{-1}$ at 160° or 4°K . Typical HDO spectra were shown in Fig. 3.1.

(ii) Results of Warming Cubic Ice Containing HDO

Frequencies, half-height widths and absorbances were obtained as in section 3.1(b). However, to inhibit personal systematic bias the spectra were analyzed randomly with respect to temperature and during analysis no reference to temperature was permitted. Because of $2 \text{ cm}^{-1}/\text{div}$ recording, HDO peak frequencies were read to $\pm 0.5 \text{ cm}^{-1}$. No attempt was made to subtract the $3\nu_R(\text{H}_2\text{O})$ weak absorption from $\nu_{\text{OD}}(\text{HDO})$ absorption and consequently $\nu_{\text{OD}}(\text{HDO})$ frequencies are slightly low. Baselines for absorbances and half-height widths were drawn from 3394 to 3140 cm^{-1} for $\nu_{\text{OH}}(\text{HDO})$ and from 2480 cm^{-1} to 2340 cm^{-1} for $\nu_{\text{OD}}(\text{HDO})$.

(a) HDO frequencies. The behaviour of $\nu_{\text{OH}}(\text{HDO})$ frequency with increasing temperature is shown in Fig. 3.6. The data were derived from one set of spectra during a single warming period. Errors in instrumentation and in the methods of data evaluation limited the precision to $\pm 1 \text{ cm}^{-1}$.

Pertinent parameters from Fig. 3.6 are compiled in Table III.IV. The low temperature limiting frequency was obtained by extrapolating the data to 0°K . Although the data are non-linear, they can be approximated by two straight lines--a low and a high temperature line. The low and high temperature frequency dependences were evaluated from these lines and the "freeze-in" temperature was chosen as their point of intersection. There is a slight indication of irregular behaviour between 45° and 70°K (Fig.3.6). Sample sublimation above 180°K did not appear to affect the frequency data.

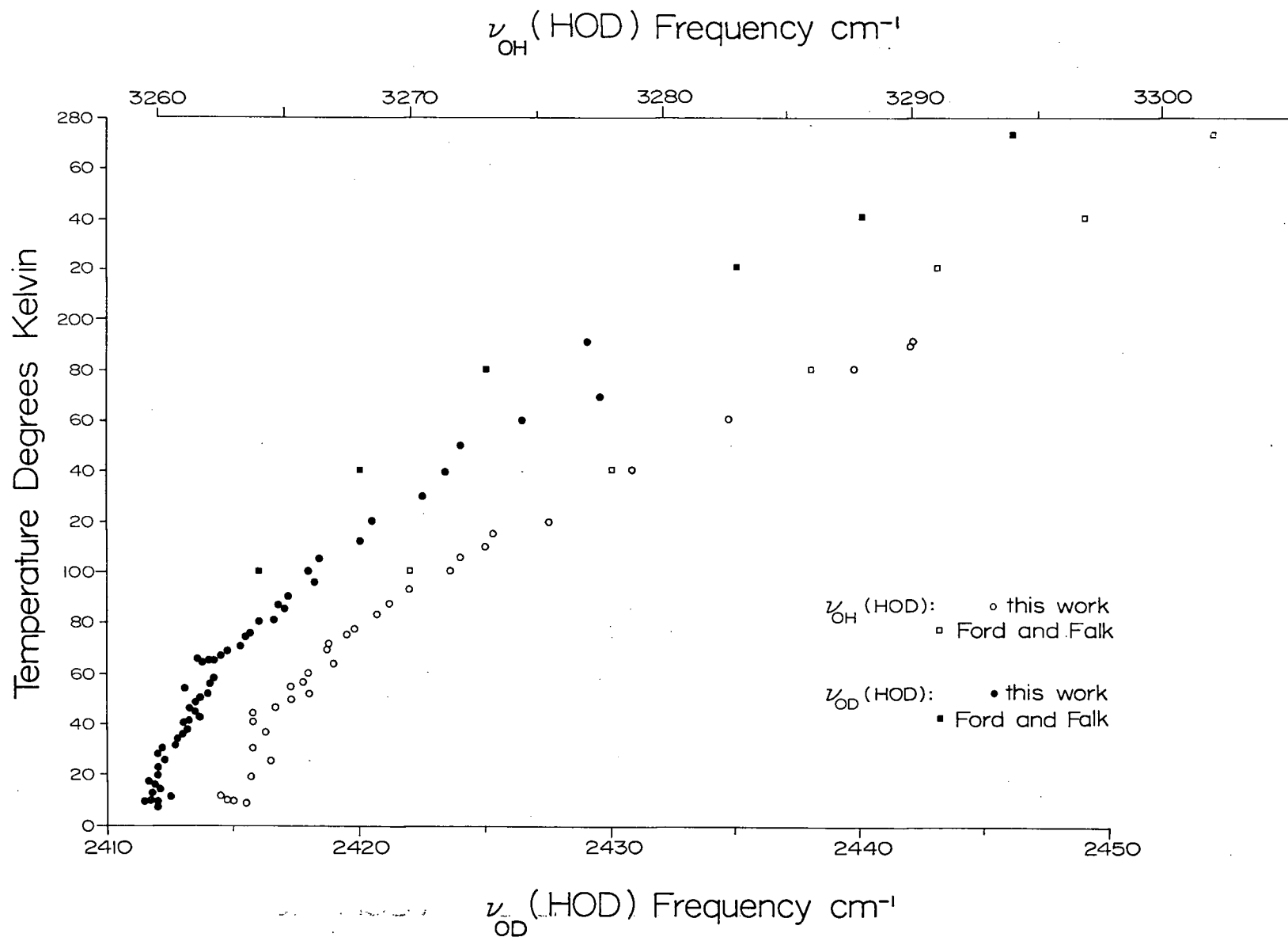


Fig. 3.6 The shifts of HDO stretching frequencies for cubic ice I. The temperatures are not corrected for source beam heating, +10°K should be added. Open points represent $\nu_{OH}(\text{HDO})$ and solid points represent $\nu_{OD}(\text{HDO})$. Data of Ford and Falk (100) is included for comparison.

Table III.IV The low temperature behaviour of the HDO stretching modes in the H₂O and D₂O environments of cubic ice I.

		$\nu_{\text{OH}}(\text{HDO})$	$\nu_{\text{OD}}(\text{HDO})$
Low Temperature Limit	cm ⁻¹	3263.5 ± 1	2412.0 ± 1
Ratio $\nu_{\text{OH}}/\nu_{\text{OD}}$		1.354 ± 0.001	
Linear Low Temperature Dependence	cm ⁻¹ /°K	0.047 ± 0.005	0.047 ± 0.005
Linear High Temperature Dependence	cm ⁻¹ /°K	0.200 ± 0.005	0.123 ± 0.005
"Freeze-in" Temperature	°K	80 ± 5	68 ± 5
Irregularities	°K	45 - 70	~60

Behaviour of $\nu_{\text{OD}}(\text{HDO})$ is shown in Fig. 3.6 and some parameters are compiled in Table III.IV. The comments made above concerning $\nu_{\text{OH}}(\text{HDO})$ apply equally well to $\nu_{\text{OD}}(\text{HDO})$.

The peak and shoulder near 800 cm⁻¹ in the samples of D₂O (4.0% HDO) [tracing C, bottom of Fig. 3.1] were assigned to HDO librations, $\nu_{\text{R}}'(\text{HDO})$ and $\nu_{\text{R}}(\text{HDO}) + \nu_{\text{T}}(\text{D}_2\text{O})$ respectively. (For ease of notation $\nu_{\text{R}} + \nu_{\text{T}}$ is designated ν_{R}' .) Temperature variations of $\nu_{\text{R}}(\text{HDO})$ and $\nu_{\text{R}}'(\text{HDO})$ are shown in Fig. 3.7 and some parameters are compiled in Table III.V. As shoulder positions are

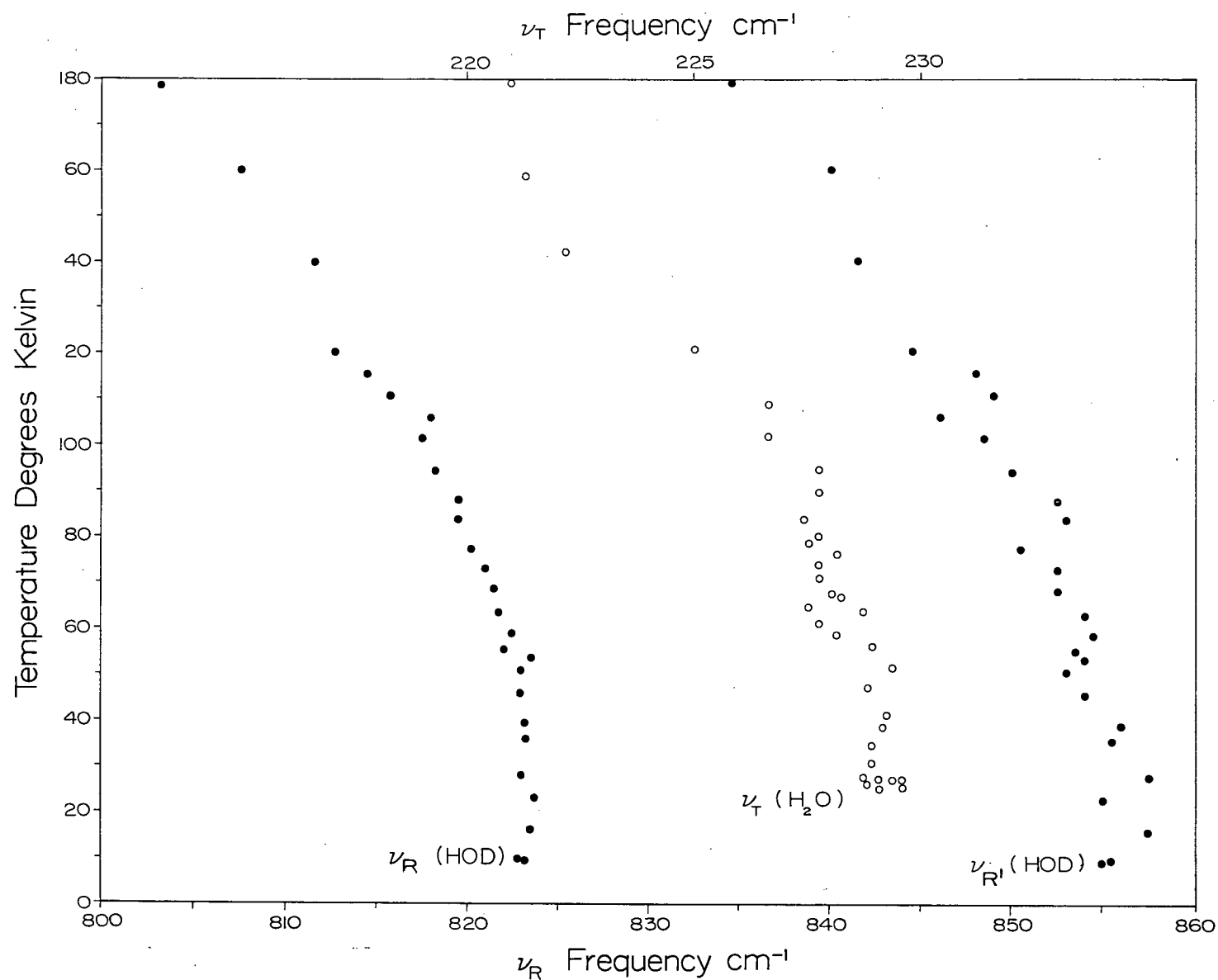


Fig. 3.7 The shifts of ν_R (HDO), ν_R' (HDO) and ν_T (H₂O) for cubic ice I during warm-up. The librational shoulder ν_R' (HDO) is assigned as ν_R (HDO) + ν_T (D₂O). Temperatures are uncorrected for source heating.

Table III.V The low temperature behaviour of the HDO librational modes in cubic ice I for dilute solutions of HDO in H₂O and D₂O.

		$\nu_R(\text{HDO})$	$\nu_R(\text{HDO}) + \nu_T(\text{D}_2\text{O})$
Low Temperature Limit	cm ⁻¹	823.3 ± 0.5	856.2 ± 1.5
Linear Low Temperature Dependence	cm ⁻¹ /°K	< -0.02	< -0.04
Linear High Temperature Dependence	cm ⁻¹ /°K	-0.147 ± 0.012	-0.154 ± 0.022
"Freeze-in" Temperature	°K	55 ± 5	65 ± 5
Irregularities	°K	105 - 120	--

difficult to determine accurately, ν_R' data have a higher error than ν_R --in this case ± 1.5 cm⁻¹. Spectra and data were obtained as in section 3.1.

(b) HDO half-height widths. The $\nu_{\text{OH}}(\text{HDO})$ and $\nu_{\text{OD}}(\text{HDO})$ half-height widths, Fig. 3.8, were obtained from the same sets of spectra as were the frequencies in the preceding section. Details of the plots are compiled in Table III.VI.

Errors in $\Delta\nu_{\text{OH}}^{1/2}(\text{HDO})$ (± 0.75 cm⁻¹) resulted from 1) inaccuracies in assigning baselines (± 0.005 absorbance), 2) errors in estimating 1/2 I for I = 1.0 absorbance (± 0.01 absorbance), and 3) errors in estimating widths

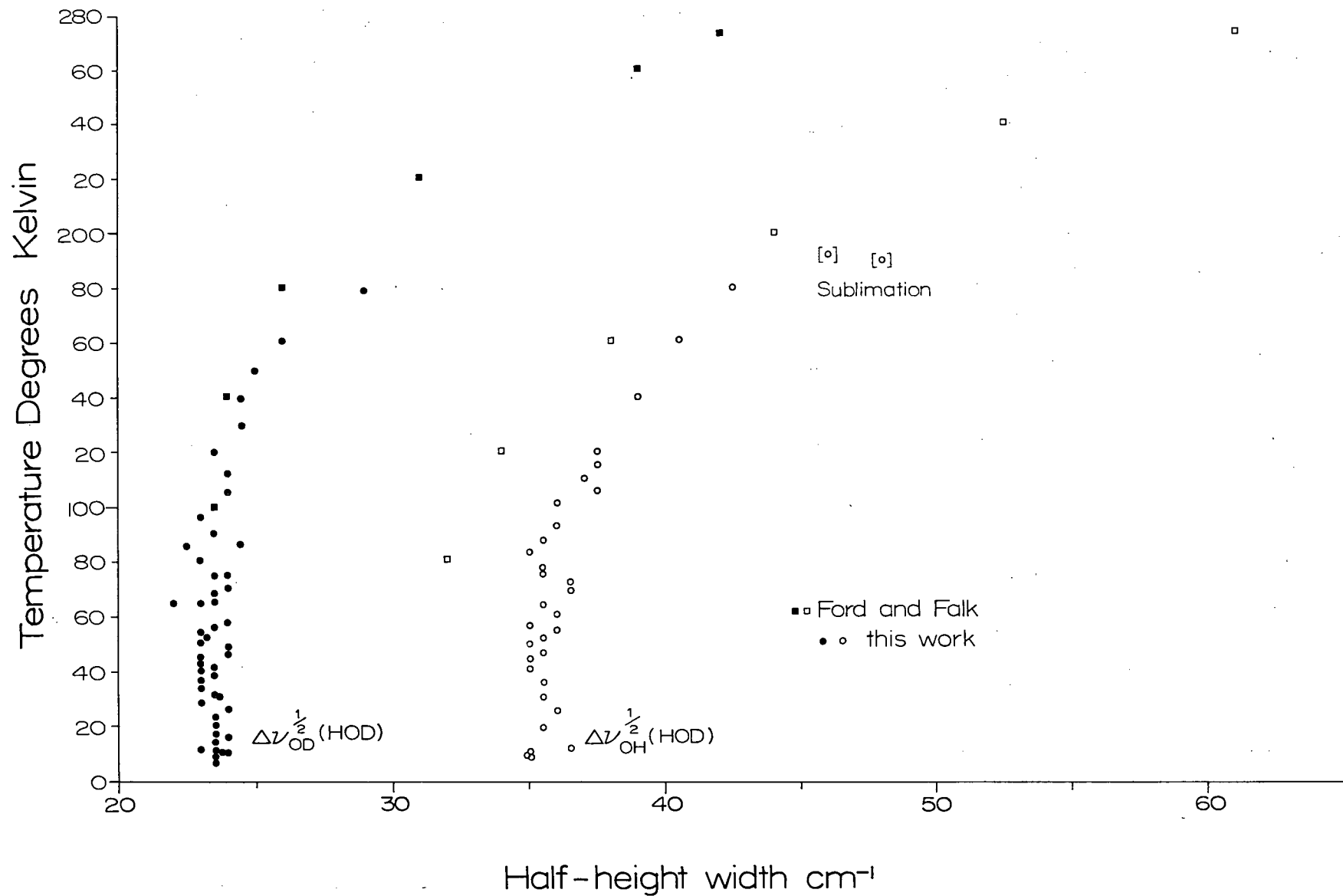


Fig. 3.8 The shifts of HDO stretching modes half-height widths during warm-up of cubic ice I. These data were obtained from the same spectra as were the frequencies of Fig. 3.6. Temperatures are uncorrected.

Table III.VI The low temperature behaviour of the HDO stretching modes half-height widths for HDO in H₂O and D₂O cubic ice I.

		$\nu_{\text{OH}}(\text{HDO})$	$\nu_{\text{OD}}(\text{HDO})$
Low Temperature Limit	cm^{-1}	35.5 ± 0.75	23.5 ± 0.75
Ratio $\Delta\nu_{\text{OH}}/\Delta\nu_{\text{OD}}$		1.51	
Linear Low Temperature Dependence	$\text{cm}^{-1}/^{\circ}\text{K}$	< 0.02	< 0.03
Linear High Temperature Dependence	$\text{cm}^{-1}/^{\circ}\text{K}$	0.066 ± 0.005	0.044 ± 0.005
"Freeze-in" Temperature	$^{\circ}\text{K}$	87 ± 5	105 ± 5

($\pm 0.5 \text{ cm}^{-1}$). Because of sample sublimation, data for $\Delta\nu_{\text{OH}}^{\frac{1}{2}}(\text{HDO})$ obtained above 190°K do not extrapolate into those obtained at lower temperatures.

Errors in $\Delta\nu_{\text{OD}}^{\frac{1}{2}}(\text{HDO})$ (estimated to be $\pm 1.0 \text{ cm}^{-1}$) resulted from 1) inaccuracies in assigning baselines due to an underlying $3\nu_{\text{R}}(\text{H}_2\text{O})$ absorption (± 0.01 absorbance), 2) errors in estimating $1/2 I$ for $I = 0.70$ absorbance (± 0.005 absorbance), and 3) errors in estimating widths ($\pm 0.5 \text{ cm}^{-1}$).

In both cases above the HDO half-height widths were quoted and plotted only to the nearest 0.5 cm^{-1} .

(c) HDO absorbances. Peak heights (I) of $\nu_{OH}(HDO)$ and $\nu_{OD}(HDO)$ were measured (with errors of ± 0.01 and ± 0.005 abs. units respectively) from consistent baselines on the same sets of spectra as were frequency and half-height width. Absorbance data (I) are plotted in Fig. 3.9 and the details are listed in Table III.VII. Normalization of the two sets of intensities was not attempted.

Peak heights underwent a relatively smooth, continuous decrease from 28° to $190^\circ K$. Data obtained with the sample above $190^\circ K$ indicate a sharp decrease in I as the sample sublimed. No estimate was made of cumulative sample loss due to sublimation during the whole experiment.

A slight, concave discontinuity centered at $125^\circ K$ appears in an otherwise convex curve for these data. The data appear constant below $35^\circ K$ indicating I ($\nu_{OD}(HDO)$) varied by less than -0.24×10^{-3} absorbance/ $^\circ K$.

Table III.VII The low temperature behaviour of the HDO stretching modes peak heights for cubic ice I.

	$I(\nu_{OH}(HDO))$	$I(\nu_{OD}(HDO))$
Low Temperature Limit absorbance	0.945	0.540
Linear Low Temperature Dependence absorbance/ $^\circ K$	-0.69×10^{-3}	-0.24×10^{-3}
Linear High Temperature Dependence absorbance/ $^\circ K$	-2.26×10^{-3}	-1.07×10^{-3}
"Freeze-in" Temperature $^\circ K$	79 ± 5	76 ± 5
Irregularities $^\circ K$	130(?)	125

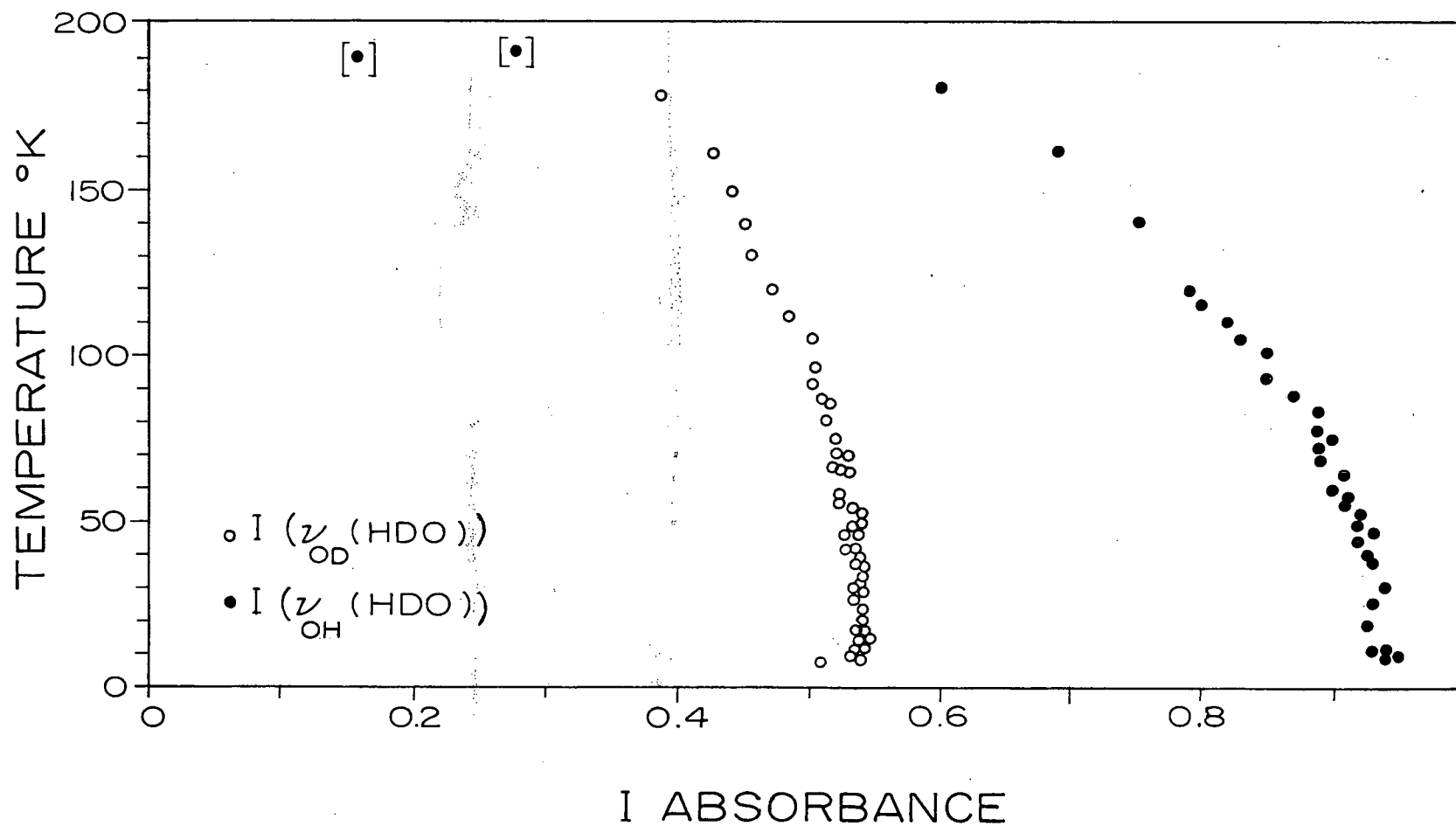


Fig. 3.9 The shifts of the HDO stretching mode peak heights or absorbances (I) during warm-up of a cubic ice I sample. The I data were obtained from the same spectra as were the frequencies and $\Delta\nu$ of Figs. 3.6 and 3.8.

B. Temperature Dependence of H₂O and D₂O Absorptions

Eight H₂O and D₂O absorptions provided less accurate measures of the primary spectral parameters than the three HDO absorptions, but they did yield information on cubic ice I.

(i) Experimental

Five sets of spectra from five specimens were recorded on the P.E. 421 or P.E. 301 spectrophotometers in the liquid helium dewar. Details of sample composition and preparation are given in Table III.VIII. General H₂O absorptions were observed in samples E and F and their results were combined with those of cubic samples A and B. General D₂O absorptions were observed in samples H and I and their results were combined with those of sample C. Samples E, F, H and I were observed on CsI in the P.E. 421. The $\nu_T(\text{H}_2\text{O})$ absorptions were observed in a separate sample (G) with polyethylene windows on the P.E. 301.

P.E. 421 function settings were again identical within one set of spectra and as consistent as possible between samples. Specific conditions were given in section 3.1. Only small alterations in instrument purging, reference beam attenuation and optical wedge settings were made.

The P.E. 301 was used in the I/I_0 mode between 666 cm^{-1} and 160 cm^{-1} with Bodenseewerk purging and no evacuated reference cell. Spectra were scanned at $40\text{ cm}^{-1}/\text{min.}$ and recorded at $4.4\text{ cm}^{-1}/\text{div.}$ Spectral slit widths varied but were usually less than 4 cm^{-1} .

Table III.VIII Details of depositing and annealing of H₂O, D₂O and HDO bearing ice I samples.

Sample	E H ₂ O	F H ₂ O(D ₂ O)	G H ₂ O	H D ₂ O	I D ₂ O(H ₂ O)
Deposition Temperature (°K)	85	85	85	85	85
Time to warm from 85°K to 185°K (min.)	12	15	17	17	15
Maximum annealing Temperature (°K)	186	183	187	185	180
Time maintained at maximum annealing temperature (min.)	2	3	2	1	2
Time to cool from 185°K to 85 °K (min.)	5	4	4	5	6
Time to cool from 85°K to 8°K (min.)	30	24	18 (25°K)	21	18
Time maintained at 8°K (min.)	245	170	269 (25°K)	210	123
Length of warmup run (min.)	243	166	433	920	348

(ii) Results of Warming H₂O and D₂O Cubic Ice I

Frequency data were obtained as in section 3.1B. The sets of spectra were analyzed randomly with respect to temperature as in section 3.2A(ii). Each complete set of spectra was analyzed one band at a time. Because of the breadth of H₂O and D₂O bands, frequency data were accurate only to ± 2.5 cm⁻¹.

(a) Fundamental H₂O and D₂O frequencies. The ν_3 frequencies are plotted as a function of temperature in Fig. 3.10 and some plot parameters are compiled in Table III.IX. From Fig. 3.10 and Table III.IX it is apparent that liquid nitrogen and liquid helium cell data (samples A - B and E - F) do not concur.

For $\nu_3(\text{D}_2\text{O})$ no data were obtained between 51° and 83°K since a sudden slight rise in cryostat pressure (from traces of condensed residual O₂ and N₂) caused heat losses between the nitrogen shield and the helium dewar. Although the pressure rose only from 6.8×10^{-6} Torr to 15×10^{-6} Torr and dropped to 8.2×10^{-6} in 2 - 3 minutes, the pressure rise was sufficient to rapidly warm the helium dewar and sample block.

The ν_1 frequency variations during sample warming are plotted in Fig. 3.11 and some details of the behaviour are given in Table III.IX. For $\nu_1(\text{D}_2\text{O})$ the helium and nitrogen cell data agree reasonably well. For $\nu_1(\text{H}_2\text{O})$ a high scatter of points did not permit evaluation of low temperature dependence. No data was obtained between 51° and 83°K for the same reasons as with ν_3 , a rapid pressure rise.

Helium and nitrogen cell ν_2 data do not agree (Fig. 3.12). Details of the plots are given in Table III.IX. Data for three helium cell samples and two nitrogen cell samples are plotted (including unannealed sample data at

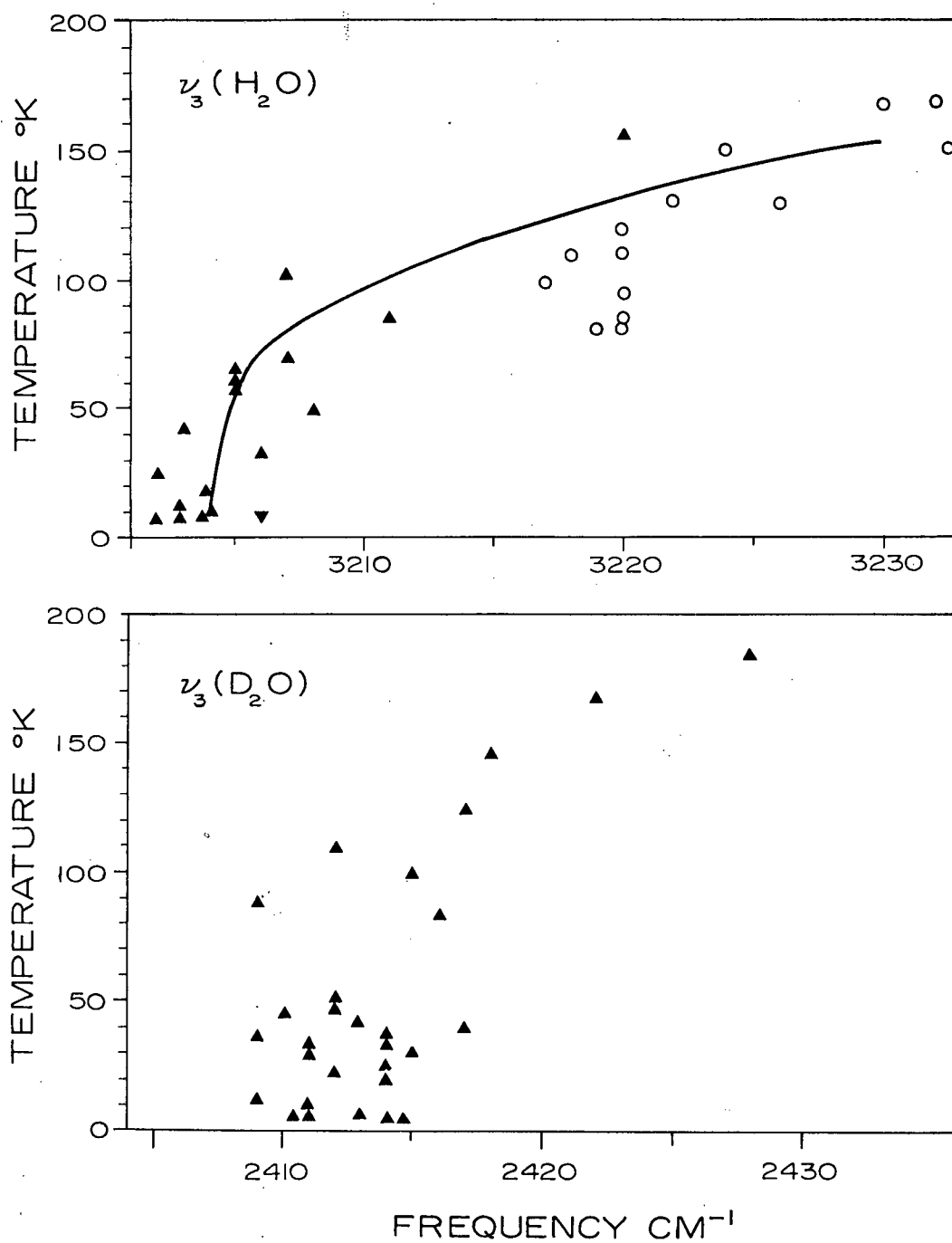


Fig. 3.10 The shifts of cubic ice I ν_3 during warm-up. For H_2O the open circles represent data from experiments between 83° and 180°K on a Hornig-Wagner all-glass cell. Temperatures are uncorrected for source beam heating.

Table III.IX The temperature dependences of cubic ice I H_2O and D_2O vibrational absorptions.

	Low temperature limit	Low temperature dependences	High temperature dependences	Freeze-in temperature
H_2O	cm^{-1}	$\text{cm}^{-1}/^\circ\text{K}$	$\text{cm}^{-1}/^\circ\text{K}$	$^\circ\text{K}$
$\nu_1 + \nu_{\text{T}}$	3334 ± 4	0.08 ± 0.05	$+ 0.20 \pm 0.08$	80 ± 10
ν_3	3204 ± 2 (3215 ± 5)	0.03 ± 0.03 --	$+ 0.17 \pm 0.05$ ($+ 0.19 \pm 0.04$)	70 ± 10
ν_1	3133 ± 3		$+ 0.34 \pm 0.03$	65 ± 5
$3\nu_{\text{R}}$	2239 ± 3	< -0.09	$- 0.12 \pm 0.03$	70 ± 10
$\nu_2/2\nu_{\text{R}}$	1562 ± 4 (1605 ± 10)	< 0.14 --	-- (0.36 ± 0.10)	
ν_{R}'	881 ± 7	--	$- 0.19 \pm 0.08$	80 ± 20
ν_{R}	832 ± 5	--	$- 0.18 \pm 0.06$	75 ± 10
ν_{T}	229.2 ± 0.75		$- 0.102 \pm 0.012$	95 ± 5

Table III.IX (Continued)

	Low temperature limit	low temperature dependences	High temperature dependences	Freeze-in temperature
D_2O	cm^{-1}	$cm^{-1}/^{\circ}K$	$cm^{-1}/^{\circ}K$	$^{\circ}K$
$\nu_1 + \nu_T$	2464 ± 3	--	0.17 ± 0.05	80 ± 30
ν_3	2413 ± 4	< 0.06	0.13 ± 0.04	100 ± 20
ν_1	2320 ± 5	--	0.19 ± 0.03	70 ± 10
$3\nu_R$	1637 ± 3	< -0.07	-0.11 ± 0.03	60 ± 5
$\nu_2/2\nu_R$	1189 ± 2	0.13 ± 0.03	0.08 ± 0.05	50 ± 10
ν_R'	663 ± 6	--	-0.10 ± 0.05	100 ± 10
ν_R	630 ± 4	--	-0.11 ± 0.04	65 ± 15

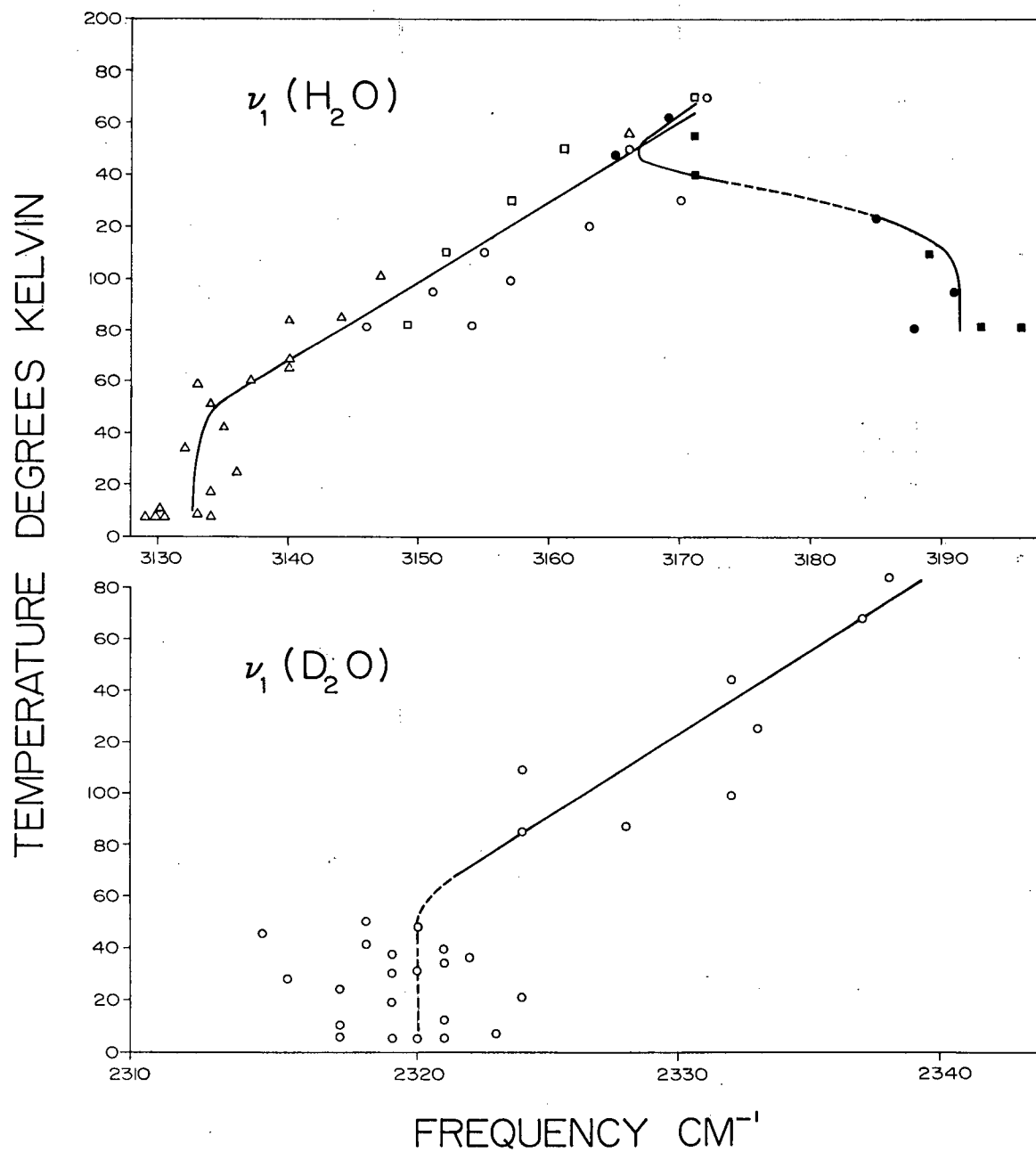


Fig. 3.11 The shifts of cubic ice I ν_1 during warm-up. For H_2O typical annealing run data are included for pre- and post-annealing behaviour (open circles and squares).

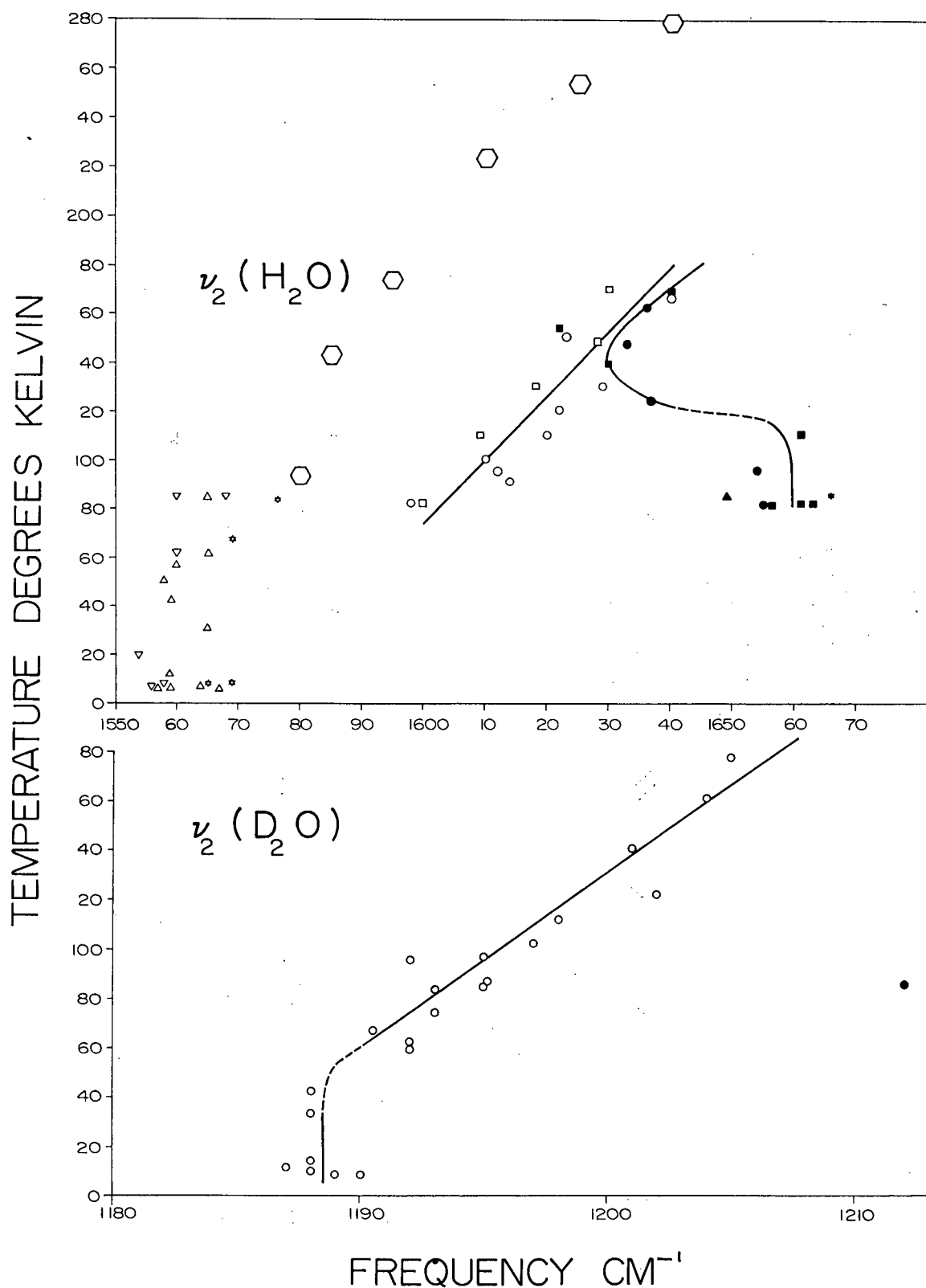


Fig. 3.12 The shifts of ν_2 in cubic ice I during warm-up. For comparison to the helium cell data, nitrogen cell data for pre and post-annealing behaviour are included. Pimentel and Zimmerman's (97) data are also included for hexagonal ice I. Temperatures are uncorrected.

83°K for the helium runs). The $\nu_2(\text{D}_2\text{O})$ data were not obtained from the same set of spectra as the more intense ν_3 and ν_1 absorption data.

Data relating the ν_R frequency temperature dependence are plotted in Fig. 3.13 and important parameters obtained from the figure are listed in Table III.IX. For $\nu_R(\text{H}_2\text{O})$, helium and nitrogen cell data are in good agreement. Because the ν_R band is broad the maximum was difficult to determine accurately. Consequently, the low temperature data are poor and a low-temperature/frequency dependence could not be approximated.

The nature of translational H_2O absorptions is shown in Fig. 3.14. The peak frequency temperature dependence is given in Fig. 3.15. An irregular shift of 1.5 cm^{-1} occurs between 55 and 60°K and the frequency is invariant from 155° to 200°K. The details of the graph are listed in Table III.IX.

Several features of $\nu_T(\text{H}_2\text{O})$ were observed. The intersection of two lines along peak sides was read to $\pm 0.50 \text{ cm}^{-1}$ while shoulder positions were estimated to within $\pm 3 \text{ cm}^{-1}$. The peak near 165 cm^{-1} is distorted because of the rapid energy drop at the end of a grating range. Frequencies of peaks, minima, shoulder edges and baseline at 25°K are listed in Table III.X.

(b) Overtone and combination frequencies. The $(\nu_1 + \nu_T)$ data are plotted in Fig. 3.16 and summarized in Table III.IX: One can see that the helium and nitrogen cell data agree. However, the data are too poor to permit an approximation of a linear low temperature dependence.

Both the H_2O and D_2O $3\nu_R$ frequencies (Fig. 3.17) decrease with increasing temperature at rates indicated in Table III.IX. Again the helium and nitrogen cell data agree near 80°K.

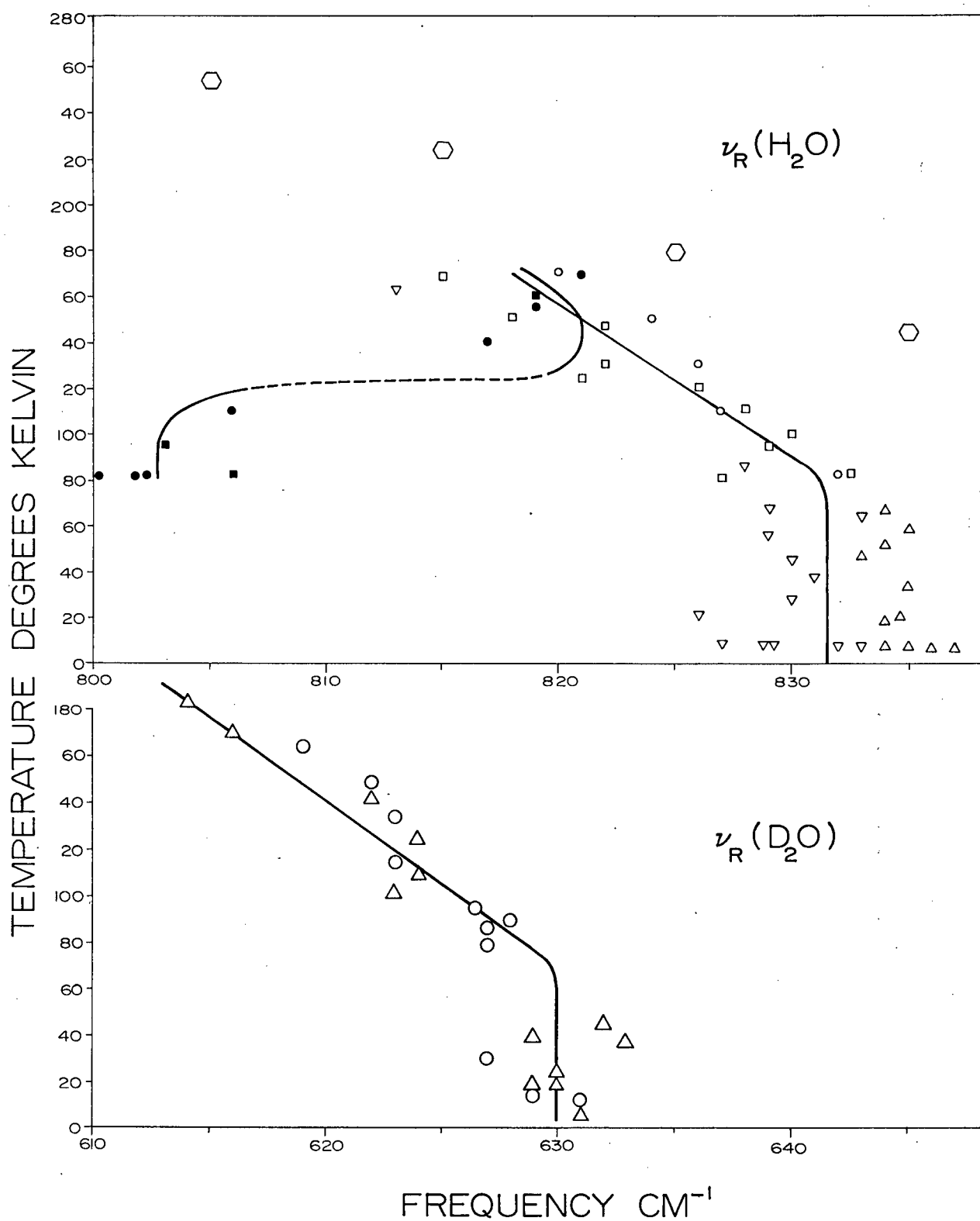


Fig. 3.13 The shifts of ν_R for cubic ice I during warm-up. For H_2O Pimentel and Zimmerman's (97) data and liquid nitrogen cell data are included for comparison.

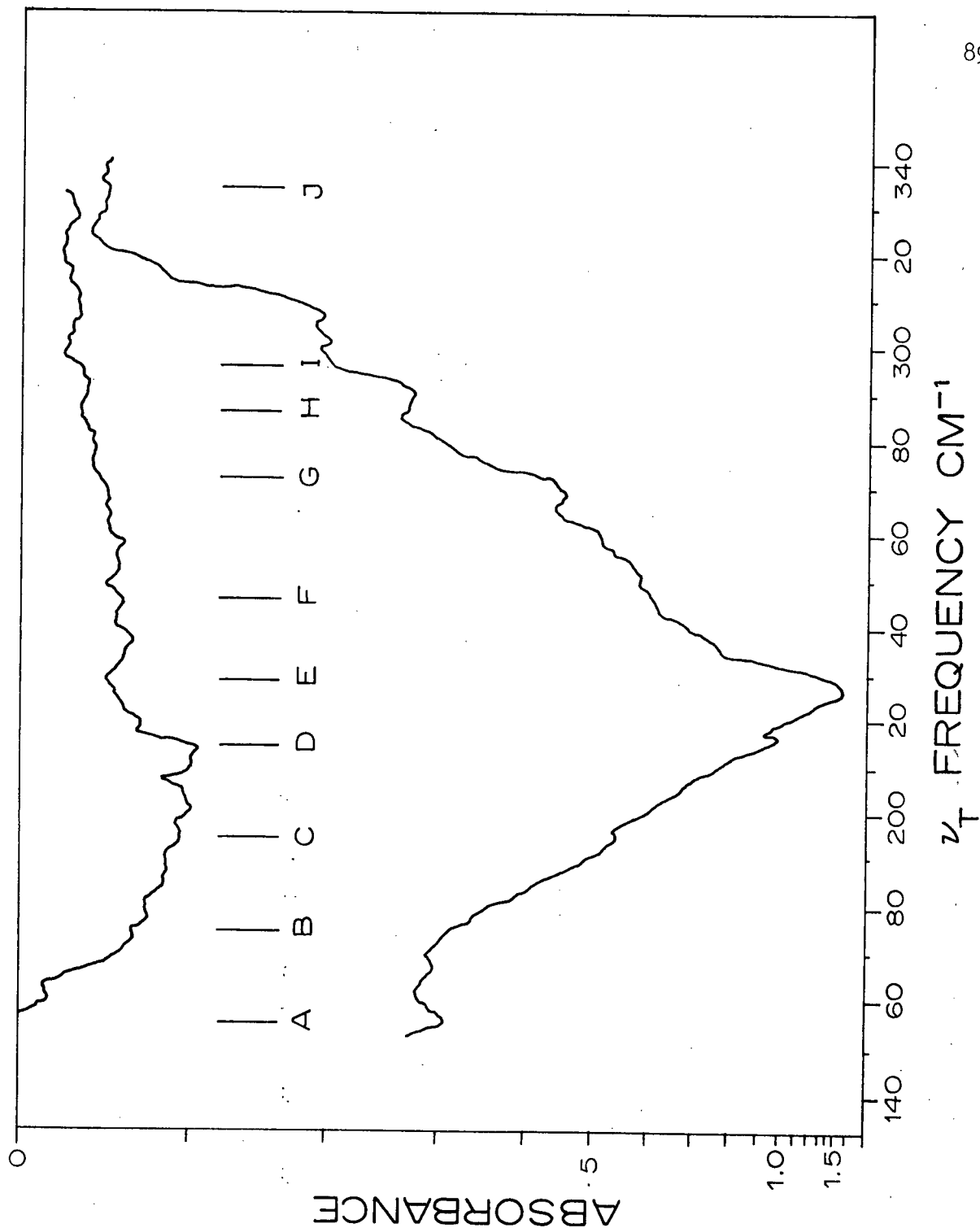


Fig. 3.14 The cubic ice I $\nu_T(\text{H}_2\text{O})$ band at 83°K and the background spectrum through the blank cell at 83°K. The feature near 218 cm^{-1} arises from a filter change.

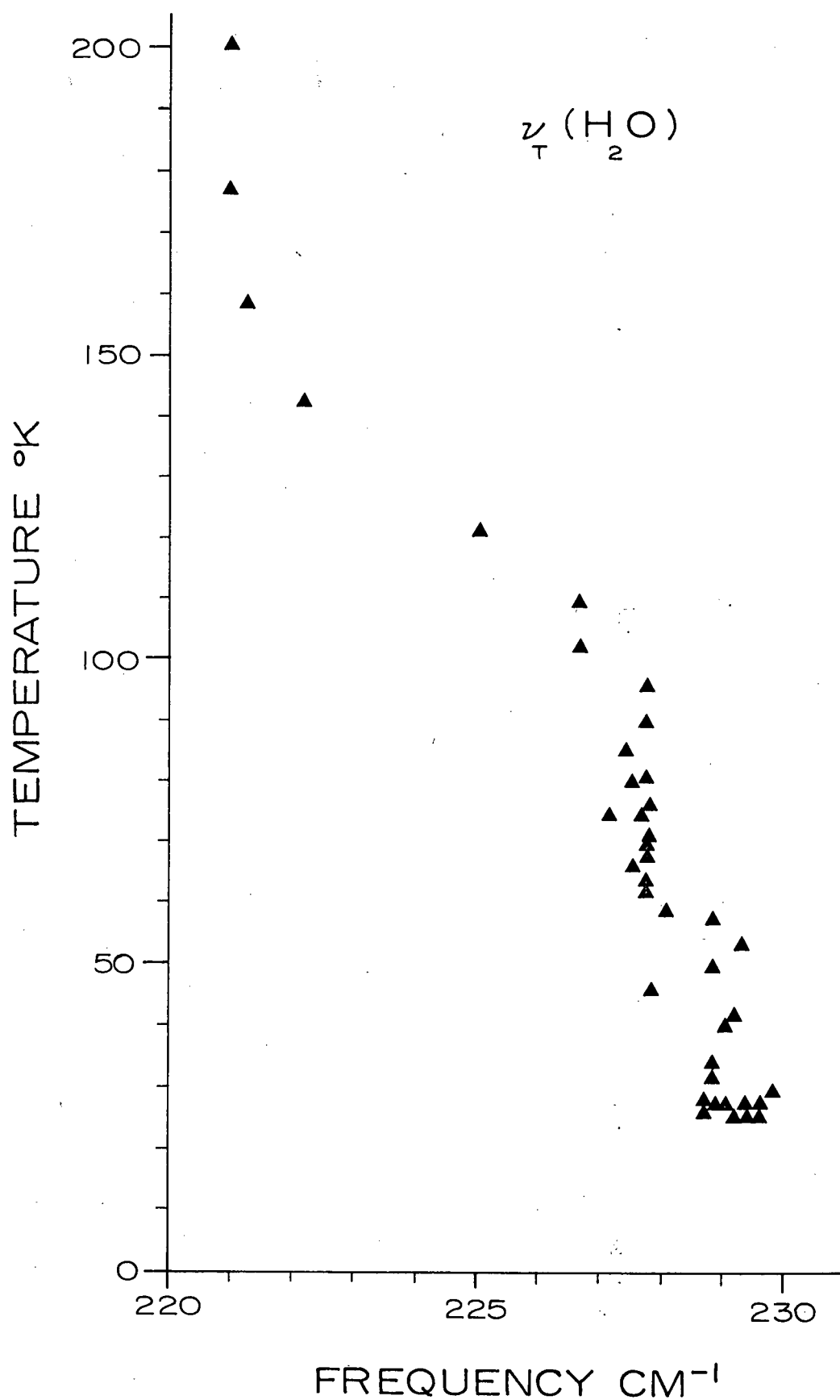


Fig. 3.15 The shifts of $\nu_T(\text{H}_2\text{O})$ for cubic ice I during warm-up. The sample was mounted on a polyethylene window 0.25 cm thick. The cell temperature did not reach helium temperature with the source on or off after 3 hours of cooling. Temperatures are uncorrected for source heating.

Table III.X The interpretation of the $\nu_T(\text{H}_2\text{O})$ features for comparison to previous results.

$\nu_T(\text{H}_2\text{O})$ Feature	Description	Frequency cm^{-1}
A	peak	<161
B	minimum	176.5 ± 1
C	shoulder edge	193 ± 3
D	shoulder edge	214 ± 3
E	peak	$229.6 \pm .5$
F	shoulder edge	246 ± 3
G	shoulder edge	272 ± 3
H	shoulder edge	286 ± 3
I	shoulder edge	295 ± 3
J	baseline	334 ± 3

The $(\nu_R + \nu_T)$ data are plotted in Fig. 3.18 and summarized in Table III.IX. This band is a poorly defined shoulder on the intense ν_R band and thus could only be estimated to within $\pm 7 \text{ cm}^{-1}$. Helium and nitrogen cell data are not in good agreement. Low temperature dependences could not be defined.

(c) H_2O and D_2O half-height widths. Data for cubic ice I (H_2O) were plotted in Figs. 3.4 and 3.5 of section 3.1. The half-height widths of the composite stretching band and the composite librational band increased with increasing temperature. However, the composite $(\nu_2, 2\nu_R)$ band half-height width decreased with increasing T.

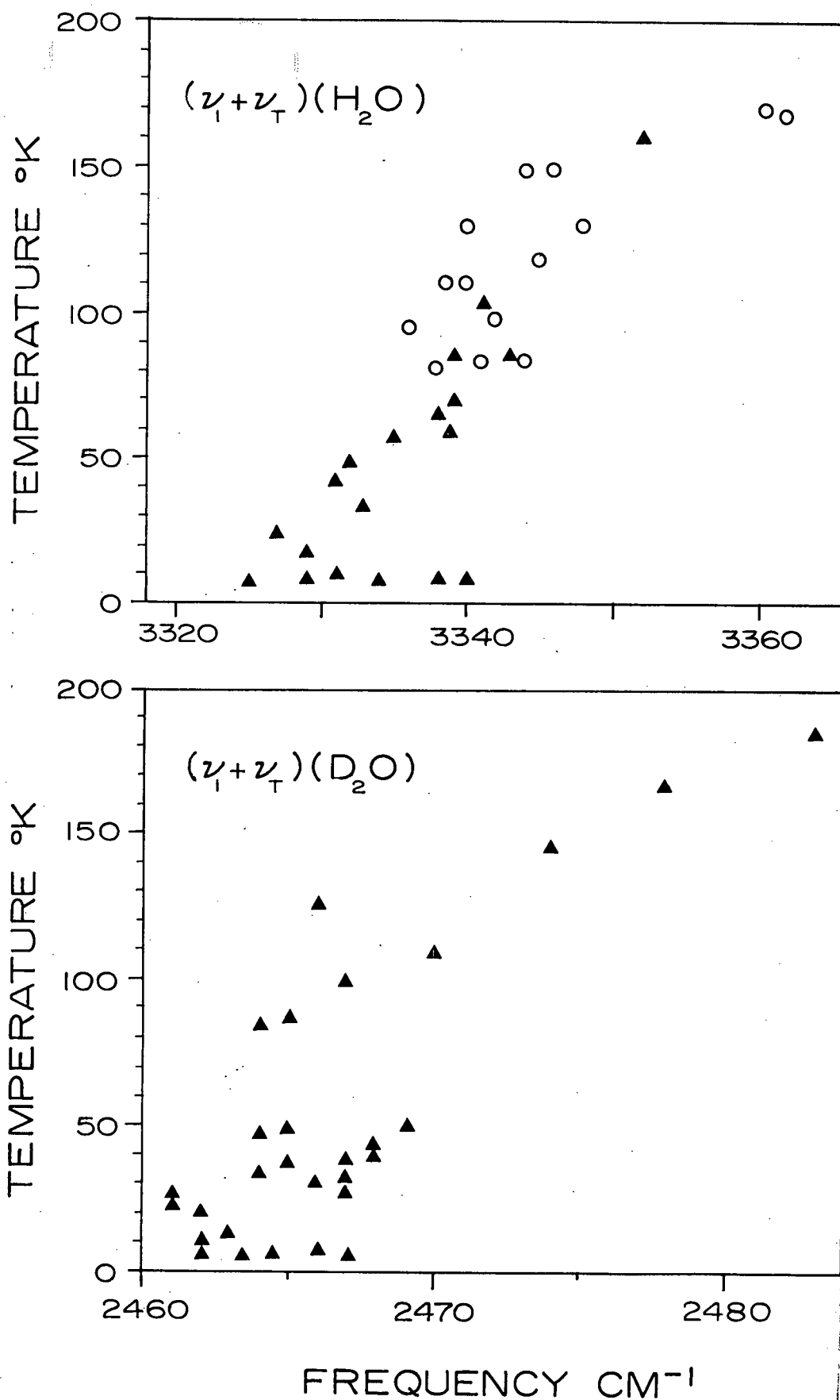


Fig. 3.16 The shifts of $(\nu_1 + \nu_T)$ for cubic ice I during warm-up. For H_2O the nitrogen cell data are included. Temperatures are uncorrected.

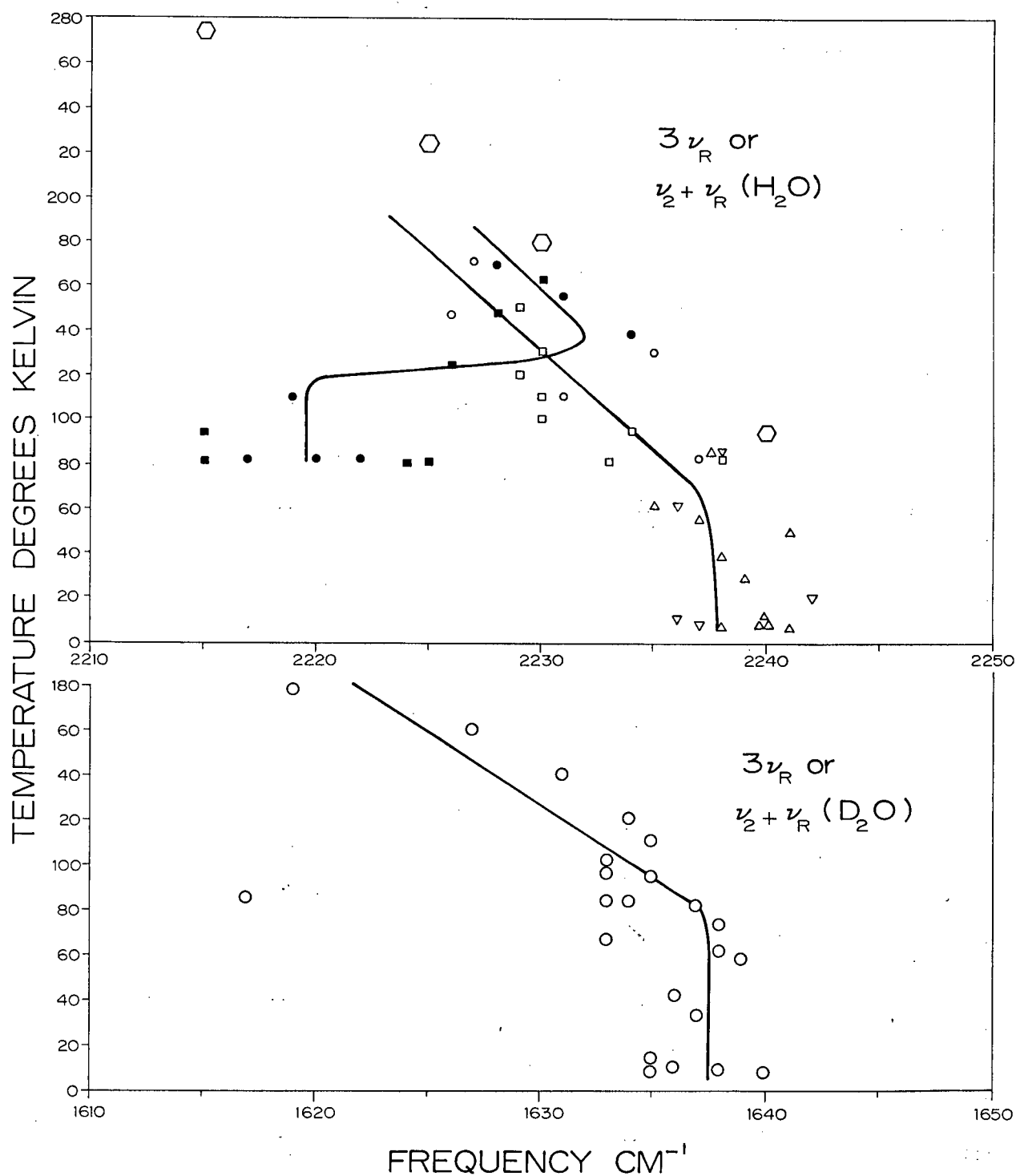


Fig 3.17 The shifts of $3\nu_R$ for cubic ice I during warm-up. For H_2O annealing data and data of Pimentel and Zimmerman (97) are included. Temperatures are uncorrected.

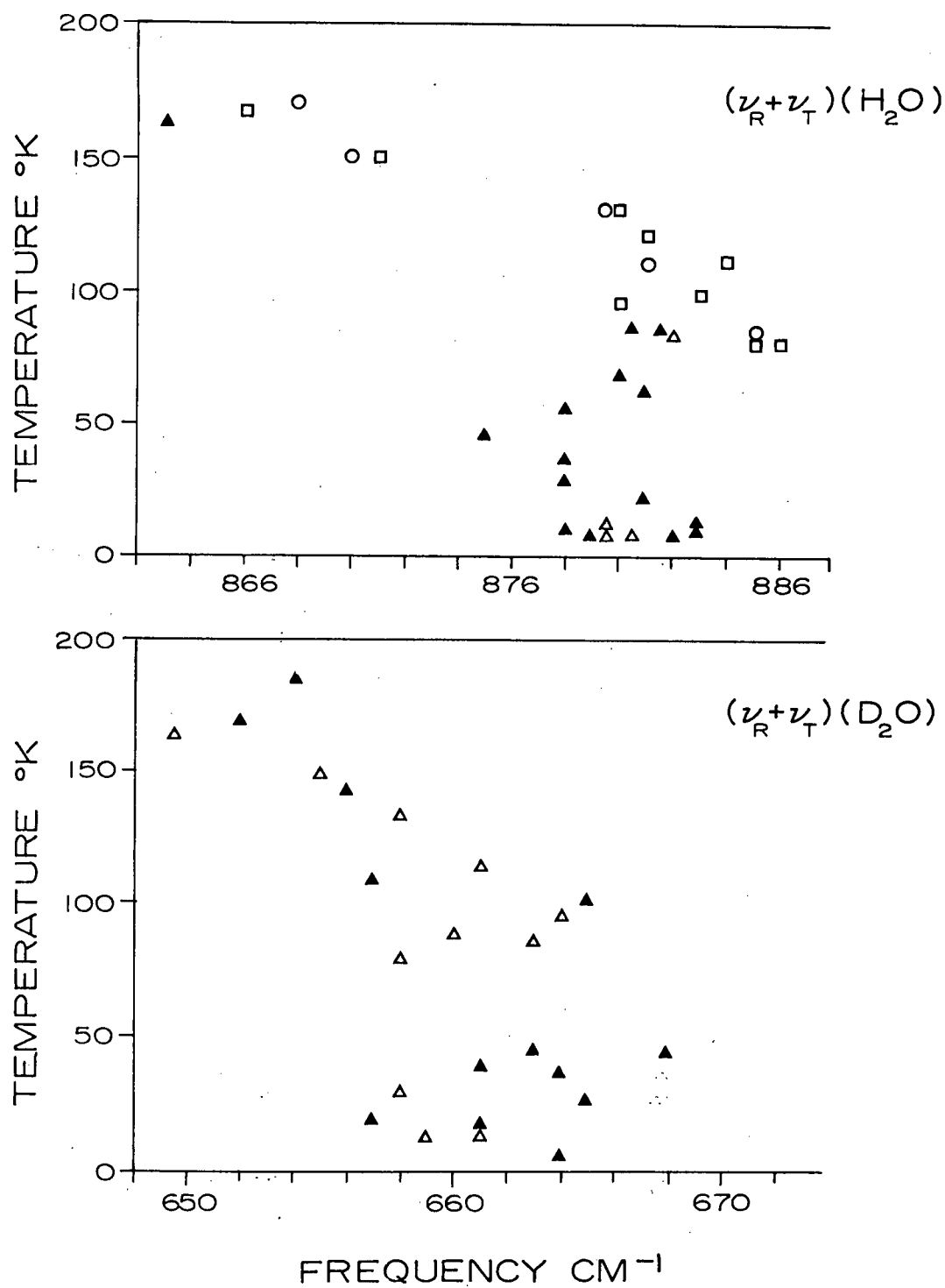


Fig. 3.18 The shifts of $(\nu_R + \nu_T)$ for cubic ice I during warm-up. Nitrogen and helium cell data are included for H_2O .

3.3 The H₂O, D₂O and HDO Ice I Absorptions at 83°K

In this section are listed the details of the H₂O, D₂O and HDO vitreous and cubic ice I absorptions at 83°K for comparison in Chapter 4 to the literature values.

A. Experimental

Typical spectra of vitreous and cubic ice were shown in Fig. 3.1: $\nu_T(\text{H}_2\text{O})$ was shown in Fig. 3.14. The samples, spectra and methods of treatment were described in sections 3.1 and 3.2.

B. Results at 83°K

Vitreous and cubic ice I have the same skeletal absorption spectra (Fig. 3.1) but are easily distinguished in details of band structure, frequency and width. Frequencies observed for the H₂O, HDO and D₂O systems at 83°K are compiled in Tables III.XI, III.XII and III.XIII respectively. Results of previous workers are included for comparison.

(i) H₂O Absorptions at 83°K

Spectra of vitreous and cubic ice I obtained in this work are in sharp contrast and exhibit features not previously observed.

The stretching band of cubic ice I is composed of one peak and two well defined shoulders--3340 (2442)(sh)cm⁻¹, 3210(2416) cm⁻¹ and 3149 (2392)(sh)cm⁻¹. (D₂O data are given in brackets.) In contrast, vitreous ice I has very weak absorptions at 3686(2720) cm⁻¹ and 3640 cm⁻¹ in addition to a peak at 3253(2436) cm⁻¹ and two poorly defined shoulders at

Table III.XI(a) The frequencies and assignments for cubic and hexagonal ice I of the present and previous workers.

Assignment	This Work				Whalley and Bertie(a)			Hornig and Haas (b)			Giguere and Harvey(c)			Val'kov and Maslenkova(d)			Ockman (e)
	Vitreous	Cubic			100°K			83°K			100°K			77°K			100°K
	93°K	93°K															
	cm ⁻¹	cm ⁻¹			cm ⁻¹			cm ⁻¹			cm ⁻¹			cm ⁻¹			cm ⁻¹
ν_3 olig	3686 vw	--															
ν_1 olig	3640 vw	--															
$\nu_1 + \nu_T$	~3367 sh	3340	ssh		3350	shs	(ν_1)3360	Msh						3321 (2)			3340
ν_3	3253 vs	3210±5 (3217±5)*	vs		3220±5	s	(ν_3)3210	vs		3260				3210 (4)			3224
ν_1	~3191 sh	3149	ssh		3140	shs	(2 ν_2)3125	Msh						3088 (10)			3140
3 ν_R	2220 w	2235	w		2266±20	vbw	2225	s		2250							2235
ν_2	1660 m	1570±10 (1604 5)*	m		1650±30	vbw	1585	s									1580
	1570 sh	--															
	--	(1130 msh)**															
$\nu_R + \nu_T$	846 ssh	881	ssh		900	sh											
ν_R	802 s	833	s		840	s	850			850							846
	--	~780	sh		770	sh											
	~675 sh	~690	sh		660	sh											
$\nu_R - \nu_T$	535 msh	570	msh		555	sh											

* data from sample A section 3.1; ** observed only in samples annealed above 200°K.

(a) Ref. 95 (b) Ref. 106 (c) Ref. 98 (d) Ref. 99 (e) Ref. 108.

Table III.XI(b) The translational lattice mode features of vitreous, cubic and hexagonal ice I.

$\nu_T(\text{H}_2\text{O})$	This Work		Giguere and Arrauudeau(a)		Whalley(b)	Pimentel(c)
	93°K Vitreous	93°K Cubic	113°K Vitreous	173°K Cubic	100°K Hexag.& Cub.	93°K Hexag.
	cm ⁻¹	cm ⁻¹				
high frequency limit	326 ± 3	334 ± 3			~328	(330)*
shoulder	301	296	295	293	300-310	(305)
shoulder	271	267	259	257	~275	(275)
change of slope		246			~240	
peak	212.8±0.5	227.8±0.5	225 (ms)	223 m	229.2	229
change of slope		211			220	
change of slope		197			200	
shoulder		191	190	188	190	
minimum		173			180.5	
peak		162	154 (m)	152	164	

* taken from Fig. 3 of Ref. (97).

(a) Ref. 89 (b) Ref. 95 (c) Ref. 97.

Table III.XII Comparison of the present and previous HDO vibration frequencies near 90°K.

Assignment	This work 93°K		Whalley and Bertie (a)	Hornig and Haas (b)	Ford and Falk (c)	Hornig et al. (d)
	Vitreous	Cubic	100°K	83°K	93°K	83°K
	cm ⁻¹	cm ⁻¹	cm ⁻¹	cm ⁻¹	cm ⁻¹	cm ⁻¹
ν_{OH} HDO in D ₂ O	3304 m	3266 s	3277 ± 4 s	3275 vs	3270 ± 5	3300
ν_{OD} HDO in H ₂ O	--	(2442) wsh	2445 msh	2442 s		
	2437 m	2416 s	2421 ± 4 s	2416 vs	2418 ± 3	2440
	--	(2392) wsh	2395 msh	2393 s		
				1975 w		
$\nu_2(HDO)$				1490 s		1470
$\nu_R + \nu_T$ HDO in D ₂ O	--	854 wsh				
ν_R HDO in D ₂ O	792 w	819 mw	822 ± 6 m			800 620
HDO in H ₂ O			515 ± 10 m			

(a) Ref. 95 (b) Ref. 106 (c) Ref. 100 (d) Ref. 105.

Table III.XIII The frequencies and assignments of D₂O ice I (vitreous, cubic, hexagonal) near 90°K for the present and previous workers.

Assignment	This work Vitreous	93°K Cubic	Whalley and Bertie (a) 100°K hex.and cub.	Hornig and Haas (b) 83°K cubic	Giguere and Harvey (c) 100°K hexagonal	Val'kov and Maslenkova (d) 100°K hexagonal
	cm ⁻¹	cm ⁻¹	cm ⁻¹	cm ⁻¹	cm ⁻¹	cm ⁻¹
ν_3 olig	2720					
ν_1 olig	--	--				
$\nu_1 + \nu_T$	2499 ssh	2465	2485 ± 10 msh	$(\nu_1, 2\nu_2)^+$ 2495 msh		2542 (0.5)
ν_3	2436 s	2413	2425 ± 5 s	(ν_3) 2432 vs	2450	2424 (3)
ν_1	2372 ssh	2321	2332 ± 5 s 2240 vwsh	$(\nu_1, 2\nu_2)^-$ 2336 s		2291 (10)
$3\nu_R$	1617 w	1635	1650 ± 30	1635 s	1630	
ν_2	1212 m	1194	1210 ± 10	1210 s	1210	~1240
$\nu_R + \nu_T$	ssh	661	675 sh			
ν_R	600 s	627	640 s		630	
$\nu_R - \nu_T$			425 sh			

(a) Ref. 95 (b) Ref. 106 (c) Ref. 98 (d) Ref. 99.

3367(2499) cm^{-1} and 3191(2372) cm^{-1} . For H_2O cubic ice I, the liquid helium and liquid nitrogen experimental ν_3 data do not agree at 83°K (Fig. 3.10).

Two distinct values of $\nu_2(\text{H}_2\text{O})$ are indicated among liquid helium experiments and some liquid nitrogen experiments. All helium runs and some nitrogen runs gave $\nu_2(83^\circ\text{K})$ at 1570 cm^{-1} . A few nitrogen runs with thin samples gave $\nu_2(83^\circ\text{K})$ at 1604 cm^{-1} . Atmospheric H_2O absorptions may have attenuated the weak $\nu_2(\text{H}_2\text{O})$ absorptions of thin samples.

Ice samples annealed with care above 200°K showed two distinctions from those annealed below 200°K. The former gave spectra with a distinct shoulder at 1130 cm^{-1} (on the side of ν_2). As well, a deep minimum appeared between the 1130 cm^{-1} shoulder and the ν_R band. Pimentel's (97) spectra showed the same features although he offered no explanations for them.

Inspection of the cubic ice I H_2O ν_T band (Fig. 3.14) shows two peaks and three shoulders. However, Whalley's (87) theory showed that additional ν_T features yield important information on the densities of phonon states. Accordingly, ten features of $\nu_T(\text{H}_2\text{O})$ at 93°K were reported in Table III.X. In contrast, the vitreous ice I ν_T band had no low frequency shoulder or peak. As well the 267 cm^{-1} shoulder was poorly defined.

(ii) D_2O Absorptions at 83°K

D_2O ice I has the same sets of spectral features as H_2O ice I. Vitreous D_2O ice spectra have a weak oligomeric absorption at 2720 cm^{-1} which has not been reported previously for ice. Oligomeric absorptions are absent in cubic D_2O sample spectra. As in H_2O ice I, the stretching band shoulders are better defined in cubic than in vitreous ice. The

problems caused by atmospheric H_2O attenuations encountered in H_2O ice I were eliminated by more efficient purging.

(iii) HDO Absorptions at 83°K

Only three HDO absorptions were observed, the OH and OD stretches and an HDO libration. In vitreous samples the three absorptions were broad, relatively weak and without shoulders. In cubic samples the ν_{OH} band had no shoulders, the ν_{OD} band had two shoulders and the ν_{R} band had one shoulder. No $\nu_{\text{R}}(\text{HDO})$ absorption was observed near 600 cm^{-1} for HDO in H_2O .

3.4 Summary of Ice I Results

A. Vitreous-Cubic Ice I Transformation

1. All H_2O absorptions shift irreversibly in the temperature range 115 - 145°K; internal modes shift to lower frequencies while lattice modes shift to higher frequencies.
2. Above 150°K, vitreous and cubic frequency data concur and shift reversibly with respect to temperature.
3. Oligomeric H_2O absorptions are absent above 125°K.
4. Upon sample devitrification the absorptions are shifted, sharpened and better defined.
5. D_2O and HDO absorptions appear to have the same behaviour as those of H_2O .
6. Composite-band half-height widths exhibited unusual behaviour in the case of $(\nu_2, 2\nu_{\text{R}})$.

B. HDO in Cubic Ice I

1. Dilute concentrations of HDO in H_2O and D_2O gave accurate measures of frequency, half-height widths and absorbances as a function of temperature.
2. Plots of the HDO data provided low temperature limits, linear low and high temperature dependences and indications of irregular behaviour.
3. A new absorption was observed as a shoulder on $\nu_{\text{R}}(\text{HDO})$ and is designated $\nu_{\text{R}}(\text{HDO}) + \nu_{\text{T}}(\text{D}_2\text{O})$ or $\nu_{\text{R}}'(\text{HDO})$.
4. Internal mode cubic ice I HDO absorptions shift reversibly to higher frequency and lattice mode HDO frequencies shift reversibly to lower frequencies as a function of increasing temperature.
5. HDO stretching mode half-height widths increased as a function of increasing temperature.
6. HDO stretching mode absorbances decreased as a function of increasing temperature.

C. H_2O and D_2O in Cubic Ice I

These results provided measures of eight H_2O and seven D_2O absorptions that were less accurate, but of the same nature, as those from HDO.

CHAPTER FOUR

DISCUSSION OF ICE I

The data from cubic and vitreous ice I ir spectra contribute to detailed understandings of: 1) the origins of the absorptions, 2) the process of the vitreous-cubic phase transformation, and 3) the effects of increasing temperature, increasing $R(O\cdots O)$ and decreasing hydrogen bond strength on the H_2O , D_2O , and HDO vibrations and potential well.

4.1 The Ice I Vitreous-Cubic Phase Transformation

The x-ray and electron diffraction experiments (58) indicated that the structure of the solid formed by condensing H_2O vapour at low temperatures depended on the rate of deposition and the substrate temperature: Amorphous, cubic and hexagonal ices were observed. The thermodynamic studies of the irreversible phase transformations indicated varying transformation temperature ranges and degrees of crystallinity. The confusion with respect to vitreous, cubic and hexagonal sample formation is reflected in the variations among the ir spectra of various authors (95, 97, 98, 105). Bertie and Whalley (88,95) obtained spectra of mulled, crystalline samples (checked by x-ray diffraction) and they criticized the use of a "recipe" such as that of Beaumont et al. (65).

With ir observations Zimmerman and Pimentel (97) pointed out the need to devitrify solids condensed from the vapour. While they were the first to detect the irreversible shift in the ir spectra between vitreous and cubic ice, they did not study the transformation in detail.

The transformation process was observed in this work in every H_2O ir absorption except $\nu_{\text{T}}(\text{H}_2\text{O})$, but the results of the transformation for all H_2O , HDO and D_2O bands were recorded. The spectra gave four concurrent measures of the transformations: 1) the degree of increased hydrogen bonding, 2) the transformation temperature range, 3) the change in vibrational energy, and 4) the phase transformation rate. The studies showed that cubic samples formed by transformation of the vitreous phase gave as good spectra as mulled, crystalline samples (95).

A. General Discussion

Some general comments apply to all the H_2O band maxima in their behaviour before, during and after the vitreous-cubic phase transformation. Between $83 \pm 3^\circ\text{K}$ and $120 \pm 10^\circ\text{K}$ all H_2O band maxima had constant frequencies (Fig. 3.2). The absence of frequency shifts is indicative of no changes in the degree of hydrogen bonding. Below $120 \pm 10^\circ\text{K}$ the thermal kinetic energy was insufficient to allow molecular reorientation, softening of the glass, and hydrogen bond formation.

The H_2O band maxima all shifted irreversibly during the vitreous-cubic transformation. However, the data (page 62) indicated different transformation temperature ranges for different bands: Ranges from $115 \pm 5^\circ$ to $130 \pm 5^\circ\text{K}$ and $130 \pm 5^\circ$ to $145 \pm 5^\circ\text{K}$ were found for ν_{R} and $\nu_1 + \nu_{\text{T}}$. The differences appear to be caused by the increasing period the sample was held at one temperature while the spectra were recorded.

For example, frequencies plotted in Fig. 3.2 show that ν_{R} was constant up to 100°K and was completely shifted to the cubic ν_{R} frequency at 125°K .

That indicates, on first inspection, that the transformation for $\nu_R(\text{H}_2\text{O})$ started at $115 \pm 5^\circ\text{K}$, about 10°K lower than for other bands. Such a conclusion is incorrect.

Specifically consider the positions of the data indicated by solid triangles (\blacktriangledown) at 125°K in Fig. 3.2 for all six bands. The data were obtained from one sample during one run at constant temperature. At 125°K the $\nu_1 + \nu_T$ band was unshifted from the vitreous frequency, the ν_3 and ν_1 bands were only slightly shifted, the $3\nu_R$ band was shifted approximately one-half the total shift towards $3\nu_R$ cubic, the ν_2 band was shifted three-quarters the total shift and ν_R was completely shifted. The amount of shift is proportional to the time the sample was held at 125°K . In this work, spectra were scanned from 4000 to 530 cm^{-1} in 20 minutes. Thus for $\nu_1 + \nu_T$, ν_3 , ν_1 , $3\nu_R$, ν_2 and ν_R the vitreous sample had been progressively annealed at 125°K for 3.7, 4.4, 4.7, 10.2, 13.4 and 18.3 minutes respectively. By the time ν_R was recorded the sample had completely transformed. If the transformation rate is assumed to be linear, then a plot of $(\nu_v - \nu_c)_t / (\nu_v - \nu_c)_{t=\infty}$ (where t is the time at 125°K and $t = \infty$ is maximum annealing shift) against time in minutes gives the transformation rate at 125°K as $5.5 \times 10^{-2} \text{ min}^{-1}$.

One concludes that the transformation temperature ranges listed in Table III.I for $\nu_1 + \nu_T$, ν_3 , ν_1 , $3\nu_R$ and ν_2 were artificially elevated by the recording technique. The transformation temperature range for all bands must be consistent, $120 - 135 \pm 5^\circ\text{K}$ (corrected for sample window heating).

During the transformation the lattice modes ν_R and $3\nu_R$ shifted irreversibly to higher frequency while the molecular modes shifted irreversibly to lower frequency due to large alterations to the intramolecular and intermolecular potentials which occurred. The shifts of molecular modes are

consistent with the formation of more and/or stronger hydrogen bonds. During the transformation the molecules attained sufficient thermal kinetic energy to permit molecular reorientation, the low polymers were then free to form long chains with complete hydrogen bonding, four per molecule. The complete sets of strong hydrogen bonds hindered libration and translation and increased the frequencies of those bands.

After the irreversible shift had occurred, i.e. above 150°K, and during all subsequent warming-cooling cycles the spectra had a reversible temperature dependence: the lattice modes decreased in frequency and the molecular modes increased in frequency as temperature increased. The sample devitrification was completed by warming to $185 \pm 5^\circ\text{K}$ for 2 - 5 minutes, followed by recooling to 83°K.

At 83°K the effects of reorientation and hydrogen bond formation (lengthening $r(\text{O-H})$ and orbital rehybridization) were measured for H_2O , D_2O and HDO . If the frequency shifts between cubic and vitreous ice did rise from hydrogen bond formation, then the relative effects on H_2O , D_2O and HDO frequencies should have been the same provided all the vitreous samples had comparable degrees of microcrystallinity. The frequency shifts would ideally be in the ratio $\Delta v_i(\text{H}_2\text{O}) / \Delta v_i(\text{D}_2\text{O})$ near 1.4, where $\Delta v_i = v_i(\text{cubic}) - v_i(\text{vitreous})$ for the i -th vibrational mode. Only the peaks v_3 and v_R give reasonable agreement with the ideal ratio, i.e. 1.6 ± 0.3 and 1.1 ± 0.30 respectively. All the other bands were poorly defined and the ratios range from 0.79 ± 0.5 to 3.1 ± 0.5 for $v_1 + v_T$ and v_2 respectively. A modified product rule $\Delta v_1 \Delta v_2(\text{H}_2\text{O}) / \Delta v_1 \Delta v_2(\text{D}_2\text{O})$ does not improve the ratio.

For 4.00 % HDO in D_2O $\Delta v_R(\text{HDO}) = \Delta v_R(\text{D}_2\text{O}) = +27 \text{ cm}^{-1}$, $\Delta v_3(\text{H}_2\text{O}) / \Delta v_{\text{OH}}(\text{HDO}) = 0.94$ and $\Delta v_3(\text{D}_2\text{O}) / \Delta v_{\text{OD}}(\text{HDO}) = 1.1$: None of these are in agreement with the ideal ratio. The ratio for $\Delta v_{\text{OH}}(\text{HDO}) / \Delta v_{\text{OD}}(\text{HDO}) = 1.8$ is much

higher than 1.4. The observed ratios of the cubic ice I fundamental frequencies are near 1.35 and one deduces that $\Delta\nu_{\text{OH}}(\text{HDO})$ is too large, $\Delta\nu_{\text{OD}}(\text{HDO})$ is too small (compared to pure H_2O and D_2O) or both. However, since samples were not identically deposited, they would have had different degrees of self-annealing, and different frequency displacements from the cubic ice values.

Each band will now be considered in turn.

B. Fundamental Lattice Mode Transformations

(i) The $\nu_{\text{T}}(\text{H}_2\text{O})$ Transformation

The ν_{T} band had remarkable differences between the vitreous and cubic samples at 83°K: The vitreous band was broad and featureless while the cubic band was narrow and had nine features. That is understandable from the very different nature of the two solids. For example, since the positions of the atoms in a vitreous solid are ideally completely irregular, then forces acting on the atoms are irregular and the normal vibrations of the solid are also irregular (87). The resulting range of translational energy levels, and range of transitions among the levels, is very broad. Combined with the collapse of normal phonon selection rules (87), a very broad ν_{T} (vitreous) band is expected and observed. In contrast, cubic ice I has regular, long range ordering of oxygen atoms, but irregular, short range ordering of the protons (orientational disorder). Whalley (87) has shown that the orientational disorder does not have a significant irregular effect on the mechanical vibrations of cubic ice, but that it does affect the local electric oscillations. Consequently, one obtains a structured ν_{T} (cubic) band whose features are indicative of the crystalline state. It is suf-

ficient here to compare our vitreous and cubic ν_T data (83°K) to those of Whalley (88) and Giguere (89).

Consider the ν_T data given on pages 89, 90, and 91 of Chapter 3. That ν_T (cubic), 227.8 cm^{-1} , was 7% higher than ν_T (vitreous) is understandable simply on the basis of the increased number of hydrogen bonds, the deepened hydrogen bond potential and increased force constants, and the increased hinderance to translation. These effects resulted from extension of hydrogen bonding closer to the limit (4 bonds/molecule), reduction of the mean O----O distance, and a change in the density in cubic crystals. However, in reality the explanation for the frequency shift may not be so simple. Formation of a well defined Brillouin zone in cubic samples may entail complex changes in the densities of states and selection rules from those of the vitreous sample.

The half-height width of ν_T (vitreous) was 62.8 cm^{-1} , in sharp contrast to that of ν_T (cubic) which was very nearly one-third of that value, 23.2 cm^{-1} . Increases in the densities of states at the Brillouin zone boundaries probably accounts for this dramatic change.

That the peak height of ν_T (cubic), 1.285 absorbance, was almost exactly double that of ν_T (vitreous) is probably due to two effects. The first effect is again the increased density of states in cubic ice I for $k \approx 0$ transitions. The second effect arises from the increase in oscillating dipole moments in completely hydrogen bonded lattices as compared to weaker dipoles in partially hydrogen bonded glasses.

The ν_T (vit.) band of this work compares very well with Whalley's (88) ν_T (vit.) but not with Giguere's (89) ν_T (vit.). The ν_T (vit.) band had no 162 cm^{-1} peak or 173 cm^{-1} minimum, as Whalley (88) also reported.

However, Whalley's ν_T (vitreous) peak was 9 cm^{-1} higher than observed here, 212.8 cm^{-1} . He did not list the positions of other vitreous band features and it is hard to determine if the difference is only due to calibration errors. [On the basis of the two sets of ν_T (cubic) features, the latter seems unlikely.] In contrast Giguere's (89) ν_T (vit.) band showed too much structure and suggested a largely crystalline sample. The present work supports Whalley's observations of ν_T (vit.).

For ν_T (cubic) the results of this work agree in general features with both Whalley (88) and Giguere (89). However the two peaks in the present work are nearly 2 cm^{-1} lower than Whalley reported, probably due to a calibration error. Whalley found that all cubic samples, either condensed from the vapour or formed under pressure and milled, gave the same ν_T absorptions. Since ν_T observed in this work agrees with his results, one can conclude that the sample deposition and devitrification techniques used here gave legitimate cubic ice I samples with respect to ν_T .

(ii) The ν_R Transformation

At 83°K vitreous ice $\nu_R(\text{H}_2\text{O})$ had two distinct and two faint features: a distinct peak (802 cm^{-1}) and a distinct shoulder (535 cm^{-1}), and two faint shoulders (846 cm^{-1} and 675 cm^{-1}). However, vitreous ice $\nu_R(\text{HDO})$ and $\nu_R(\text{D}_2\text{O})$ each had only a single feature. In contrast, cubic ice $\nu_R(\text{H}_2\text{O})$ had five features (one peak and four shoulders) while $\nu_R(\text{HDO})$ and $\nu_R(\text{D}_2\text{O})$ had two features each (a peak and a high frequency shoulder). The HDO high frequency shoulder, $\nu_R(\text{HDO}) + \nu_T(\text{D}_2\text{O})$, has not been previously reported. Changes in frequency and half-height width between the ν_R bands of vitreous and cubic H_2O ice samples were shown in Figs. 3.2 and 3.4 (pages 64 and 66) and the results of devitrification for $\nu_R(\text{H}_2\text{O}, \text{D}_2\text{O}, \text{HDO})$ were given in

Table III.I (page 62).

After the vitreous sample was annealed at $185 \pm 5^\circ\text{K}$ for 2 - 3 minutes and recooled to 83°K , one found all the ν_R features had shifted to higher frequency and that three new features appeared. Precisely, $\nu_R(\text{H}_2\text{O})$ shifted by $+31 \text{ cm}^{-1}$, $\nu_R(\text{HDO})$ by $+27 \text{ cm}^{-1}$ and $\nu_R(\text{D}_2\text{O})$ by $+27 \text{ cm}^{-1}$. As for ν_T , the ν_R shift to higher frequency may be simply understood on the basis of hydrogen bonding. Cubic ice has more and stronger hydrogen bonds than vitreous ice. The results are a deeper hydrogen bond potential, larger hydrogen bond force constants, increased hinderance to libration and increased absorption frequency. However, as for ν_T , complex changes in the crystal entail complex changes in the solid librations, densities of states and selection rules. The final explanation of ν_R behaviour must combine the changes in hydrogen bond potential with the lattice vibration theory.

The plot of half-height widths ($\Delta\nu_R^{1/2}$) of the composite band ($\nu_R, \nu_R + \nu_T$) was shown in Fig. 3.4 (page 66). It also indicated a "depressed" ν_R transformation temperature range ($115 - 130 \pm 5^\circ\text{K}$). However, the low range may be explained as in section 4.1A (page 105) for $\nu_R(\text{freq.})$. One also sees that the behaviour of $\Delta\nu_R^{1/2}$ above 130°K did not conform to the reversible behaviour of fully annealed cubic samples, i.e. the half-height width continued to decrease. Finally, on completing the annealing and recooling of the sample to 83°K , one found that the disorder broadening due to irregular O positions was removed but that there remained the orientational disorder broadening. The half-height widths at 83°K decreased in the following way:

	H ₂ O	HDO	D ₂ O	H ₂ O/D ₂ O
$\Delta v^{\frac{1}{2}}(\text{vit.})$	220 cm ⁻¹	88 cm ⁻¹	~200 cm ⁻¹	1.10
$\Delta v^{\frac{1}{2}}(\text{cub.})$	195	51	140	1.30
$\Delta v^{\frac{1}{2}}(\text{cub.})$				
$\Delta v^{\frac{1}{2}}(\text{vit.})$	0.89	0.58	~0.70	1.27

The differences may be due simply to errors in determining baselines, intensities and widths, or may arise from differences in microcrystallinity among the three vitreous samples formed.

C. Fundamental Molecular Mode Transformations

(i) The $v_2/2v_R$ Transformation

Absorptions between 1000 and 1800 cm⁻¹ in H₂O ice have been variously assigned to $2v_R$ or v_2 . All previous workers (95,97,105,106,108) reported only a single feature in this range for both H₂O and D₂O ices (vitreous or cubic). However, Zimmermann and Pimentel's (97) Fig. 1 for cubic ice has shoulders at 1100 and 1530 cm⁻¹ and a peak at 1615 cm⁻¹. They treated the 1615 cm⁻¹ peak and 1530 cm⁻¹ shoulder as one band centered at 1580 cm⁻¹ (83°K) in cubic H₂O ice.

Most thick vitreous H₂O ice spectra recorded in this work had two features, a peak at 1660 ± 10 cm⁻¹ and a shoulder at 1570 ± 20 cm⁻¹. In contrast, cubic samples annealed below 190°K only had a peak at 1570 ± 10 cm⁻¹. Cubic samples annealed to 205°K had a peak at 1570 ± 10 cm⁻¹ a shoulder at 1130 cm⁻¹, and a deep minimum at 1050 cm⁻¹, much like Zimmermann and Pimentel's (97) spectra. While the final assignments of the bands are left

until section 4.3 (page 175), it seems logical to consider the vitreous 1570 cm^{-1} shoulder and the 1660 cm^{-1} peak as being either ν_2 or $2\nu_R$. Corresponding features were not observed in vitreous D_2O ice I.

The reasons for shifts to lower frequencies, $\Delta\nu_2(\text{H}_2\text{O}) = -56\text{ cm}^{-1}$ and $\Delta\nu_2(\text{D}_2\text{O}) = -18\text{ cm}^{-1}$, have been explained by Zimmermann and Pimentel (97) on the basis of a weakened molecular potential and decreased force constants. However, the large differences between ν_2 shifts for H_2O and D_2O , observed here, is not understood. In Fig. 3.5 (page 67) one saw that the vitreous $\Delta\nu_2^{\frac{1}{2}}$ was constant at 350 cm^{-1} up to $115 \pm 5^\circ\text{K}$ and broadened to 390 cm^{-1} at $125 \pm 5^\circ\text{K}$. Above 125°K $\Delta\nu_2^{\frac{1}{2}}$ had a negative, reversible temperature dependence, $-1.64\text{ cm}^{-1}/^\circ\text{K}$. All other vitreous H_2O , HDO and D_2O bands were narrower after the transformation and subsequently broadened with increasing temperature in the cubic phase.

The anomalous behaviour of $\Delta\nu_2^{\frac{1}{2}}(\text{H}_2\text{O})$ may be explained if the vitreous ice band is composed of a medium ν_2 absorption slightly below 1570 cm^{-1} and a $2\nu_R$ absorption slightly above 1660 cm^{-1} . Although ν_2 and $2\nu_R$ both must narrow upon devitrification, their frequencies both shift away from 1570 cm^{-1} yielding a net broader $\nu_2/2\nu_R$ band. For this explanation it is also necessary that the peak absorbance of $2\nu_R$ decrease in the cubic phase. The negative temperature dependence of the ν_2 band results from the shift of a weak underlying $2\nu_R$ to lower frequency (towards 1600 cm^{-1}) and the shift of ν_2 to higher frequency (towards 1600 cm^{-1}) with increasing temperature. As the two absorptions further coalesce, the composite band becomes narrower. However, the frequency dependence of the cubic band is determined by the more intense ν_2 absorption.

The ν_2 frequencies obtained for crystalline ice formed from the vapour

(this work, 97, 105, 106) do not agree with Whalley's (95) work. For all phases of ice Whalley found ν_2 to be higher than 1650 cm^{-1} . The ν_2 results of this work support Ockman's (108) observations for samples formed from the liquid. Ockman's (108) reflection spectra indicated a weak maximum at 1600 cm^{-1} . It is possible that Whalley's (95) mulling technique gave a different reflection spectrum than occurs for thin films and enhanced the high frequency portion of his ν_2 . His results showed the mulling agent decreased reflection and scattering compared to powder spectra. On the other hand, reflection and scattering may be severe for thin films.

Finally, the weak shoulder and deep minimum (1130 cm^{-1} and 1050 cm^{-1}) may have arisen from a strong Christiansen filter effect on the high frequency side of ν_R .

(ii) The ν_{STR} Transformations

In the region from 3000 to 4000 cm^{-1} one observes the symmetric and asymmetric O-H stretching frequencies from H_2O molecules in various degrees of polymerization and the combinational absorption of ν_1 with the lattice modes. The corresponding O-D stretches are found between 2000 - 2800 cm^{-1} . Data for ν_1 and ν_3 of H_2O , HDO and D_2O in the vitreous and cubic phases were shown in Figs. 3.2 and 3.4 (pages 61 and 66) and were compiled in Table III.I (page 62).

(a) The ν_1 shoulder. The low frequency shoulder (ν_1) was very poorly defined (at 83°K) in vitreous ice ($3191 \pm 15 \text{ cm}^{-1}$) but was better defined in cubic ice ($3149 \pm 10 \text{ cm}^{-1}$). In contrast, for D_2O ice the ν_1 shoulder was well defined for both vitreous and cubic ice I ($2372 \pm 10 \text{ cm}^{-1}$ and 2321 cm^{-1}).

Like other molecular modes, ν_1 shifted to lower energy because of weaker molecular bonds, a shallower potential well and weaker force constants.

(b) The ν_3 peak. The vitreous ice stretching band frequency at 83°K was 3253 cm^{-1} while for cubic ice ν_3 was 3217 cm^{-1} , a shift of -36 cm^{-1} ($\Delta\nu_3(\text{D}_2\text{O}) = -23 \text{ cm}^{-1}$). The explanation for a negative shift follows from ν_1 above.

(c) The HDO modes. The vitreous ice HDO absorptions were listed in Table III.I, $\nu_{\text{OD}} = 2437 \text{ cm}^{-1}$ and $\nu_{\text{OH}} = 3304 \text{ cm}^{-1}$. The cubic ice HDO frequencies were shifted -21 and -38 cm^{-1} respectively from their vitreous values. Reference to Table III.I shows that these shifts correspond very well to the ν_3 shifts of D_2O and H_2O respectively. The vitreous-cubic transformation had the same effect on $\nu_{\text{OD}}(\text{asymm.})$ or $\nu_{\text{OH}}(\text{asymm.})$ of H_2O , HDO and D_2O molecules whether they were in an H_2O or D_2O lattice. There appear to be no differences among the couplings of HDO, H_2O and D_2O molecules for either vitreous or cubic ice I. Finally, the explanation for the direction of shift follows from previous discussion.

The HDO stretch half-height widths sharpened from 77 to 23.5 cm^{-1} and 115 to 35.5 cm^{-1} between the vitreous and cubic phases (at 83°K). In vitreous ice both the O positional disorder and proton orientational disorder contributed to the widths. In cubic ice the O positions were ordered, but the proton disorder broadening remained. Even in the cubic phase the uncoupled HDO molecules had $\Delta\nu^{\frac{1}{2}}$ values about twice as large as expected for ordered solids. For example, Whalley (96) found $\Delta\nu^{\frac{1}{2}}(\text{HDO})$ data of $8 - 13 \text{ cm}^{-1}$ for an ordered high pressure ice.

The HDO peaks were uninhibited by band overlap and provided an excellent probe for making accurate transformation rate studies of vitreous

ice. The dilute H / D isotopic substitution should be employable in rate studies of other disordered systems.

(d) The oligomeric modes. All vitreous H_2O and D_2O ice samples observed in this work had very weak absorptions between 3600 and 3700 cm^{-1} in H_2O (near 2620 cm^{-1} in D_2O). Typical H_2O peaks were shown in Fig. 3.3 (page 64) and the frequencies were listed in Table III.II (page 65). These absorptions occurred quite close to the vapour phase monomeric frequencies. Shurvell (115) and Van Thiel et al. (117) studied the absorptions from dilute concentrations of H_2O and D_2O in various matrices. Van Thiel et al. assigned the (ν_3, ν_1) monomeric, dimeric and trimeric H_2O (in an N_2 matrix at 20°K) absorptions to $(3725$ and $3625\text{ cm}^{-1})$, $(3691$ and $3546\text{ cm}^{-1})$, and $(3510$ and $3355\text{ cm}^{-1})$ respectively. For D_2O Shurvell reported (ν_3, ν_1) monomer and dimer absorptions for an N_2 matrix at $(2765$ and $2655\text{ cm}^{-1})$ and $(2725$ and $2650\text{ cm}^{-1})$ respectively. Our frequencies appear to rise from dimeric systems. We observed half-height widths of $15 - 20\text{ cm}^{-1}$ which were slightly smaller than in matrix isolation, $20 - 30\text{ cm}^{-1}$. Their oligomeric peaks were stable up to the softening temperatures of the matrix used, generally less than 30°K . Oligomeric absorptions observed in this work were stable up to the softening temperature of the H_2O glassy matrix, 125°K . That corresponds to the temperature of onset of peak shift in other bands, i.e. the temperature of molecular reorientation. The high softening temperature is consistent with the increased van der Waals forces in molecular solids compared to rare gas solids. For example, Shurvell (115) observed that H_2O oligomers were stable up to 80°K in a CCl_4 matrix.

For this work, one understands that the softening permits short-range molecular diffusion and reorientation resulting in progressively higher polymerization. The monomeric, oligomeric and medium polymers disappear as well as their absorptives. The high frequency side of the ν_{STR} band was greatly sharpened.

One can estimate the fraction of the sample which was in the form of dimers. In this work the ratio of ν_3 absorbances for dimeric and fully polymerized H_2O is 1 to 70. Work by Ikawa and Maeda (118) on the crystalline solid (complete polymer) and by Ferriso and Ludwig (119) on the vapour phase (monomeric H_2O) showed that the extinction coefficients of monomeric and fully polymeric H_2O are in the ratio 1 to 30. Thus one finds 1 part of monomeric-dimeric H_2O to 2.3 parts of completely polymerized H_2O . There remains an unknown portion of the sample in intermediate stages of polymerization. However, while this estimate seems to be very high, the point is that a considerable amount of oligomeric H_2O and D_2O sample was formed by our condensation technique.

(e) The $\Delta\nu^{\frac{1}{2}}$ of the band ($\nu_1, \nu_3, \nu_1 + \nu_T$). The half-height width ($\Delta\nu^{\frac{1}{2}}$) of the composite band ($\nu_1, \nu_3, (\nu_1 + \nu_T)$) sharpened from $325 \pm 10 \text{ cm}^{-1}$ to $285 \pm 10 \text{ cm}^{-1}$ ($83^\circ K$) between vitreous and cubic ice. The band sharpened irreversibly between $115 \pm 5^\circ K$ and $125 \pm 5^\circ K$ by the specific loss of approximately 20% of the high frequency absorption. Such absorption arises from medium length H_2O and D_2O polymers with incomplete hydrogen bonding. In addition, the band sharpened by the increase of O positional ordering and the smaller range of molecular potential energies.

D. Combination and Overtone Mode Transformations

(i) The $3\nu_R$ Transformation

Absorption near 2200 cm^{-1} in H_2O ice and near 1600 cm^{-1} in D_2O ice has been variously assigned to $3\nu_R$ and $\nu_2 + \nu_R$. Specifically, the H_2O absorption had a single feature, a peak at 2220 or 2235 cm^{-1} in vitreous or cubic ice. The shift upon annealing was to higher frequency, and was also found for ν_R and ν_T . The nature of the shift was given in Fig. 3.2 (page 61) while data was given in Table III.I (page 62).

Cubic ice absorptions, 2235 and 1635 cm^{-1} for H_2O and D_2O (at 83°K), agreed very well with the single crystal observations of Ockman (108), Table III.XI. As well, Haas and Hornig's (106) and Giguere and Harvey's (98) results were comparable. However, Whalley's (95,96) results were consistently higher. As for ν_2 , the differences in Whalley's results may have arisen from changes in the reflection spectrum caused by the mulling agents.

The shift by $+15\text{ cm}^{-1}$ (for H_2O) to higher frequency upon devitrification may provide a clue to the origin of this band. If the band is $\nu_2 + \nu_R$ then one would expect the shift $\Delta(\nu_2 + \nu_R)$ to be proportional to $\Delta\nu_2 + \Delta\nu_R = (-56 + 31) = -25\text{ cm}^{-1}$ for H_2O . If the band is $3\nu_R$ then one would expect $\Delta(3\nu_R)$ to be proportional to $3(\Delta\nu_R) = +93\text{ cm}^{-1}$. The observed shift to higher frequency by $+15\text{ cm}^{-1}$ in H_2O and $+18\text{ cm}^{-1}$ in D_2O supports the $3\nu_R$ assignment.

Finally, the $3\nu_R$ results suggest that our cubic sample formation technique is adequate since the results are consistent with results from crystalline samples prepared from the liquid, i.e. the results of Ockman (108) and Giguere (98).

(ii) The $(\nu_1 + \nu_T)$ Transformation

The high frequency shoulder $(\nu_1 + \nu_T)$ was very poorly defined in vitreous ice, but was well defined in cubic ice. As for other molecular modes, $(\nu_1 + \nu_T)$ shifted irreversibly towards lower frequency (-27 cm^{-1} for H_2O and -34 cm^{-1} for D_2O) between 130 and $145 \pm 5^\circ\text{K}$. Comments made above with respect to the origin of the molecular mode shifts and the temperatures of transformation also apply to $(\nu_1 + \nu_T)$.

E. Confidence in the Cubic Ice I Samples

Does devitrification provide a good cubic sample of iceI? Beaumont et al. (65) found that the vitreous-cubic transformation took only a few minutes to finish even at 150°K . As well they found that vitreous ice transformed cleanly to cubic ice. On the other hand, Dowell and Rinfret (74) estimated only a 30 per cent conversion to cubic ice and an average cubic crystallite size (embedded in the remaining 60% vitreous ice) of 400 \AA . The results of Dowell and Rinfret (74) necessitate a heat of cubic-hexagonal phase transformation of 24 cal/gm . Such an evolution of heat was unobserved at higher temperatures by Beaumont et al. In fact they estimated the heat of cubic-hexagonal transformation to be less than 1.5 cal/gm .

If the samples in the present work were only 30% cubic ice with 60% vitreous ice remaining, then the spectra of annealed samples should have been characteristic of vitreous ice and might have exhibited separate maxima from cubic and vitreous ice. Only one stretching peak was observed and the bands matched very closely the spectra of hexagonal ice I (95). These facts support Beaumont's interpretation of the vitreous-cubic transformation.

The evidence suggests samples prepared in this work were transformed fully to cubic ice I. The presence of significant amounts of residual vitreous ice would have broadened the stretching bands asymmetrically, giving a tail on the high frequency side. The half-height widths and band shapes of spectra in Fig. 3.1 compared very favourably with spectra of hexagonal ice I formed from the liquid.

Deposition rates in these experiments lie near the maximum set by Beaumont et al. (65) --0.04 gm/cm²/hour. Assuming a $\nu_3(\text{H}_2\text{O})$ extinction coefficient of 140 for hexagonal ice I (119) the sample thickness was 0.5 - 1.0 microns. The volume of ice I sample was at least 1.4×10^{-4} cm³. At a density of 0.924 gm/cm³ one had a minimum sample of 1.3×10^{-4} gms. Such samples were applied in two bursts, of two seconds duration each, onto a window initially at 83°K. By assuming a 1.0 cm² image, the rate of deposition was at least 0.04 gm/cm²/hour.

During the deposition, 1.3×10^{-4} gms of H₂O vapour release 0.09 cal (assuming the heats of sublimation of amorphous and hexagonal ice I_h are the same). There was sufficient heat of condensation to induce localized heating and to permit diffusion of individual molecules. The extent of heating and diffusion, or the amount of self-annealing, depended on the rate of dissipation of heat at the window-sample surface.

Several attempts, under various conditions, were made to form hexagonal ice. However, all attempts to anneal samples above 210°K led to almost instantaneous sublimation since the samples were uncovered. Such sublimation has also been the experience of other workers (120).

The extensive sharpening and alteration of the bands between vitreous and cubic ice I was due to two effects. The first was the diffusion and

reorientation of individual molecules into lattice sites in the cubic unit cell. The cubic unit cells put all molecules in the same electrical environment, but where the mechanical vibrations were broadened by asymmetries in proton orientation at equivalent unit cell sites.

The second effect was the extension of low, medium, and high polymer H_2O clusters of the vitreous phase into fully hydrogen bonded networks of the cubic phase. During the process of crystallization the clusters amalgamated into larger units where the deformed or absent hydrogen bonds at the contact surfaces between clusters (or crystallites) represented only a small fraction of the total number of hydrogen bonds.

4.2 Temperature Dependence of Cubic Ice I Absorptions

Accurate measurements of shifts in frequencies and half-height widths in H_2O , D_2O and HDO spectra between $4^\circ K$ and $200^\circ K$ permit accurate correlations of the shifts to changes in $R(O\cdots O)$ and changes in hydrogen bond strength. In this section values of $R(O\cdots O)$ for cubic ice I are calculated over the range $10^\circ - 200^\circ K$ and plotted against $\nu_{OH}(HDO)$ and $\nu_{OD}(HDO)$. That plot is compared to the predictions of an empirical equation which relates $\nu_{OH}(HDO)$ to $R(O\cdots O)$. In addition, values of $\omega_{OH}(HDO)$ and $X_{OH}(HDO)$ are calculated from $\nu_{OD}(HDO)$ and $\nu_{OH}(HDO)$ as a function of temperature.

A. Dependence of HDO Bands on Temperature

A few general remarks can be made concerning the low temperature limits and temperature dependences of all the absorption bands. The low temperature limiting frequencies were obtained by extrapolation to 0°K simply as a matter of convenience. The individual frequencies had virtually the same values when extrapolated to 5° or 0°K. There is the danger that the properties of ice are irregular below 5°K. However, Flubacher et al. (83) proved that the thermodynamics of ice I are well behaved down to 2°K.

The low temperature limiting frequencies, half-height widths and peak heights are for H₂O molecules at the distance of minimum approach. The O····H potential is deepest and the O-H potential is shallowest. The conditions at minimum approach permit the largest orbital overlap and degree of hydrogen bond covalency, the largest electrostatic effects, and the largest contribution of CT. As well, the low temperature limiting frequency gives the 0 → 1 energy level spacing for minimum root-mean-squared (RMS) amplitudes of H₂O translation and O-H vibration. Finally, the contours of the bands are least distorted by hot bands and vibrational perturbations of the potential.

As the temperature was raised the ice I sample expanded, giving increasing R(O····O) and resulted in the weakening of the O····H bonds and a strengthening of the O-H bonds. Hence the lattice mode and molecular mode force constants could be understood to decrease and increase respectively, i.e. the frequencies respectively decreased and increased. While the crystals expanded continuously and non-linearly during warm-up, the frequency-temperature dependence was approximated by two straight lines. The lines

corresponded to regions of slow and fast crystal expansions. Below 50°K the effects of $\Delta R(0 \cdots 0)$, changes in RMS amplitude of translation and hot bands ($v = 1 \rightarrow 2$) were small.

Finally, some irregularities or discontinuities in the temperature dependences indicate possible changes in the solid phase or changes in energy level populations.

(ii) Dependence of HDO Frequencies on Temperature

(a) $\nu_R(\text{HDO})$ and $\nu_R'(\text{HDO})$. A full discussion of the origin and nature of the librational modes is given in section 4.4. As expected, the temperature dependences were negative for both bands, $-0.02 \text{ cm}^{-1}/^\circ\text{K}$ below 55°K and $-0.147 \text{ cm}^{-1}/^\circ\text{K}$ above 55°K. Below 55°K the effects of ν_R and ν_T hot bands should have been negligible. Above 55°K, however, ν_R and ν_T hot bands may have contributed significantly to the changes in band frequency, width and height.

For $\nu_R(\text{HDO})$ (Fig. 3.7) one saw an apparent discontinuity between 105° and 120°K. The change in slope may have arisen from significant population of molecular mode hot bands. The "hot" molecules would be decoupled from the remaining lattice molecules, and would have weaker hydrogen bonds. Consequently, smaller librational frequencies would be seen.

(b) $\nu_{\text{OH}}(\text{HDO})$ from 4.00% HDO in D_2O . The shallow molecular potential is demonstrated by the low temperature limiting $\nu_{\text{OH}}(\text{HDO})$ frequency, i.e. 3263.5 cm^{-1} at 0°K compared to 3268 cm^{-1} and 3288 cm^{-1} at 80° and 180°K respectively.

The HDO frequency-temperature plot (Fig. 3.6) showed unambiguously that the frequency shift was continuous and non-linear in the high and

low temperature approximations. Since there is little point in doing a least-mean-squares fit to some arbitrary function, the data were approximated on a bilinear basis. Up to $45 \pm 5^\circ\text{K}$ $\nu_{\text{OH}}(\text{HDO})$ was constant within the random point scatter, $\pm 0.75 \text{ cm}^{-1}$. Within the sensitivity of the experimental technique and the spectrophotometer, changes in $\nu_{\text{OH}}(\text{HDO})$ due to changes in $R(\text{O}\cdots\text{O})$ and the effects of ν_{OH} combination bands with translational hot bands are insignificant below 45°K .

Linear low temperature dependence was assumed for $\nu_{\text{OH}}(\text{HDO})$ below 80°K ($+0.047 \pm 0.005$) $\text{cm}^{-1}/^\circ\text{K}$. Above 45°K one saw a definite effect due to increasing $R(\text{O}\cdots\text{O})$, the shift of frequency exceeds the point scatter. Thus the thermal expansion data of Brille and Tippe (60) suggest that when $\Delta R(\text{O}\cdots\text{O}) > \pm 0.0001 \text{ \AA}/^\circ\text{K}$ significant changes in $\nu_{\text{OH}}(\text{HDO})$ occur.

Linear high temperature dependence was assumed for $\nu_{\text{OH}}(\text{HDO})$ between 80° and 190°K , i.e. $+0.200 \pm 0.005 \text{ cm}^{-1}/^\circ\text{K}$. Data of this work are in good agreement with the data of Ford and Falk (100). Their data were shown in Fig. 3.6 and were obtained from the best straight line through their Fig. 2. One sees that the steadily increasing $R(\text{O}\cdots\text{O})$ in a cubic ice lattice yields a steadily increasing $\nu_{\text{OH}}(\text{HDO})$ frequency. The specific dependence of ν_{OH} on $R(\text{O}\cdots\text{O})$ is given in the following section (page 137).

There was a slightly irregular shift of $\nu_{\text{OH}}(\text{HDO})$ between 45°K and 70°K in Fig. 3.6. The irregularity may have been due to a partial order-disorder phase transformation predicted to be near 60°K by Pitzer and Polissar (70). However, they pointed out that the period of transition was probably greater than 24 hours. That period is far in excess of our very rapid cooling time of 15 - 20 minutes. An order-disorder phase transformation is also unsupported by any comparable shift in half-height width.

Alternately, the irregularity may have arisen from a transformation from an as yet uncharacterized low temperature ice phase, or from one of the disordered high pressure ices. A low temperature phase transformation in ice I_h was not indicated by heat capacity experiments (82), although C_p had a slight irregularity near 80°K. The ir irregularity represents only 1 - 2% of the total frequency and is probably undetectable in C_p experiments since molecular modes contribute little to C_p .

(c) $\nu_{OD}(\text{HDO})$ from 5.94% HDO in H_2O . The general comments made above with respect to $\nu_{OH}(\text{HDO})$ apply as well to $\nu_{OD}(\text{HDO})$: However, there are differences in details. Specific differences can be seen in Fig. 3.6 and Table III.IV (pages 71 and 72). The low temperature limiting $\nu_{OD}(\text{HDO})$ frequency was $2412.0 \pm 1 \text{ cm}^{-1}$. The ratio of HDO frequencies, ν_{OH}/ν_{OD} , is 1.354 ± 0.001 . That ratio is the same as reported by Whalley (96) for ices I, II and III and is very close to the vapour phase ratio of 1.360. From the ratios one can show that the HDO anharmonicity, as discussed by Whalley (96), was the same at 0°K as he found at 100°K, i.e. about 100 cm^{-1} . At both temperatures it is 25% larger than in the vapour phase. This does not mean the anharmonicity is independent of temperature as is shown in the next section.

The temperature dependence of $\nu_{OD}(\text{HDO})$ was different from that of $\nu_{OH}(\text{HDO})$ in several ways. The $\nu_{OD}(\text{HDO})$ data were constant within the point scatter up to $30 \pm 5^\circ\text{K}$ in contrast to $45 \pm 5^\circ\text{K}$ for $\nu_{OH}(\text{HDO})$. The low temperature dependences of ν_{OH} and ν_{OD} were the same. However, the high temperature dependence of ν_{OD} was $(+0.123 \pm 0.005) \text{ cm}^{-1}/^\circ\text{K}$ ($\Delta\nu_{OH}/\Delta T$ was 1.626 times higher, $0.200 \text{ cm}^{-1}/^\circ\text{K}$). The differences in the high temperature dependences probably arose from differences in the physical properties of

the two mediums. The ν_{OH} data are from HDO in D_2O while the ν_{OD} data are from HDO in H_2O .

Consider the percentage shift from the low temperature limiting frequencies for the asymmetric stretches in HDO, D_2O and H_2O ,

$$\text{percentage shift} = \frac{\nu_{\text{STR}}^{\text{T}} - \nu_{\text{STR}}^{\text{O}}}{\nu_{\text{STR}}^{\text{O}}} \times 100$$

where $\nu_{\text{STR}}^{\text{T}}$ is the stretching frequency at temperature T,
and $\nu_{\text{STR}}^{\text{O}}$ is the low temperature limiting frequency.

One might have expected ν_3 in H_2O and D_2O to shift by the same percentage of the low temperature frequencies. However, between 10° and 160°K the ν_3 shifts of H_2O and D_2O increased from $0.6 \times 10^{-2}\%$ to $82 \times 10^{-2}\%$ and 0.0% to $36 \times 10^{-2}\%$ respectively. The ν_3 stretching frequencies do not shift proportionally. The shifts of $\nu_{\text{OH}}(\text{HDO})$ and $\nu_{\text{OD}}(\text{HDO})$ are not proportionally the same, nor do they compare to the percentage shifts of ν_3 in H_2O and D_2O . The $\nu_{\text{OD}}(\text{HDO})$ shift was faster than for $\nu_3(\text{D}_2\text{O})$ at all temperatures, while the $\nu_{\text{OH}}(\text{HDO})$ shifted proportionally faster than $\nu_3(\text{H}_2\text{O})$ only below 100°K. The percentage shift from the low temperature limiting frequencies were:

Temperature °K	$\nu_{\text{OH}}(\text{HDO})$	Percentage Shift $\nu_{\text{OD}}(\text{HDO})$	$\times 10^2$ $\nu_3(\text{H}_2\text{O})$	$\nu_3(\text{D}_2\text{O})$
20	0.9	0.4	0.6	0
40	2.5	3.7	1.8	1.2
60	7.0	9.1	4.0	3.7
80	14.4	17.4	9.3	7.0
100	23.6	26.1	21.2	11.6
20	35.2	36.1	37.4	17.0
40	46.9	46.0	60.5	25.2
60	59.4	57.6	81.7	36.0
80	73.2	70.1	--	55.9
200	89.2	84.2	--	--

Dantl (64) found the thermal expansion coefficients for H_2O and D_2O lattices were the same above 120°K . Hence, differences in $\Delta R/\Delta T$ seem to be an unlikely source of the dispersion. The difference in temperature dependences may arise from differences in HDO coupling to H_2O and D_2O lattices. If HDO coupling to D_2O decreases faster than to H_2O then the $\text{OH}(\text{HDO})$ hydrogen bond to D_2O must weaken faster and the $\nu_{\text{OH}}(\text{HDO})$ frequency must shift faster than $\nu_{\text{OD}}(\text{HDO})$.

The $\nu_{\text{OD}}(\text{HDO})$ data are not in as good agreement with the data of Ford and Falk (100) as for $\nu_{\text{OH}}(\text{HDO})$. Again their data are from the best straight line through their Fig. 2. The ν_{OD} slopes agree but their data are displaced 2 cm^{-1} to lower frequency. This is probably due to differences in instrument calibration.

(ii) Dependence of HDO Frequencies on $R(\text{O}\cdots\text{O})$

The relationship between ν_{OH} and $R(\text{O}\cdots\text{O})$ for a large family of molecules was studied by various authors (27-30) and several empirical relationships were proposed (28,29,32) by neglecting specific differences in molecular properties. The empirical relationships give only an average $\nu_{\text{OH}}/R(\text{O}\cdots\text{O})$ behaviour. The HDO frequencies observed in this work permit the $\nu_{\text{OH}}/R(\text{O}\cdots\text{O})$ dependence for one molecular system to be accurately evaluated.

(a) Observed HDO frequency dependence on calculated $R(\text{O}\cdots\text{O})$. The observed HDO frequencies are known as a function of temperature (page 71) but not directly as a function of $R(\text{O}\cdots\text{O})$. One requires the variation of $R(\text{O}\cdots\text{O})$ in cubic ice I as a function of temperature.

A detailed study of the temperature dependence of the lattice parameters of cubic ice I has not been reported in the literature. However, the

cubic ice I lattice parameter was given by Wyckoff (62) for 143°K, $a_0(\text{H}_2\text{O}) = 6.350 \pm 0.008 \text{ \AA}$ and $a_0(\text{D}_2\text{O}) = 6.351 \pm 0.008 \text{ \AA}$. For hexagonal ice I, Brille and Tippe (60) made a detailed study of the lattice parameters between 13° and 193°K: a_0 , c_0 and the linear thermal expansion coefficients were evaluated every 20° from 13° to 193°K. In addition, x-ray diffraction (58) and ir (95) studies indicated that the nature of the hydrogen bonding and the nearest-neighbour configurations are the same in hexagonal and cubic ice I. On that basis we assumed the linear thermal expansion coefficient of cubic ice I ($\alpha_{a_0}^{\text{cub.}}$) to be the average of the expansion coefficients of hexagonal ice I ($\alpha_{a_0}^{\text{hex}}(T) + \alpha_{c_0}^{\text{hex}}(T)$), i.e.

$$\alpha_{a_0}^{\text{cub}}(T) = \frac{1}{2}(\alpha_{a_0}^{\text{hex}}(T) + \alpha_{c_0}^{\text{hex}}(T)) \text{ at temperature } T.$$

Values of $\alpha_{a_0}^{\text{cub}}(T)$ were determined every 10°K in the interval 10° to 200°K by the following method. Brille and Tippe's (60) ten a_0 and c_0 parameters were plotted as a function of temperature. Twenty values of $\alpha_{a_0}^{\text{hex}}(T)$ and $\alpha_{c_0}^{\text{hex}}(T)$ were determined at ten temperatures between 20° and 200°K, two values at each temperature. The pairs of coefficients at each temperature were obtained from intervals of 2° above and below that temperature, i.e.

$$\alpha_{a_0}^{\text{hex}}(150^\circ\text{K}) = \frac{1}{2}[\alpha_{a_0}^{\text{hex}}(148^\circ-150^\circ) + \alpha_{a_0}^{\text{hex}}(150^\circ-152^\circ)]$$

In the same way $\alpha_{c_0}^{\text{hex}}(T)$ was evaluated. From the ten values of $\alpha_{a_0}^{\text{hex}}(T)$ and $\alpha_{c_0}^{\text{hex}}(T)$, ten values of $\alpha_{a_0}^{\text{cub}}$ were obtained, Fig. 4.1.

Using Wyckoff's (62) $a_0^{\text{cub}}(\text{H}_2\text{O})$ at 143°K (6.350 Å) and the linear thermal expansion coefficients in Fig. 4.1, the cubic ice I lattice parameter $a_0^{\text{cub}}(T)$ was calculated every 2°K down from 143° to 10°K and every 2°K up from 143° to 200°K, $a_0^{\text{cub}}(T)$ is shown in Fig. 4.2. [Since the $a_0^{\text{cub}}(\text{H}_2\text{O})$ and $a_0^{\text{cub}}(\text{D}_2\text{O})$ lattice parameters were the same within experimental error,

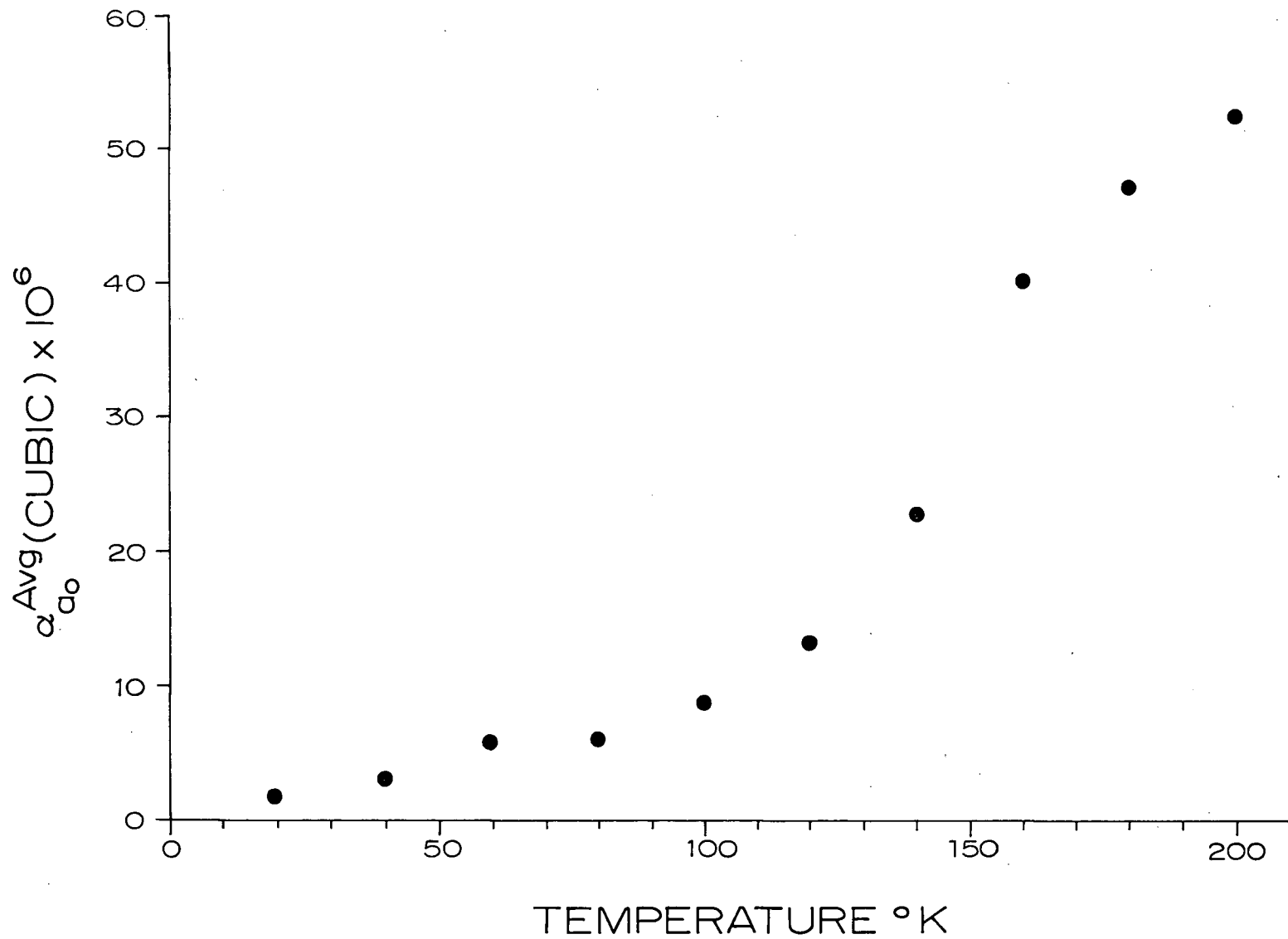


Fig. 4.1 The linear thermal expansion coefficient of cubic ice I as a function of temperature calculated from the hexagonal ice I data of Brille and Tippe (60).

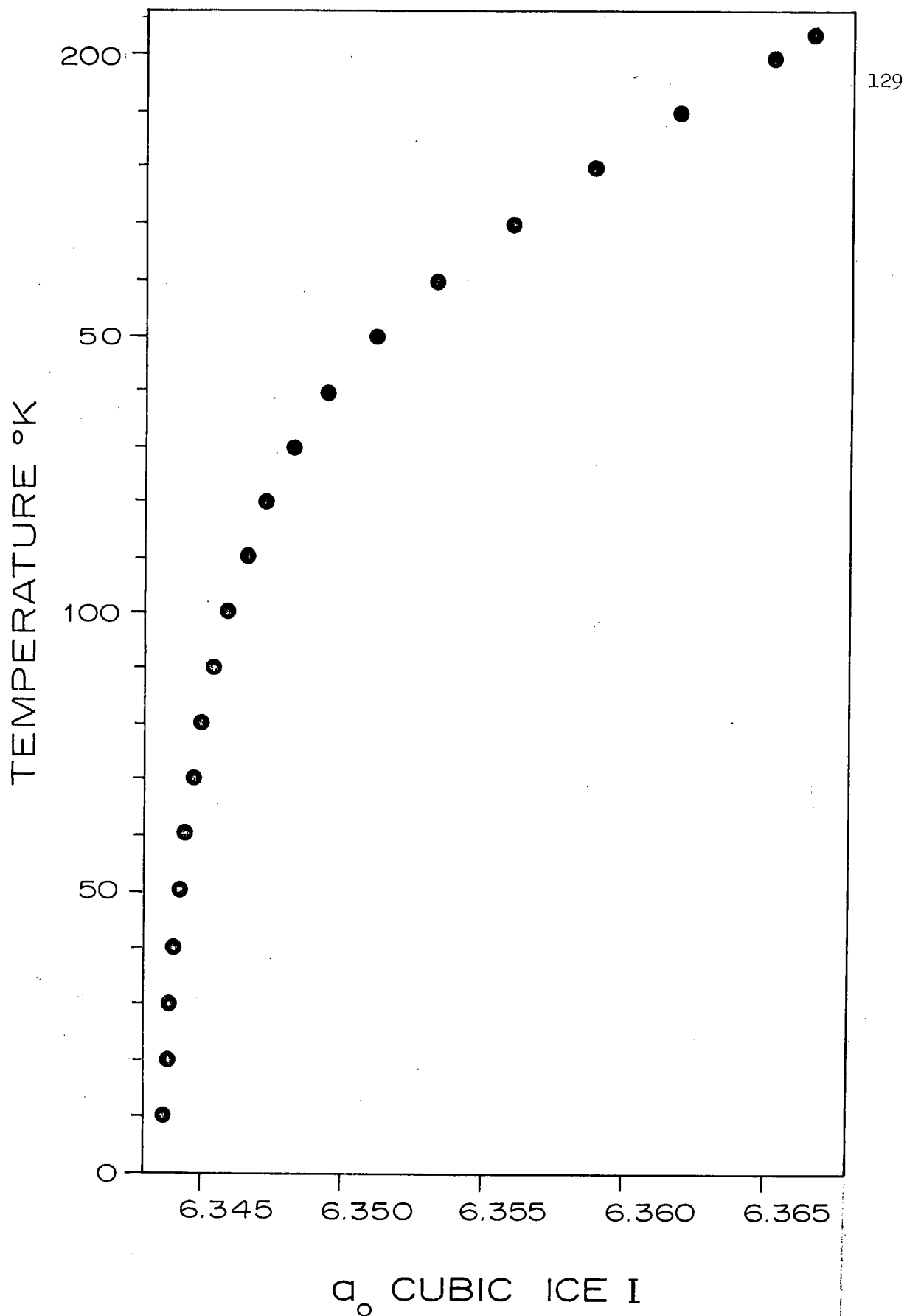


Fig. 4.2 The cubic ice I lattice parameter as a function of temperature. The values were calculated from the experimental a_0 at 143°K and the calculated thermal expansion coefficients.

only the $a_o^{\text{cub}}(\text{H}_2\text{O})$ parameter was evaluated.] For the cubic ice I unit cell the distance $R(\text{O}\cdots\text{O}) = (\sqrt{3}/4)a_o^{\text{cub}}(\text{T})$. The resulting cubic ice I $\text{O}\cdots\text{O}$ distances are plotted in Fig. 4.3 as a function of temperature.

HDO stretching frequencies from section 3.2A are plotted as a function of $R(\text{O}\cdots\text{O})$ in Fig. 4.4. Frequency and $R(\text{O}\cdots\text{O})$ were correlated as a function of common temperature. The frequencies were plotted as a function of the experimentally measured temperature, uncorrected for source beam heating ($+10^\circ\text{K}$ at 83°K) since the error may not be a linear function of temperatures.

Both the $\nu_{\text{OH}}(\text{HDO})$ and $\nu_{\text{OD}}(\text{HDO})$ plots were linear from 150° to 200°K :

$$\frac{\Delta\nu_{\text{OH}}(\text{HDO})}{\Delta R(\text{O}\cdots\text{O})} = 1.921 \times 10^3 \frac{\text{cm}^{-1}}{\text{\AA}}$$

and

$$\frac{\Delta\nu_{\text{OD}}(\text{HDO})}{\Delta R(\text{O}\cdots\text{O})} = 1.281 \times 10^3 \frac{\text{cm}^{-1}}{\text{\AA}}$$

However, the $\nu_{\text{OH}}(\text{HDO})$ frequency should be plotted as a function of $R(\text{O}\cdots\text{O})$ for D_2O ice I, since the ν_{OH} data were obtained from a sample of 4.0% HDO in D_2O . There is no experimental evidence to suggest that the linear thermal expansion coefficients of the H_2O and D_2O ices are different. However, it may be incorrect to assume the same behaviour since the amplitudes of translation, libration and vibration are different.

From Fig. 4.4 one sees that the frequency-- $R(\text{O}\cdots\text{O})$ dependence is also linear between 30° and 100°K :

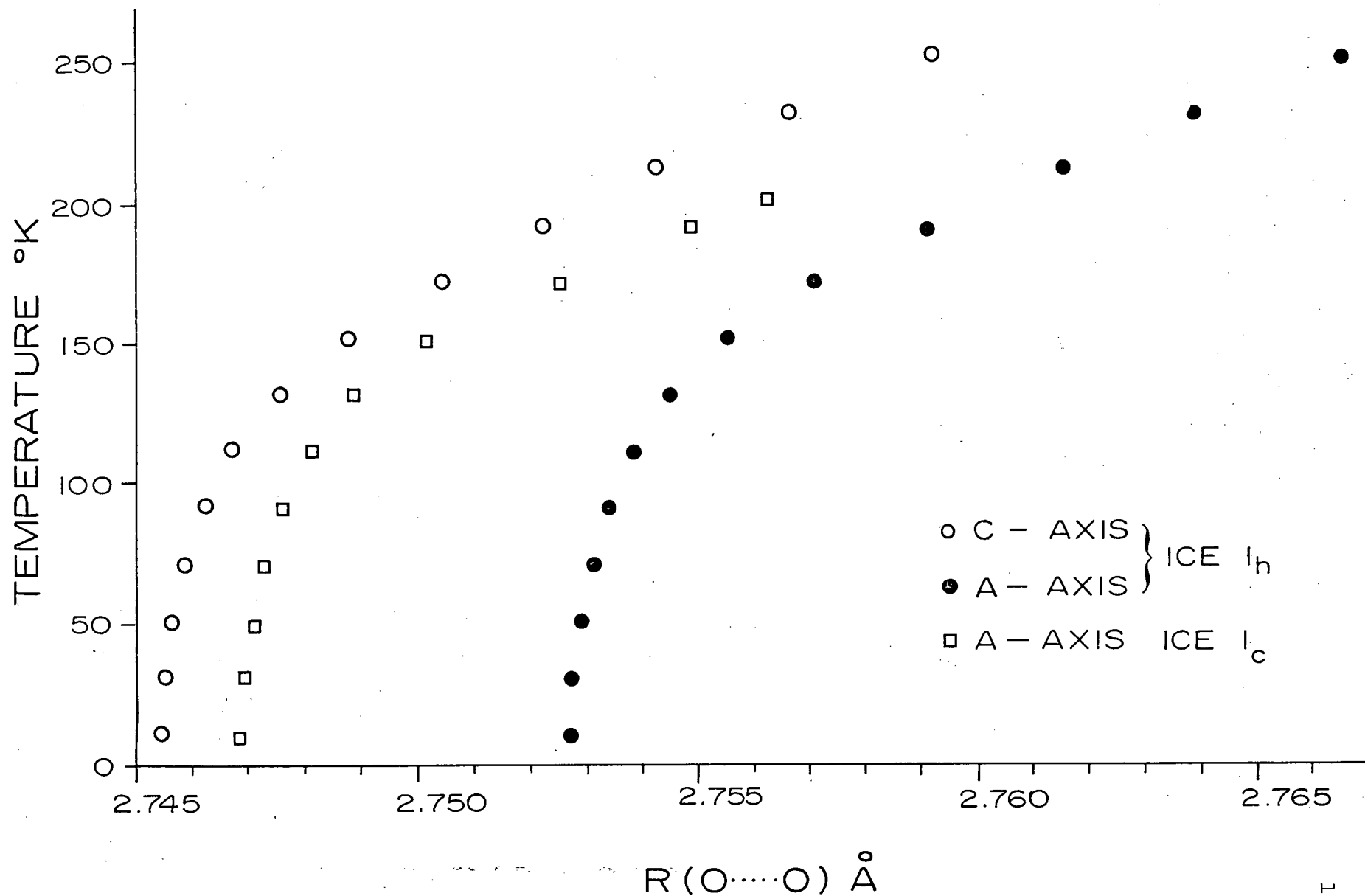


Fig. 4.3 The calculated O...O distance in cubic ice I as a function of temperature compared to hexagonal ice I O...O distances from experimental data.

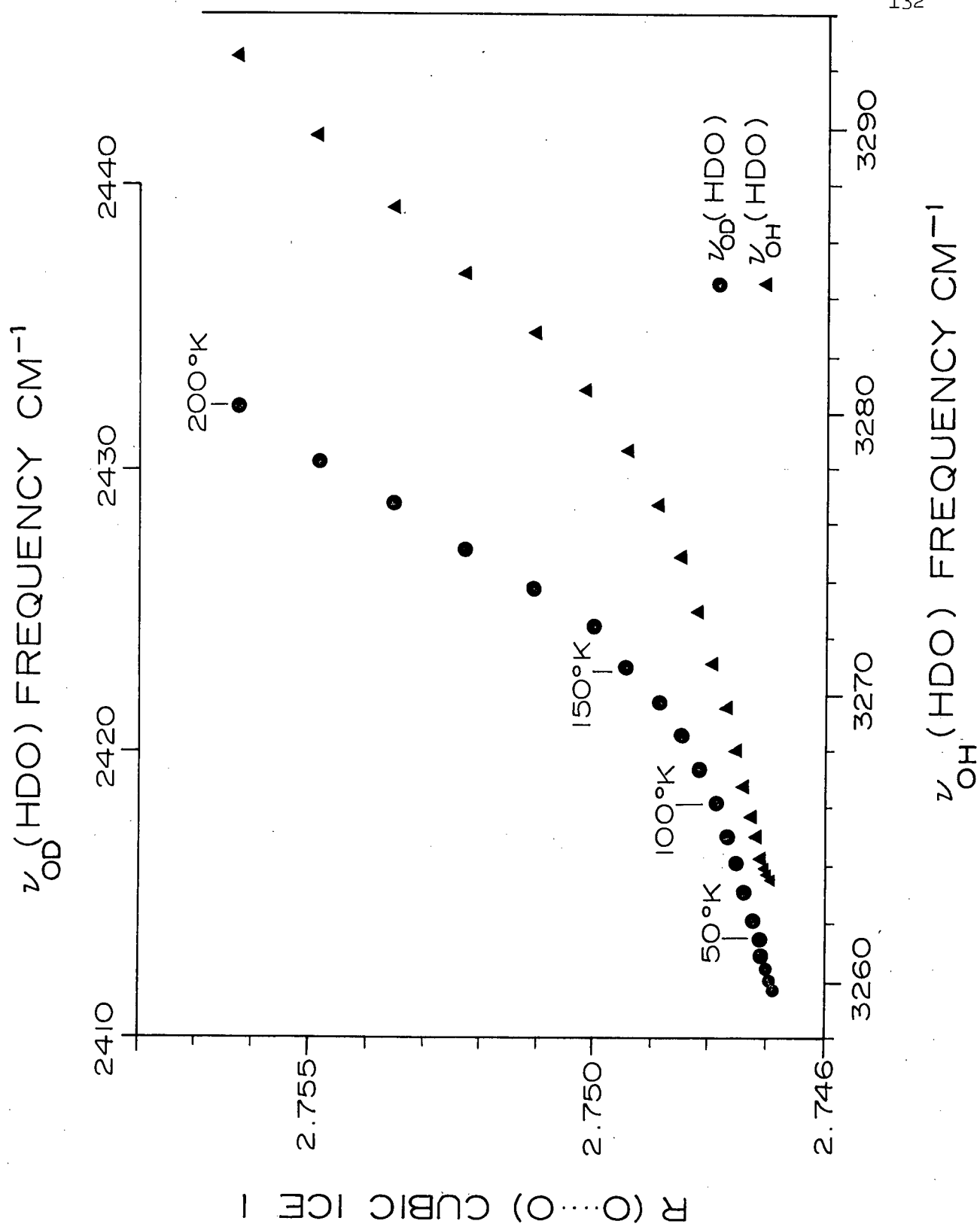


Fig. 4.4 The HDO stretching frequencies in cubic ice I as a function of $R(O \cdots O)$. Frequency and $R(O \cdots O)$ were correlated at common temperature.

$$\frac{\Delta\nu_{\text{OH}}(\text{HDO})}{\Delta R(\text{O}^{\circ}\cdots\text{O})} = 8.202 \times 10^3 \text{ cm}^{-1}/\text{\AA}^{\circ}$$

$$\frac{\Delta\nu_{\text{OD}}(\text{HDO})}{\Delta R(\text{O}^{\circ}\cdots\text{O})} = 6.629 \times 10^3 \text{ cm}^{-1}/\text{\AA}^{\circ}$$

Below 30°K the frequency shift was negligible. Between 100° and 150°K the frequency-- $R(\text{O}^{\circ}\cdots\text{O})$ dependences were non-linear. The points of intersection of the low and high temperature linear dependences were at 125°K (2.7487 \AA) for both $\nu_{\text{OH}}(\text{HDO})$ and $\nu_{\text{OD}}(\text{HDO})$.

For 100°K Whalley (95) assumed a $\Delta\nu/\Delta R$ dependence of $3000 \text{ cm}^{-1}/\text{\AA}^{\circ}$ to support his argument that the deviation of $\text{O}^{\circ}\cdots\text{O}$ distances arising from orientational disorder was only a few hundredths of an angstrom. The tangent to $\nu_{\text{OH}}(\text{HDO})$ vs. $R(\text{O}^{\circ}\cdots\text{O})$ at 100°K in Fig. 4.4 has $\Delta\nu/\Delta R$ equal to $6.750 \times 10^3 \text{ cm}^{-1}/\text{\AA}^{\circ}$, showing that Whalley's estimate was low by a factor of about two.

As well, Whalley (96) found that the most intense $\nu_{\text{OH}}(\text{HDO})$ bands for ices II, III and V were 3323, 3318 and 3350 cm^{-1} respectively. Using $\Delta\nu/\Delta R$ above, then the displacements of 51, 46 and 78 cm^{-1} from ice I $\nu_{\text{OH}}(\text{HDO})$ (3272 cm^{-1}) were caused by larger $\text{O}^{\circ}\cdots\text{O}$ distances. Specifically, the most intense $\nu_{\text{OH}}(\text{HDO})$ absorptions in ices II, III and V had $R(\text{O}^{\circ}\cdots\text{O})$'s larger than cubic ice I (100°K) by 0.008, 0.007 and 0.012 \AA . Ice II also had two other $\nu_{\text{OH}}(\text{HDO})$ absorptions (3357 and 3373 cm^{-1}) which suggest two other sets of $\text{O}^{\circ}\cdots\text{O}$ distances. They are longer than $R(\text{O}^{\circ}\cdots\text{O})$ cubic (2.748 \AA) by 0.013 and 0.015 \AA respectively. Thus ice II appears to have three distinct $\text{O}^{\circ}\cdots\text{O}$ bond lengths, 2.756, 2.761 and 2.763 \AA .

Ice III had one additional peak at 100°K, 3326 cm^{-1} . That could be due to a second distinct $\text{O}\cdots\text{O}$ distance, which is longer than $R(\text{O}\cdots\text{O})$ cubic by 0.008 \AA . Thus ice III has two sets of $\text{O}\cdots\text{O}$ distances, 2.755 and 2.756 \AA .

Ice V has only a single $\text{O}\cdots\text{O}$ distance, 2.760 \AA .

How well the $\Delta\nu/\Delta R$ relationships of ice I apply to other ices is not certain. The estimates of $R(\text{O}\cdots\text{O})$ above are only approximate.

At 0°K the half-height width for $\nu_{\text{OH}}(\text{HDO})$ in D_2O cubic ice I was found to be 35.5 cm^{-1} . That indicates that the $\text{O}\cdots\text{O}$ distances vary by less than $\pm 0.004\text{ \AA}$ from the average value in cubic ice I at 0°K. The $\Delta\nu_{\text{OH}}^{1/2}(\text{HDO})$ rose to 42.5 cm^{-1} at 180°K. Thus the $R(\text{O}\cdots\text{O})$ deviation must have been less than 0.022 \AA . Since the observed $\Delta\nu^{1/2}$ data were twice the expected width for an ordered phase (96), then the deviations in $R(\text{O}\cdots\text{O})$ arising from orientational disorder were less than 1/2 the above values, ± 0.002 and $\pm 0.011\text{ \AA}$ for 0° and 180°K respectively. Similarly by using $\Delta\nu_{\text{OD}}^{1/2}(\text{HDO})$ and $\Delta\nu_{\text{OD}}/\Delta R$ one finds dispersions in $R(\text{O}\cdots\text{O})$ of ± 0.002 and $\pm 0.010\text{ \AA}$ at 0° and 180°K.

As one would expect the dispersions of $R(\text{O}\cdots\text{O})$ in H_2O and D_2O are equal but the changes in force constants are related by approximately $1/\sqrt{2}$.

Clearly one does not expect the HDO frequencies to be a linear function of $R(\text{O}\cdots\text{O})$ over all values of $R(\text{O}\cdots\text{O})$. If the hydrogen bond is truly partially electrostatic and partially covalent in nature then the strength of the hydrogen bond should increase as $(1/R(\text{O}\cdots\text{O}))^2$ as temperature is increased. Correspondingly the covalent nature of the bond will

change non-linearly. The effects of such changes in hydrogen bond strength are seen in the observed non-linear behaviour and in the four-fold increase in $\Delta\nu/\Delta R$.

(b) Comparison of observed and empirical $\Delta\nu/\Delta R$ relations. The detailed study of $\nu_{OH}(HDO)$ absorption as a function of temperature and its correlation to $R(O\cdots O)$ permitted detailed checks of empirical relations between stretching frequencies and hydrogen bond lengths in ice I. Many workers (27,28,33) have made correlations from data of large numbers of compounds in different hydrogen bonding families. The linear relationship of Pimentel and Sederholm (28),

$$\Delta\nu = 4.43 (10^3) (2.84 - R) \text{ cm}^{-1},$$

satisfies neither the behaviour of $\Delta\nu/\Delta R$ in a family of $O-H\cdots O$ compounds as Nakamoto *et al.* (27) found, nor the behaviour of ice I as was shown in Fig. 4.4.

Recently Bellamy and Owen (33) gave a formula relating the frequency shift (from the monomeric frequency) to a maximum effective hydrogen bond length and the measured $O\cdots O$ distance:

$$\Delta\nu_{str} = C \left[\left(\frac{d}{R} \right)^{12} - \left(\frac{d}{R} \right)^6 \right]$$

where $\Delta\nu_{str}$ = shift of the stretching frequency from the gas phase value,

d = the sum of the collision radii of two oxygen atoms in Angstroms ($d = 3.35 \overset{o}{\text{\AA}}$),

R = the $O\cdots O$ distance in Angstroms,

and C = the constant of proportionality between the potential and the frequency shift.

For a family of $\text{O}-\text{H}\cdots\text{O}$ hydrogen bonding compounds, Bellamy and Owen (33) suggested a constant value of $C = 50 \text{ cm}^{-1}$. Their predicted $\Delta\nu_{\text{str}}$ agreed very well with the observed values, particularly at long $\text{O}\cdots\text{O}$ lengths, for a family of $\text{O}-\text{H}\cdots\text{O}$ systems.

By using the $R(\text{O}\cdots\text{O})$ values determined in section (a) above for 10°K and 130°K , two values of the constant C were determined for ice I:

$$C(10^\circ\text{K}) = 58.890 \text{ cm}^{-1},$$

$$C(130^\circ\text{K}) = 57.767 \text{ cm}^{-1}.$$

The constants were determined by substituting the $\Delta\nu_{\text{str}}$ values between $\nu_{\text{OH}}(\text{HDO})$ of the vapour phase (3757.5 cm^{-1}) and the cubic ice I values ($10^\circ\text{K } 3263.8 \text{ cm}^{-1}$ and $130^\circ\text{K } 3276.8 \text{ cm}^{-1}$). The constants were then used to calculate $\Delta\nu_{\text{str}}(R)$. Since the thermal expansion of cubic ice I is only small between 10°K and 200°K , Bellamy and Owen's (33) formula could only be checked over a small range of $\text{O}\cdots\text{O}$ distances. The predictions of Bellamy and Owen's formula and the observed $\Delta\nu/\Delta R$ relation are shown in Fig. 4.5.

For the constant determined at 130°K the predicted behaviour was good above 130°K but did not follow the observed trend below 130°K . Over the $\text{O}\cdots\text{O}$ range 2.7470 \AA to 2.7570 \AA Bellamy and Owen's formula predicted $\Delta\nu/\Delta R = 2,263 \text{ cm}^{-1}/\text{\AA}$. Experimentally $\Delta\nu/\Delta R = 7,360 \text{ cm}^{-1}/\text{\AA}$ from 2.7470 \AA to 2.7480 \AA (10° to 110°K) and $\Delta\nu/\Delta R = 2,144 \text{ cm}^{-1}/\text{\AA}$ from 2.7485 \AA to 2.7570 \AA (130° to 200°K). Thus above 130°K Bellamy and Owen's formula reproduces the ice I experimental behaviour well. Below 130°K ($R(\text{O}\cdots\text{O})$ less than 2.7485 \AA) their formula fails.

Bellamy and Owen (33) started from the Lippincott-Schroeder potential and made certain assumptions about the intermolecular interaction. The Lippincott-Schroeder potential (25) consists of four terms, one term being

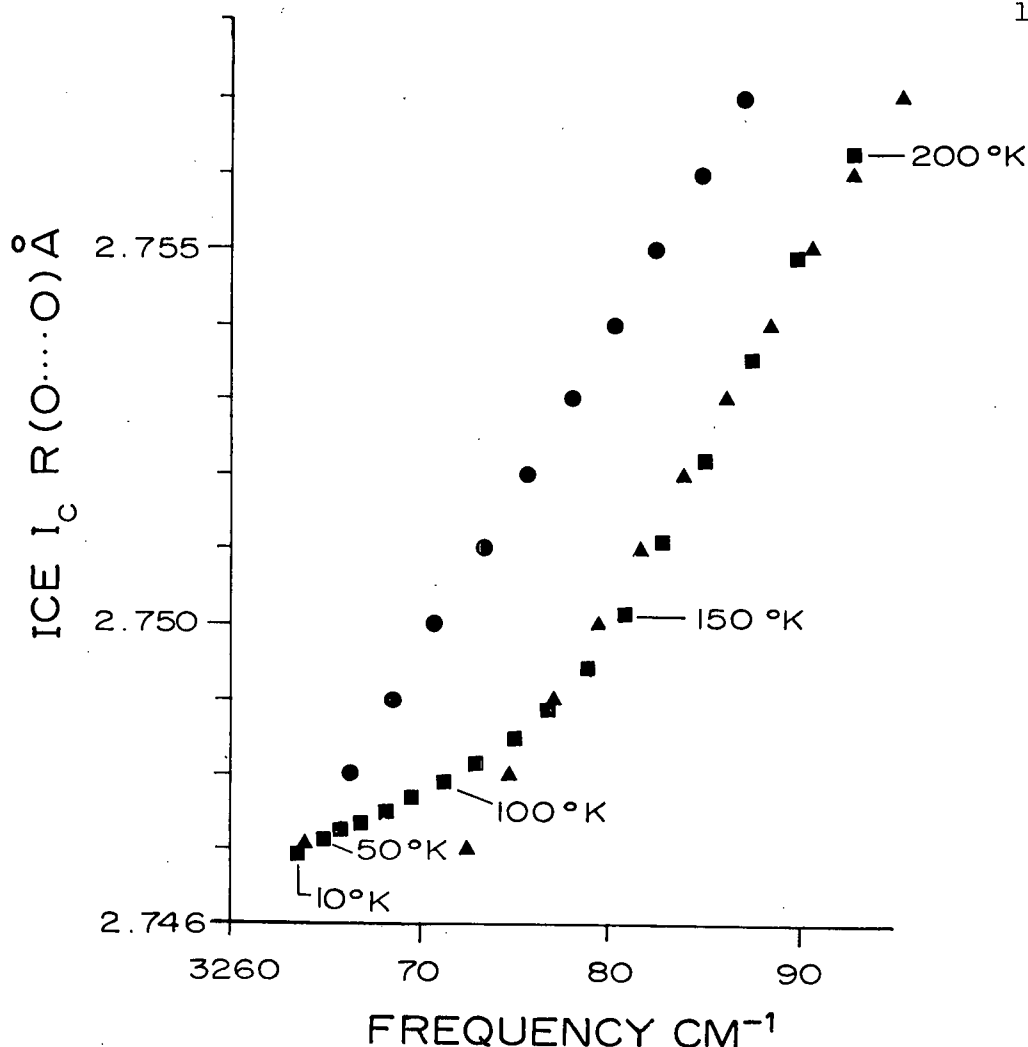


Fig. 4.5 The stretching frequency-- $R(O\cdots O)$ dependence. The observed frequencies are plotted against the $R(O\cdots O)$ distances estimated for cubic ice I from hexagonal ice I linear thermal expansion coefficients and are indicated by solid squares (\blacksquare). The predicted $\Delta\nu/\Delta R$ behaviour based on Bellamy and Owen's formula are shown as circles and triangles (\bullet , \blacktriangledown).

due to van der Waals repulsive forces. Bellamy and Owen investigated the van der Waals repulsion on the basis of a Lennard-Jones 6-12 potential by assuming the interaction of non-bonding filled orbitals was similar to that of non-polar spherical atoms. Bellamy and Pace (32) suggested that if the van der Waals repulsion originates largely in the lone-pair/lone-pair repulsions of the two oxygen atoms then the 6-12 provides a good distance/energy relation. The relation between the potential energy and the frequency

shift was assumed to be linear.

From our results the assumptions of Bellamy and Pace (32) and Bellamy and Owen (33) are not contradicted between 130° and 200°K, but are contradicted below 130°K. That suggests that the van der Waals repulsion does not originate only in the lone-pair/lone-pair repulsions below 130°K, or that some complex change occurred in the system. The depopulation of $\Delta\nu_{\text{str}}$ hot bands below 130°K is an unlikely source of the discrepancy since that would have resulted in a shift to higher frequency as temperature was lowered, in opposition to the observed increase in shift to lower frequency.

It is possible that the O-H stretching amplitude affects the strength of an individual hydrogen bond (and hence the frequency shift) by increased modulation of the potential energy as temperature increases reaching a limiting value at 130°K. However, the experimental amplitudes (5) continued to increase above 130°K and did not reach a limiting value, i.e. between 73° and 173°K the RMS amplitude of O-H stretch increased by 0.042 Å and between 173° and 273°K it increased by 0.028 Å. On the other hand, that does not mean that the modulation of the potential energy did not approach a limiting value.

The Bellamy and Owen (33) formula reproduced the $\Delta\nu/\Delta R$ results for a large number of molecules observed near 300°K, while our results were obtained below 200°K. One is tempted to look for a property common to all samples above 130°K. Such properties may be the population of translational

hot bands and large amplitudes of translation. Molecular translation would modulate the $O\cdots O$ distance and hence the hydrogen bond energy. Larger amplitudes of translation would result in increased modulation of the potential, weaker hydrogen bonds and smaller shifts. If the translational amplitude modulation increases from 0°K to a limiting value at 130°K and above then the discrepancy can be understood. At room temperature the modulation of the hydrogen bond would be approximately the same in all molecules.

(c) The HDO anharmonicity (X_{OH}) and the HDO harmonic frequency (ω_{OH}) and their dependences on temperature and $R(O\cdots O)$. According to Nibler and Pimentel (121) the anharmonicity X_{OH} of HDO in the vapour phase is 91.2 cm^{-1} . For cubic ice I Haas and Hornig (106) predicted X_{OH} (from overtone data) to be 125 cm^{-1} while Bertie and Whalley (96) estimated it to be 100 cm^{-1} (by a modified product rule). While Bertie and Whalley's (96) estimate was very approximate, the point is that the anharmonicity increases only a little from the vapour phase.

Since we did not observe the first overtone of $\nu_{\text{OH}}(\text{HDO})$ (near 6200 cm^{-1}) the HDO anharmonicity must be estimated by the method of Bertie and Whalley (96).

Application of free molecule theory to solids, particularly hydrogen bonded solids, is suspect but the method yields useful qualitative information. For a free, bent XY_2 molecule one finds that

$$\begin{aligned}\nu_1 &= \omega_1 - 2X_{11} - X_{12} - X_{13} \\ \nu_2 &= \omega_2 - 2X_{22} - X_{21} - X_{23} \\ \nu_3 &= \omega_3 - 2X_{33} - X_{31} - X_{32} .\end{aligned}$$

If X_{ij} ($i \neq j$) are assumed to be small and are neglected then

$$v_1 = \omega_1 - 2X_{11}$$

$$v_2 = \omega_2 - 2X_{22}$$

$$v_3 = \omega_3 - 2X_{33}$$

For isotopic substitution one can employ the Teller-Redlich product rule

$$\rho = \frac{\omega_a^i \omega_b^i \dots \omega_e^i}{\omega_a \omega_b \dots \omega_e} \quad \text{over 1 symmetry representation}$$

and by analogy to the diatomic case one also knows that

$$\frac{X_{jj}^i}{X_{jj}} = \frac{\omega_j^i \omega_j^i}{\omega_j \omega_j}$$

For v_3 of H_2O and D_2O the application is straightforward since v_1 and v_2 are of a_1 symmetry while v_3 is of b_1 symmetry (assuming the C_{2v} point group).

Then

$$\rho = \frac{\omega_3^i}{\omega_3} \quad \text{and} \quad \frac{X_{33}^i}{X_{33}} = \left(\frac{\omega_3^i}{\omega_3} \right)^2 = \rho^2$$

Hence, one can write for H_2O

$$v_3 = \omega_3 - 2X_{33}$$

and for D_2O

$$v_3^i = \omega_3^i - 2X_{33}^i = \rho \omega_3 - 2\rho^2 X_{33}$$

By assuming that ρ of the vapour phase (say from Nibler and Pimentel's harmonic data) applies also to the solid and by using the observed v_3 H_2O and D_2O frequencies, then the two equations can be solved for ω_3 and X_{33} of ice I.

For HDO the problem is more complex. The strict product rule would be

$$\rho = \frac{\omega_{OH} \omega_{OD} \omega_{HOD} \omega_{T_x} \omega_{T_y} \omega_{R_z}^{\text{HDO}}}{\omega_1 \omega_3 \omega_2 \omega_{T_x} \omega_{T_z} \omega_{R_y}^{\text{H}_2\text{O}}} .$$

Even by assuming that the librational and translational force constants approach zero and the frequencies approach zero (which they obviously do not), the product rule is still complex

$$\rho = \frac{\omega_{OH} \omega_{OD} \omega_{HOD}}{\omega_1 \omega_3 \omega_2} .$$

As an approximation we can treat the problem as a diatomic molecule H-(OD) with the isotopic analogue D-(OH). Then the product rule is

$$\rho = \frac{\omega_{OD}}{\omega_{OH}} .$$

The expected value of ρ is given by

$$\begin{aligned} \frac{i_{OH}}{\omega_{OH}} &= \frac{|G^i|}{|G|} = \left[\frac{m_D^{-1} + (m_O + m_H)^{-1}}{m_H^{-1} + (m_O + m_D)^{-1}} \right] \\ &= 0.7278 . \end{aligned}$$

From the vapour data of Nibler and Pimentel (121) one finds $\rho = 0.7261$.

Briefly the method of Bertie and Whalley (96) involved assuming such a modified product rule for HDO, where

$$\rho = \frac{\omega_{OD}(\text{ice})}{\omega_{OH}(\text{ice})} = \frac{\omega_{OD}(\text{vapour})}{\omega_{OH}(\text{vapour})}$$

and

$$\frac{X_{OD}}{X_{OH}} = \rho^2 .$$

Then
$$\nu_{OH} = \omega_{OH} - 2X_{OH} \quad \text{and} \quad \nu_{OD} = \rho\omega_{OH} - 2\rho^2X_{OH}$$

where $\rho = 0.72608$ of the vapour phase. The anharmonicity of the HDO stretching vibrations in ice I was then given by

$$X_{OH}(T) = \frac{\nu_{OD}(T) - \rho\nu_{OH}(T)}{2\rho(1 - \rho)}$$

Hence the anharmonicity can be determined as a function of temperature between 10° and 200°K. The harmonic HDO frequency and the HDO anharmonicities calculated in this way are shown in Figs. 4.6 and 4.7 respectively. While the magnitude of the calculated anharmonicity is not accurate, the trend in $X_{OH}(T)$ indicates some fundamental changes in the hydrogen bonded system. Between 10° and 80°K X_{OH} underwent a regular increase of 4% and from 80° to 200°K X_{OH} underwent a regular decrease of 4%. The low temperature limiting anharmonicity was 105.6 cm^{-1} , the low temperature dependence was $3.25 \times 10^{-2} \text{ cm}^{-1}/^\circ\text{K}$, and the high temperature dependence was $-3.75 \times 10^{-2} \text{ cm}^{-1}/^\circ\text{K}$. The anharmonicity reached a maximum at 80°K. The temperature dependence of ω_{OH} was $0.138 \text{ cm}^{-1}/^\circ\text{K}$ if it was assumed to be linear. The maximum in the anharmonicity is also seen in the harmonic frequency. The anharmonicity was also plotted as a function of $R(O\cdots O)$, Fig. 4.8. That plot looks surprisingly like a Lennard-Jones 6-12 potential energy curve.

The harmonic HDO frequency and the anharmonicity of HDO stretches as a function of temperature were estimated from observed $\nu_{OH}(\text{HDO})$ and $\nu_{OD}(\text{HDO})$ frequencies. Hence, the variations of ω_{OH} and X_{OH} as a function of temperature arise from all sources present in the cubic ice I crystals.

There appear to be two major sources of changes in the anharmonicity as a function of temperature. As the crystal is cooled from 200°K to 5°K it contracts and $R(O\cdots O)$ decreases. The hydrogen bond energy increases,

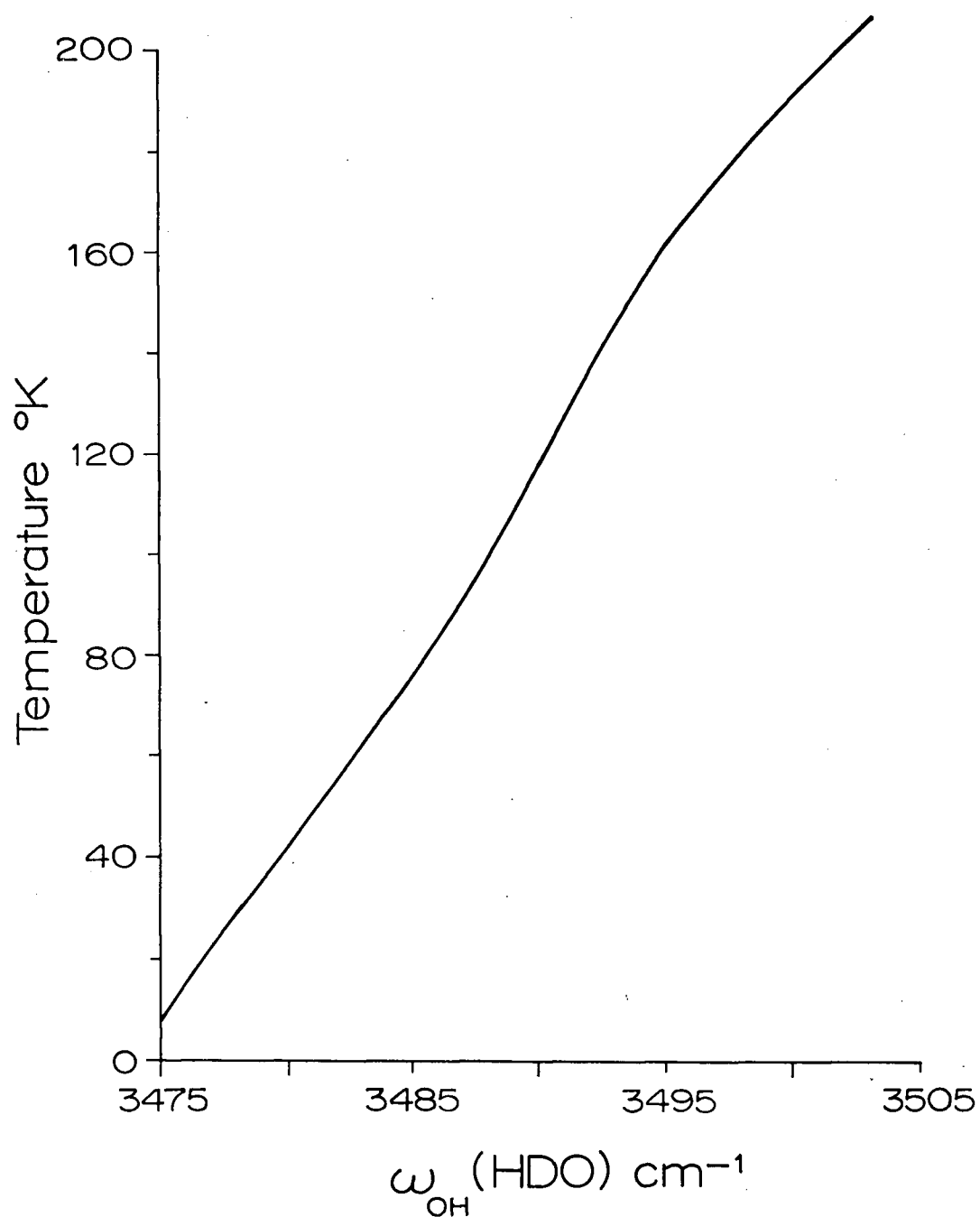


Fig. 4.6 The harmonic HDO stretching frequency for cubic ice I as a function of temperature. The ω_{OH} (HDO) was estimated from observed HDO cubic ice I frequencies.

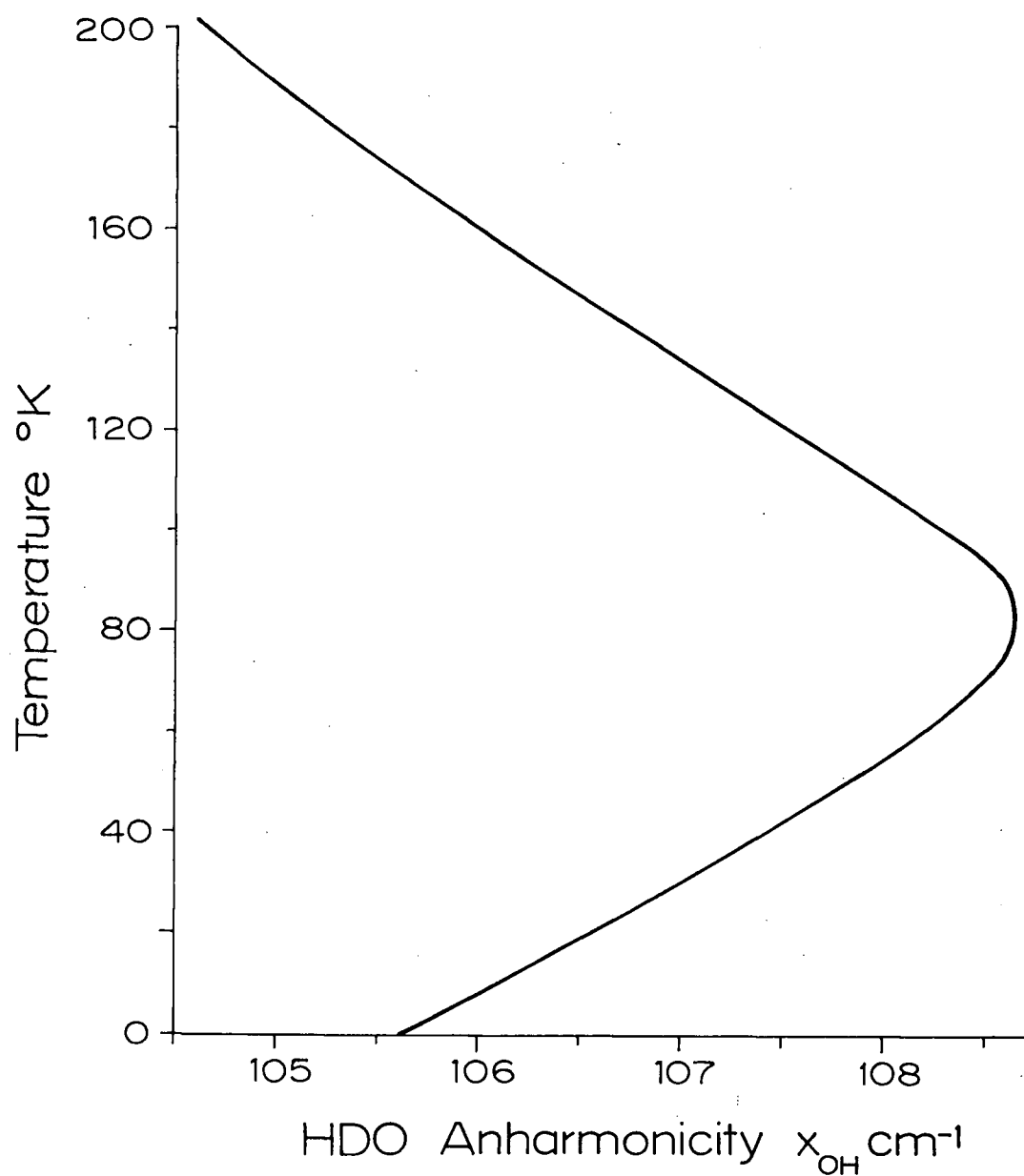


Fig. 4.7 The HDO cubic ice I anharmonicity as a function of temperature. The x_{OH} values were estimated from observed HDO stretching frequencies and the ρ value of the vapour phase.

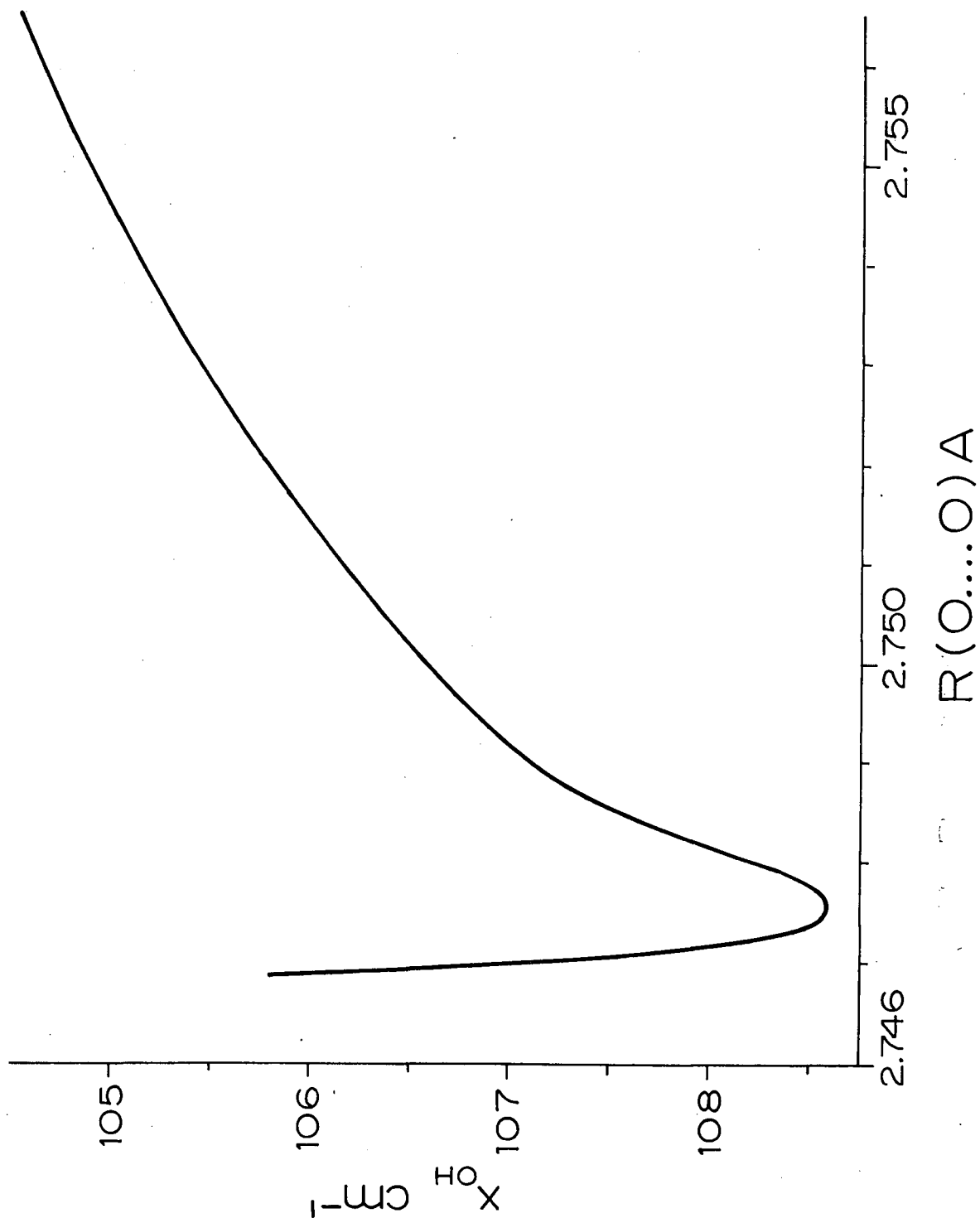


Fig. 4.8 The dependence of the anharmonicity X_{OH} on the $R(O \cdots O)$ distance between 10°K and 200°K. 145

the observed HDO stretching frequencies and the predicted harmonic frequency decrease, and the anharmonicity increases as long as $R(O \cdots O)$ is decreasing. Hence one would expect a steady increase in the contribution of increasing hydrogen bond energy to the total anharmonicity down to about 80°K (the

$R(O\cdots O)$ freeze-in temperature). Changes in $R(O\cdots O)$ and the hydrogen bond energy are very small below $80^\circ K$.

The other source of anharmonicity is probably due to changes in the amplitudes of O-H stretch and HDO translation. The O-H stretching amplitude must be discussed in terms of the total population distribution among all the energy levels. Below $200^\circ K$ virtually all of the molecules must be in the ground vibrational state. As was indicated previously, the O-H amplitudes have been measured experimentally (ref. 5, page 78) and increased from 0.150 \AA at $1^\circ K$ to 0.221 \AA at $200^\circ K$ in H_2O ice Ih. Corresponding O-D amplitudes for D_2O were 0.129 \AA at $1^\circ K$ and 0.217 \AA at $223^\circ K$. Thus the anharmonicity experienced by the molecules can be expected to decrease below $200^\circ K$.

As well, the RMS amplitude of translation decreases from $200^\circ K$ to $1^\circ K$. Since ν_{OH} , X_{OH} , and ω_{OH} are all strongly coupled to the instantaneous $R(O\cdots O)$, then decreases in the range of $R(O\cdots O)$ through decreased amplitudes of translation will give a smaller range of X_{OH} and a net smaller X_{OH} .

We suggest that: 1) below $80^\circ K$ ΔX_{OH} from changes in amplitudes is greater than ΔX_{OH} due to changes in hydrogen bond energy, 2) at $80^\circ K$ the two kinds of ΔX_{OH} are equal, and 3) that above $80^\circ K$ ΔX_{OH} (hydrogen bond energy) is greater than ΔX_{OH} (amplitude).

(d) Correlation of the HDO stretching frequencies to the RMS amplitudes of translation. Since the HDO stretching frequencies are a function of $R(O\cdots O)$ and since the rate of increase of $R(O\cdots O)$ depends on the RMS amplitude of molecular translation, then it is interesting to consider the relationship between ν_{str} and $\langle \Delta r^2 \rangle^{\frac{1}{2}}$ as a function of temperature.

Decius (122) gave the mean-square displacement from the equilibrium distance between two atoms resulting from all modes of vibration as:

$$\langle \Delta r_t^2 \rangle = \sum_k L_{tk}^2 \langle Q_k^2 \rangle \quad [1]$$

where Δr_t = the displacement distance of internal coordinate t due to all normal coordinates, k ,

L_{tk} = the element of the matrix transforming normal coordinate k into internal coordinate t ,

and Q_k = the k -th normal coordinate.

The mean-square amplitude of the k -th normal coordinate ($\langle Q_k^2 \rangle$) was given by Morino et al. (123) as:

$$\langle Q_k^2 \rangle = \frac{h}{8\pi^2 c \nu_k} \coth \frac{h c \nu_k}{2kT} \quad [2]$$

where ν_k = the vibrational frequency of the k -th normal mode in cm^{-1} ,

k = Boltzman's constant,

T = the temperature in degrees Kelvin,

c = the velocity of light, and

h = Planck's constant.

The formulas [1] and [2] were derived for the isolated, free molecule case.

In a rigorous treatment of ice it would be necessary to consider all internal and lattice modes in the sum over k .

Cubic ice I has two H_2O molecules per primitive unit cell and there are three non-zero translational, six librational and six internal vibrational modes. If the pair of H_2O molecules is considered as a weakly bonded diatomic molecule, $(\text{H}_2\text{O}) \cdots (\text{H}_2\text{O})$, then there is one normal mode of vibration, the

$R(O\cdots O)$ stretch. The mean-square amplitude of translation between two H_2O molecules can then be estimated. Equations [1] and [2] give

$$\langle \Delta R^2 \rangle = \langle \Delta r^2 \rangle = LL' \frac{h}{8\pi^2 c \nu_T} \coth \frac{h c \nu_T}{2kT}$$

and for the $(H_2O)_2$ "diatom" $LL' = G$, which is easily evaluated for H_2O or D_2O . The RMS amplitude of displacement is then given by

$$\langle \Delta r^2 \rangle^{\frac{1}{2}} = \left[\frac{h}{m_i 4\pi^2 c \nu_T} \coth \frac{h c \nu_T}{2kT} \right]^{\frac{1}{2}} \quad [3]$$

where m_i is the mass of H_2O or D_2O , and the variation of $\langle \Delta r^2 \rangle^{\frac{1}{2}}$ as a function of temperature can be calculated by using the observed $\nu_T(H_2O)$ frequencies.

Two sets of $\langle \Delta r^2 \rangle^{\frac{1}{2}}$ were calculated between 10° and $200^\circ K$. In both cases the $\nu_T(H_2O)$ frequencies used were from the best smooth curve through the experimental points (Fig. 3.15). Since the $\nu_T(H_2O)$ frequency varied by less than 5% between $10^\circ K$ and $200^\circ K$, one set of $\langle \Delta r^2 \rangle^{\frac{1}{2}}$ was calculated at constant ν_T , i.e. $\nu_T = 227.0 \text{ cm}^{-1}$ at $80^\circ K$. That is reasonable since $1/T$ dominates the function. A corresponding set of $\langle \Delta r^2 \rangle^{\frac{1}{2}}$ for D_2O were calculated using the H_2O frequencies and D_2O masses. These data are compiled in Table IV.I and are plotted in Fig. 4.9. For comparison, a set of H_2O

$\langle \Delta r^2 \rangle^{\frac{1}{2}}$ were calculated using the full range of observed frequencies. Those data are also compiled in Table IV.I. The only significant change was a slight decrease in the low temperature values and a slight increase in the high temperature values.

Plots of $R(O\cdots O)$ against $\langle \Delta r^2 \rangle^{\frac{1}{2}}$ at equal temperatures and of $\nu_{OH}(HDO)$ and $\nu_{OD}(HDO)$ against $\langle \Delta r^2 \rangle^{\frac{1}{2}}$ are given in Figs. 4.10 and 4.11 respectively.

TABLE IV.I The RMS amplitudes of translation calculated from H_2O ν_{T} and compared to results of thermodynamic calculations.

Temperature	$\langle \Delta r^2 \rangle^{\frac{1}{2}}$ H_2O const. ν_{T}	$\langle \Delta r^2 \rangle^{\frac{1}{2}}$ H_2O $\nu_{\text{T}}(\text{T})$	$\langle \Delta r^2 \rangle^{\frac{1}{2}}$ D_2O const. ν_{T}	$\langle \Delta r^2 \rangle^{\frac{1}{2}}$ H_2O (a)	$\langle \Delta r^2 \rangle^{\frac{1}{2}}$ D_2O (a)
	$^{\circ}\text{K}$	$\times 10^2 \text{ \AA}$	$\times 10^2 \text{ \AA}$	$\times 10^2 \text{ \AA}$	$\times 10^2 \text{ \AA}$
1				9.2	9.0
10		9.08	9.04	8.61	
20		9.08		8.61	
30		9.08	9.04	8.61	
40		9.08		8.62	
50		9.10	9.06	8.63	
60		9.12		8.65	
70		9.17	9.14	8.70	
80		9.25		8.77	
90		9.33	9.32	8.85	
100		9.44		8.95	13.2
10		9.57	9.59	9.07	
20		9.70		9.20	14.5
30		9.84	9.96	9.34	
40		10.0		9.49	
50		10.2	10.4	9.65	
60		10.4		9.82	
70		10.5	10.7	9.99	
80		10.7		10.1	
90		10.9	11.2	10.3	
200		11.1		10.5	18.5
223					19.5
273				21.5	21.4

(a) Ref. 84.

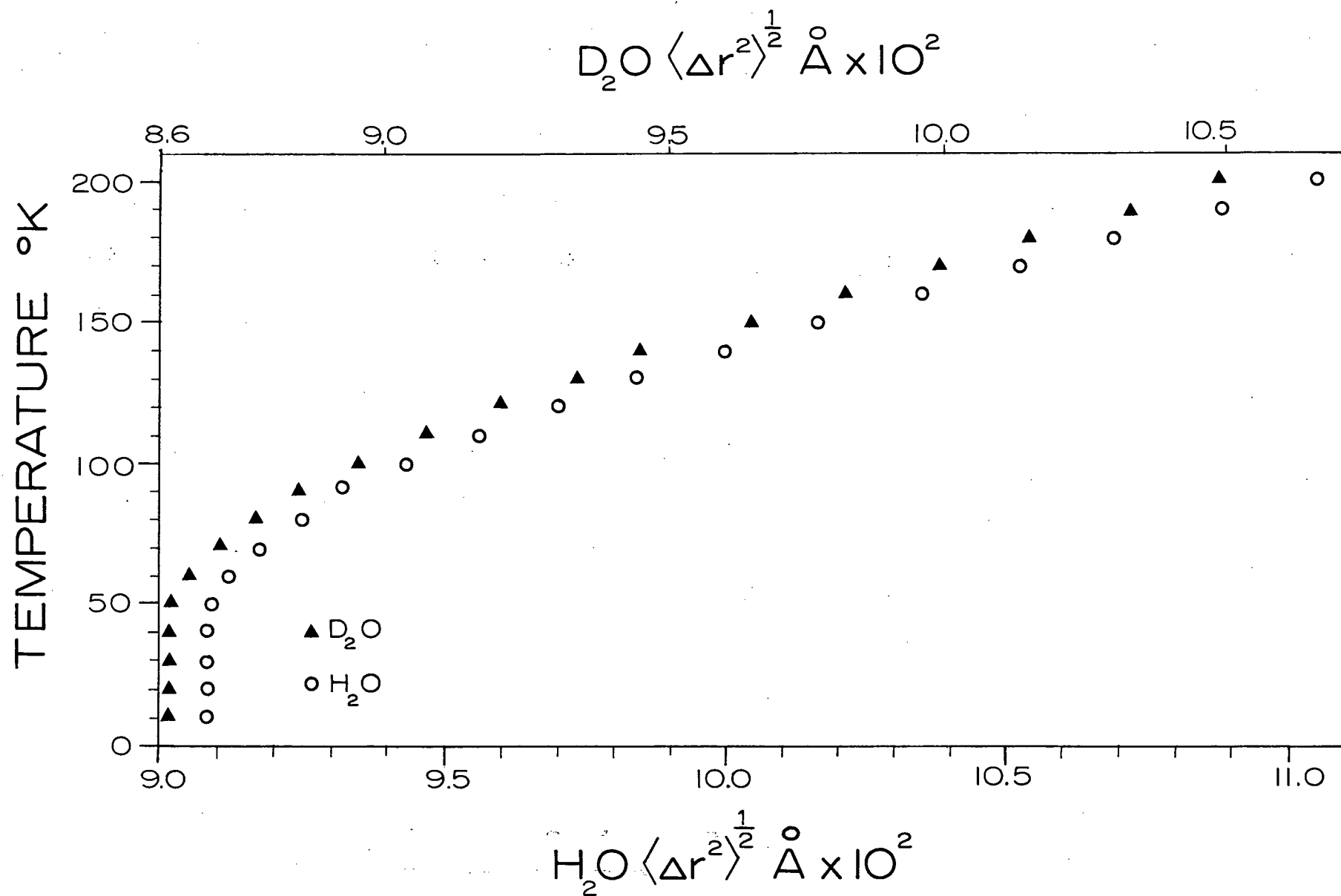


Fig. 4.9 The RMS amplitudes of H₂O and D₂O translation calculated with a constant $\nu_T(\text{H}_2\text{O})$ assuming an $(\text{H}_2\text{O})_2$ diatomic unit cell model.

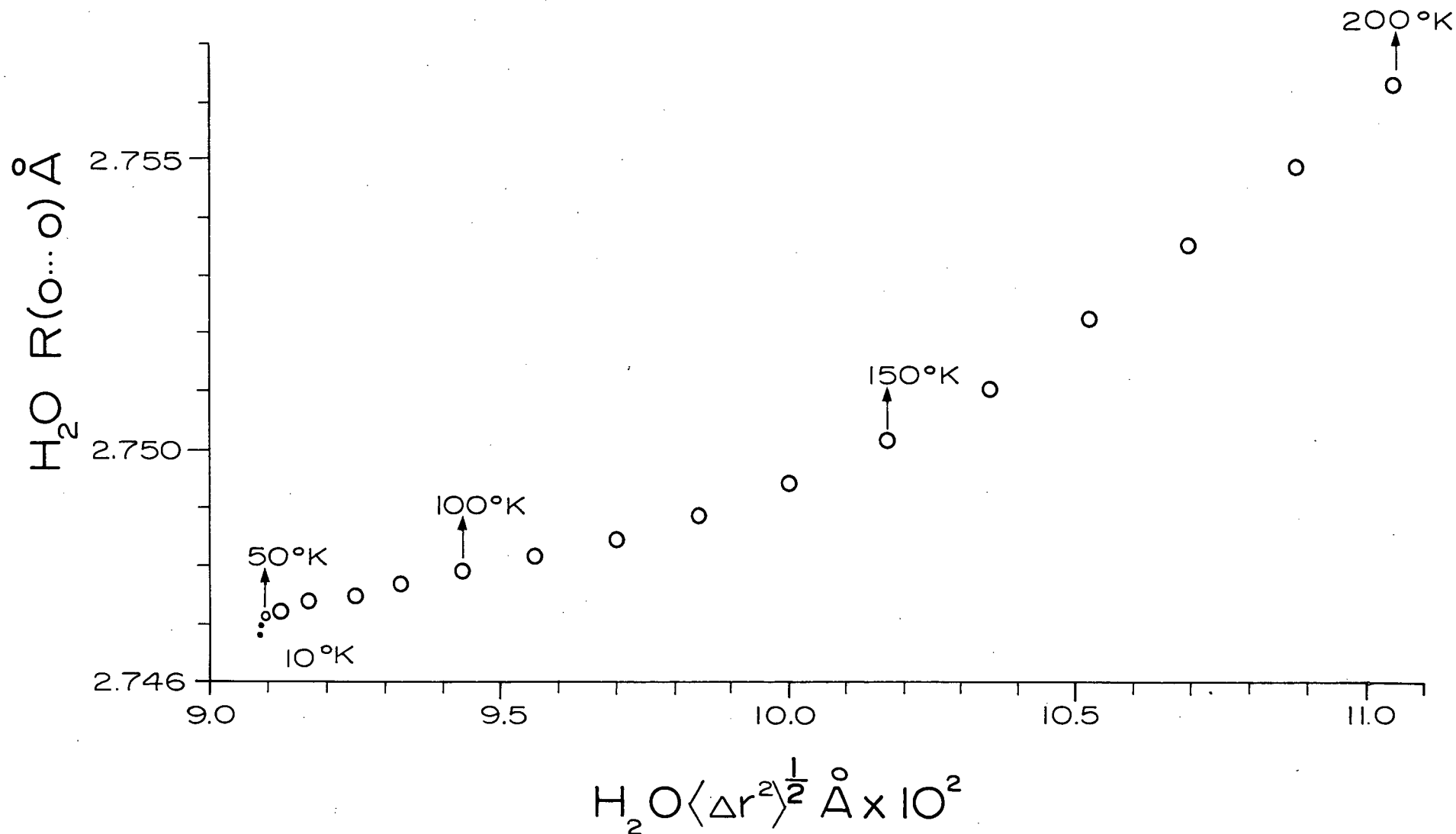


Fig. 4.10 The correlation of RMS amplitude of translation to the calculated O...O distance in cubic ice I. $R(O \cdots O)$ and $\langle \Delta r^2 \rangle^{1/2}$ were correlated as a function of common temperature.

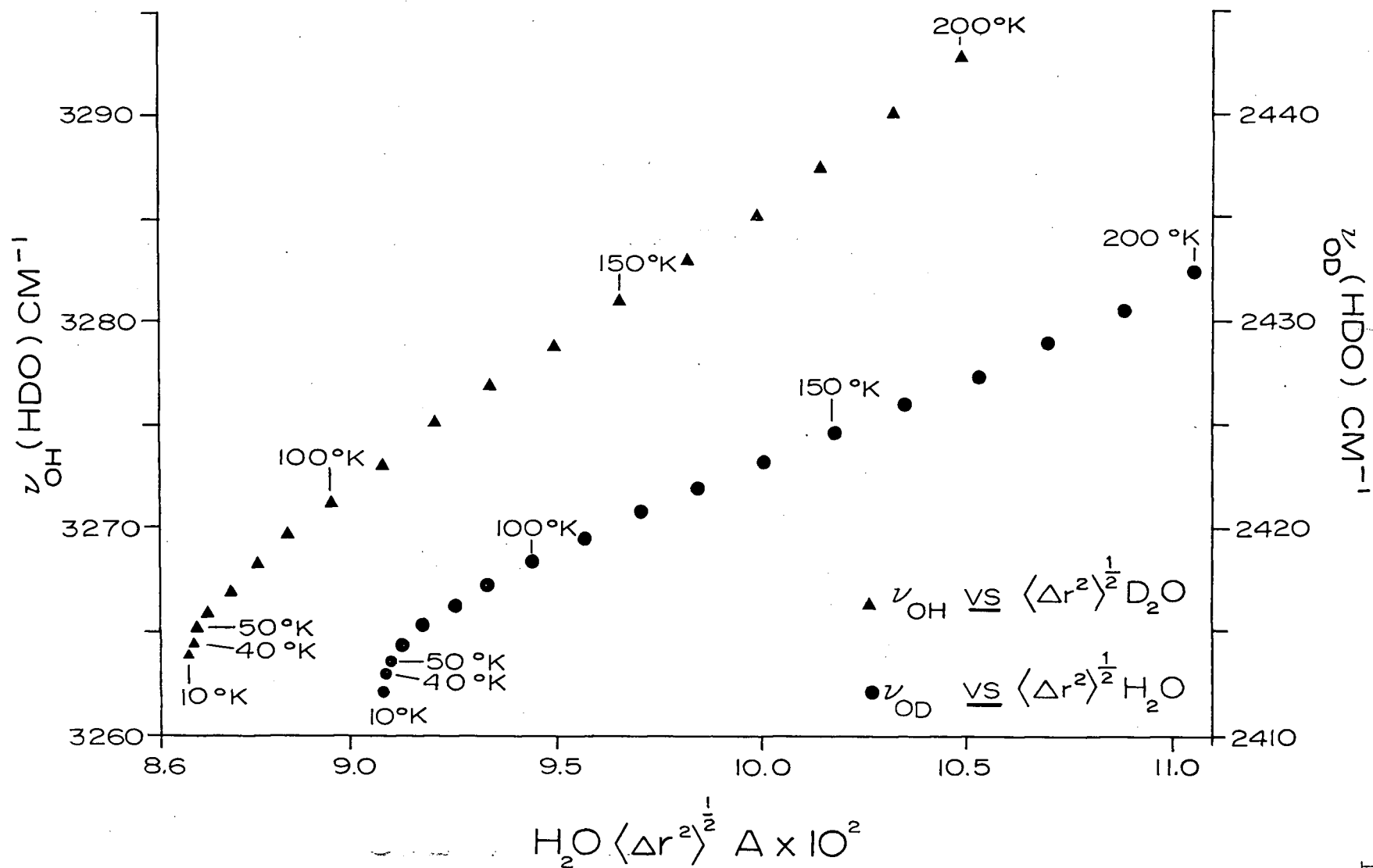


Fig. 4.11 The dependence of the observed HDO stretching frequencies on the RMS amplitudes of translation of H_2O and D_2O . The frequencies continued to decrease although the $\langle \Delta r^2 \rangle^{\frac{1}{2}}$ became constant at low temperatures.

From Table IV.I one sees that the RMS amplitudes of translation for H_2O and D_2O agree at low temperatures, i.e., below 10°K , quite well with those calculated by Leadbetter (84) from thermodynamic data. His data appears to be linear in temperature over the whole range, 1° to 273°K . However, the temperature dependences of our calculated $\langle \Delta r^2 \rangle^{1/2}$ are non-linear and are much smaller than his. Between 100° and 200°K his RMS amplitude increased by $5.3 \times 10^{-4} \text{ }^\circ\text{A}/\text{cm}^{-1}$ while ours increased by $1.6 \times 10^{-4} \text{ }^\circ\text{A}/\text{cm}^{-1}$. For H_2O ice I at 200°K we calculated RMS amplitudes of $0.111 \text{ }^\circ\text{A}$ while he calculated $0.185 \text{ }^\circ\text{A}$. There are probably several reasons for our low estimate, among which are neglect of translational hot bands above 50°K , neglect of two other translational modes, and the inadequacy of the free molecule theory. The contributions of the larger amplitudes of molecules in excited translational states must certainly increase drastically as the temperature approaches 200°K , with as much as 15% of the sample in excited states. The contribution of the lattice fundamental at 160 cm^{-1} to the individual molecular amplitude must be even larger than for the 229 cm^{-1} fundamental chosen above, although the apparent density of states is less.

The plot of $\langle \Delta r^2 \rangle^{1/2}$ against $R(\text{O}\cdots\text{O})$ in Fig. 4.10 showed that below 50°K our calculated RMS amplitude was constant although our calculated $\text{O}\cdots\text{O}$ distance was still decreasing. As well, below 50°K the frequencies continued to decrease. These results also support the conclusion that below 100°K factors other than $R(\text{O}\cdots\text{O})$ affected the HDO stretching frequencies.

(iii) HDO Stretch Half-Height Widths

As can be seen from Fig. 3.8, the low temperature, limiting half-height widths for $\nu_{OD}(\text{HDO})$ and $\nu_{OH}(\text{HDO})$ were 23.5 cm^{-1} and 35.5 cm^{-1} respectively. At 100°K $\Delta\nu_{OD}^{\frac{1}{2}}(\text{HDO})$ was 23.5 cm^{-1} and $\Delta\nu_{OH}^{\frac{1}{2}}(\text{HDO})$ was 35.5 cm^{-1} which compared very well with the data of Ford and Falk (100) (23.5 cm^{-1} and 33 cm^{-1} respectively) at similar temperatures. Ford and Falk (100) took great care to ensure they had very low and well known concentrations of HDO in D_2O and H_2O . For the dilute samples of HDO in H_2O and D_2O used in this work, care was taken to prevent accumulative exchange between atmospheric H_2O and D_2O liquid during handling. In our HDO in D_2O samples, exchange of D_2O with unwanted H_2O absorbed on preparative surfaces or H_2O vapour in the atmosphere enriched the concentration of HOD. The fact that our $\Delta\nu_{OH}^{\frac{1}{2}}(\text{HDO})$ was somewhat larger than Ford and Falk's (100) indicated our HDO/ D_2O concentration was more than the 4.00% intended. Our $\Delta\nu_{OH}^{\frac{1}{2}}(\text{HDO})$ was probably broader than Falk's, due to increased coupling. Our widths were still much narrower than those observed by Whalley (96), i.e. $\Delta\nu_{OH}^{\frac{1}{2}}(\text{HDO}) = 50 \text{ cm}^{-1}$ and $\Delta\nu_{OD}^{\frac{1}{2}}(\text{HDO}) = 30 \text{ cm}^{-1}$.

It is important to recognize that the coupling-broadening does not necessarily originate from HDO-HDO pairs. Since at least one HDO stretching frequency is always coupled to the host, even at low concentration, and since the ν_3 (H_2O or D_2O) bands are both very broad distributions of frequencies, then HDO may have a quite broad range of interaction energies with H_2O and D_2O neighbouring molecules. The consequent range of perturbations inflicted on the isolated HDO frequency also may be broad. Hence, as the concentration of HDO molecules increases, the group of HDO molecules will be exposed to

a wider range of perturbations giving increased $\Delta\nu^{\frac{1}{2}}$ even in the absence of HDO-HDO pairs. Clearly, the number of HDO molecules coupled to the fewer lattice molecules with stretching frequencies far down the sides of the ν_3 band (fewer than the number oscillating at the central frequency) increases as the concentration of HDO increases. The absorption by such molecules increases in importance in the total HDO absorption. Our data for $\nu_{OD}^{(HDO)}$ from 5.94% D₂O in H₂O showed good agreement since exchange with atmospheric H₂O was only very slow and tended to deplete HDO rather than increase it.

Half-height widths of stretching modes in the high pressure ices were indicated by Whalley (96) to be: $\Delta\nu_{OD}^{\frac{1}{2}} = 5 \text{ cm}^{-1}$ and $\Delta\nu_{OH}^{\frac{1}{2}} = 18 \text{ cm}^{-1}$ for ices II and III. There was obviously a dramatic change in the ice crystal in transforming between ice I and ices II or III. Whalley (96) and others (100, 105, 106) suggested a number of reasons for the observed ice band widths. The postulates can be condensed into four main mechanisms. The first mechanism was first mentioned by Hornig (106), but Bertie and Whalley (96) have described it in more detail. The mechanism suggested the band width arose from closely spaced transitions between a range of closely spaced ground state energies and corresponding closely spaced first excited states found over a mole of crystal. It was understood that any individual molecule had only one narrow ground state and first excited state, but that over the whole crystal the sets of equivalent molecules sat in sites of varying O-H····O energies. The variation of O-H····O energies arose from the variation in O····O distances prescribed at equivalent oxygen sites by disorder allowed in the proton orientations. A result of the proton orientational disorder at equivalent oxygen positions in the set of unit cells

was the loss of site symmetry. Consequently, all vibrations became a or a' and the selection rules collapsed to one general selection rule allowing transitions between all forms of combination and overtone levels. The second mechanism of stretching region broadening was through Fermi resonance of any fundamental (or the fundamental sum and difference bands with low frequency lattice modes) with other overtone and combination bands such as $2\nu_2$, $4\nu_R$, and $\nu_2 + 2\nu_R$. Notice that because of the lack of site symmetry through proton orientational disorder, Fermi resonance between any two near-degenerate levels was possible, not just between $2\nu_2$ and ν_1 as was expected from crystal site symmetry. The third mechanism invoked Heisenberg's uncertainty principle. Specifically, the energy level uncertainty, ΔE , was increased by a shortened half-life, $\Delta t^{\frac{1}{2}}$, of the upper state by either proton tunnelling to an ionized state or by resonance interaction between the excited fundamental vibration and overtones of lattice modes giving the ground state, fundamental internal mode and excited lattice vibrations. Both proton tunnelling and ejection from the excited vibration to nearby upper lattice modes constituted radiationless transitions. The fourth mechanism of broadening was through the occurrence about the fundamental of sum and difference bands of the fundamental with low frequency translational lattice modes and the occurrence of nearby hot lattice modes.

The fact that neither $\Delta\nu_{OD}^{\frac{1}{2}}(\text{HDO})$ nor $\Delta\nu_{OH}^{\frac{1}{2}}(\text{HDO})$ underwent a smooth, continuous decrease at temperatures below 100°K shows that the mechanisms of hot bands and difference bands as sources of broadening are not significant. If the observed stretching modes were broadened by difference and hot bands involving lattice modes, then the stretching modes should have undergone significant sharpening once the higher lattice energy levels were

depopulated at low temperatures: The stretching modes were not significantly sharpened as far down as 10°K. A simple calculation of the ratios of numbers of molecules in the ground, 1st, 2nd and 3rd excited states for ν_T ($= 229 \text{ cm}^{-1}$) and ν_R ($= 832 \text{ cm}^{-1}$) showed that at 10°K all upper levels were effectively depopulated. These observations removed mechanism four from consideration as a source of broadening.

The observed "freeze-in" of half-height width supported mechanism one, the proton orientational disorder mechanism. For that mechanism, as the sample was cooled and the lattice contracted, the mean deviation from the ideal symmetry site of the oxygen atoms decreased. Since the mean deviation of $\text{O} \cdots \text{O}$ distances was also a measure of the range of hydrogen bond energies and the range of stretching frequencies, then as $R(\text{O} \cdots \text{O})$ decreased and $\langle \Delta r^2 \rangle^{1/2}$ decreased so should the stretching band width. Once the $\text{O} \cdots \text{O}$ distances were invariant, so was the half-height width.

A further modification to the stretching mode of dilute HDO molecules in a parent lattice was in lattice coupling. Ideally one wanted to compare the uncoupled OH stretch to the coupled OH stretch in identical crystal fields or lattice environments. At best one compared uncoupled, but perturbed OH stretch to coupled OH stretch in identical electron distributions. However, the periodic modulation of the electrons by lattice modes was different for the two cases. The conclusion is that if the stretching modes were broadened by lattice modes then the effect of broadening of OH(HDO) stretch by the D_2O lattice was different than the broadening of OH(H_2O) stretch by the H_2O lattice since H_2O and D_2O have different lattice fundamental frequencies and amplitudes.

The half-height widths had a near-linear temperature dependence of $13.5 \times 10^{-2} \text{ cm}^{-1}/^{\circ}\text{K}$ for $\nu_{\text{OH}}(\text{HDO})$ and $7.0 \times 10^{-2} \text{ cm}^{-1}/^{\circ}\text{K}$ for $\nu_{\text{OD}}(\text{HDO})$ in the high temperature range from 100° to 190°K . Those data compare well with our interpretation of the data of Ford and Falk (100) in the temperature range 100° to 200°K , $\Delta\nu_{\text{OH}}^{\frac{1}{2}}(\text{HDO})$ changed by $4.5 \times 10^{-2} \text{ cm}^{-1}/^{\circ}\text{K}$. In the temperature range from 100° to 273°K we deduced from Falk's data that the slope of $\Delta\nu_{\text{OH}}^{\frac{1}{2}}(\text{HDO}) = 16.2 \times 10^{-2} \text{ cm}^{-1}/^{\circ}\text{K}$ and of $\Delta\nu_{\text{OD}}^{\frac{1}{2}}(\text{HDO}) = 10.7 (10^{-2}) \text{ cm}^{-1}/^{\circ}\text{K}$. Our experimental data lie within their results, and our scatter of data is significantly lower than theirs.

(iv) Dependence of HDO Peak Heights on Temperature

The HDO stretching mode peak heights (I) and half-height widths were used to approximate the area of $\nu_{\text{OH}}(\text{HDO})$ as a function of temperature. Simple triangles were constructed which had heights equal to the peak height on a linear absorbance scale and a base at $1/2$ of $\frac{1}{2}(\Delta\nu^{\frac{1}{2}})$. The area of two such triangles, extended to the baseline, was assumed to represent the integrated intensity (A) approximately. Typical results are given below:

Temperature $^{\circ}\text{K}$	$\Delta\nu^{\frac{1}{2}}$ cm^{-1}	I absorbance	A cm^2
10	35.5	0.94	133.5
50	35.5	0.92	130.6
100	36.5	0.85	124.1
150	39.7	0.72	114.5
180	42.5	0.60	103.2

The slow, smooth decrease in $\nu_{\text{OH}}(\text{HDO})$ peak height seems to predominate in the decreased band area and is consistent with the concept of a weakening hydrogen bond and a decrease in molecular dipole with increasing $R(\text{O}....)$ as temperature increases.

Above 190°K the samples sublimed rapidly and presumably a small amount of the original decrease was due to cumulative sample loss by sublimation. A slightly concave portion of the I ($\nu_{\text{OD}}(\text{HDO})$) between 110° and 140°K indicated first a more rapid and then a less rapid decrease in hydrogen bond energy. Some unusual heat capacity effects were noticed near 110°K (82), but it is not certain that the effects are related.

B. Dependence of H₂O and D₂O Bands on Temperature

(i) Fundamental Lattice Mode Temperature Dependences

(a) The H₂O translational mode. Cubic ice I (Fd3m) has two molecules per unit cell which provide six translational modes, of which three are zero frequency translations of the whole finite crystal. Whalley and Bertie (87, 88) developed a theory for hexagonal and cubic ice I which incorporates proton orientational disorder in the description of ν_T . They deduced from an approximate density of states relation that points of inflection, minima and shoulders, as well as peaks, are associated with specific branches of the optical and acoustical modes. The lattice modes of hexagonal ice I were also observed by neutron inelastic scattering (92, 93). Our observed $\nu_T(\text{H}_2\text{O})$ structural absorption features were given in Table III.IXb along with some previous results (88, 92, 93). The poor definition of the absorption features (other than the 229 cm⁻¹ peak maximum) made it impossible to follow their temperature dependences. The features recorded here at 83°K agreed with the null results of Bertie and Whalley (88) and the condensation results of Giguere and Arraudeau (89). The lowest temperature indicated by the (Au-Co) / (Ag-Au) thermocouple for this experiment was 25°K, probably due to some solidified N₂ (l) used to precool the helium dewar.

The low temperature (25°K) limiting values of the ν_T features exhibited no special behaviour. From 25° to 70°K the ν_T maximum underwent a stage of invariant frequency up to $55 \pm 5^\circ\text{K}$, and an apparent shift by 2 cm⁻¹ to lower frequency between $55 \pm 5^\circ$ and $70 \pm 5^\circ\text{K}$. From 70° to 90°K ν_T was relatively constant in frequency, while above 90°K ν_T had a con-

tinuous, near linear shift towards lower frequency of $-0.093 \text{ cm}^{-1}/^{\circ}\text{K}$. Above 160°K ν_{T} (max.) remained constant at $221 \pm 0.5 \text{ cm}^{-1}$. In comparison, Zimmermann and Pimentel's (97) data indicated a slope of $-0.081 \text{ cm}^{-1}/^{\circ}\text{K}$ from 90°K to 250°K . The dependence (rate of change) of ν_{T} on the hydrogen bond energy was less than for the molecular modes, i.e. a given change in hydrogen bond energy had 0.5 to 0.3 times the effect on ν_{T} as it did on ν_{R} or the molecular modes. The sensitivity (minimum detectable change) of ν_{T} to hydrogen bond energy changes was the same as for ν_{R} , ν_1 , ν_2 and ν_3 , i.e. sensitive to changes of $\pm 0.0001 \text{ }^{\circ}\text{A}/^{\circ}\text{K}$ in $\text{R}(\text{O}\cdots\text{O})$.

The origin of the sharp shift near 55°K is unknown, but it may have arisen from a change in the crystal structure (and hence the unit cell and Brillouin zone), or a change in proton ordering. A similar effect was observed for HDO stretching modes and it was correlated to the predicted (70) ordering near 70°K .

(b) The H_2O and D_2O librations. The low temperature limiting $\nu_{\text{R}}(\text{H}_2\text{O})$ frequency (832 cm^{-1}) and $\nu_{\text{R}}(\text{D}_2\text{O})$ frequency (630 cm^{-1}) exhibited no special behaviour attributable to excited state depopulation, ordering of protons, or decreased anharmonicity. From 42° to $70 \pm 10^{\circ}\text{K}$ the frequency scatter of data points was large, $\pm 5 \text{ cm}^{-1}$ for $\nu_{\text{R}}(\text{H}_2\text{O})$ and $\pm 3 \text{ cm}^{-1}$ for $\nu_{\text{R}}(\text{D}_2\text{O})$ (Fig. 3.13). Within these frequency limits the absorption maximum was constant. The freeze-in temperature for $\nu_{\text{R}}(\text{H}_2\text{O})$ and $\nu_{\text{R}}(\text{D}_2\text{O})$ was $70 \pm 10^{\circ}\text{K}$ and agreed with other H_2O and D_2O bands but did not conform to our more precise measurements on HDO peaks. The sensitivity of $\nu_{\text{R}}(\text{H}_2\text{O}$ and $\text{D}_2\text{O})$ to changed hydrogen bond energy through $\Delta\text{R}(\text{O}\cdots\text{O})$ was larger than HDO, i.e.

$> 0.0001 \text{ Å}/^\circ\text{K}$. Between 70°K and 180°K $\nu_R(\text{H}_2\text{O}$ and $\text{D}_2\text{O})$ exhibited linear temperature dependences of $-0.18 \text{ cm}^{-1}/^\circ\text{K}$ and $-0.11 \text{ cm}^{-1}/^\circ\text{K}$ respectively. Again the frequency scatter of points was large and a curvilinear dependence may be true, as was indicated for $\nu_R(\text{HDO})$ (Fig. 3.7). Liquid nitrogen and liquid helium cell data agreed in their overlap region for $\nu_R(\text{H}_2\text{O})$. Zimmermann and Pimentel's (97) data for $\nu_R(\text{H}_2\text{O})$ indicated a slightly curvilinear temperature dependence of about $-0.22 \text{ cm}^{-1}/^\circ\text{K}$. Their points were approximately 10 cm^{-1} higher in frequency than ours: They chose the band center and ignored any ν_R band structure (indicated in their spectra). Details of the origins, possible theoretical treatments, and the nature of the ν_R modes will be given in section 4.4.

(ii) Fundamental Molecular Mode Temperature Dependences

(a) The ν_1 and ν_3 stretching modes. The low temperature limiting frequencies for ν_1 and ν_3 of H_2O and D_2O were 3133 (2320) cm^{-1} and 3204 (2413) cm^{-1} respectively. As for HDO that extrapolation to 0°K may not have been valid, but the thermodynamic data was regular down to 2°K (83). The effects of proton ordering should not be seen since the time for such a process is very long below 60°K (70). As well, translational, librational and vibrational excited levels are all depopulated at 5°K : Further effects from depopulation should have been negligible. Also, nuclear spin and electron spin perturbations (i.e. as in ortho-para hydrogen) were expected to be very small. No changes in hydrogen bonding were expected since the lattice was no longer contracting.

From 4.2°K to 60°K , ν_1 and ν_3 (H_2O and D_2O) absorptions were invariant within the errors of measurement. Over that temperature range the crystal

expanded very slowly, less than $0.0001 \text{ Å}/^\circ\text{K}$. Accompanying changes in $R(0\cdots 0)$ and ν_1 or ν_3 were too small to be detected by this ir absorption technique. The large frequency scatter in points was pre-determined by the uncertainty in peak and shoulder positions. The $\nu_3(\text{H}_2\text{O})$ data from liquid helium and nitrogen cells did not completely agree (Fig. 3.10). Liquid nitrogen cell data indicated a "freeze-in" frequency near 3215 cm^{-1} . Liquid helium cell data indicated a "freeze-in" frequency near 3204 cm^{-1} . The data were collected during warm-up from 77°K and 4.2°K respectively. The discrepancy may be explained if the ν_3 absorption peak underwent a type of "hysteresis" during cooling from 77°K to 4.2°K , frequency shift lagged behind temperature decrease. Since the samples were always held at 4.2°K for three hours, sufficient time may have been given for completion of the hysteresis loop before warm-up observations began: Observations of ν_3 frequency shift during a cooling cycle are required to test that possibility. Data from the same two cells for $\nu_1(\text{H}_2\text{O})$ (Fig. 3.11) also suggested hysteresis although the separation of points was not as well defined. Only the results from the liquid helium cell were obtained for ν_1 and ν_3 of D_2O .

Above 60°K the ν_1 and ν_3 modes underwent regular shifts to the progressively higher frequencies associated with progressively decreased hydrogen bond strengths. The explanation follows that of $\nu_{\text{OH}}(\text{HDO})$.

The ir high temperature dependences of ν_1 and ν_3 for cubic ice I agree with the Raman observations of Val'kov and Maslenkova (90). The Raman and ir ν_3 (H_2O and D_2O) observations concurred directly. However, the ν_1 (H_2O and D_2O) Raman observations were all shifted (by 55 and 32 cm^{-1} respectively) to lower frequency than the ir observations. By adding a constant value of 55 cm^{-1} to the $\nu_1(\text{H}_2\text{O})$ and of 32 cm^{-1} to the $\nu_1(\text{D}_2\text{O})$

Raman data at all temperatures, then the Raman and ir data agreed. The following temperature dependences were observed by Val'kov and Maslenkova (90):

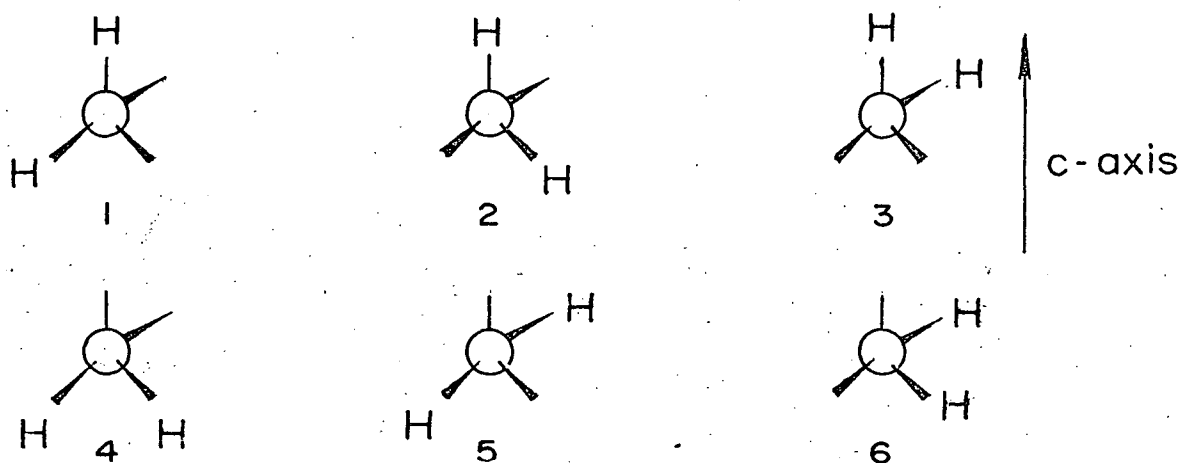
		Raman cm ⁻¹ /°K	IR cm ⁻¹ /°K
H ₂ O	$\frac{\Delta v_1}{\Delta T}$	0.254	0.26
	$\frac{\Delta v_3}{\Delta T}$	0.246	0.24
	$\frac{\Delta(v_1 + v_T)}{\Delta T}$	0.222	0.20
D ₂ O	$\frac{\Delta v_3}{\Delta T}$	0.198	0.22
	$\frac{\Delta v_1}{\Delta T}$	0.143	0.14

$$\Delta T = 203 - 77^\circ\text{K} = 126^\circ\text{K}.$$

The equivalence of Raman and IR temperature dependences for v_1 and v_3 shows that the hydrogen bond coupling of neighbours was independent of the applied electromagnetic radiation.

There is a potentially interesting extension of these cubic ice I temperature dependences to hexagonal ice I. It is known that the linear thermal expansion coefficients of hexagonal ice I are not equal (60) and that the O····O distances parallel and non-parallel to the c-axis are not equal, Fig. 4.3. Hence, the temperature dependences of $R(O\cdots O)_c$, i.e. parallel to the c-axis, and $R(O\cdots O)_a$ are not equal and the single crystal spectra of the ac face of hexagonal ice I, polarized parallel and perpen-

pendicular to the c-axis, should be distinguishable. For example, consider the six possible arrangements of the four protons about any one oxygen atom in hexagonal ice,



Then the three arrangements 4,5 and 6 have both protons along the shorter $O \cdots O$ distances and will give one band of frequencies. The 1,2 and 3 arrangements, however, have asymmetric O-H bond lengths leading to a distorted potential and frequencies distinct from cases 4,5 and 6. The frequencies observed parallel to the c-axis should be intermediate between those observed perpendicular to c and those expected if both protons had the $R(O \cdots O)$ along c.

One can predict the values and temperature dependences for $\nu_3(\text{H}_2\text{O})$ and D_2O) of O-H stretches parallel and non-parallel to the hexagonal c-axis. From the temperature dependences of $\nu_3(\text{H}_2\text{O})$ and $\nu_3(\text{D}_2\text{O})$ (Fig. 3.10) and the temperature dependence of $R(\text{O}^{\cdots}\text{O})$ in cubic ice I (Fig. 4.3), one can determine the $R(\text{O}^{\cdots}\text{O}) - \nu_3$ correlations for H_2O and D_2O , Fig. 4.12. Then knowing the hexagonal $R(\text{O}^{\cdots}\text{O})_c$ and $R(\text{O}^{\cdots}\text{O})_a$ parameters as a function of temperature one can obtain a set of $\nu_3(\text{H}_2\text{O})$ and $\nu_3(\text{D}_2\text{O})$ frequencies parallel and non-parallel to the c-axis, Fig. 4.13.

For $\nu_3(\text{H}_2\text{O})$ of hexagonal ice one sees that at 150°K the asymmetric stretching frequencies would be 3214 and 3229 cm^{-1} parallel and non-parallel to the c-axis, while at 100°K the values would be 3202 and 3225 cm^{-1} . Similarly for $\nu_3(\text{D}_2\text{O})$ the 150°K values are 2417 and 2429 cm^{-1} , and the 100°K values are 2411 and 2425 cm^{-1} . Ockman (108) was not able to detect the differences at 139°K probably because of the breadth of the bands, i.e. because $\Delta\nu_3$ is probably greater than 100 cm^{-1} , and because of the relatively small split between the bands.

In contrast the bands due to dilute concentrations of HDO in H_2O or D_2O are narrower and absorptions parallel and non-parallel to the hexagonal c-axis should be separable. Sets or predicted $\nu_{\text{OH}}(\text{HDO})$ and $\nu_{\text{OD}}(\text{HDO})$ frequencies in the two directions were determined as above (i.e. from Figs. 3.6 and 4.3) and are plotted in Fig. 4.14. Thus at 150°K $\nu_{\text{OH}}(\text{HDO})$ along a and a should be separated by 16 cm^{-1} and at 100°K by 26 cm^{-1} , while $\nu_{\text{OD}}(\text{HDO})$ along c and a would be separated by 11 cm^{-1} and 18 cm^{-1} respectively. Accurate measurement of the differences in the a and c temperature dependences

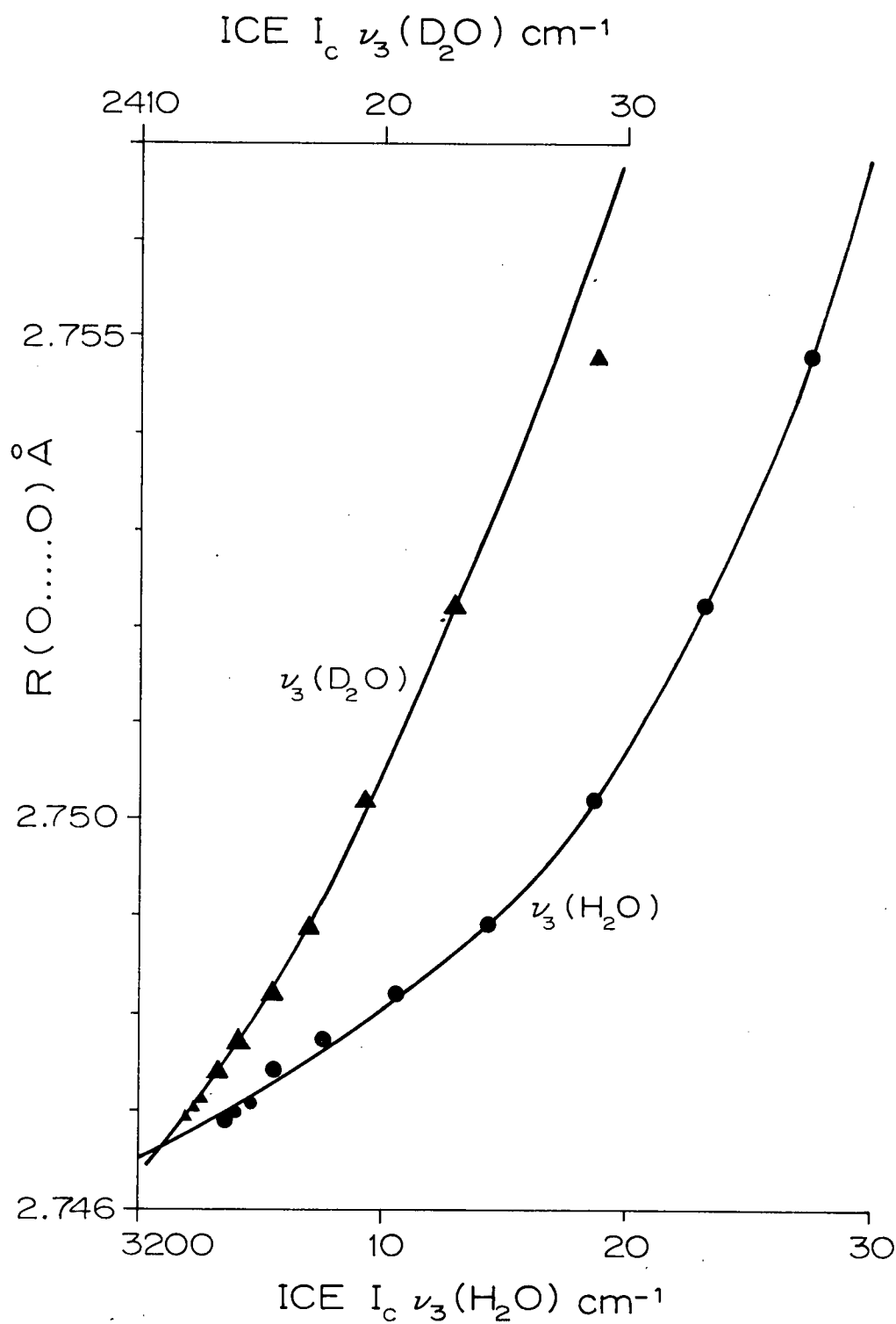


Fig. 4.12 The correlations of ν_3 of H_2O and D_2O to the $O \cdots O$ distances as a function of common temperature. The frequency data were uncorrected for source beam heating.

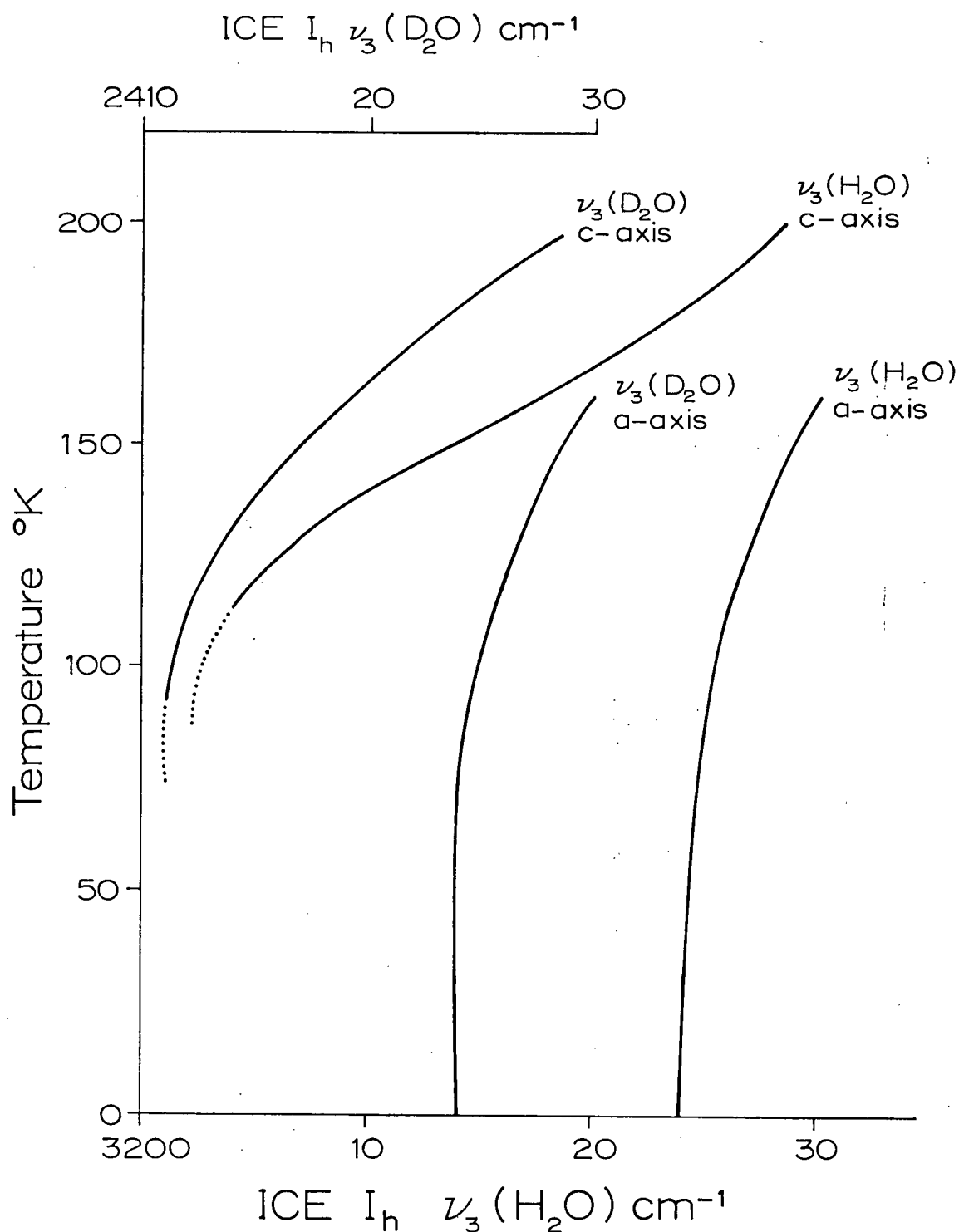


Fig. 4.13 The calculated ν_3 frequencies of H₂O and D₂O in hexagonal ice I along the c and a axis as a function of temperature.

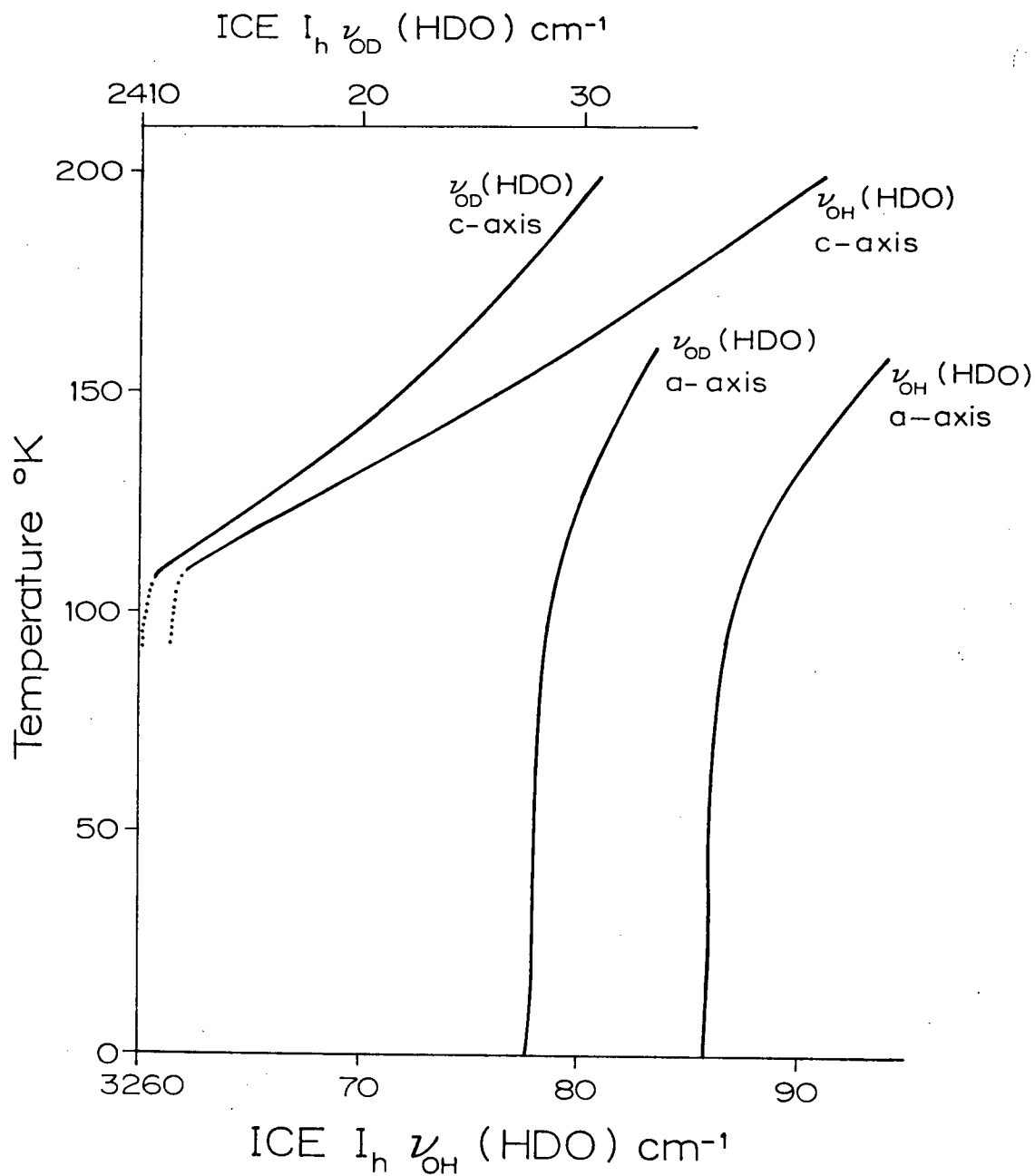


Fig. 4.14 The calculated $\nu_{OH}(\text{HDO})$ and $\nu_{OD}(\text{HDO})$ frequencies for HDO in hexagonal ice I and along the c and a axis as a function of temperature.

should yield valuable information on the anisotropic deformation of the hydrogen bond in hexagonal ice I.

(b) The ν_2 bending mode. Absorptions near 1600 cm^{-1} and 1200 cm^{-1} in cubic ice I (H_2O and D_2O) were very near the corresponding vapour phase ν_2 fundamental absorptions of 1595 cm^{-1} and 1179 cm^{-1} respectively. Doubts arose in the previous literature assignments (Tables III.XI and III.XIII) of these ice frequencies to either ν_2 or $2\nu_R$, which should nearly coincide. In fact, these absorptions in ice appear to be composite overlapping ν_2 and $2\nu_R$ peaks as was previously described (page 112). The inconsistency between the liquid helium and liquid nitrogen cell ν_2 data (Fig. 3.12) may have arisen from a temperature hysteresis, *i.e.* the lagging of frequency shift behind the temperature drop during cooling. Zimmermann and Pimentel's (97) results (Fig. 3.12) tend to discount that possibility for $\nu_2(\text{H}_2\text{O})$. Their results from liquid nitrogen experiments agree with the present results from liquid helium experiments. Much of the disparity in the present results probably arose from reference beam uncompensation for the liquid nitrogen cell data. The strong atmospheric water vapour absorption below 1595 cm^{-1} and above 1615 cm^{-1} may have distorted the $\nu_2(\text{H}_2\text{O})$ ice band severely, while a gap in the vapour spectrum between 1595 and 1615 cm^{-1} may have presented an artificial $\nu_2(\text{H}_2\text{O})$ ice maximum. However, such a maximum would be independent of the ice sample temperature.

For $\nu_2(\text{H}_2\text{O})$ the liquid nitrogen cell data indicated a low temperature limiting frequency of 1605 cm^{-1} , while the liquid helium cell data indicated a low temperature limiting ν_2 frequency of 1560 cm^{-1} : Zimmermann and Pimentel's data were extrapolated to near 1570 cm^{-1} . Whalley (96) found the ν_2 maxima in high pressure H_2O ices were above 1680 cm^{-1} and

argued that $\nu_2(\text{ice}) > \nu_2(\text{vapour})$. However, $2\nu_R$ may be more intense than ν_2 in these cases. Whalley's (96) ν_2 frequency for cubic and hexagonal ice I at 110°K in an isopentane mull was more than 25 cm^{-1} higher than observed here, or by Ockman (108) ($\nu_2 = 1580 \text{ cm}^{-1}$) and Hornig (106) ($\nu_2 = 1585 \text{ cm}^{-1}$). The reflectivities of Whalley's (95,96) mulled samples may have been significantly different than for our condensed samples leading to his higher apparent maxima. However, Ockman found only a small (0.5%) increase in the one percent general reflectivity of crystalline ice over the range 1500 cm^{-1} to 1700 cm^{-1} , the maximum reflectivity was at 1575 cm^{-1} at 110°K. It is also possible that sample formation by vapour condensation accentuated the reflectivity, creating an artificial low frequency maximum in our results.

For D_2O the liquid helium cell data indicated a low temperature limiting ν_2 frequency of 1189 cm^{-1} , however the D_2O liquid nitrogen cell experiments were not attempted. The region near 1200 cm^{-1} was free from atmospheric H_2O vapour attenuations and the recorded D_2O spectrum was free of atmospheric absorption distortions. The D_2O observation of 1189 cm^{-1} is greater than the D_2O vapour frequency, 1179 cm^{-1} . In contrast, Hornig (106) and Ockman (108) observed $\nu_2(\text{D}_2\text{O})$ to be even higher, i.e. near 1210 cm^{-1} at $100 \pm 10^\circ\text{K}$. These D_2O results were contrary to our $\nu_2(\text{H}_2\text{O})$ helium data as well as the nitrogen data of others, as noted above. Possibly in D_2O the relative positions of $2\nu_R$ and ν_2 are altered from that of H_2O , giving a different peak maximum relative to the vapour.

Maximum $\nu_2/2\nu_R(\text{H}_2\text{O})$ absorption was constant over the temperature range 5°K to $70 \pm 10^\circ\text{K}$, while maximum $\nu_2/2\nu_R(\text{D}_2\text{O})$ absorption was constant

over the temperature range 5°K to $50 \pm 10^{\circ}\text{K}$. The low D_2O "freeze-in" temperature of 50°K was probably due to insufficient data. The cubic ice $\text{I } \nu_2/2\nu_{\text{R}}$ band exhibited the same dependence as the stretching modes in this low temperature range, constancy within $\pm 8 \text{ cm}^{-1}$. As a check on hysteresis in this temperature range, detailed observations should be made during fast and slow cooling, *i.e.* cooling in 10 - 20 min. and 150 - 200 min. respectively. The $\nu_2/2\nu_{\text{R}}$ absorption also exhibited the same sensitivity to changes in hydrogen bond length (energy) as did the stretching modes, *i.e.* it was sensitive to changes in $\text{R}(\text{O}\cdots\text{O})$ greater than $0.0001 \text{ \AA}/^{\circ}\text{K}$.

The question of whether $\nu_2(\text{ice})$ is less than or greater than ν_2 (vapour) is still unanswered. If the $\nu_2/2\nu_{\text{R}}(\text{D}_2\text{O})$ absorption maximum was due to more intense ν_2 transitions then $\nu_2 \text{ ice} > \nu_2 \text{ vapour}$. If $2\nu_{\text{R}}(\text{D}_2\text{O})$ was the more intense transition then $2\nu_{\text{R}}(\text{D}_2\text{O}) \text{ ice} > \nu_2(\text{D}_2\text{O}) \text{ vapour}$ and $\nu_2(\text{D}_2\text{O}) \text{ ice}$ may be less than $\nu_2 \text{ vapour}$. Positive high temperature dependence indicated the peak maximum was ν_2 and not $2\nu_{\text{R}}$, since ν_{R} (and presumably $2\nu_{\text{R}}$) had a negative frequency temperature dependence. The temperature dependence of the $\nu_2/2\nu_{\text{R}}$ H_2O absorption was also positive for either liquid helium or liquid nitrogen data. The maximum of absorption must then be $\nu_2(\text{H}_2\text{O})$ and $2\nu_{\text{R}}$ must be masked. Whether $\nu_2(\text{H}_2\text{O}) \text{ ice}$ was greater than or less than $\nu_2(\text{H}_2\text{O}) \text{ vapour}$ could not be unambiguously determined.

Maximum $\nu_2/2\nu_{\text{R}}(\text{H}_2\text{O}$ and $\text{D}_2\text{O})$ absorptions had approximately linear, positive temperature dependences of $0.37 \text{ cm}^{-1}/^{\circ}\text{K}$ and $0.15 \text{ cm}^{-1}/^{\circ}\text{K}$ respectively over the temperature range from 60° to 180°K . In contrast the H_2O data of Zimmermann and Pimentel (97) indicated a slope of $0.281 \text{ cm}^{-1}/^{\circ}\text{K}$

in the range from 90°K to 253°K. The relatively small temperature dependence of $\nu_2/2\nu_R(\text{D}_2\text{O})$ may have resulted from the closer coincidence of $\nu_2(\text{D}_2\text{O})$ and $2\nu_R(\text{D}_2\text{O})$ than in H_2O . If the H_2O and D_2O bands had the same structure then their temperature dependences should have been simply related since their changes in $R(0\cdots 0)$ were nearly the same.

(iii) The Combination and Overtone Mode Temperature Dependences

(a) The $3\nu_R$ or $(\nu_2 + \nu_R)$ mode. Broad weak absorptions near 2235 cm^{-1} and 1635 cm^{-1} in H_2O and D_2O cubic ice I exhibited temperature dependences of $-0.14 \text{ cm}^{-1}/^\circ\text{K}$ and $-0.15 \text{ cm}^{-1}/^\circ\text{K}$ respectively over the temperature range from 30° to 180°K. Both the H_2O and D_2O bands were less than one-half as intense as their corresponding $\nu_2/2\nu_R$ bands. First consider the H_2O ice absorption at 2238 cm^{-1} . If the absorption arose from a $\nu_2 + \nu_R$ transition then the temperature dependence should have been positive, i.e. $\Delta\nu_R/\Delta T = -0.17 \text{ cm}^{-1}/^\circ\text{K}$ and $\Delta\nu_2/\Delta T = +0.36 \text{ cm}^{-1}/^\circ\text{K}$, therefore $(\Delta\nu_2 + \Delta\nu_R)/T = +0.19 \text{ cm}^{-1}/^\circ\text{K}$. However, the temperature dependence was observed to be negative. If the absorption arose from a $3\nu_R$ transition then the temperature dependence should have been negative, i.e. $\Delta(3\nu_R)/\Delta T = -0.51 \text{ cm}^{-1}/^\circ\text{K}$. As was seen in Fig. 3.17, Pimentel's data (97) agrees well with ours, his slope was $-0.12 \text{ cm}^{-1}/^\circ\text{K}$ compared to our measured value of $-0.15 \text{ cm}^{-1}/^\circ\text{K}$. The measured $\Delta(3\nu_R)/T = -0.15 \text{ cm}^{-1}/^\circ\text{K}$ was nearly the same as $\Delta\nu_R/\Delta T = -0.17 \text{ cm}^{-1}/^\circ\text{K}$ and one-third the predicted rate of $-0.51 \text{ cm}^{-1}/^\circ\text{K}$. Anharmonicity increases from the larger amplitudes at increased temperature could not be the source of this result.

Either the 2235 cm^{-1} H_2O absorption was a ν_R fundamental, or the $3\nu_R$ anharmonicity was decreasing with increased temperature, or energy level population redistribution was affecting the results. Such a high

frequency fundamental lattice mode seems unlikely, as do such large effects from populational redistribution. Alternately decreased anharmonicity of $3\nu_R$ and ν_R from decreased hydrogen bond energy may be larger than the increased anharmonicity arising from increased amplitude of libration at higher temperatures.

Consider the D_2O absorption at 1637 cm^{-1} where the same considerations apply as for H_2O . Absorption arising from $D_2O(\nu_2 + \nu_R)$ transitions would exhibit zero temperature dependence; $\Delta(\nu_2 + \nu_R)/\Delta T = (\Delta\nu_2/\Delta T) + (\Delta\nu_R/\Delta T)$ ^{obs.} ^{obs.}
 $= +0.15\text{ cm}^{-1}/^\circ\text{K} - 0.15\text{ cm}^{-1}/^\circ\text{K} = 0$. The temperature dependence was observed to be distinctly negative, $-0.15\text{ cm}^{-1}/^\circ\text{K}$. In fact $\nu_R(D_2O)$ and the 1637 cm^{-1} D_2O band had the same observed temperature dependences.

Low temperature limiting $3\nu_R$ absorption was 2235 cm^{-1} for H_2O and 1635 cm^{-1} for D_2O . That implied an approximate H_2O low temperature limiting anharmonicity for $3\nu_R(H_2O)$ (from $\nu_R = 833\text{ cm}^{-1}$) of -258 cm^{-1} and for $3\nu_R(D_2O)$ (from $\nu_R = 627\text{ cm}^{-1}$) of -253 cm^{-1} . The apparent H_2O and D_2O $3\nu_R$ anharmonicities were nearly equal. Now the parent transitions underwent considerable isotopic shift: $\nu_R(H_2O) = 833\text{ cm}^{-1}$ and $\nu_R(D_2O) = 627\text{ cm}^{-1}$. The H_2O anharmonicity of -258 cm^{-1} represented 11.5 percent of the observed absorption band frequency, 2235 cm^{-1} . The increased D_2O percent anharmonicity was unexpected for the mass substitution made. For example, in the vapour phase the anharmonicity of H_2O ($x_{11} = -43.8\text{ cm}^{-1}$, $x_{22} = -19.5\text{ cm}^{-1}$, $x_{33} = -46.4\text{ cm}^{-1}$) is almost halved in D_2O ($x_{11} = -22.8\text{ cm}^{-1}$, $x_{22} = -10.44\text{ cm}^{-1}$, $x_{33} = -24.9\text{ cm}^{-1}$) for ν_1 , ν_2 , and ν_3 (124), since the amplitudes of D_2O motion are smaller. Similar behaviour was expected for the solid, but the observed $3\nu_R(D_2O)$ anharmonicity was not one-half that of $3\nu_R(H_2O)$. Thus the large shifts of $3\nu_R$ below the expected frequencies cannot be simply

explained as anharmonicities.

The large shifts of $3\nu_R(\text{H}_2\text{O}, \text{D}_2\text{O})$ below the expected frequencies ($3\nu_R$ observed = 2235 cm^{-1} , $3(\nu_R) = 3(833) = 2499 \text{ cm}^{-1}$) may arise from different maximum transition moments for the band of ground state librational energies for the ν_R and $3\nu_R$ transitions. The extreme case is: molecules occupying the higher energies of the band have maximum transition moments for $(0 \rightarrow 1)$ transitions and minimum transition moments for $(0 \rightarrow 3)$ transitions, while molecules occupying the lower energies of the band have minimum transition moments for $(0 \rightarrow 1)$ transitions and maximum transition moments for $(0 \rightarrow 3)$ transitions. The maximum of the $(0 \rightarrow 1)$ ν_R transition would occur above the center of the energy band and the maximum of the $(0 \rightarrow 3)$ ν_R transition would occur below the center of the energy band. In support of this recall that the ν_R absorption had a $\Delta\nu_R^{1/2}$ of about 125 cm^{-1} , indicating a very large librational energy range.

Data on $3\nu_R$ from spectra recorded during warm-up from 5°K to 60°K showed that the $3\nu_R$ energy level had the same sensitivity to hydrogen-bond changes as the internal modes, i.e. it was insensitive to changes in hydrogen-bond energy from changes in $\text{R}(\text{O}\cdots\text{O})$ that were less than $0.0001 \text{ Å}/^\circ\text{K}$. Data from the liquid nitrogen and liquid helium cells agreed satisfactorily. The $3\nu_R$ freeze-in temperatures for H_2O and D_2O , $70 \pm 10^\circ\text{K}$, concurred with previous data.

(b) The $(\nu_1 + \nu_T)$ band. The high frequency shoulder on the cubic ice I stretching band had low temperature limits of 3334 and 2464 cm^{-1} for H_2O and D_2O respectively (Table III.IX). Those frequencies are 201 and 144 cm^{-1} higher than the low temperature limiting low frequency shoulders at 3133 and 2320 cm^{-1} respectively. The high temperature dependences of the high frequency shoulders were 0.20 and $0.17 \text{ cm}^{-1}/^\circ\text{K}$, compared

to 0.34 and $0.19 \text{ cm}^{-1}/^{\circ}\text{K}$ for the low frequency shoulders (Table III.IX). If the high frequency shoulders are in fact due to $(\nu_1 + \nu_T)$ transitions then the ν_1 to $(\nu_1 + \nu_T)$ displacement should have been 229 cm^{-1} (observed 201 cm^{-1}) for H_2O and the temperature dependence of $(\nu_1 + \nu_T)$ of H_2O should have been approximately $(\Delta\nu_1/\Delta T) + (\Delta(\nu_1 + \nu_T)/\Delta T)$ or $(0.34 - 0.10) \text{ cm}^{-1}/^{\circ}\text{K}$. That value of $0.24 \text{ cm}^{-1}/^{\circ}\text{K}$ agrees well with the observed $\nu_1 + \nu_T$ value of $0.20 \text{ cm}^{-1}/^{\circ}\text{K}$. For D_2O the high frequency shoulder appears to be composed of $\nu_1(\text{D}_2\text{O})$ and the LA translational mode near 160 cm^{-1} . The temperature dependence of $\nu_T(\text{D}_2\text{O})$ is not known however.

(iv) The Half-Height Widths Temperature Dependences

The temperature dependence of the composite stretching region band half-height width was positive (page 66), as expected. There appear to be two sources of the increasing width. One obvious effect common to all the modes was the increase in the amplitudes of vibration. A second source of broadening arose from increasing $\text{R}(\text{O}\cdots\text{O})$: The increasing range of $\text{O}\cdots\text{O}$ distances gave a larger range of hydrogen bond energies and a broader range of possible transitions. Above 160°K (Fig. 3.4) the $\Delta(\nu_1, \nu_3, \nu_1 + \nu_T)^{1/2}$ data are not reliable since sample sublimation had a pronounced effect.

The observed temperature dependence of $\Delta(\nu_R, \nu_R + \nu_T)^{1/2}$ (Fig. 3.4) may have been anomalous. The scatter of data points was nearly as large as the range of points between 10°K and 200°K : The high temperature data was just outside the error limits of the low temperature data. As well, the temperature dependence of $\Delta(\nu_R, \nu_R + \nu_T)^{1/2}$ seems to be too small. It would be interesting to study the origin of ν_R in the solid, liquid and

vapour phases about the triple point as well as the origin of ν_R as the critical point is approached from the vapour phase.

The temperature of $\Delta(\nu_2, 2\nu_R)^{\frac{1}{2}}$ (Fig. 3.5) was opposite to that of $\Delta(\nu_R, \nu_R + \nu_T)^{\frac{1}{2}}$ and $\Delta(\nu_1, \nu_3, \nu_1 + \nu_T)^{\frac{1}{2}}$ in the amorphous and cubic ice I phases. An explanation was given in section 4.1C(i) (page 111).

4.3 Assignments of the Cubic Ice I Absorption Bands

A. The Fundamental Lattice Modes

(i) The Translational Modes

Two peaks (162 and 227.8 cm^{-1}) and three shoulders (191, 267 and 296 cm^{-1}) were observed at 93°K for H_2O cubic ice I. The features of the band differed only slightly from those of Bertie and Whalley (88). In this work no calculations were made which disagreed with the assignments of Bertie and Whalley.

(ii) The Librational Modes

The low temperature limiting frequencies of the observed librations are in the ratio, $\nu_R/(\nu_R + \nu_T) = 0.963$. That compares to the same ratios in H_2O and D_2O of 0.9444 and 0.953 respectively. The peak to shoulder separations at 10°K were:

$$\begin{aligned} [(\nu_R + \nu_T) - \nu_R]_{\text{H}_2\text{O}} &= 50 \pm 5 \text{ cm}^{-1} \\ [(\nu_R + \nu_T) - \nu_R]_{\text{HDO}} &= 33 \pm 1.5 \text{ cm}^{-1} \\ [(\nu_R + \nu_T) - \nu_R]_{\text{D}_2\text{O}} &= 31 \pm 5 \text{ cm}^{-1} \end{aligned}$$

If the shoulder did arise by a combination transition of $\nu_R(\text{HDO})$ and $\nu_T(\text{host})$, then the value of ν_T to apply to HDO is that of the host D_2O since at a concentration of 4.0% HDO in D_2O the lattice dynamics must surely be dominated by the D_2O molecules for any reasonable model. The fact that the D_2O peak to shoulder separation is 31 cm^{-1} supports this conclusion. As well, the peak to shoulder separations of pure D_2O and of HDO in D_2O agree well. Presumably HDO in H_2O should have a ν_R peak to $(\nu_R + \nu_T)$ shoulder separation of about 50 cm^{-1} . However, that has not been observed yet by any workers.

Recent work by Trevino (93) quoted experimental data of neutron inelastic scattering from hexagonal ice I and compared that data to the results of a theoretical model based on cubic ice I. His hypothesis noted that the Raman and ir observations from 50 to 3500 cm^{-1} are the same for cubic and hexagonal ice I, and assumed that the basic dynamical lattice unit of cubic ice (one O atom surrounded tetrahedrally by 4 others) was a suitable model for hexagonal ice. That is supported by the fact that the nearest-neighbour configurations are the same. Trevino's (93) theory also assumed that the protons are in ordered positions, which they are not. However, the basic translational unit in ice is the O atom and the orientation of protons is relatively insignificant in this case.

For hexagonal ice I at 150°K the neutron inelastic scattering experiments (93) demonstrated lattice maxima at 63 cm^{-1} (TA) depending on the assignment of peaks. Other workers (92) found (for H_2O hexagonal ice I at 261°K) lattice modes at 60 and 70 cm^{-1} . Clearly there exists a high density of H_2O translational states near $50 \pm 10 \text{ cm}^{-1}$ at 150°K for hexagonal H_2O ice I. The corresponding modes for D_2O cubic ice I at 10°K may be lower than 50 cm^{-1} since the mass difference would shift the frequency

to $0.9484 \times 50 \text{ cm}^{-1} = 47.5 \text{ cm}^{-1}$.

The observed neutron band width in H_2O was 50 cm^{-1} . Of the broad band of real translational frequencies, the maximum transition moments do not have to occur over the same sections of the band for ir absorption and neutron inelastic scattering. The ir transition moment maximum may lie at lower frequencies than the neutron scattering transition moment maximum. Further, the overlap in the ir of ν_R and $(\nu_R + \nu_T)$ brings the instrumentally traced, summed absorptions closer together, i.e. if ν_R and $(\nu_R + \nu_T)$ could be resolved completely their peak positions would be separated by more than 50, 33 and 31 cm^{-1} for H_2O , HDO and D_2O respectively. One may conclude that a single librational mode and a combination librational-translational mode were observed for HDO . Since ν_{R_x} and ν_{R_y} are expected to be about equally intense, and since only one band was observed, then ν_{R_x} and ν_{R_y} must be exactly or nearly degenerate. The same conclusions seem appropriate for H_2O and D_2O .

B. The Fundamental Molecular Modes

(i) The Stretching Modes

There are many conflicting assignments of the three main ir absorption features near 3200 cm^{-1} for H_2O and 2400 cm^{-1} for D_2O . Ockman (108) assigned the low frequency shoulder to ν_1 , the main peak to ν_3 , and the high frequency shoulder to $(\nu_3 + \nu_T)$, while Hornig et al. (105) assigned the three bands as $2\nu_2$, ν_3 , and ν_1 . In contrast, Bertie and Whalley (95) assigned the low frequency shoulder and the main peak as a pair of bands composed of coupled $\nu_1 - \nu_3$ vibrations, and they eliminated the distinction

between ν_1 and ν_3 absorption bands of H_2O and D_2O . We propose that the low frequency shoulder is ν_1 , the main peak is ν_3 and the high frequency shoulder is $(\nu_1 + \nu_T)$ in agreement with the Raman results of Val'kov and Maslenkova (99) and as Ockman (108) interpreted them.

The stretching frequencies of HDO do not lie at the positions expected on the basis of H_2O and D_2O shifts in cubic ice I. This result will be discussed in terms of a theory proposed by Pimentel and Hrostowski (101) and Hornig and Hiebert (102) in the early 1950's: They suggested that the two major effects on molecular vibrations in solids, crystal-field perturbations and inter-molecular coupling, were separable by dilute isotopic substitution.

(a) The H_2O and D_2O stretching modes. For the Raman spectra of hexagonal ice I Val'kov and Maslenkova (99) found peaks at 3088, 3210 and 3321 cm^{-1} of relative intensities 10:4:2. The 3088 cm^{-1} peak had a polarization ratio of less than 0.75, while the 3210 cm^{-1} peak was depolarized. The 3088 cm^{-1} Raman peak was unambiguously of a_1 symmetry, i.e. the ν_1 symmetric stretch mode.

The suggestion of Bertie and Whalley (95,96) that ν_1 and ν_3 are coupled and indistinguishable cannot be entirely correct. If the ν_1 and ν_3 bands of coupled vibrators were largely mixed into two bands equally of ν_1 and ν_3 character, then the same set of energy levels would have been present for both the Raman and ir transitions, however the selection rules would change. For the mixed energy levels one would expect equally intense peaks at 3088 and 3210 cm^{-1} , contrary to the 10 to 4 observed intensity ratio. Hence the ν_1 and ν_3 energy levels appear to be separated (lack of

non-resonant coupling) while $\nu_1 - \nu_1$ and $\nu_3 - \nu_3$ resonance coupling of neighbours may still be effective.

There remains the problem of the disparity between the ν_1 ir and Raman frequencies, at $100 \pm 10^\circ\text{K}$, i.e. $\nu_1(\text{ir}) = 3149 \text{ cm}^{-1}$ and $\nu_1(\text{Raman}) = 3088 \text{ cm}^{-1}$ at $100 \pm 10^\circ\text{K}$. Similarly in D_2O ice I the ν_1 results were 2321 and 2291 cm^{-1} respectively. Recall that both the symmetric and asymmetric stretching modes appear to be very broad bands due to $\nu_1 - \nu_1$ and $\nu_3 - \nu_3$ resonance coupling. Of the complete set of ν_1 energy levels, the same portions of the band need not be both Raman and ir active nor with the same intensity factor. Thus for the Raman scattering only a narrow band in the lower one-half of the ν_1 band was active while for the ir a large range of frequencies was observed and the maximum intensity occurred at a higher frequency. For the asymmetric ν_3 mode the same portions of the band of frequencies was ir and Raman active. This may indicate a fundamental difference in $\nu_1 - \nu_1$ and $\nu_3 - \nu_3$ resonance coupling.

Thus the Raman scattering from hexagonal ice I indicated that in the ir absorption spectra the low frequency shoulder was ν_1 and the main peak was ν_3 , i.e. $\nu_3(\text{H}_2\text{O}) = 3210 \text{ cm}^{-1}$ and $\nu_3(\text{D}_2\text{O}) = 2413 \text{ cm}^{-1}$. By assuming that the two ν_3 assignments are correct, then the ratio of $\nu_3(\text{ice})/\nu_3(\text{vapour})$ is 0.8546 for H_2O and 0.8655 for D_2O . If the effects of hydrogen bonding are the same on all O-H bonds, then ν_1 and ν_3 are expected to be in the same order as in the vapour phase and should have the same relative displacements from the vapour phase frequencies, Fig. 4.15. The $\nu_3(\text{H}_2\text{O})$ cubic ice I absorption (3210 cm^{-1}) is 0.8546 times the $\nu_3(\text{H}_2\text{O})$ vapour frequency (3756 cm^{-1}). In order to preserve the displacement due to hydrogen bonding

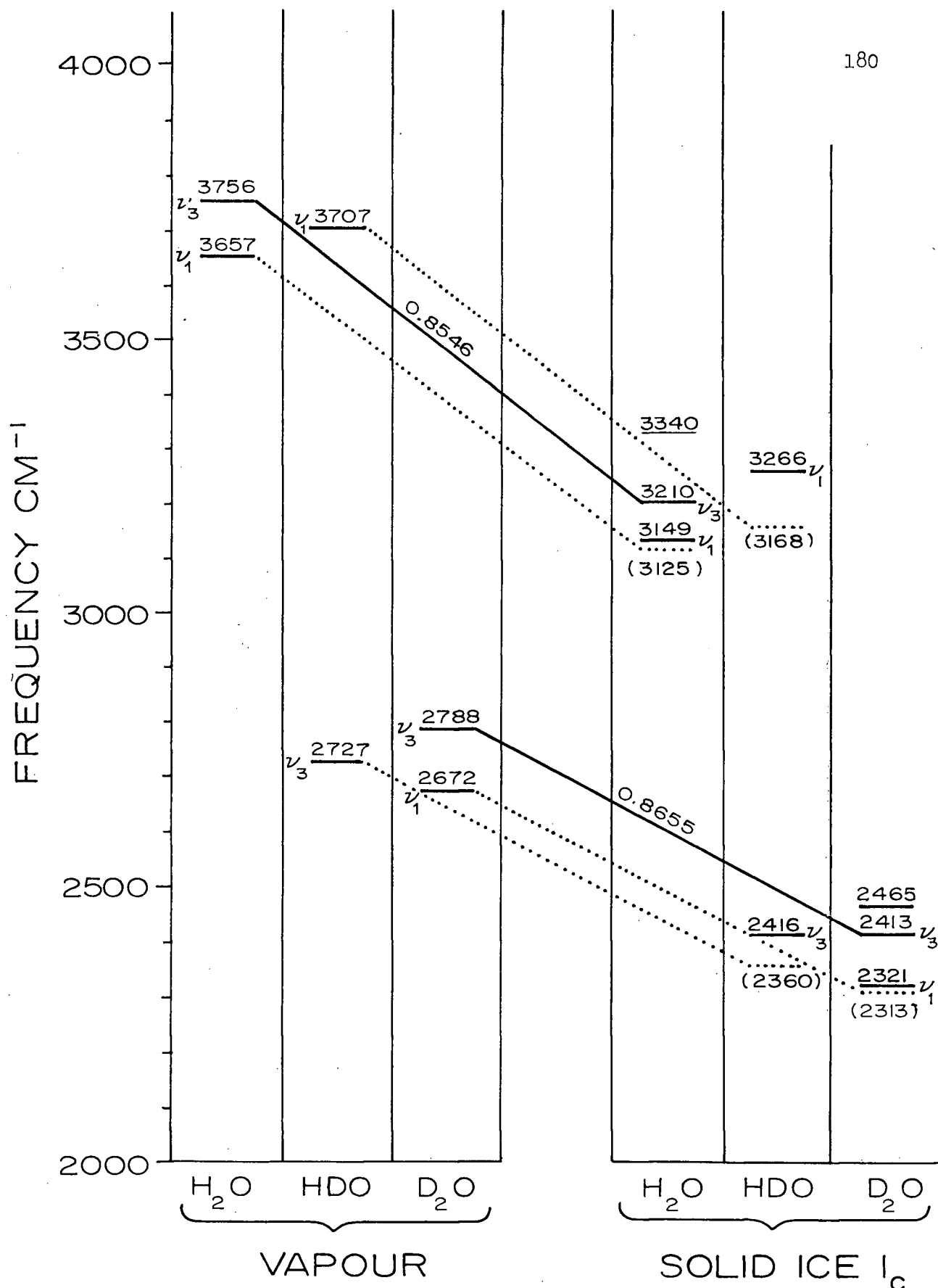


Fig. 4.15 The observed vapour phase and cubic ice I phase. H_2O , HDO and D_2O frequencies are shown as solid horizontal lines. The ratios of $v_3(\text{ice})/v_3(\text{vapour})$ are shown on the diagonal solid lines. The H_2O , HDO and D_2O ice frequencies predicted with those ratios are shown as dotted horizontal lines.

then the $\nu_1^P(\text{H}_2\text{O})$ ice (where p stands for predicted) frequency would have to be $0.8546 \times 3657 \text{ cm}^{-1} = 3125 \text{ cm}^{-1}$, compared to the observed $\nu_1(\text{H}_2\text{O})$ frequency of 3149 cm^{-1} . By similar arguments $\nu_1^P(\text{D}_2\text{O}) = 0.8655 \times 2671 \text{ cm}^{-1} = 2313 \text{ cm}^{-1}$, compared to the observed value of 2321 cm^{-1} . The predicted ν_1 frequencies, which preserved the relative effects of hydrogen bonding on ν_3 and ν_1 , agree very well with the observed ir results. The agreement is probably better than indicated since the observed ir ν_1 band was shifted to higher frequency by overlap with the adjacent ν_3 band.

The alternate assignment of observed ice peaks which also retains the $\nu_1 - \nu_3$ order is $\nu_1 = 3210 \text{ cm}^{-1}$ and $\nu_3 = 3340 \text{ cm}^{-1}$. The ratio of $\nu_3(\text{ice})/\nu_3(\text{vapour})$ is then 0.8858 and the predicted ν_1^P frequency is 3253 cm^{-1} , compared to the ir result, $\nu_1 = 3210 \text{ cm}^{-1}$. Neither the $\nu_1^P(\text{H}_2\text{O})$ nor the $\nu_1^P(\text{D}_2\text{O})$ frequency was a good approximation to an observed ir band. The second assignments of ν_1 and ν_3 were rejected.

The reasonable assumption of equal effects on ν_1 and ν_3 due to hydrogen bonding gives predicted frequencies in good agreement with observed features. The accepted assignments were $\nu_1 = 3149 \text{ cm}^{-1}$ and $\nu_3 = 3210 \text{ cm}^{-1}$, while the 3340 cm^{-1} shoulder was probably $(\nu_1 + \nu_T)$.

(b) The HDO stretching modes. Use of dilute isotopic substitution to separate the crystal field and resonance coupling perturbations (101,102) was originally suggested for studying the molecular vibrations of DCl under the influence of an HCl crystal field, but in the absence of intermolecular resonance coupling. The extensions of that concept to polyatomic molecules, which have more than one normal coordinate and where rapid isotopic exchange may occur, has led to some misinterpretations of experimental results, i.e. as in H_2O in D_2O (106,95). Because of the rapid isotopic exchange it

is impossible to isolate D_2O in H_2O or H_2O in D_2O at low concentrations. One obtains a dilute solution of HDO and very, very dilute residues of H_2O or D_2O . Now HDO has C_s molecular symmetry and three internal coordinates, an OH stretch, an O-D stretch and an HOD bend. It is unreasonable to expect both of the HDO stretching modes to be completely uncoupled from the stretching modes of the H_2O or D_2O lattice. Just such an assumption by Hornig et al. (106) and by Bertie and Whalley (95) has resulted in misinterpretation of the ice I HDO ir results.

As a first approximation to ice I, consider the ir observations for HDO, H_2O and D_2O in the vapour phase, Fig. 4.15. One HDO stretching mode lies almost exactly midway between ν_3 and ν_1 of H_2O , while the other HDO stretch is observed nearly midway between ν_3 and ν_1 of D_2O . That is entirely understandable since the symmetric and asymmetric H_2O modes may be considered as constructed from a basis of two isolated O-H (HDO) stretches which interact weakly. Hornig et al. (105,106) claimed that such a picture of the H_2O and D_2O potentials should extend to the solid as well, i.e. in ice I they expected the HDO modes to lie between the ν_1/ν_3 modes of H_2O and D_2O . For ice I (Fig. 4.15) $\nu_{OH}(HDO)$ was observed between two ir H_2O features, while $\nu_{OD}(HDO)$ was almost coincident with a central ir D_2O feature. Ignoring the weight of Raman data to the contrary, Hornig et al. assigned $\nu_3(H_2O)$ to 3210 cm^{-1} and $\nu_1(H_2O)$ to 3360 cm^{-1} with $\nu_{OH}(HDO)$ between them at 3275 cm^{-1} . Their central aim appears to have been the preservation of the $\nu_{OH}(HDO)$ observed position between ν_3 and ν_1 of H_2O .

Bertie and Whalley's (95) discussion of the relationships between HDO, H_2O and D_2O stretches was confusing. They also assumed the nature of the H-OD (in D_2O) stretch was the same as the H-OH(in H_2O) stretch.

The above ratios of $\nu_3(\text{ice})/\nu_3(\text{vapour})$ for H_2O and D_2O (Fig. 4.15) yield interesting results when applied to HDO (vapour) frequencies. The observed vapour phase frequencies of HDO stretching are 3707 and 2727 cm^{-1} . The predicted HDO frequencies using the H_2O and D_2O ν_3 ratios (0.8546 and 0.8655) are $\nu_{\text{OH}}^{\text{P}}(\text{HDO}) = 3168 \text{ cm}^{-1}$ and $\nu_{\text{OD}}^{\text{P}}(\text{HDO}) = 2360 \text{ cm}^{-1}$ compared to the observed HDO frequencies of 3263 cm^{-1} and 2413 cm^{-1} respectively. Thus the predicted frequencies lie close to the $\nu_1 - \nu_3$ mid-points, in agreement with the concept of Hornig *et al.* (105,106), but do not agree with the observed HDO frequencies.

On the basis of our assignments the observed $\nu_{\text{OH}}(\text{HDO})$ stretch (Fig. 4.16) was outside and above the $\nu_1 - \nu_3$ interval of pure H_2O . Correspondingly, the $\nu_{\text{OD}}(\text{HDO})$ stretch was just above $\nu_3(\text{D}_2\text{O})$, Fig. 4.16. A clear explanation of the mispositioning of the HDO stretches can be found by considering the coupling of HDO to H_2O and D_2O lattices.

Consider the case of 4.0% HDO in a D_2O cubic ice I lattice. Of the two HDO stretches only $\nu_{\text{OD}}(\text{HDO})$ can undergo reasonably strong near-resonance coupling to $\nu_3(\text{D}_2\text{O})$: $\nu_{\text{OH}}(\text{HDO})$ is "uncoupled" from the lattice vibrations. One then compares the observed $\nu_{\text{OH}}(\text{HDO})$ to ν_1 and ν_3 of H_2O on the assumption of equal hydrogen bond effects, Fig. 4.16. However, $\nu_{\text{OH}}(\text{HDO})$ lies 86 cm^{-1} above the $\nu_1 - \nu_3(\text{H}_2\text{O})$ midpoint. A possible explanation is a lengthened $\text{DO-H}\cdots\text{OH}_2$ distance due to the very process of uncoupling. For example the covalent character of the hydrogen bond is dependent upon an equal sharing of e^- among the overlapped orbitals. If the orbital following of e^- about vibrating nuclei is not at the same rate then the hydrogen bond may be weakened.

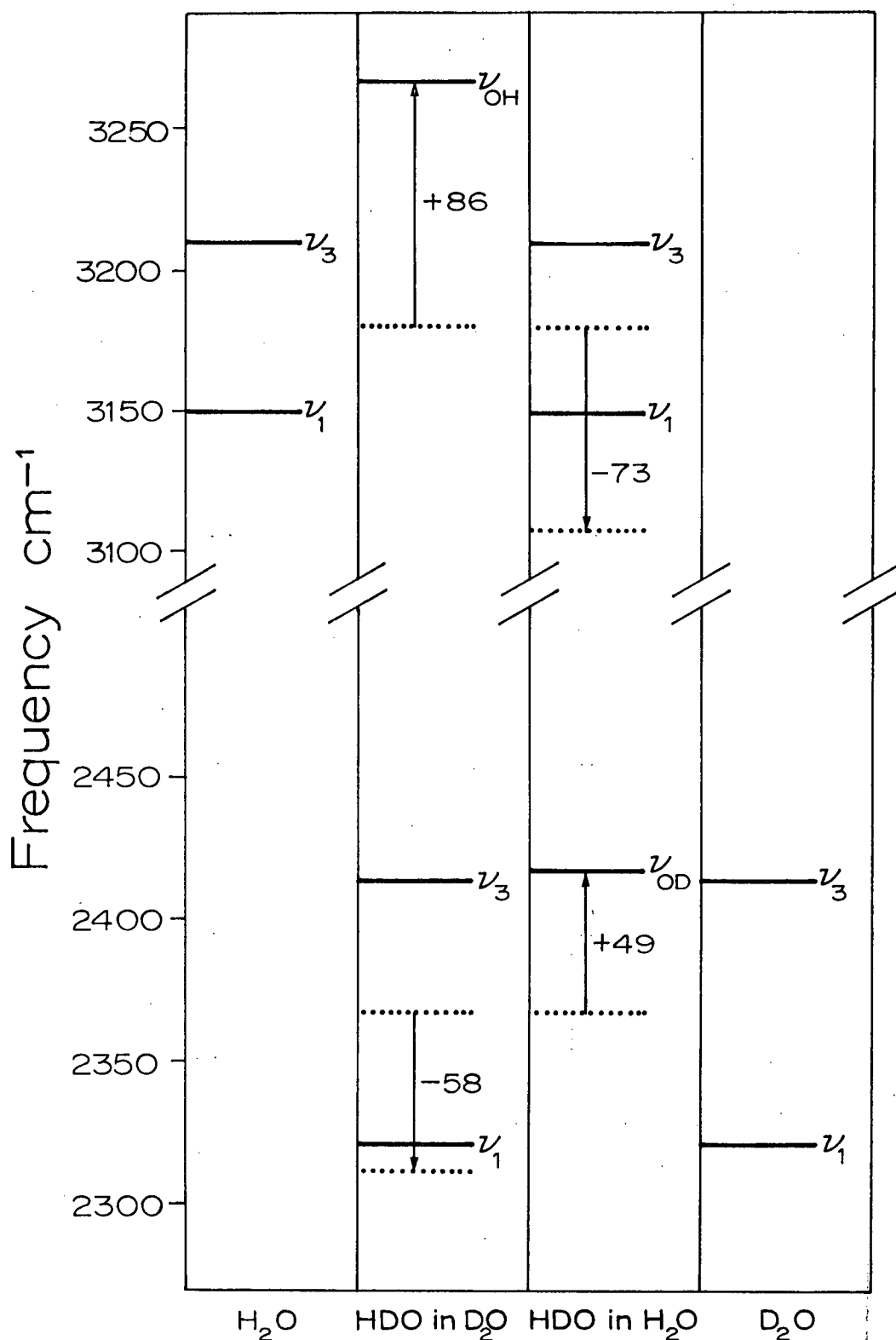


Fig. 4.16 The relative positions of the observed H_2O , HDO and D_2O stretching vibrations are shown as horizontal solid lines. The expected positions of the HDO absorptions before and after the effects of uncoupling, are shown as dotted horizontal lines.

From section 4.2A(ii) we found that $\Delta v_{OH}/\Delta R(O\cdots O) = 1,921 \text{ cm}^{-1}/\text{\AA}$. Hence, a Δv_{OH} of 86 cm^{-1} implies the DOH-D₂O $R(O\cdots O)$ distance was longer than "expected" by 0.045\AA . Correspondingly the HOD-D₂O $R(O\cdots O)$ distance should have been shorter than expected by 0.045\AA and v_{OD} (HDO in D₂O) would have been 58 cm^{-1} lower than expected (but it was unobservable lying under $v_1(\text{D}_2\text{O})$), at 2311 cm^{-1} . (The $v_1 - v_3$ midpoints are 3180 and 2367 cm^{-1} for H₂O and D₂O respectively.)

For 5.94% HDO in H₂O v_{OD} (HDO) was found at 2416 cm^{-1} , 49 cm^{-1} above the center of $v_1 - v_3(\text{D}_2\text{O})$ for cubic ice I, Fig. 4.16. That implies the uncoupling had lengthened $R(O\cdots O)$ for HO-D \cdots H₂O by 0.038\AA . Similarly $R(O\cdots O)$ for DO-H \cdots H₂O must have been shorter by 0.038\AA and v_{OH} (HDO) would have been lower than normal by 73 cm^{-1} , at 3107 near $v_1(\text{H}_2\text{O})$.

For HDO in H₂O and D₂O the point is that one HDO mode was coupled to the lattice and the other was uncoupled: The act of uncoupling weakened the hydrogen bond, lengthened one $R(O\cdots O)$ and shortened the other three $R(O\cdots O)$ of HDO. Consequently the uncoupled frequency was shifted to higher frequency and the other was shifted to lower frequency.

Our explanation of the observed positions of HDO frequencies in relation to the H₂O and D₂O frequencies cannot be readily confirmed by any meaningful calculation or conceived experiment. However it serves to point out an important fact in dilute isotopic substitution studies in solids: The molecules of mixed analogues are not all uncoupled from the lattice. The method is not generally useful nor applicable to molecules with mixed isotopes unless one recognizes that unusual effects can occur.

(ii) The Bending Mode

The position of the $1570\ (1604)\ \text{cm}^{-1}$ H_2O cubic ice I absorption (Table III.XI) indicates it could be either ν_2 or $2\nu_R$ and possibly overlapping $\nu_2/2\nu_R$ absorptions. The vapour phase $\nu_2(\text{H}_2\text{O})$ frequency is $1595\ \text{cm}^{-1}$. The frequency shift upon annealing was to lower frequency (Fig. 3.2) a characteristic of molecular modes and thus favours the ν_2 assignment. As well, the cubic ice I frequency shift was to higher frequency and similarly favoured ν_2 . However the half-height width increased upon annealing and for cubic ice I it decreased with increasing temperature (Figs. 3.12 and 3.5 and page 67). That data favours a combined $\nu_2/2\nu_R$ absorption. The ν_2 absorption was more intense than the underlying $2\nu_R$ and was probably centered below $1595\ \text{cm}^{-1}$, i.e. near $1570\ \text{cm}^{-1}$. Similarly for D_2O the $\nu_2/2\nu_R$ band was found at $1194\ \text{cm}^{-1}$.

C. The Overtone and Combination Modes(i) The $3\nu_R$ Modes

The $2235\ \text{cm}^{-1}$ H_2O and $1635\ \text{cm}^{-1}$ D_2O absorptions have been interpreted as both $3\nu_R$ and $\nu_2 + \nu_R$ (Table 0.5). The bands shifted to higher frequency upon annealing and as cubic ice I the frequencies shifted down (Figs. 3.2 and 3.17): Both of those facts indicate a lattice mode and we assign the absorption to $3\nu_R$. However, there is at least one disconcerting factor, the relative intensities of ν_R , $2\nu_R$ and $3\nu_R$ that were observed. One expects the overtone intensities to fall very rapidly and thus the intensity of $3\nu_R$ should be much less than $2\nu_R$. However the $3\nu_R$ absorption is only about $1/4$ less intense than the combined $\nu_2/2\nu_R$ absorption, and

that indicates that $2\nu_R$ is less intense than $3\nu_R$. However, the interpretation in terms of individual molecular librations is weak and a complete solid state treatment is necessary.

(ii) The ($\nu_1 + \nu_T$) Mode

The shoulder at 3340 cm^{-1} in H_2O and 2465 cm^{-1} in D_2O cubic ice I has been variously assigned as ν_1 , $\nu_3 + \nu_T$ and $\nu_1 + \nu_T$ (Table 0.5). Our previous discussion on the stretching modes of H_2O , D_2O and HDO (page 181) eliminated the ν_1 assignment. The peak to high-shoulder separation (ν_3 to " $\nu_3 + \nu_T$ ") is 130 cm^{-1} while the low to high frequency shoulder separation (ν_1 to " $\nu_1 + \nu_T$ ") is 191 cm^{-1} . The latter separation lies closer to our observed $\nu_T(\text{H}_2\text{O})$ band maximum and favours the $\nu_1 + \nu_T$ assignment. In addition, the Raman data (99) favours a $\nu_1 + \nu_T$ assignment on the basis of frequency separation and relative intensities, i.e. the relative ν_1 , ν_3 to $\nu_1 + \nu_T$ intensities are 10:4:2.

4.4 The Librations of HDO , H_2O and D_2O

A. The Moments-of-Inertia Models

Past treatments of the librational lattice modes of the ices have dwelt upon the association of the librations to free rotation of oriented-gas or gas phase molecules (85,89). Implicit in such treatments have been comparisons of the moments-of-inertia (I) about the three principal axes of H_2O , HDO and D_2O . Blue (85) was the first to evaluate the librational frequencies through moments-of-inertia. We have extended the calculations

to include weighted lone-pair orbital contributions to the moments.

(i) The Non-Interacting Molecules Model

The molecular parameters and the positions of the principal axes are shown in Fig. 4.17. The moments-of-inertia are given in Table IV.II as well as the differences between the HDO, H₂O and D₂O moments. Under the molecular symmetries, librations about the H₂O and D₂O z-axes are ir inactive, while libration of HDO about z is ir active due to the loss of C_{2v} symmetry and the orientation of the molecular dipole at 17°54' to the z-axis. However, $\nu_{Rz}(\text{HDO})$ is expected to be weak compared to ν_{Ry} and ν_{Rx} due to the small dipole reorientation. Notice that $\nu_{Rx}(\text{HDO})$ gives asymmetrically bent O-H····O and O-D····O hydrogen bonds. The D atom sweeps 0.004 Å/deg arc while the H atom sweeps 0.012 Å/deg arc in a classical approach.

The HDO moments are split between the H₂O and D₂O moments-of-inertia, Table IV.II. Hornig et al. (105) pointed out that on the basis of moments-of-inertia the observed HDO librations would be expected to split between the H₂O and D₂O librational frequencies. From the differences in the moments one sees that $I_x(\text{HDO})$ is nearer $I_{x\text{H}_2\text{O}}$, $I_z(\text{HDO})$ is nearer $I_z(\text{D}_2\text{O})$, and $I_y(\text{HDO})$ is midway between $I_y(\text{H}_2\text{O})$ and $I_y(\text{D}_2\text{O})$. It does not necessarily follow that the HDO librational frequencies will be observed in a corresponding manner.

HDO librational absorption was observed here only for HDO in a D₂O matrix: One peak and one shoulder were observed at 823 cm⁻¹ and 856 cm⁻¹ respectively (page 74). Assuming that the librational frequencies for HDO, H₂O and D₂O can be defined by a single function such as Blue's

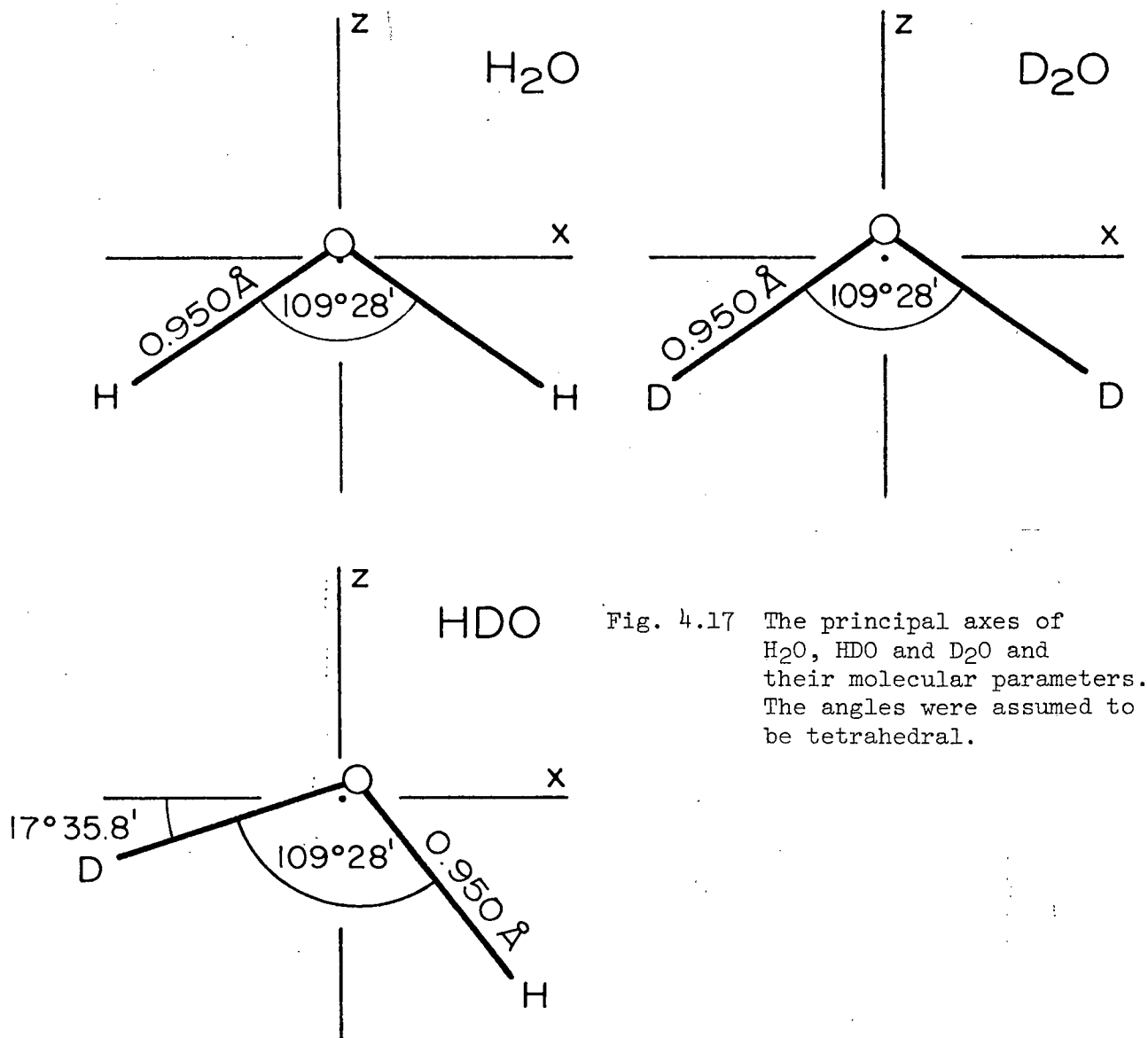


Fig. 4.17 The principal axes of H_2O , HDO and D_2O and their molecular parameters. The angles were assumed to be tetrahedral.

(page 27) then $\nu_{\text{Rx}}(\text{HDO})$ should be relatively weakly coupled to any libration of the D_2O lattice since the HDO and D_2O librational frequencies observed were about 90% separated.

One of the absorptions at 856 and 823 cm^{-1} must contain at least $\nu_{\text{Rx}}(\text{HDO})$ since it has the lowest moment-of-inertia and is expected to be closest to the H_2O values. The other feature above cannot be due to $\nu_{\text{Ry}}(\text{HDO})$ nor $\nu_{\text{Rz}}(\text{HDO})$ since the peak-shoulder separation was too small,

Table IV.II The moments-of-inertia of H_2O , HDO and D_2O and a comparison of HDO to H_2O and D_2O . The parameters used to calculate the principal moments-of-inertia are given in the text.

	H_2O	D_2O	HDO
I_x	0.89×10^{-40}	1.61×10^{-40}	1.08×10^{-40}
I_y	2.91	5.63	4.23
I_z	2.01	4.02	3.15
	units gms-cm^2 / molecule		

Comparison of moments

$$\begin{aligned}
 I_x(\text{HDO}) - I_x(\text{H}_2\text{O}) &= 0.19 \times 10^{-40} & I_x(\text{D}_2\text{O}) - I_x(\text{HDO}) &= 0.53 \times 10^{-40} \\
 I_y(\text{HDO}) - I_y(\text{H}_2\text{O}) &= 1.32 & I_y(\text{D}_2\text{O}) - I_y(\text{HDO}) &= 1.40 \\
 I_z(\text{HDO}) - I_z(\text{H}_2\text{O}) &= 1.14 & I_z(\text{D}_2\text{O}) - I_z(\text{HDO}) &= 0.87
 \end{aligned}$$

33 cm^{-1} . As mentioned earlier, the shoulder appears to be due to $(\nu_R + \nu_T)$ absorption.

Alternately the peak and shoulder may have resulted from nearly degenerate $\nu_{R_x}(\text{HDO})$ and $\nu_{R_y}(\text{HDO})$ absorptions. Such an event implies that either I_x and I_y of HDO are degenerate through coupling, or that the librations cannot be treated on the basis of moments-of-inertia. Both of these possibilities will be treated in detail.

Assume that the librations of HDO, H₂O and D₂O can be simply related to the principal moments-of-inertia by Blue's (85) formula (page 27). Since the oxygen atoms lie close to each of the principal axes then the r_{On}^2 are all small and since the restoring forces on the oxygen atoms are all small then Blue's equation reduces to:

$$\nu_{R_n}(\text{cm}^{-1}) = \frac{1}{2\pi c I_n} \left[\frac{1}{2} (k_{H_{1n}} r_{H_{1n}}^2 + k_{H_{2n}} r_{H_{2n}}^2) \right]^{1/2} \quad [4]$$

where: ν_{R_n} is the librational frequency about axis n

$k_{H_{1n}} = k_{H_{2n}} = k_{H_n}$ on the basis of symmetry

and $r_{H_{1n}}^2$ is the distance of atom H₁ normal to axis n.

Using the calculated moments-of-inertia from Table IV.II one obtains the librational frequencies in terms of the k_{H_n} force constants:

	H ₂ O	HDO	D ₂ O
$\nu_{R_x} =$	2.45 k_H	2.60 k_H'	1.83 k_D
$\nu_{R_y} =$	2.77 k_H	2.33 k_H'	1.99 k_D
$\nu_{R_z} =$	2.90 k_H	2.23 k_H'	2.05 k_D

It is implicit in this treatment that the three librations of each molecule are non-degenerate. On the basis of the above equations the lowest observed frequencies of H₂O and D₂O must be associated with the ν_{R_x} 's since they have the lowest force constant coefficients: Thus $\nu_{R_x}(\text{H}_2\text{O}) = 833 \text{ cm}^{-1}$, and $\nu_{R_x}(\text{D}_2\text{O}) = 627 \text{ cm}^{-1}$. Using those frequencies the force constants are

$$k_H(\text{H}_2\text{O}) = (1.15 \pm 0.03) 10^5 \text{ dynes/cm}$$

$$k_D(\text{D}_2\text{O}) = (1.17 \pm 0.03) 10^5 \text{ dynes/cm}$$

For HDO, $\nu_{R_y}(\text{HDO})$ has the smallest force constant coefficient and we assign that (on a trial basis) to the 819 cm^{-1} peak. Then the HDO force constant,

k_H' , is $(1.24 \pm 0.03)10^5$ dynes/cm, in reasonable agreement with the H_2O and D_2O force constants. By applying the above three force constants to the remaining functions one obtains the following set of frequencies:

	H_2O	HDO	D_2O
ν_{R_x}	<u>833</u> cm^{-1}	916 cm^{-1}	<u>627</u> cm^{-1}
ν_{R_y}	940	<u>819</u>	682
ν_{R_z}	984	785	702

where the observed frequencies which were used to define the force constants are underlined. Since libration about the y principal axis entails a greater distortion of one HDO hydrogen bond than for ν_{R_x} of H_2O and D_2O then the slightly larger HDO force constant is understandable.

Of the nine frequencies listed above three were assigned from experimental observation. From the remaining six frequencies, two were expected to be ir inactive (i.e. $\nu_{R_z}(H_2O)$ and $\nu_{R_z}(D_2O)$) while a third one ($\nu_{R_z}(HDO)$) is expected to be very weak. That leaves three predicted frequencies to compare with experiment: $\nu_{R_y}(H_2O)$, $\nu_{R_x}(HDO)$ and $\nu_{R_y}(D_2O)$. Only the prediction of $\nu_{R_y}(D_2O)$ at 682 cm^{-1} lies near an observed band, the D_2O cubic ice I band at 661 cm^{-1} . However, even that prediction is out by more than 20 cm^{-1} . As well, there were no observed absorptions near the 940 cm^{-1} or 916 cm^{-1} predicted frequencies. Therefore, $\nu_{R_y}(H_2O)$, $\nu_{R_x}(HDO)$ and $\nu_{R_y}(D_2O)$ are either weak or inactive ir absorptions. Alternatively those modes may be ir active and strong but degenerate with the other librational modes.

The conclusion must be that I_x and I_y are degenerate or Blue's formula is invalid. The moments-of-inertia can be made nearly degenerate by considering the masses of the detached (more distant) two protons as being attached to the lone-pair orbitals. As well, Blue's formula (85) oversimplifies the problem since it ignores the motion of the four adjacent molecules through the hydrogen bonds.

(ii) The Weighted Lone-Pairs Model

Consider one H_2O molecule as being suspended with neutral density in a cubic ice I lattice. The supporting lattice can be considered as having two principal effects. First, the principal moments of the two protons attached to the central molecule ($O-H\cdots O$) are decreased through reduction of their real masses to an effective mass by the "buoyancy" of the surrounding lattice through the hydrogen bonds. The mass "lost" by the two central protons is gained in the lone-pair orbitals of two neighboring molecules. Similarly, the two lone-pair orbitals of the central molecule gain an effective mass from the two detached protons ($O\cdots H-O$) associated with the central molecule hydrogen bonds. Hence the lone-pair effective masses restore the moments-of-inertia to near their initial values.

The second effect on the moments-of-inertia which arises from hydrogen bonding is the movement of the two attached protons away from, and the two detached protons closer to the central oxygen atom. Notice that cooling the sample decreases $R(O\cdots O)$ and tends to centralize the four protons further. If the four protons were centered between $O\cdots O$ and had masses equally shared by the pairs of oxygen atoms, then the molecules would be restrained spherical tops, $I_x = I_y = I_z$.

A pseudo-symmetric top is approximated by smaller masses working at longer distances, i.e. weighted lone-pairs acting at the detached proton distance of $1.79 \overset{\circ}{\text{\AA}}$ and a reduced protonic mass acting at the O-H distance of $0.95 \overset{\circ}{\text{\AA}}$. The point is that if the moments-of-inertia I_x and I_y are equal for H_2O and D_2O then by Blue's (85) formula ν_{R_x} and ν_{R_y} should be degenerate.

Consider the effect of reduced protonic masses and effective lone-pair masses where the molecular parameters will be assumed to be:

$$r_{\text{OH}} = r_{\text{OD}} = 0.950 \overset{\circ}{\text{\AA}}$$

$$R(\overset{\circ}{\text{O}} \cdots \text{H}) = R(\overset{\circ}{\text{O}} \cdots \text{D}) = 1.790 \overset{\circ}{\text{\AA}}$$

$$\text{mass of oxygen} = 15.999 \text{ gms/mole}$$

$$\text{the attached protons are } H_1 \text{ and } H_2$$

$$\text{the detached protons are } H_3 \text{ and } H_4$$

$$\text{the masses of } H_1 \text{ and } H_2 = 0.75(1.008) \text{ gms/mole}$$

$$= 0.756 \text{ gms/mole}$$

$$\text{the masses of } H_3 \text{ and } H_4 = 0.25 (1.008) \text{ gms/mole}$$

$$= 0.252 \text{ gms/mole}$$

(This is called the $(3/4, 1/4)$ effective mass option.) The moments-of-inertia of $\text{H}_2\text{O} \cdots \text{H}_2$ are:

$$I_x = 3.43 \times 10^{-40} \text{ gm-cm}^2/\text{molecule}$$

$$I_y = 3.15 \times 10^{-40}$$

$$I_z = 3.30 \times 10^{-40}$$

Substituting those values of the moments into Blue's (85) formula, [4], where the contributions of the oxygen force constants are still small, then:

$$\nu_{R_x}(\text{H}_2\text{O}, 3/4, 1/4) = 2.87(0.282 k_H + 3.20 k'_H) \frac{\text{sec}}{\text{gm-cm}}$$

$$\nu_{R_y}(\text{H}_2\text{O}, 3/4, 1/4) = 2.99(0.602 k_H + 2.14 k'_H)$$

$$\nu_{R_z}(\text{H}_2\text{O}, 3/4, 1/4) = 2.92(0.902 k_H + 1.10 k'_H)$$

where k_H is the O-H...O bending force constant

and k'_H is the O...H-O bending force constant.

Our model supposes that ν_{R_x} and ν_{R_y} of H_2O are degenerate at 833 cm^{-1} . By solving the first two expressions above one finds

$$k_H = 0.60 \times 10^5 \text{ dynes/cm}$$

$$\text{and } k'_H = 0.21 \times 10^5 \text{ dynes/cm.}$$

Using those values of k_H and k'_H in the third expression above, then $\nu_{R_z}^{\text{calc}}(\text{H}_2\text{O}, 3/4, 1/4)$ is 831 cm^{-1} which is degenerate with ν_{R_x} and ν_{R_y} within error.

How well do $k_H(\text{H}_2\text{O})$ and $k'_H(\text{H}_2\text{O})$ apply to $\text{D}_2\text{O} \cdots \text{D}_2$? Using the above molecular parameters and deuterium effective masses of $0.75(2.014)$ gms/mole for the attached pair (D_1 and D_2) and masses of $0.25(2.014)$ gms/mole for the detached pair (D_3 and D_4) then the $\text{D}_2\text{O} \cdots \text{D}_2$ moments-of-inertia are:

$$I_x = 6.84(10^{-40}) \text{ gm-cm}^2/\text{molecule}$$

$$I_y = 6.28(10^{-40})$$

$$\text{and } I_z = 6.59(10^{-40}).$$

The corresponding set of expressions from Blue's formula are:

$$\nu_{R_x}^{\text{calc}}(\text{D}_2\text{O}, 3/4, 1/4) = 2.03(0.268 k_H + 3.20 k_H') = 586 \text{ cm}^{-1}$$

$$\nu_{R_y}^{\text{calc}}(\text{D}_2\text{O}, 3/4, 1/4) = 2.12(0.902 k_H + 1.13 k_H') = 588 \text{ cm}^{-1}$$

$$\nu_{R_z}^{\text{calc}}(\text{D}_2\text{O}, 3/4, 1/4) = 2.07(0.602 k_H + 2.14 k_H') = 591 \text{ cm}^{-1}$$

where k_H and k_H' of H_2O were used. The three D_2O librational frequencies are reasonably degenerate and lie 6% below the main observed band at 627 cm^{-1} . This is as much accuracy as can be expected from so simple a model. By invariance of the potential energy to symmetry operations $k_H(\text{O}_1\text{-H}_1\cdots\text{O}_2) = k_H(\text{O}_1\text{-H}_2\cdots\text{O}_3)$ and $k_H'(\text{O}_1\text{-H}_3\cdots\text{O}_4) = k_H'(\text{O}_1\text{-H}_4\cdots\text{O}_5)$. However, it does not follow that $k_H(\text{O-H}_{1,2}\cdots\text{O}) = k_H'(\text{O}\cdots\text{H}_{3,4}\text{-O})$, since they are not interchangeable by site or point symmetry.

That k_H' is 0.309 times k_H may be rationalized on the following basis. The potential for libration is the same in all directions normal to $\text{R}(\text{O}\cdots\text{O})$; i.e. the "potential" has a conical cross-section along the $\text{O}\cdots\text{O}$ axis. While the shape of the potential is the same at protons H_1 and H_2 as well as being the same at H_3 and H_4 , only the moments of the forces acting at the two protonic distances must be equal. Since the $\text{O-H}_{1,2}$ and $\text{O}\cdots\text{H}_{3,4}$ distances are 0.94 and 1.79 Å respectively, then the ratio $(r_{\text{OH}})^2/\text{R}(\text{O}\cdots\text{H})^2 = 0.345$. The moment of the force acting at H_1 and H_2 is $k_{\text{Hr}}^2_{\text{OH}} = 0.53 \times 10^{-11}$ dyne-cm compared to the moment acting at H_3 and H_4 , $k_H' \text{R}(\text{O}\cdots\text{H})^2 = 0.67 \times 10^{-11}$ dyne-cm.

There is at least one disconcerting fact about this model that is seen for the case of 4.0% HDO in D_2O . The effective masses added to the HDO lone-pairs are 0.25 times the deuterium mass not the protonic mass. Thus HDO librational frequencies would be calculated nearer to the D_2O values than the H_2O values, contrary to our observations.

Another weighted lone-pairs option was investigated, the (H₂O, 1, 1/4) option. In this model the two attached protons were assigned full protonic masses, while the two detached protons were assigned masses of 0.25 times the full mass. Such a model seems unreasonable since the mass sums are not conserved. By the same treatment as above one finds:

$$k_H(\text{H}_2\text{O}, 1, 1/4) = 0.783 \times 10^5 \text{ dynes/cm}$$

$$k'_H(\text{H}_2\text{O}, 1, 1/4) = 0.213 \times 10^5 \text{ dynes/cm.}$$

The predicted $\nu_{Rz}(\text{H}_2\text{O})$ frequency is 829 cm^{-1} for this model and the predicted D₂O frequencies are 582, 592 and 586 cm^{-1} , much as for the (3/4, 1/4) model. Notice that the moments of the forces acting at H_{1,2} and H_{3,4} are now nearly equal, $0.69 \times 10^{-11} \text{ dyne-cm}$ and $0.67 \times 10^{-11} \text{ dyne-cm}$ respectively.

In summary let us consider the results of the two models considered. First, Blue's (85) formula for non-interacting molecules gave three non-degenerate, widely separated frequencies for the three librations. That is contrary to the observed spectra and must be rejected. Secondly, for degenerate ν_{Rx} and ν_{Ry} the moments-of-inertia must be equal. Using a weighted lone-pairs model it was necessary to consider two kinds of hydrogen bond bending force constants, which were not accurately transferable between H₂O and D₂O molecules. As well, the hydrogen bond bending force constants calculated were about as large as the molecular HOH bending force constant, i.e. Zimmermann and Pimentel (97) found the HOH bending force constant in ice to be $0.49 \times 10^5 \text{ dynes/cm}$. The value of $0.60 \times 10^5 \text{ dynes/cm}$ seems to be an unsatisfactorily high O-H···O bending force constant.

B. The H_2O_3 Model of Ice

An alternate approach to the librations of H_2O , HDO and D_2O molecules in ice is the normal coordinate analysis of an extended molecule, H_2O_3 . The structure and parameters of the H_2O_3 molecule are shown in Fig. 4.18. For a freely rotating and translating H_2O_3 molecule there are nine degrees of freedom and nine internal coordinates (R) are defined as:

$$\begin{array}{ll} R_1 = \Delta r_1 & R_5 = \Delta \phi \\ R_2 = \Delta r_2 & R_6 = \Delta \theta_1 \\ R_3 = \Delta r_3 & R_7 = \Delta \theta_2 \\ R_4 = \Delta r_4 & R_8 = \Delta \theta'_1 \\ & R_9 = \Delta \theta'_2 \end{array}$$

A similar model was studied by Zimmermann and Pimentel (97) in order to calculate the hydrogen bond bending and stretching force constants associated with molecular libration and translation.

With C_{2v} point symmetry the H_2O_3 molecule has the reducible representation composed of $5a_1$, $2a_2$, $5b_1$ and $3b_2$ irreducible representations. The representations of vibration, translation and rotation of the H_2O_3 molecule, as well as the representations of the sets of symmetry coordinates, are shown below:

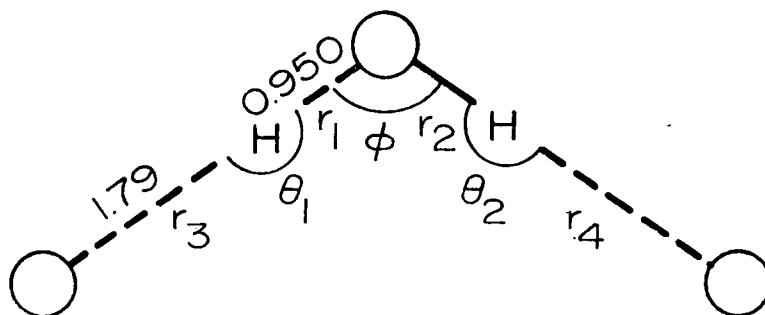


Fig. 4.18 The H_2O_3 model of H_2O in ice I. The OOO and HOH angles were assumed to be tetrahedral. The hydrogen bond bending coordinates θ_1 and θ_2 are in the HOH plane and θ'_1 and θ'_2 are perpendicular to them.

C_{2v}	E	C_2	σ_{xz}	σ_{yz}		
a_1	1	1	1	1	T_z	$\alpha_{xx}, \alpha_{yy}, \alpha_{zz}$
a_2	1	1	-1	-1	R_z	α_{xy}
b_1	1	-1	1	-1	$T_x \quad R_y$	α_{xz}
b_2	1	-1	-1	1	$T_y \quad R_x$	α_{yz}
$\Gamma(\text{H}_2\text{O}_3)$	15	-1	5	1	$5a_1 + 2a_2 + 5b_1 + 3b_2$	
$\Gamma(\text{Rot.})$	3	-1	-1	-1	$a_2 + b_1 + b_2$	
$\Gamma(\text{Trans.})$	3	-1	1	1	$a_1 + b_1 + b_2$	
$\Gamma(\text{vib.})$	9	1	7	-1	$4a_1 + a_2 + 3b_1 + b_2$	
$\Gamma_1(R_1, R_2)$	2	0	2	0	$a_1 + b_1$	
$\Gamma_2(R_3, R_4)$	2	0	2	0	$a_1 + b_1$	
$\Gamma_3(R_5)$	1	1	1	1	a_1	
$\Gamma_4(R_6, R_7)$	2	0	2	0	$a_1 + b_1$	
$\Gamma_5(R_8, R_9)$	2	0	-2	0	$a_2 + b_2$	

The symmetry coordinates of H_2O_3 are:

$$\left. \begin{aligned} S_1 &= 1/\sqrt{2} (R_1 + R_2) \\ S_2 &= 1/\sqrt{2} (R_3 + R_4) \\ S_3 &= R_5 \\ S_4 &= 1/\sqrt{2} (R_6 + R_7) \end{aligned} \right\} a_1 \quad \left. \begin{aligned} S_5 &= 1/\sqrt{2} (R_1 - R_2) \\ S_6 &= 1/\sqrt{2} (R_3 - R_4) \\ S_7 &= 1/\sqrt{2} (R_5 - R_6) \\ S_8 &= 1/\sqrt{2} (R_8 - R_9) \\ S_9 &= 1/\sqrt{2} (R_8 + R_9) \end{aligned} \right\} \begin{matrix} b_1 \\ a_2 \\ b_2 \end{matrix}$$

In matrix notation the transformation from internal to symmetry coordinates is

$$\underline{S} = \underline{U} \underline{R}$$

where \underline{S} and \underline{R} are column matrices of symmetry and internal coordinates, and \underline{U} is an orthogonal matrix. The solution of the secular equation is simpler in symmetry coordinates and the \underline{F} and \underline{G} matrices must also be transformed from internal coordinates ($\underline{F}(\underline{R})$ and $\underline{G}(\underline{R})$) to symmetry coordinates ($\underline{F}(\underline{S})$ and $\underline{G}(\underline{S})$) by the transformations

$$\begin{aligned} \underline{F}(\underline{S}) &= \underline{U} \underline{F}(\underline{R}) \underline{U}^T \\ \underline{G}(\underline{S}) &= \underline{U} \underline{G}(\underline{R}) \underline{U}^T \end{aligned}$$

The $\underline{F}(\underline{S})$ and $\underline{G}(\underline{S})$ matrices each are diagonalized into block form containing a $(4 \times 4)a_1$, $a(3 \times 3)b_1$, $a(1 \times 1)a_2$ and $a(1 \times 1)b_2$ block. The form of $\underline{G}(\underline{S})$ in terms of $\underline{G}(\underline{R})$ elements and the numerical values of the $\underline{G}(\underline{S})$ blocks are given in Table IV.III. The form of the $\underline{F}(\underline{S})$ elements in terms of $\underline{F}(\underline{R})$ elements is the same as shown in Table IV.III for $\underline{G}(\underline{S})$.

Before proceeding further with the normal coordinate analysis, the normal modes of vibration, rotation and translation of $\underline{\text{H}_2\text{O}}$ in ice I must be assigned to the internal vibrations of the $\underline{\text{H}_2\text{O}_3}$ molecule as represented

Table IV.III The symmetric G matrix elements in terms of the internal coordinates and their numerical values for the H_2O_3 model in units of $(\text{gm}^{-1} \text{ \AA}^2 \text{ moles})$.

$$a_1 \quad G(S) = \begin{vmatrix} g_{11}^+ & g_{12} & g_{13}^+ & g_{14} & 2g_{15} & g_{16}^+ & g_{17} \\ g_{13}^+ & g_{14} & g_{33}^+ & g_{34} & 2g_{35} & g_{36}^+ & g_{37} \\ 2g_{15} & & 2g_{35} & & g_{55} & & 2g_{56} \\ g_{17}^+ & g_{16} & g_{36}^+ & g_{37} & 2g_{56} & g_{66}^+ & g_{76} \end{vmatrix} = \begin{vmatrix} 1.034 & 0.992 & 0.088 & 0.062 \\ 0.992 & 1.055 & 0 & 0 \\ 0.088 & 0 & 2.393 & 2.511 \\ 0.062 & 0 & 2.511 & 2.733 \end{vmatrix}$$

$$b_1 \quad G(S) = \begin{vmatrix} g_{11}^- & g_{12} & g_{13} & g_{16}^- & g_{17} \\ g_{13} & g_{33}^- & g_{34} & g_{36} & \\ g_{16}^- & g_{17} & g_{36} & g_{66}^- & g_{76} \end{vmatrix} = \begin{vmatrix} 1.076 & 0.992 & 0.062 \\ 0.992 & 1.055 & 0 \\ 0.062 & 0 & 2.595 \end{vmatrix}$$

$$a_2 \quad G(S) = [g_{88} - g_{89}] = 2.595$$

$$b_2 \quad G(S) = [g_{88} + g_{89}] = 2.733$$

by the symmetry coordinates above. The displacement vectors of each kind of internal H_2O_3 coordinate are shown in Fig. 4.19. The corresponding displacement vectors of the symmetry coordinates constructed from those internal coordinates are shown in Fig. 4.20. The H_2O ice I normal mode associated with each H_2O_3 internal vibration is listed in Fig. 4.20.

The symmetry coordinates S_7 , S_8 and S_9 , which correspond to ν_{R_x} , ν_{R_z} , and ν_{R_y} respectively, are of particular interest for this discussion.

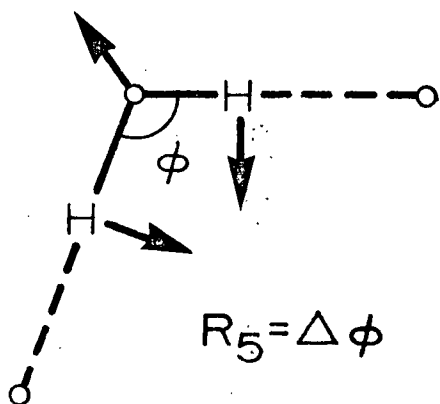
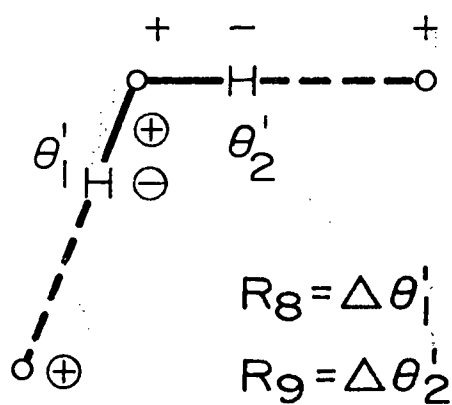
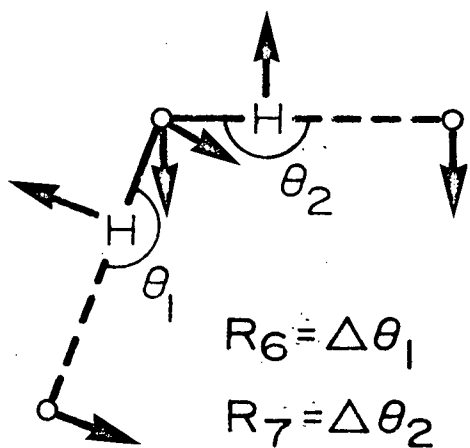
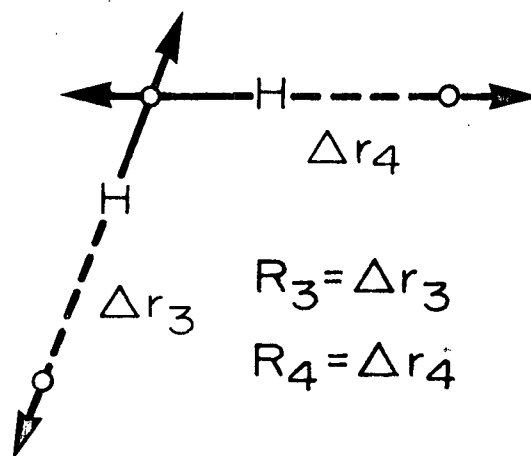
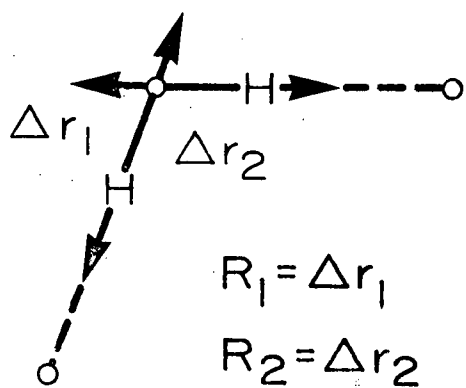


Fig. 4.19 The internal coordinates of the H_2O_3 model shown as symmetrically equivalent pairs. The displacement vectors are not to scale and give only an approximate representation of the coordinates.

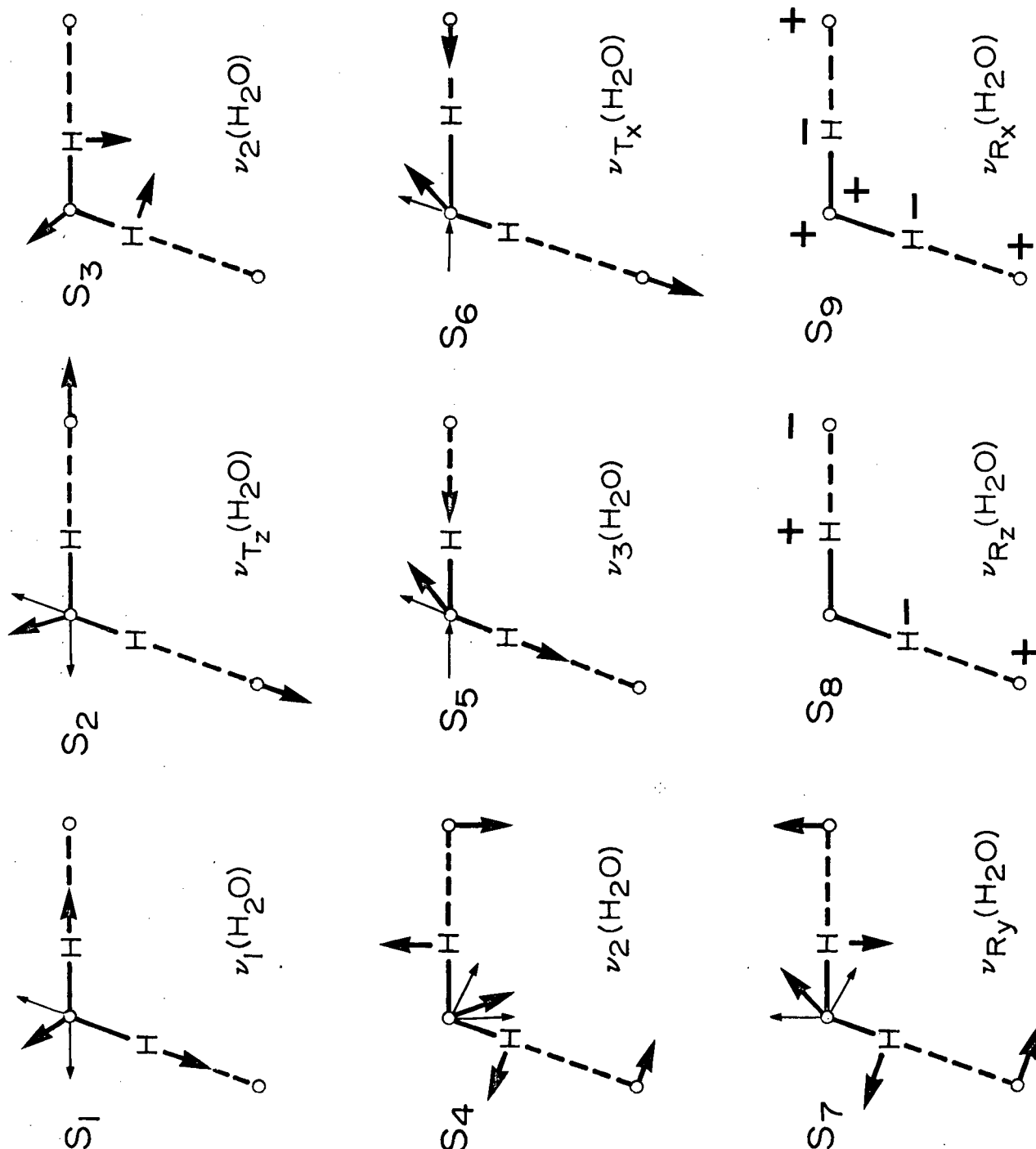


Fig. 4.20 The symmetry coordinates of the H_2O_3 model were constructed as simple linear combinations of the internal coordinates. Each symmetry coordinate was assigned to an H_2O ice I normal mode simply on the basis of the diagrammatic representation.

Inspection of G_{77} , G_{88} and G_{99} in Table IV.III shows that the two librations (ν_{R_x} and ν_{R_z}) are "kinetically" degenerate and that ν_{R_y} is very nearly degenerate with them:

$$G_{77} = g_{66} - g_{67} \quad \nu_{R_x}$$

$$G_{88} = g_{66} - g_{67} \quad \nu_{R_z}$$

$$G_{99} = g_{66} + g_{67} \quad \nu_{R_y}$$

If the forces restraining libration about x and y are equal (which they are for H_2O_3 by symmetry) then ν_{R_x} is degenerate with ν_{R_y} .

The secular equation can be solved for the diagonal symmetry force constants by an iteration formula given by Green (125):

$$k_{ii}^{n+1} = \lambda_i \left\{ G_{ii} + \sum_{j \neq i} \frac{(G_{ij})^2 k_{ij}^{n+1}}{\lambda_i - \lambda_j} \right\}^{-1} \dots\dots\dots [5].$$

The b_2 block is trivial and gave the solution of $k_{99} = 0.149 \times 10^5$ dyne-cm when ν_{R_x} was assigned to the peak at 833 cm^{-1} . The a_2 block is also trivial and gave the solution $k_{88} = 0.157 \times 10^5$ dyne-cm, in good agreement with k_{99} (ν_{R_x} and ν_{R_z} were assumed to be degenerate at 833 cm^{-1}).

For the $(3 \times 3)b_1$ block the S_5 , S_6 and S_7 symmetry coordinates were associated with $\nu_3(H_2O)$, $\nu_{T_x}(H_2O)$ and $\nu_{R_y}(H_2O)$, respectively. Applying the iteration formula:

$$k_{55}^i = \lambda_5 \left\{ G_{55} + \frac{(0.992)^2 k_{66}^{i-1}}{\lambda_5 - \lambda_6} + \frac{(0.062)^2 k_{77}^{i-1}}{\lambda_5 - \lambda_7} \right\}^{-1}$$

$$k_{66}^i = \lambda_6 \left\{ G_{66} + \frac{(0.992)^2 k_{55}^{i-1}}{\lambda_6 - \lambda_5} \right\}^{-1}$$

$$k_{77}^i = \lambda_7 \left\{ G_{77} + \frac{(0.062)^2 k_{55}^{i-1}}{\lambda_7 - \lambda_5} \right\}^{-1}$$

where $\lambda_i = (\nu_i/1303.1)^2$. Initial force constants $k_{ii}^0 = 1.000$ were assumed and the formulas converged to ± 0.001 in eleven iterations. The force constants determined were:

$$k_{55} = 5.481 \times 10^5 \text{ dynes/cm}$$

$$k_{66} = 0.192 \times 10^5 \text{ dynes/cm}$$

$$k_{77} = 0.154 \times 10^5 \text{ dyne-cm}$$

Notice that the symmetry force constant associated with ν_{Ry} , $k_{77} = 0.154 \times 10^5$ dynes/cm, does not agree with those of ν_{Rx} and ν_{Rz} .

Finally the $(4 \times 4)a_1$ block was solved for the H_2O_3 symmetry force constants. The S_1 , S_2 , S_3 and S_4 symmetry coordinates were assigned to $\nu_1(H_2O)$, $T_z(H_2O)$, $\nu_2(H_2O)$ and $\nu_2'(H_2O)$ respectively. The symmetry coordinate was assumed to be a redundant, non-genuine H_2O bending mode, although it was a genuine mode of H_2O_3 . As a redundant coordinate terms due to S_4 in $\underline{F}(S)$ and $\underline{G}(S)$ were set equal to zero. Then the symmetry block reduced to a $(3 \times 3)a_1$ matrix.

Using the observed ν_1 , ν_T and ν_2 frequencies of H_2O (Table III.XI) and initial force constants of $k_{ii} = 1.000$, then the three iteration formulas converged in fifteen steps to:

$$k_{11} = 5.369 \times 10^5 \text{ dynes/cm}$$

$$k_{22} = 0.231 \times 10^5 \text{ dynes/cm}$$

$$k_{33} = 0.601 \times 10^5 \text{ dyne-cm}$$

With better choices of initial force constants, the formulas converged in four to five steps to $\pm 0.001 \times 10^{-5}$ dynes/cm. To convert k_{33} , k_{77} , k_{88} and k_{99} units from dyne-cm to dynes/cm it is only necessary to divide by the lengths of the arms forming the bending coordinates. The set of H_2O internal mode force constants were estimated:

$$k_{11}(\nu_1) = 5.369$$

$$k_{55}(\nu_3) = 5.482$$

$$k_{33}(\nu_2) = 0.666 \times 10^5 \text{ dynes/cm}$$

Of the three possible H_2O translations only two force constants were estimated:

$$k_{22}(T_z) = 0.231$$

$$k_{66}(T_y) = 0.192 \times 10^5 \text{ dynes/cm.}$$

Finally, three force constants associated with the three possible librations were estimated:

$$k_{99}(R_x) = 0.088$$

$$k_{77}(R_y) = 0.091$$

$$k_{88}(R_z) = 0.092 \times 10^5 \text{ dynes/cm.}$$

The above symmetry force constants were transformed back to internal coordinates force constants for comparison to those of other workers. For example, the symmetry force constants in terms of internal force constants are:

$$k_{11}(\nu_1) = k(r_1r_1) + k(r_1r_2)$$

$$k_{55}(\nu_3) = k(r_1r_1) - k(r_1r_2)$$

$$k_{33}(\nu_2) = k(\phi\phi)$$

$$k_{99}(R_x) = k(\theta_1'\theta_1') + k(\theta_1'\theta_2')$$

$$k_{77}(R_y) = k(\theta_1\theta_1) - k(\theta_1\theta_2)$$

$$k_{22}(T_z) = k(r_3r_3) + k(r_3r_4) \quad k_{88}(R_z) = k(\theta_1'\theta_1') - k(\theta_1'\theta_2')$$

$$k_{66}(T_y) = k(r_3r_3) - k(r_3r_4)$$

Thus one found that the internal coordinates force constants for H_2O are (in 10^5 dynes/cm):

internal	translational (O.....O stretch)	librational (O-H.....O bend)
$k(r_1 r_1) = 5.425$	$k(r_3 r_3) = 0.212$	$k(\theta_1' \theta_1') = 0.090$
$k(r_1 r_2) = -0.056$	$k(r_3 r_4) = 0.019$	$k(\theta_1' \theta_2') = -0.002$
$k(\phi\phi) = 0.666$		$*k(\theta_1 \theta_1) = 0.093$
		$*k(\theta_1 \theta_2) = -0.002$

Since the other symmetry coordinate involving θ_1 and θ_2 was assumed redundant and eliminated, then $k(\theta_1 \theta_1)$ could only be evaluated by assuming that $k(\theta_1 \theta_2) \equiv k(\theta_1' \theta_2') = -0.002 \times 10^5$ dynes/cm.

A set of D_2O force constants was estimated in the same way (from D_2O_3) as for H_2O . The results of the H_2O and D_2O ice I force constant models are listed in Table IV.IV along with the results of Zimmermann and Pimentel (97) and Trevino (93). Our $k(\theta_1 \theta_1)$ is an in-plane hydrogen bond bend while $k(\theta_1' \theta_1')$ is the out-of-plane bend. Our in-plane hydrogen bond bend is approximately 1.5 times Trevino's value: Part of the difference is probably due to differences in the models, Trevino's (93) was extended further and in a three-dimensional lattice while ours was planar.

The following comments can be made about the H_2O force constants estimated using the H_2O_3 model and equation [5]:

- the OH stretching force constant ($k(r_1 r_1) = 5.425 \times 10^5$ dynes/cm) is less than the gas phase value and is in the region predicted from the ratio of frequencies for harmonic oscillators,

Table IV.IV The force constants of ice I from the H_2O_3 and D_2O_3 models as well as the results of Pimentel and Zimmerman and Trevino.

Force Constant	Associated Motion	^{D₂O}	^{H₂O}	Trevino	
		Pimentel	This Work	This Work	(e)
		(a) i.r.	(f) i.r.	(f) i.r.	neutron
		(d)	(d)	(d)	(d)
k(r ₁ r ₁)	O-H str.		5.711	5.425	5.52
k(r ₁ r ₂)	O-H, O-H interaction		-0.049	-0.049	
k(r ₃ r ₃)	H····O str.	0.178	0.225	0.212	0.25
k(r ₃ r ₄)	H····O, H····O interaction		0.023	0.019	
k(θ ₁ θ ₁)	(b) O····H-O i.p.b.			0.093	0.06
k(θ ₁ θ ₂)	O····H-O, O···· H-O interaction			(-0.002)	
k(θ ₁ 'θ ₁ ')	(c) O····H-O o.p.b.	0.095	0.099	0.090	0.08
k(θ ₁ 'θ ₂ ')	interaction		-0.002	-0.002	
k(φφ)	HOH bending	0.49	0.730	0.666	0.62

(a) Pimentel and Zimmerman, Ref. 97 (b) i.p.b. = in-plane (linear) bend.

(c) o.p.b. = out-of-plane (linear) bend. (d) all force constants are

10^5 dynes/cm. (e) Trevino, Ref. 93. (f) This work, Green's formula,

H_2O_3 model.

- the hydrogen-bond stretching force constant ($k(r_3r_3) = 0.212 \times 10^5$ dynes/cm) is of the order of magnitude expected on the basis that the hydrogen bond strength (5-10 Kcal/mole) is about 1/25th of the O-H bond strength,
- the H-O-H bending force constant ($k_{33} = k(\phi\phi) = 0.666 \times 10^5$ dynes/cm) is slightly decreased from the gas phase value (0.69×10^5 dynes/cm) as expected from the shift in frequency, and
- the out-of-plane hydrogen bond bending ($O \cdots H-O$) force constant ($k(\theta_1'\theta_1') = 0.090 \times 10^5$ dynes/cm) is very small, this may be interpreted as indicating the hydrogen bond is relatively insensitive to bending through small angles.

It is interesting to notice that for every diagonal, internal coordinate force constant the D_2O values are larger than the H_2O values by 5 to 10%. The source of this effect is in the nature of the force constant model. Green's (125) formula [5] assumes a diagonal force field and a harmonic oscillator approach. Since D_2O energy levels are lower, and since D_2O internal coordinates displacements are smaller than H_2O displacements, then our D_2O "sees" a lower, more symmetric portion of the "true" potential curve. The simulated D_2O parabola is thus narrower and steeper than the simulated H_2O parabola and consequently the D_2O force constants are larger than the H_2O force constants. It is obvious that such diagonal H_2O_3 and D_2O_3 models assumed no anharmonicity in ice. Such a case seems highly unlikely in view of the strong neighbour-neighbour interaction through strong hydrogen bonds. In spite of this oversimplification, the force constants appear to give a faithful representation of the spectrum.

The test of any set of force constants, however, lies in its ability to reproduce the observed frequencies of isotopic analogues.

To check the force constants derived from H_2O_3 for the H_2O internal, translational and librational vibrations in ice, the frequencies of D_2O ice frequencies were calculated. Formula [5] was inverted and solved:

$$\lambda_i = k_{ii} \left[G_{ii} + \sum_{i \neq j} \frac{G_{ij}^2 k_{jj}}{\lambda_i - \lambda_j} \right] \quad [6]$$

where k_{ii} , k_{jj} are taken from $\text{H}_2\text{O}(\text{H}_2\text{O}_3)$

λ_j is taken to be the observed value, and

λ_i is to be calculated.

The a_2 and b_2 blocks are easily solved of course since they reduce to the form

$$\lambda_i = k_{ii} G_{ii}$$

in the absence of off-diagonal $\underline{G}(S)$ elements. The $(3 \times 3)b_1$ block and the $(3 \times 3)a_1$ (reduced from (4×4) by elimination of the redundant S_4 coordinate) yield two quadratic and one cubic equation each. The frequencies of the normal modes of D_2O ice I were found and are compared to the observed values below:

	$\nu_{\text{calc.}}$ cm^{-1}	$\nu_{\text{obs.}}$ cm^{-1}	$\nu_{\text{calc.}} - \nu_{\text{obs.}}$ cm^{-1}
ν_3	2325	2413	-88
ν_1	2258	2321	-63
ν_2	1138	1194	-56
ν_{R_x}	595	627 ^(a)	-32
ν_{R_y}	594	627 ^(a)	-33
ν_{R_z}	601	627 ^(a)	-26
T_x	229	220 ^(b)	+9
T_z	232	220 ^(b)	+12

(a) ν_{R_x} , ν_{R_y} and ν_{R_z} are assumed to be degenerate

(b) Reference 96.

The D_2O ice internal mode frequencies (ν_1, ν_2, ν_3) calculated from formula [6] using $H_2O(H_2O_3)$ force constants were all too low (-63 cm^{-1} , -56 cm^{-1} , -88 cm^{-1}) by 3 to 5%. The D_2O translational lattice frequencies calculated in the same way were too high by 5%. The modes of interest, for which the H_2O_3 model was constructed, are the librational lattice modes. Their calculated frequencies were also too low by 5 - 6%. It is interesting that the librational D_2O frequencies from the H_2O_3 model are nearly the same as those predicted for H_2O and D_2O in the weighted-lone-pair, moment-of-inertia model previously discussed. There the frequencies calculated were 586 cm^{-1} , 588 cm^{-1} and 591 cm^{-1} for ν_{Rx} , ν_{Ry} and ν_{Rz} respectively.

One can conclude that the H_2O_3 normal coordinate analysis, as a basis for H_2O/D_2O ice librations offers no improvement over a weighted lone-pairs moment-of-inertia model. The H_2O_3 model does give reasonable internal and lattice mode frequencies and reasonable ice force constants.

C. A Summary of H_2O , HDO and D_2O Librations

Three models of ice libration were presented: Blue's (85) harmonic, hindered oscillator model using moments-of-inertia, a weighted lone-pairs moments-of-inertia model, and a normal coordinate analysis of the H_2O_3 extended molecule. Blue's formula [4] gave widely dispersed ν_{Rx} and ν_{Ry} frequencies in H_2O and D_2O , i.e. separation of about 100 cm^{-1} . This did not conform to the observed ir absorption. The last two models were discussed on the assumptions that the librational modes were degenerate or nearly degenerate and that ν_{Rx} and ν_{Ry} are of equal intensity while ν_{Rz} was weak or inactive.

Transferring effective mass from a nearest-neighbour proton to the central molecule's lone-pair orbitals produced a nearly spherical top. The three principal moments-of-inertia differed by only ± 5 percent for the (H₂O, 3/4,1/4) option.

The force constants for molecular libration were $k_H = 0.60 \times 10^5$ dynes/cm at the attached proton and $k_H' = 0.21 \times 10^5$ dynes/cm at the detached proton. These two force constants were deduced from Blue's formula [4] assuming $\nu_{R_x} = \nu_{R_y} = 832 \text{ cm}^{-1}$. Application of k_H and k_H' to formula [4] in D₂O parameters predicted D₂O frequencies of:

$$\nu_{R_x} = 586 \text{ cm}^{-1}$$

$$\nu_{R_y} = 588 \text{ cm}^{-1}$$

$$\nu_{R_z} = 591 \text{ cm}^{-1}$$

The D₂O frequencies are reasonably degenerate, but lie six percent below the observed band maximum. Analogous results were obtained for an (H₂O, 1,1/4) effective mass option. Transferability of force constants among isotopic analogues was violated in the effective mass model, force constants estimated from H₂O and D₂O frequencies did not agree.

Normal coordinate analysis of the H₂O₃ extended molecule produced very good valence force constants and hydrogen-bond force constants. However, the H₂O force constants did not duplicate the D₂O frequencies. The dispersion was explained by considering the difference in shape of harmonic potential simulated by formula [5]. Degeneracy of the librational modes was acceptable in this model with respect to force constant evaluation.

Further improvements in the analysis of ice may be found by treating it as an extended three dimensional polymer. Techniques of normal coordinate analysis of polymers are now expanding. Zerbi's review (126) outlines the approach, a modification of the traditional Wilson FG method, and lists some references.

CHAPTER FIVE

CLATHRATE-HYDRATE EXPERIMENTAL DETAILS AND RESULTS

5.1 The Vitreous-Crystalline Clathrate-Mixture Phase Transformation

A. Experimental

Warm-up studies of the ir absorptions of vitreous, condensed mixtures of H_2O and guest species were completed in the liquid nitrogen cell (page 42). Stoichiometric gaseous mixtures corresponding to the three classes of clathrate-hydrate were prepared and condensed in the same manner as the ice samples (page 58). Samples studied in the first clathrate class (page 13) $6G \cdot 46H_2O$ were $G = CH_3Cl$, CH_3Br and Cl_2 , while for the second clathrate class (page 15) $8G \cdot 136H_2O$ the samples were for $G = CH_3I$, $CHCl_3$ and C_2H_5Br . Only one sample from the third class, $20G \cdot 172H_2O$ (page 15), was studied, i.e. $G = Br_2$. The conditions of sample formation and annealing are listed in Table V.I. In order to avoid separation of the clathrate mixture, all these samples were deposited through the heated metal deposition tube (page 44).

As with the H_2O , HDO and D_2O samples, the source beam was blocked when the clathrate mixture samples were warmed above $180^\circ K$, in order to prevent sublimation. As well, the cell chamber was not pumped when above $160^\circ K$. The temperatures quoted here are those which were measured by the copper-constantan thermocouple attached to the brass sample block: The sample temperatures were $10^\circ K$ higher due to source beam heating. However, the maximum annealing temperatures do not need to be corrected in that way since the source beam was off then.

Table V.I. The clathrate mixture sample histories for the deposition and annealing procedures. The deposition temperature refers to the sample block temperature with the source off.

		A	B2	C1 (C4)	D	E	F1 (F6)	G3	H
Molar gas ratio		1CH ₃ Cl: 7 H ₂ O	1CH ₃ Br: 7 H ₂ O	1CH ₃ I: 17H ₂ O	1CHCl ₃ : 17H ₂ O	1C ₂ H ₅ Br: 17H ₂ O	1Cl ₂ : 7 H ₂ O	1Cl ₂ : 7 H ₂ O	1Br ₂ : 8.6H ₂ O
Deposition Rate		10 sec	1.5 min	5 sec (--)	2 sec	3 sec	3 sec (2 min)	3 sec	3 sec
Sample Substrate		CsI	CsI	CsI	CsI	CsI	CsI	AgCl	AgCl
Deposition Temperature	°K	83	84	83 (83)	83	81	81 (82)	83	83
Annealing Time	Min	139	265	98 (105)	172	170	103 (25)	15	240
Maximum Annealing Temperature	°K	200	199	188 (189)	189	189	189 (190)	190	200
Time at Maximum Temperature	Min	12	45	16 (18)	15	16	12 (15)	11	25

All annealing processes were observed on the P.E. 421 spectrophotometer during warm-up from $85 \pm 5^\circ\text{K}$ to $180 \pm 10^\circ\text{K}$. Spectrophotometer controls were set for optimum response and were the same as for ice I (page 59) with small variations. The spectra were recorded at $85 \pm 5^\circ\text{K}$ immediately after deposition and at several temperatures between 85° and 180°K . Peaks and shoulders were assigned as for ice I (page 59).

B. Results of Devitrification

While the degree of crystallinity of the samples condensed from the vapour phase depended upon the sample history, the basic results for all the unannealed, vitreous samples were the same. Consequently, only one set of normal annealing results will be discussed in detail. Some irregularities were observed for $6\text{Cl}_2 \cdot 46\text{H}_2\text{O}$ condensed and annealed on a CsI window: Those results will be discussed separately. Each of the H_2O skeletal bands ($\nu_1 + \nu_T$), ν_3 , ν_1 , $3\nu_R$, $\nu_2/2\nu_R$ and ν_R was analyzed, as were those guest absorptions which were observed. No distinction between the classes of clathrates was noticed in this work.

(i) The Effect of Devitrification on the Lattice Peak Maxima

For the seven samples listed previously (page 215) only the results of the chloromethane clathrate mixture will be given. The six other samples (including Cl_2 on CsI) had the same behaviour within the limits of error. The frequency-temperature dependences of the main H_2O skeletal features are shown in Fig. 5.1. The absorption spectra of some unannealed and annealed samples (all at $83 \pm 3^\circ\text{K}$) are shown in Figs. 5.2, 5.3 and 5.4. Some details of the $\text{CH}_3\text{Cl} \cdot 7.67\text{H}_2\text{O}$ clathrate mixture annealing (Fig. 5.1) are

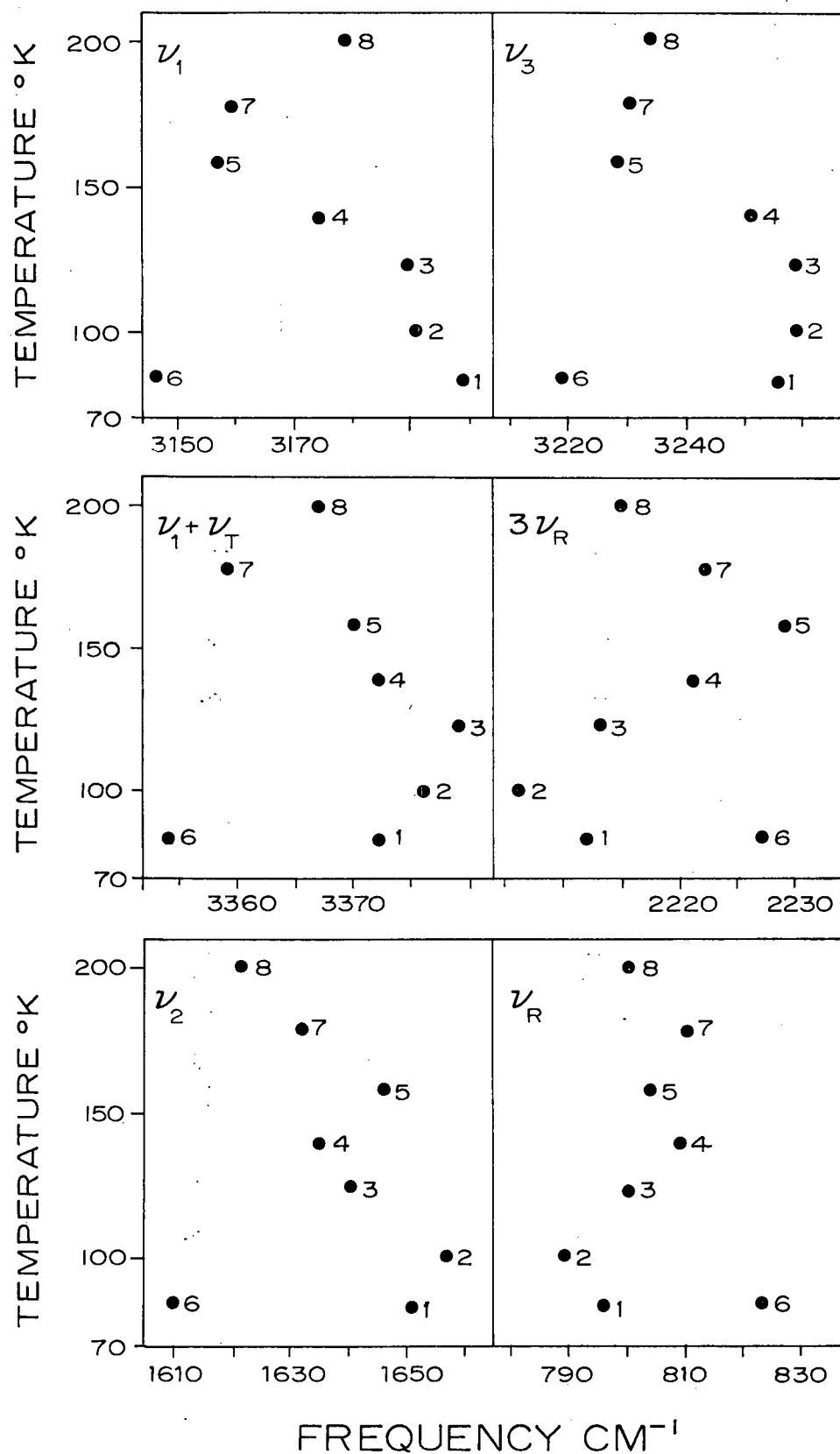


Fig. 5.1 The shifts of the unannealed clathrate mixture ($\text{CH}_3\text{Cl} \cdot 7.67\text{H}_2\text{O}$) H_2O peaks during warming from $83 \pm 3^{\circ}\text{K}$ to $200 \pm 5^{\circ}\text{K}$. The data are typical of all the clathrate mixtures and appear to be the same as for ice Iv. The data are numbered in the order of observation.

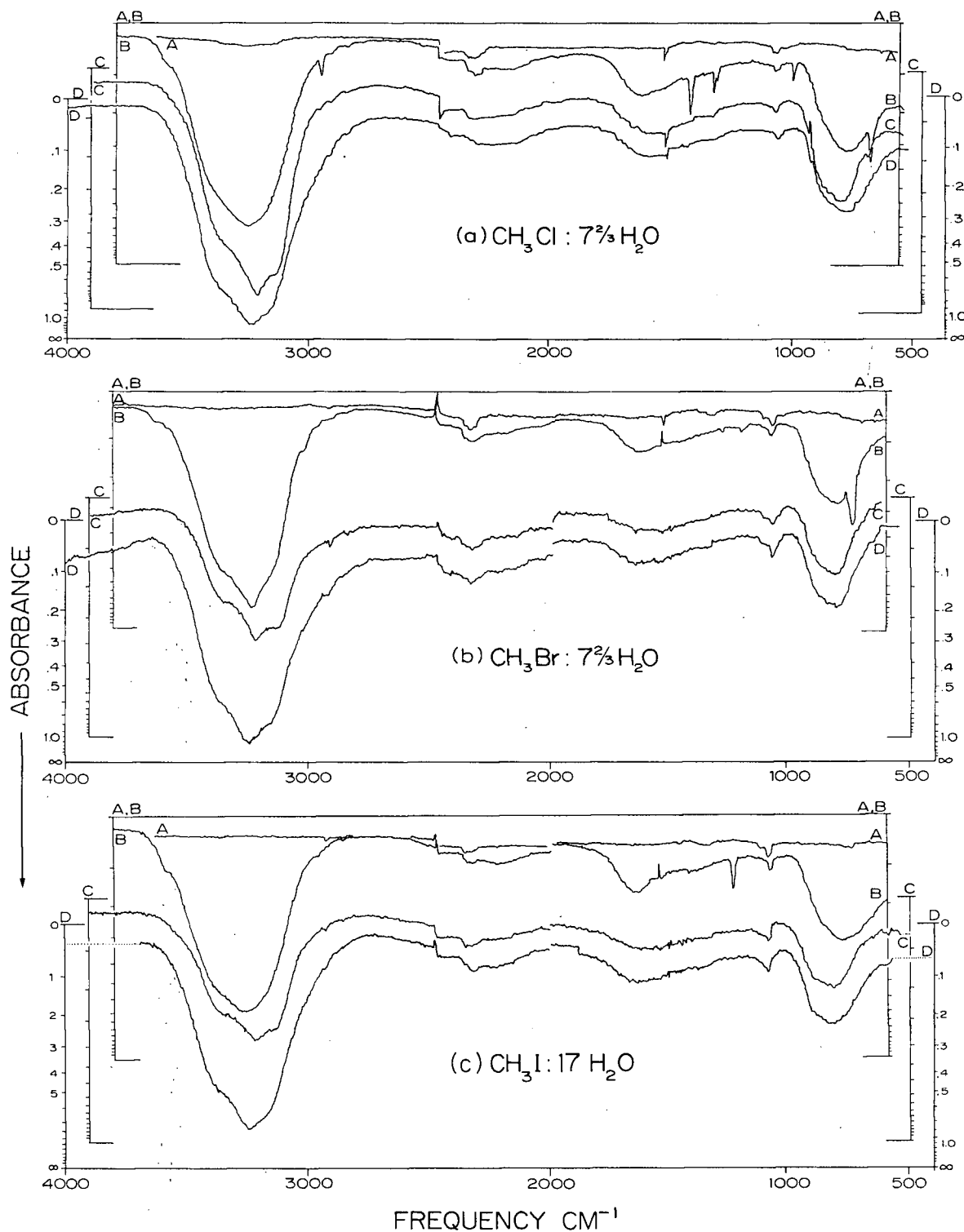


Fig. 5.2 The infrared absorption spectra of some clathrate mixtures. In all cases spectra numbered "A" are backgrounds through the low temperature cell. (a) $\text{CH}_3\text{Cl} \cdot 7.67\text{H}_2\text{O}$ unannealed at $83 \pm 3^\circ\text{K}$ (B), at $83 \pm 3^\circ\text{K}$ but annealed to $160 \pm 3^\circ\text{K}$ (C), and at 200°K (D). (b) $\text{CH}_3\text{Br} \cdot 7.67\text{H}_2\text{O}$ unannealed at $83 \pm 3^\circ\text{K}$ (B), at $83 \pm 3^\circ\text{K}$ but annealed to $158 \pm 3^\circ\text{K}$ (C) and at $189 \pm 3^\circ\text{K}$ (D). (c) $\text{CH}_3\text{I} \cdot 17\text{H}_2\text{O}$ unannealed at $83 \pm 3^\circ\text{K}$ (B), annealed to $190 \pm 5^\circ\text{K}$ but observed at $83 \pm 3^\circ\text{K}$ (C) and at $188 \pm 3^\circ\text{K}$ (D). The same frequency scale applies to all of the spectra, i.e. for each absorbance scale.

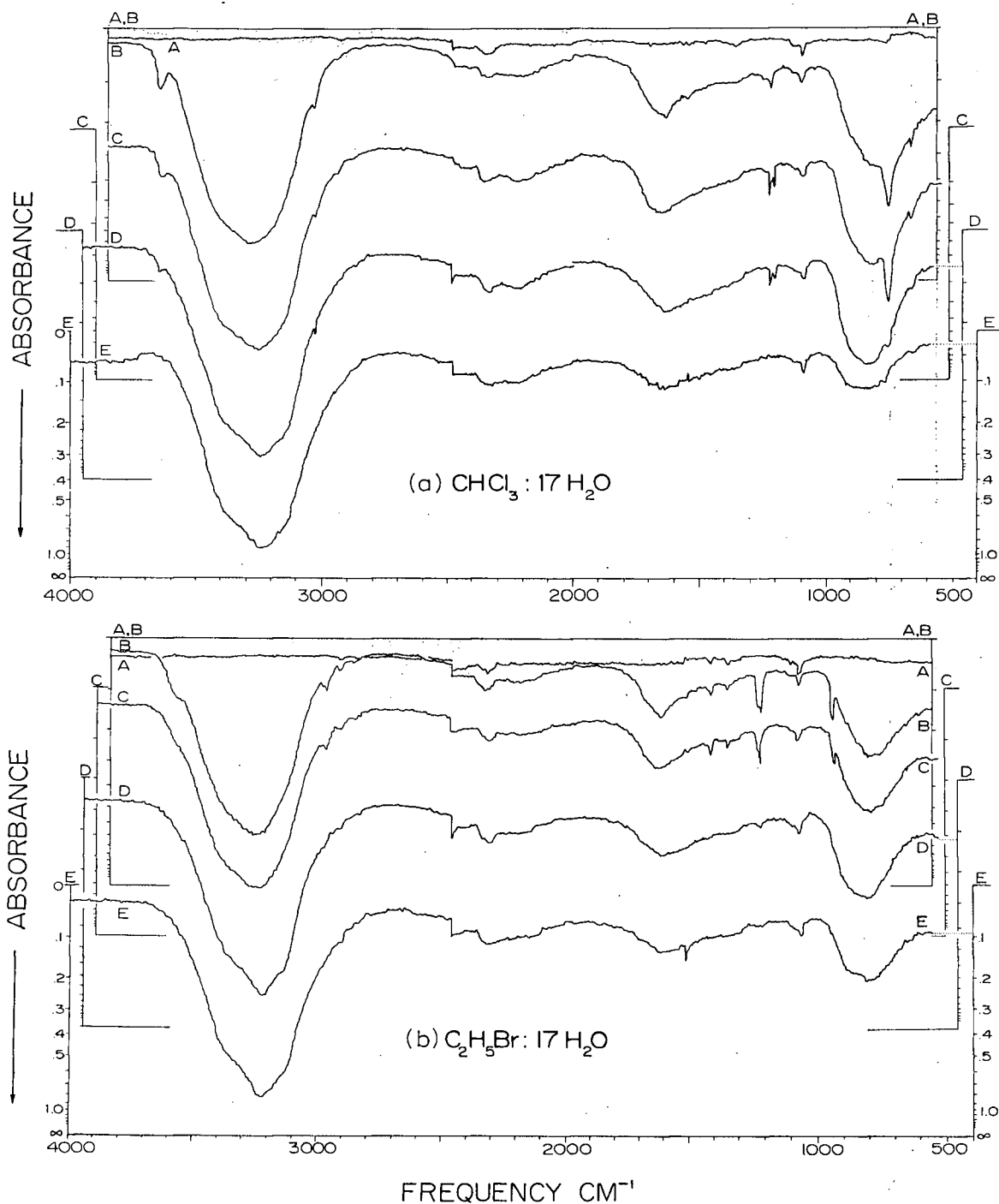


Fig. 5.3 The effects of annealing clathrate mixtures of CHCl_3 and $\text{C}_2\text{H}_5\text{Br} \cdot 17\text{H}_2\text{O}$. (a) $\text{CHCl}_3 \cdot 17\text{H}_2\text{O}$ unannealed at $83 \pm 3^\circ\text{K}$ (B), at $129 \pm 3^\circ\text{K}$ (C), at $149 \pm 3^\circ\text{K}$ (D) and at $189 \pm 5^\circ\text{K}$ (E). (b) $\text{C}_2\text{H}_5\text{Br} \cdot 17\text{H}_2\text{O}$ unannealed at $83 \pm 3^\circ\text{K}$ (B), at $129 \pm 3^\circ\text{K}$ (C), at $149 \pm 3^\circ\text{K}$ (D) and at $189 \pm 3^\circ\text{K}$ (E). The same frequency scale applies to each absorbance scale, i.e. a shorter span of frequencies is shown for D than for E.

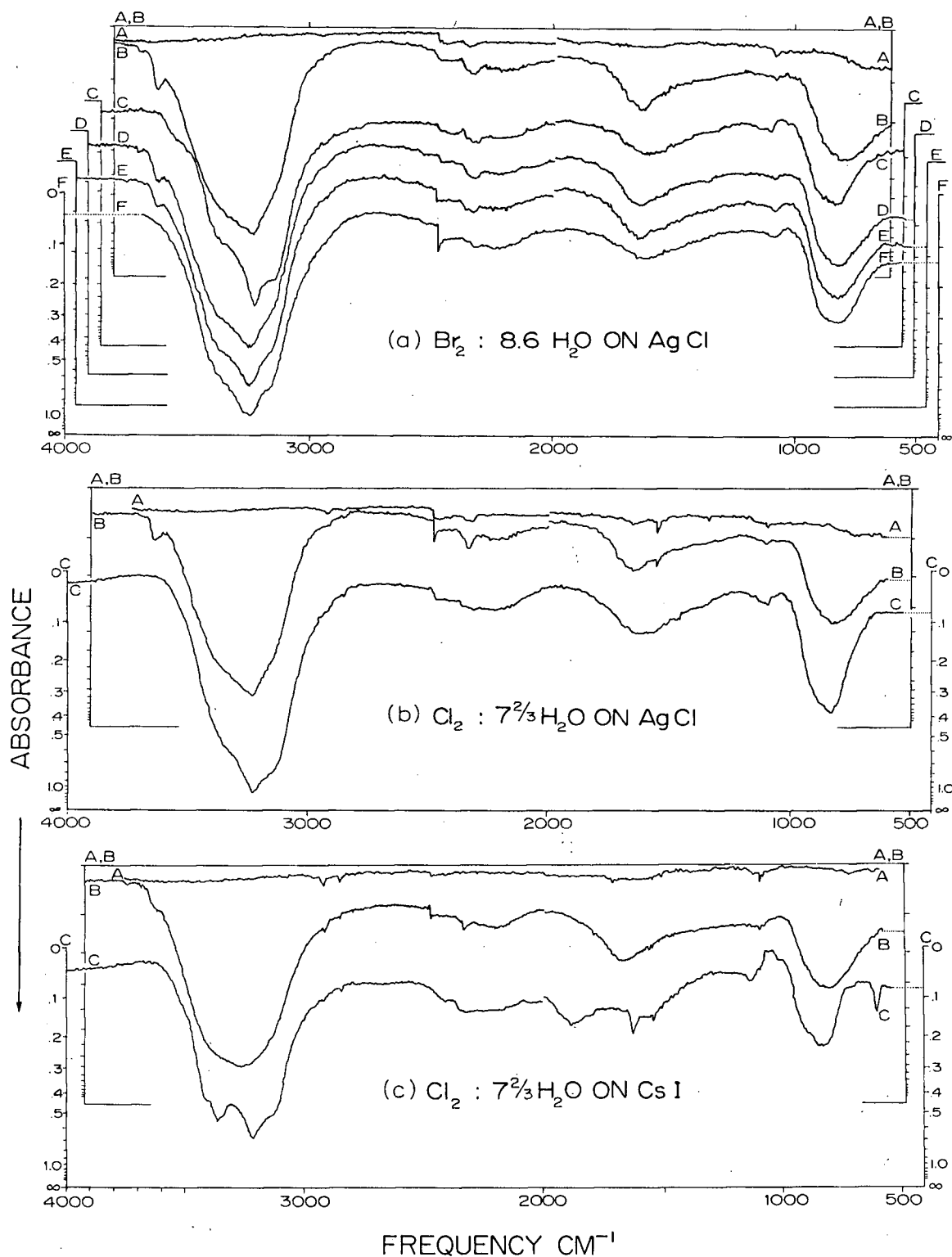


Fig. 5.4 (a) $\text{Br}_2 \cdot 8.6 \text{ H}_2\text{O}$ on AgCl unannealed at $83 \pm 3^\circ\text{K}$ (B,C), at $130 \pm 3^\circ\text{K}$ (D,E) and at $170 \pm 3^\circ\text{K}$ (F). Spectra B and C were recorded six hours apart while spectra D and E were recorded thirty minutes apart. (b) $\text{Cl}_2 \cdot 7.67 \text{ H}_2\text{O}$ on AgCl unannealed at $83 \pm 3^\circ\text{K}$ (B) and at $83 \pm 3^\circ\text{K}$ but annealed to $190 \pm 5^\circ\text{K}$ (C). (c) $\text{Cl}_2 \cdot 7.67 \text{ H}_2\text{O}$ on CsI unannealed at $83 \pm 3^\circ\text{K}$ (B) and at $83 \pm 3^\circ\text{K}$ but annealed to $190 \pm 5^\circ\text{K}$ for 15 minutes (C).

in Table V.II. As for ice I, the frequency shifts of the vitreous sample peaks were irreversible. The points in Fig. 5.1 are numbered in the sequence in which they were obtained for each band. The sixth point was obtained by cooling the sample to $83 \pm 3^\circ\text{K}$ after annealing it at $160 \pm 3^\circ\text{K}$ for 20 minutes and before warming to higher temperatures.

Table V.II The H_2O frequencies of the $\text{CH}_3\text{Cl} \cdot 7.67\text{H}_2\text{O}$ clathrate mixture before (ν^u) and after (ν^a) annealing to $200 \pm 5^\circ\text{K}$. The transformation temperature range and the temperature dependence after annealing are shown.

	82°K unannealed ν^u	82°K annealed ν^a	82°K $\Delta\nu$ $\nu^a - \nu^u$	Transformation Temperature Range	$\frac{\Delta\nu^a}{\Delta T}$
	cm^{-1}	cm^{-1}	cm^{-1}	$^\circ\text{K}$	$\text{cm}^{-1}/^\circ\text{K}$
$\nu_1 + \nu_T$	3382 ± 5	3364	-18	$(140-170) \pm 10$	0.10
ν_3	3258 ± 3	3219	-39	$(140-160) \pm 10$	0.12
ν_1	3195 ± 5	3146	-49	$(130-155) \pm 10$	0.25
$3\nu_R$	2209 ± 5	2227	+18	$(125-155) \pm 10$	-0.09
ν_2	1654 ± 3	1610	-44	$(125-140) \pm 10$	0.18
ν_R	792 ± 4	823	+31	$(115-140) \pm 10$	-0.16

The five conclusions made with respect to the ice I devitrification (page 63) apply to H_2O in these clathrate mixtures also.

Typical visual observations of the annealing process are illustrated by those for $\text{CH}_3\text{Cl} \cdot 7.67\text{H}_2\text{O}$:

- at $83 \pm 3^\circ\text{K}$ (before annealing) a transparent film around a translucent, milky-white mass about 0.25 inches in diameter,
- at $168 \pm 3^\circ\text{K}$ an opaque white mass opposite the nozzle surrounded by a thin transparent film, and
- at $188 \pm 3^\circ\text{K}$ the sample appeared to be totally white and opaque.

In general, the source image was centered on the thinner portion of the sample. The $\text{Br}_2 \cdot 8.6\text{H}_2\text{O}$ mixtures were not white, but were orange and yellow-orange depending on the thickness.

(ii) The Effects of Devitrification on the Oligomeric H_2O Bands

Weak peaks and shoulders on the high frequency side of the skeletal unannealed H_2O stretching band had the same appearance as for vitreous ice I (Fig. 3.3) and can be seen in Figs. 5.2, 5.3 and 5.4. The positions of these oligomeric H_2O absorptions for various unannealed clathrate mixtures at $83 \pm 3^\circ\text{K}$ immediately after deposition are given in Table V.III: In some cases a number of specimens were observed. The positions of the peaks depend on the rate of sample deposition. For example, the three CH_3Br sets of results were obtained from mixtures deposited through a needle valve in 4.5, 1.5 and 11 minutes respectively. The temperature dependences of the H_2O oligomeric absorptions from a number of clathrate mixtures are given in Table V.IV. With a single exception the oligomeric H_2O absorptions began to diminish in peak height between 120 and 129°K and had disappeared below 170°K , Table V.V.

Table V.III The frequencies at $83 \pm 3^\circ\text{K}$ of the weak peaks and shoulders associated with oligomeric H_2O units in several unannealed clathrate mixtures.

CH_3Cl $\cdot 7.67\text{H}_2\text{O}$	CH_3Br $\cdot 7.67\text{H}_2\text{O}$	CH_3I $\cdot 17\text{H}_2\text{O}$	CHCl_3 $\cdot 17\text{H}_2\text{O}$	$\text{C}_2\text{H}_5\text{Br}$ $\cdot 17\text{H}_2\text{O}$	Br_2 $\cdot 8.6\text{H}_2\text{O}$	CsI Cl_2 $\cdot 7.67\text{H}_2\text{O}$	AgCl Cl_2 $\cdot 7.67\text{H}_2\text{O}$	H_2O ice I_v
$\pm 5 \text{ cm}^{-1}$	$\pm 5 \text{ cm}^{-1}$	$\pm 5 \text{ cm}^{-1}$	$\pm 5 \text{ cm}^{-1}$	$\pm 5 \text{ cm}^{-1}$	$\pm 5 \text{ cm}^{-1}$	$\pm 5 \text{ cm}^{-1}$	$\pm 5 \text{ cm}^{-1}$	$\pm 5 \text{ cm}^{-1}$
3654 (vw)	3645 (vw)	3580 (w)	3689 (vww)	3643 (vw)	3691 (vww)	3689 (vww)	3635 (vw)	3687
3583 (w)	3605 (vw)		3639 (vw)	3565 (w)	3612 (vw)	3672 (vw)		3658
						3635 (w)		3637
						3687 (vww)		
						3670 (vw)		
						3617 (w)		
		3687 (vww)						
		3668 (vww)	3673 (w)				3623 (vw)	
		3648 (vww)	3636 (vw)					
	3620 (w)	3625 (vww)	3638 (vw)			3689 (vww)		
			3642 (w)			3620 (w)		
	3690 (vw)					3690 (vww)	3624 (vw)	
						3671 (vw)		
						3614 (w)		

Table V.IV The temperature dependences of the oligomeric H₂O absorption frequencies of some clathrate mixtures and unannealed ice I.

	85±3°K	94±3°K	110±3°K	125±3°K
H ₂ O Ice I _v cm ⁻¹	3687 3658 3637	3689 3674 3650 3640	3690 3647	3690
	83±3°K	109±3°K	129±3°K	149±3°K
CHCl ₃ ·17 H ₂ O cm ⁻¹	3689 (sh) 3639(0.11)	3687 (sh) 3640(0.10)	3673 (sh) 3640(0.06)	3672 (sh) 3652 (sh) 3634(0.04)
	83±3°K	110±3°K	129±3°K	150±3°K
C ₂ H ₅ Br·17 H ₂ O cm ⁻¹	3643 (wsh) 3565 (msh)	3669 (wsh) 3638 (wsh) 3569 (msh)	3658 (wsh) 3563 (msh)	
	81±3°K	109±3°K	129±3°K	149±3°K
Cl ₂ ·7.67 H ₂ O cm ⁻¹	3689 (vbw) 3672 (vbw) 3635 (wsh)	3688 (vbw) 3675 (vbw) 3630 (wsh)	3688 (vbw) 3669 (vbw) 3636 (wsh)	
	83±3°K	130±3°K	130±3°K +0.5 hours	170±3°K 83±3°K
Br ₂ ·8.6 H ₂ O cm ⁻¹	3691(0.02) 3612(0.10)	3693(0.02) 3616(0.08)	3609(0.06)	3563 (sh) 3528 (sh)

Table V.V The temperatures at which the oligomeric peak heights began to decrease (T_1) and the maximum temperature at which they were observed (T_2)

Guest	T_1	T_2
CH_3Cl	$\pm 5^\circ\text{K}$ 120	$\pm 5^\circ\text{K}$ 120
CH_3Br	120	< 138
CH_3I	120	< 140
CHCl_3	149	< 169
$\text{C}_2\text{H}_5\text{Br}$	125	< 150
Br_2	--	> 185
$\text{Cl}_2(\text{CsI})$	129	< 149
H_2O ice I_v	110	125

For the $\text{Br}_2 \cdot 8.6\text{H}_2\text{O}$ mixture the oligomeric absorptions were observed at $170 \pm 3^\circ\text{K}$ during annealing and even at $83 \pm 3^\circ\text{K}$ after annealing, Fig. 5.4. The visual appearance of the $\text{Br}_2 \cdot 8.6\text{H}_2\text{O}$ sample changed markedly during annealing above $185 \pm 3^\circ\text{K}$ (with the source beam off): The sample was annealed for 10 minutes at $185 \pm 3^\circ\text{K}$, 10 minutes at $190 \pm 3^\circ\text{K}$ and for 3 minutes at $200 \pm 3^\circ\text{K}$. After 1 minute at $200 \pm 3^\circ\text{K}$ the sample changed from orange-brown to a rusty-brown surface layer. After 3 minutes at $200 \pm 3^\circ\text{K}$ the rusty-brown layer had sublimed off.

(iii) The Effects of Devitrification on $\text{Cl}_2 \cdot 7.67\text{H}_2\text{O}$ Mixtures

Gaseous mixtures of $\text{Cl}_2 \cdot 7.67 \text{H}_2\text{O}$ condensed on CsI and annealed for long periods appeared to react with the CsI. Consequently the $\text{Cl}_2 \cdot 7.67 \text{H}_2\text{O}$ mixture was studied on two substrates, i.e. CsI and AgCl, samples F and G respectively. In all six samples were studied on CsI and three on AgCl.

(a) $\text{Cl}_2 \cdot 7.67\text{H}_2\text{O}$ on CsI (sample F). The ir absorption spectra of $\text{Cl}_2 \cdot 7.67\text{H}_2\text{O}$ at $83 \pm 3^\circ\text{K}$ before and after annealing to 189°K were shown in Fig. 5.4 (sample F_1), while the temperature-frequency dependences of the H_2O skeletal absorptions were the same as for $\text{CH}_3\text{Cl} \cdot 7.67\text{H}_2\text{O}$ (Fig.5.1). The effect of annealing $\text{Cl}_2 \cdot 7.67\text{H}_2\text{O}$ to progressively higher temperatures is shown in Fig. 5.5 (sample F_6). The visual appearance of sample F_1 before and during annealing was:

- (between 83 ± 3 and $110 \pm 3^\circ\text{K}$) a cone of opaque white material which became gradually more transparent at the base of the cone,
- (at $169 \pm 3^\circ\text{K}$) a generally opaque white sample 0.5 inches in diameter, and
- (at $83 \pm 3^\circ\text{K}$ after annealing) a uniformly white opaque sample.

The visual appearance of sample F_6 before and during annealing was the same as for sample F_1 . By visual observation no distinction could be drawn between the samples annealed to 170 ± 3 , 180 ± 3 and $190 \pm 3^\circ\text{K}$ although their spectra differed.

In the spectrum of sample F_6 the absorption between 3000 cm^{-1} and 2400 cm^{-1} increased as the sample was annealed to higher temperatures. Also notice the dramatic effect on the stretching band due to annealing to

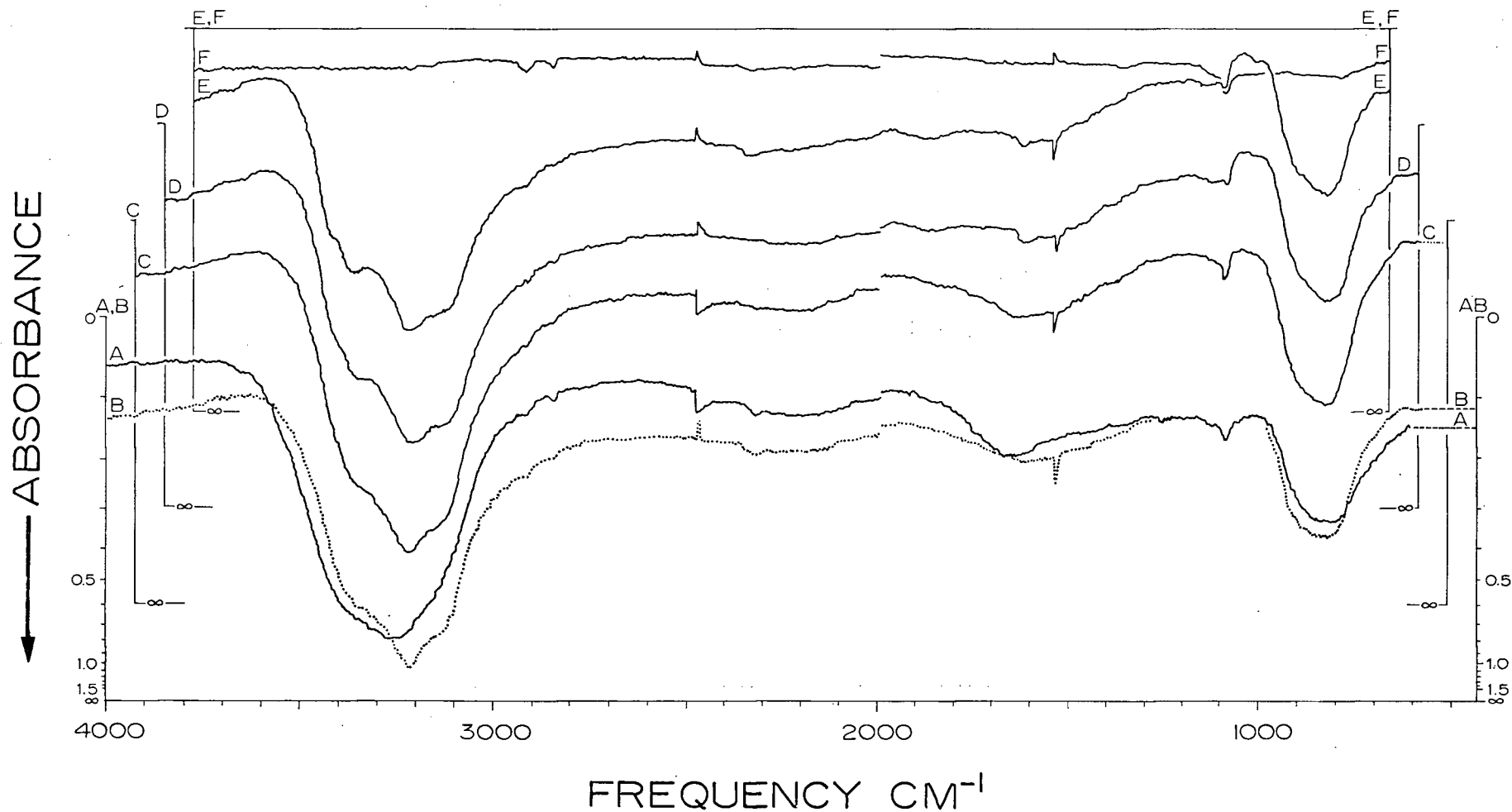


Fig. 5.5 Spectra of one sample of $\text{Cl}_2 \cdot 7.67\text{H}_2\text{O}$ on CsI at 83°K with various successive annealing times: (A) Unannealed, (B) annealed to 170°K for 15 minutes, (C) annealed after (B) to 180°K for 15 minutes, (D) then annealed to 190°K for 15 minutes, (E) then annealed to 190°K for 30 minutes, and (F), background through low temperature cell at 83°K .

$190 \pm 2^\circ\text{K}$, i.e. the intensity of the low frequency shoulder increased and a new high frequency shoulder appeared. Annealing to $170 \pm 2^\circ\text{K}$ or $180 \pm 2^\circ\text{K}$ gave only the characteristic sharpening into 1 peak and 2 shoulders. As well, the nature of the ν_2 absorption changed.

(b) $\text{Cl}_2 \cdot 7.67\text{H}_2\text{O}$ on AgCl (sample G). Detailed studies of the annealing process of amorphous solid $\text{Cl}_2 \cdot 7 \text{H}_2\text{O}$ on an AgCl substrate were not made. Spectra were recorded at $83 \pm 3^\circ\text{K}$ before and after annealing to various temperatures. The visual appearances were as before, i.e. a clear and transparent sample except for one spot opposite the nozzle before annealing and a uniform opaque white sample after annealing. Cl_2 guest absorption as might be expected was not observed and the H_2O skeletal absorption was shown in Fig. 5.4.

None of our attempts to split the $\text{Cl}_2 \cdot 7.67\text{H}_2\text{O}$ stretching band into 1 peak and 3 shoulders succeeded for samples on an AgCl window. Nor was the nature of the ν_2 band changed. As well, no increased absorption between 3000 cm^{-1} and 2400 cm^{-1} was observed. The positions of the $\text{Cl}_2 \cdot 7.67\text{H}_2\text{O}$ bands on CsI and AgCl will be discussed in section 5.3 (page 234).

5.2 Clathrate Mixture Guest Absorptions

The ir absorptions due to the guest molecules which were expected to be trapped in the cages of the H_2O host lattice were formed and observed by three techniques. In the first method (section 5.1) the stoichiometric gaseous mixtures were condensed rapidly onto a substrate held at $83 \pm 3^\circ\text{K}$ in an open chamber (section 2.4C). To ensure that the guest molecules were not diffusing out of the host lattice, a second and a third method

were investigated. The second method was condensation of the mixtures in an isolated chamber (section 2.4B), and the third method was the preparation and observation of low temperature mulls (section 2.4A) of solid clathrate mixtures (section 2.3A). Of the seven clathrate mixtures studied, $\text{Cl}_2 \cdot 7.67\text{H}_2\text{O}$ and $\text{Br}_2 \cdot 8.6\text{H}_2\text{O}$ should have no guest ir absorptions.

A. Condensation in an Open Chamber

During devitrification of these samples the temperature at which the guest absorption peak heights began to diminish and the temperature at which they were absent varied considerably from sample to sample. However, since the behaviours were generally the same only one or two cases will be described in detail.

For example, the $\text{CH}_3\text{Cl} \cdot 7.67\text{H}_2\text{O}$ guest absorptions were observed at 2957 (m), 1443 (m), 1437 (sh), 1347 (w) 1338 (vw), 1021 (vw) and 700 (ms) cm^{-1} (Fig. 5.2(a)) near the solid CH_3Cl absorptions. They were observed up to $100 \pm 3^\circ\text{K}$ with undiminished intensity and up to $160 \pm 3^\circ\text{K}$ with diminishing intensity. In contrast $\text{CH}_3\text{I} \cdot 17\text{H}_2\text{O}$ guest absorptions were undiminished up to $138 \pm 2^\circ\text{K}$ and nil at $168 \pm 2^\circ\text{K}$ for one specimen; while for a second specimen the CH_3Br absorptions were slightly diminished at $110 \pm 3^\circ\text{K}$ and slowly diminishing up to $189 \pm 3^\circ\text{K}$ (the 1235 cm^{-1} peak was still present). The guest absorptions from a number of unannealed clathrate mixtures at $83 \pm 3^\circ\text{K}$, immediately after deposition, are listed in Table V.VI. The variations of those guest absorptions as a function of temperature are given in Table V.VII and the temperatures of the onset of alteration in guest absorptions and the maximum temperature at which they were observed are given in Table V.VIII.

Table V.VI The alkyl halide guest absorptions at $83 \pm 3^\circ\text{K}$ in a number of alkyl halide clathrate mixtures before annealing began

CH_3Cl $\cdot 7.67\text{H}_2\text{O}$	CH_3Br $\cdot 7.67\text{H}_2\text{O}$	CH_3I $\cdot 17\text{H}_2\text{O}$	$\text{CHCl}_3 \cdot 17\text{H}_2\text{O}$			$\text{C}_2\text{H}_5\text{Br}$ $\cdot 17\text{H}_2\text{O}$
cm^{-1}	cm^{-1}	cm^{-1}	cm^{-1}	cm^{-1}	cm^{-1}	cm^{-1}
2957 (m)	3020 (sh)			3020 (m)	3014 (sh)	3016 (sh)
	2965 (sh)	2950 (w)	2936 (vbw)			
1443 (m)			2915 (vbw)			2985 (vw)
1437 (sh)						
	1292 (vbw)					
1347 (w)	1218 (vbw)	1238 (w)	1244 (sh)	1238 (sh)	1241 (vbw)	1238 (vbw)
1338 (vw)	1200 (sh)	1233 (sh)	1234 (w)	1214 (w)	1216 (vw)	1214 (vw)
						1254 (vw)
						1242 (vw)
1021 (vw)				1054 (vw)		955 (w)
700 (ms)	750 (s)			755 (ms)	752 (ms)	752 (ms)
						760 (sh)
				665 (w)	665 (w)	663 (w)

Table V.VII The temperature dependences of the guest absorptions during the annealing of clathrate mixtures. These data are typical of all samples.

	83±3°K	110±3°K		
	<u> </u>	<u> </u>		
CH ₃ I·17H ₂ O	2950 (w)	2960 (sh)		
	1238 (w)	1247 (w)		
	1233 (sh)	1240 (vw)		
	<u> </u>	<u> </u>		
	83±3°K	139±3°K		
	<u> </u>	<u> </u>		
	2936 (vvw)	2939 (vvw)		
	2915 (vvw)	2917 (vvw)		
	1244 (sh)	1244 (sh)		
	1234 (w)	1236 (w)		
	83±3°K	110±3°K	129±3°K	150±3°K
	<u>±2 cm⁻¹</u>	<u>±2 cm⁻¹</u>	<u>±2 cm⁻¹</u>	<u>±2 cm⁻¹</u>
C ₂ H ₅ Br·17H ₂ O	2985 (vw)	2983 (vw)	2981 (vw)	
	1254 (vw)	1255 (vw)	1252 (sh)	1258 (sh)
	1242 (vw)	1245 (w)	1245 (vw)	1245 (vvw)
	955 (w)	956 (w)	952 (vw)	
	760 (sh)	760 (sh)	763 (sh)	

Table V.VIII The temperature at which the guest absorptions peak heights began to decrease (T_1), and the maximum temperature at which they were observed (T_2).

Guest	T_1	T_2
$G \cdot 7.67H_2O$	$\pm 3^\circ K$	$\pm 3^\circ K$
CH_3Cl	100	160
CH_3Br	138	< 170
$G \cdot 17H_2O$		
CH_3I	138	< 168
	110	> 189
$CHCl_3$	129	< 189
		> 169
C_2H_5Br	110	< 170

The guest frequencies shifted very little, if at all, upon warming for devitrification, however the peaks did sharpen near $125 \pm 5^\circ K$. For example, in annealing $CHCl_3 \cdot 17H_2O$ (Fig.5.3(a)) the absorptions near 1200 cm^{-1} sharpened at $129 \pm 3^\circ K$. In fact it split into two distinct peaks at 1223 and 1203 cm^{-1} and a shoulder at 1214 cm^{-1} . As well the guest absorptions near 3000 cm^{-1} and 750 cm^{-1} sharpened at $129 \pm 3^\circ K$. Although the two $CHCl_3$ peaks at 1223 and 1203 cm^{-1} were observed as high as $149 \pm 3^\circ K$, the point is that they were unobserved after annealing.

B. Condensation in an Isolated Chamber

The condensation apparatus and the technique were described in sections 1.6 and 2.4B respectively. Stoichiometric mixtures of $\text{Cl}_2 \cdot 7.67\text{H}_2\text{O}$, $\text{SO}_2 \cdot 7.67\text{H}_2\text{O}$, $\text{CH}_3\text{Cl} \cdot 7.67\text{H}_2\text{O}$, $\text{CH}_3\text{Br} \cdot 7.67\text{H}_2\text{O}$, $\text{CCl}_3\text{F} \cdot 17\text{H}_2\text{O}$, and $\text{CH}_3\text{I} \cdot 17\text{H}_2\text{O}$ were condensed rapidly in a precooled chamber and annealed to $185 \pm 5^\circ\text{K}$ for 2 - 5 minutes. Spectra were subsequently recorded at $83 \pm 3^\circ\text{K}$ on the P.E. 112-G spectrophotometer.

The results of this method were the same as for condensation and devitrification in an open chamber. No guest absorptions were observed in the annealed samples, while the H_2O "host" absorptions were the same as for section 5.1 but with considerably more scattering. As well these samples had spectra much like $\text{Cl}_2 \cdot 7.67\text{H}_2\text{O}$ (on CsI) between 3000 and 2200 cm^{-1} (Fig. 5.4(c)).

C. Low Temperature Mulls

The technique was described in section 2.4A and spectra were recorded on the P.E. 421 spectrophotometer. The present samples were mulled from ground solids prepared by freezing-warming cycles on stoichiometric liquid mixtures. At $83 \pm 3^\circ\text{K}$ $\text{CH}_3\text{I} \cdot 17\text{H}_2\text{O}$ and $\text{CCl}_3\text{F} \cdot 17\text{H}_2\text{O}$ had no guest absorptions and the H_2O skeletal absorptions were like those reported in section 5.1 for annealed samples. However, the scattering was greater than in methods 5.2A or 5.2B.

Some guest absorptions may have been masked by the C_3H_8 and CClF_3 mulling agent absorptions, but it seems unlikely that all the CH_3I peaks would be masked by both agents. Several thicknesses of samples and amounts of mulling agent were tried, all with the same results.

5.3 Temperature Dependence of the Crystalline

Clathrate Mixture Absorptions

The results of warming annealed samples of clathrate mixtures from 4.2°K or 77°K to 200°K are in general the same as for cubic ice I, i.e. only the H₂O ir absorptions were observed. Thus only a few typical clathrate mixture results will be quoted and the remaining clathrate mixture results will be given in tabular form or as an average over all samples.

A. Temperature Dependence of the HDO Absorptions

(i) Experimental

The data reported here for $\nu_{\text{OH}}(\text{HDO})$ in $\text{CH}_3\text{Cl}\cdot 7.67\text{D}_2\text{O}$, $\text{CH}_3\text{Br}\cdot 7.67\text{D}_2\text{O}$ and $\text{CH}_3\text{I}\cdot 17\text{D}_2\text{O}$, for $\nu_{\text{OD}}(\text{HDO})$ in $\text{CH}_3\text{Br}\cdot 7.67\text{H}_2\text{O}$, and for $\nu_{\text{R}}(\text{HDO})$ in $\text{CH}_3\text{Br}\cdot 7.67\text{D}_2\text{O}$ were obtained from gaseous samples condensed in an open chamber followed by devitrification (section 5.1). The observations were made with the liquid helium dewar and the P.E. 421 spectrophotometer. Details of the sample histories were typical of those for ice I (page 69) as were details of spectrophotometer operating conditions. The HDO peak maxima were determined as before (page 69) and were estimated to within $\pm 0.5 \text{ cm}^{-1}$.

(ii) Results of Warming Clathrate Mixtures Containing HDO

(a) The HDO stretching bands. These bands appeared to be the same as in cubic ice I (Fig. 3.1) and typical spectra will not be reproduced. The temperature dependences of $\nu_{\text{OH}}(\text{HDO})$ and $\nu_{\text{OD}}(\text{HDO})$ for $\text{CH}_3\text{Br}\cdot 7.67\text{H}_2\text{O}$ are shown in Figs. 5.6 and 5.7: They are typical of the other clathrate

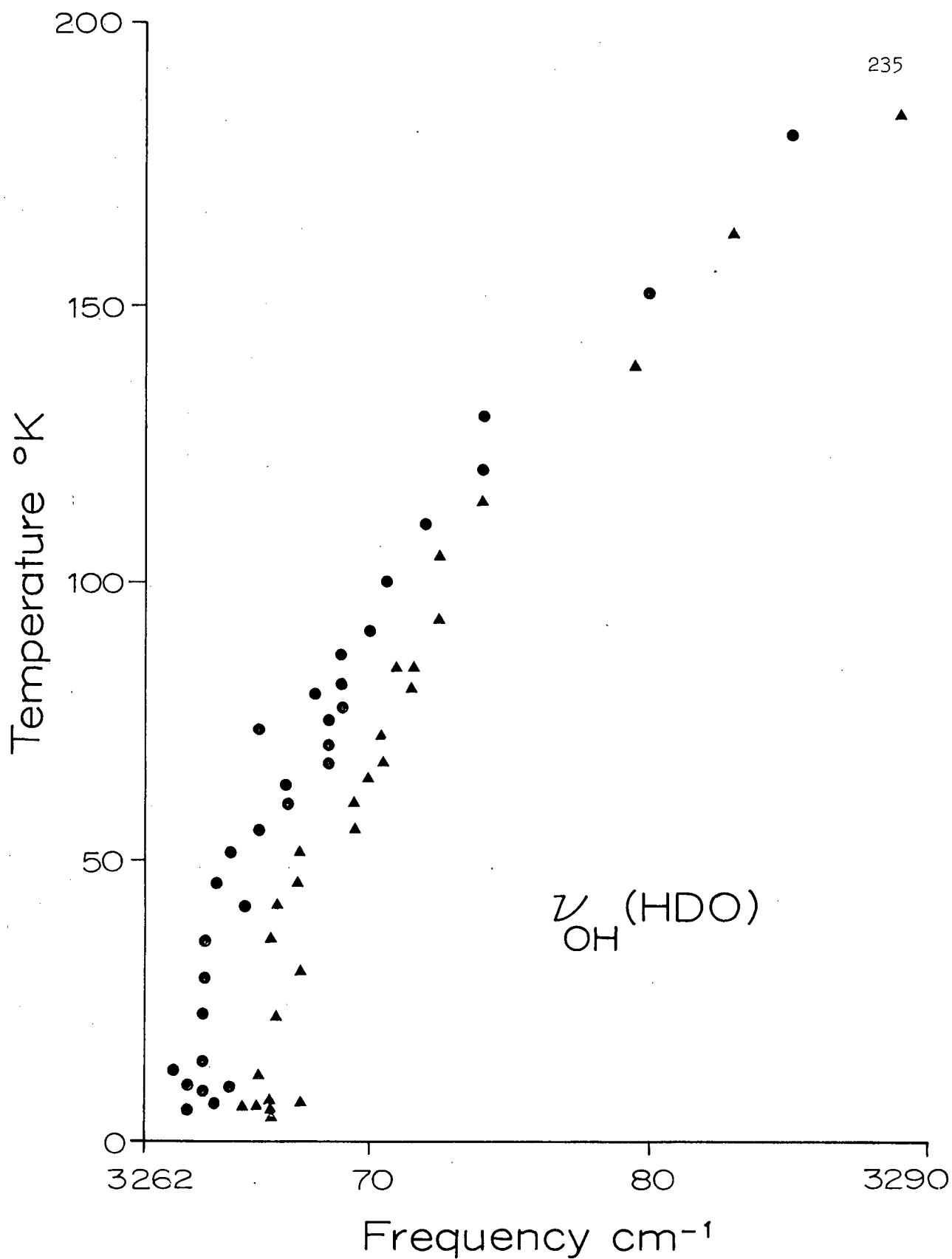


Fig. 5.6 The temperature dependence of $\nu_{\text{OH}}(\text{HDO})$ for $\text{CH}_3\text{Br} \cdot 7\text{D}_2\text{O}$ (4.00% HDO) after annealing. This was typical of all the annealed clathrate mixtures of the alkyl halides.

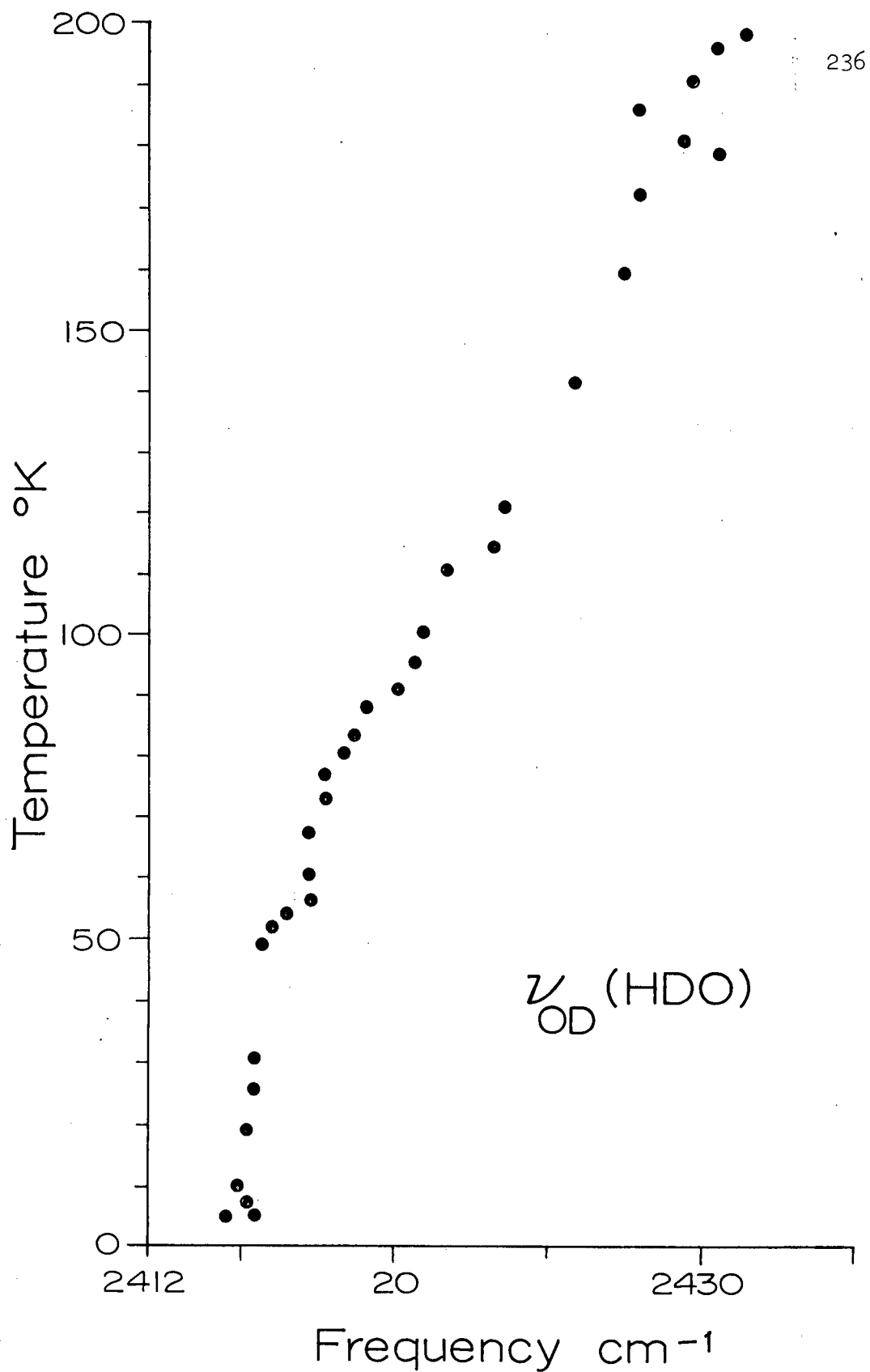


Fig. 5.7 The temperature dependence of $\nu_{OD}(\text{HDO})$ for $\text{CH}_3\text{Br} \cdot 7.67\text{H}_2\text{O}$ (5.94% HDO) after annealing. This behaviour was typical of other alkyl halide clathrate mixtures.

mixtures and are very similar to cubic ice I. The details of the frequency-temperature dependences for all clathrate mixtures containing HDO are given in Table V.IX. The samples were prepared from the same H₂O (5.94% HDO) and D₂O (4.00% HDO) specimens as were the cubic ice I samples. The peak heights and half-height widths for HDO in these clathrate mixtures behaved in the same way as for HDO in cubic ice I. Some $\Delta\nu^{1/2}$ data are given in Fig. 5.8.

Table V.IX Some parameters derived from the plots of $\nu_{OH}(HDO)$ and $\nu_{OD}(HDO)$ against temperature for four annealed clathrate mixtures.

Clathrate Guest G			CH ₃ Cl	CH ₃ Br	CH ₃ I	CH ₃ Br
Mode Observed			$\nu_{OH}(HDO)$	$\nu_{OH}(HDO)$	$\nu_{OH}(HDO)$	$\nu_{OD}(HDO)$
Low Temperature Limit	cm^{-1}	ν	3263.9	3264.0±1	3265.0±1.0	2415.0±0.5
		$\Delta\nu^{1/2}$	49.8 ±2.3	46.5±1 47.0±1.5	44.0±1.5	61.0±2.0
Low Temperature Dependence	$\frac{cm^{-1}}{^{\circ}K}$	ν	0.0375 ±0.020	0.0507 ±0.027	0.0368 ±0.03	0.0343 ±0.02
		$\Delta\nu^{1/2}$	--	--	--	--
High Temperature Dependence	$\frac{cm^{-1}}{^{\circ}K}$	ν	0.183 ±0.012	0.166 ±0.060 0.148 ±0.026	0.194 ±0.09	0.109 ±0.013
		$\Delta\nu^{1/2}$	0.074 ±0.046	0.162 ±0.039 0.148 ±0.030	0.152 ±0.060	0.080 ±0.025
"Freeze-in" Temperature, °K		ν	75±5	75±5 90±10	87±5	68±5
		$\Delta\nu^{1/2}$	100±20	100±5 0.4±5	95±5	85±5
Irregularities in Frequency Shift, °K		ν	42-48	42-65 45-67	63-75	52-57

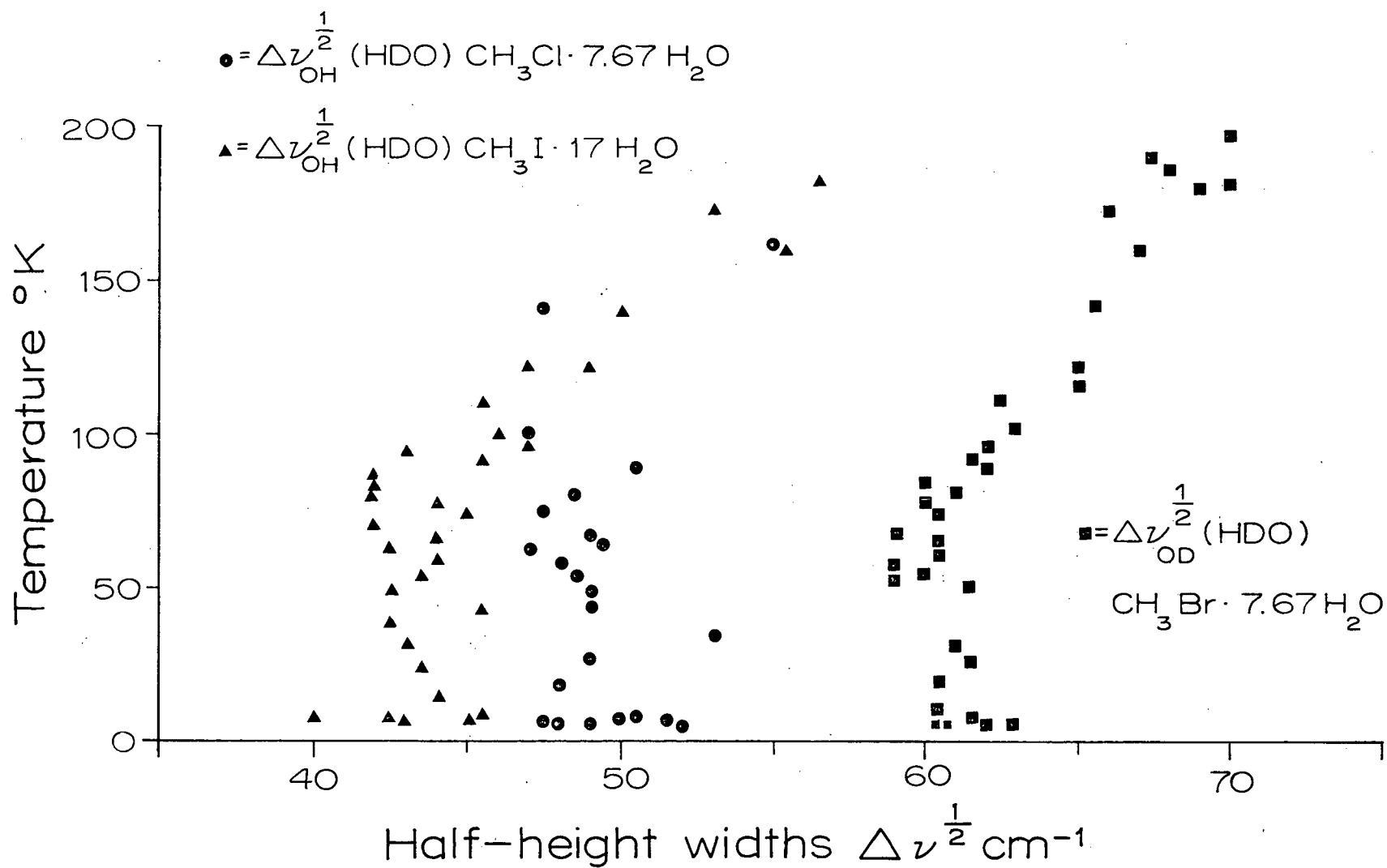


Fig. 5.8 The half-height widths for $\nu_{\text{OH}}^{\text{(HDO)}}$ and $\nu_{\text{OD}}^{\text{(HDO)}}$ in several clathrate mixtures after annealing. These data were almost twice as large as for the cubic ice I data.

(b) HDO librations. Data for $\nu_R(\text{HDO})$ of $\text{CH}_3\text{Br} \cdot 7.67\text{D}_2\text{O}$ (4.0% HDO) are given as a function of temperature in Fig. 5.9. This data is typical of other clathrate mixtures as well. The details of the temperature dependences are given in Table V.X.

B. Temperature Dependence of the H_2O and D_2O Absorptions

(i) Experimental

The H_2O and D_2O absorption features for the annealed clathrate mixtures were observed by the same methods as were cubic ice I samples (page 79). Seven H_2O absorptions were observed for each of the seven samples ($\nu_1 + \nu_T$, ν_3 , ν_1 , $3\nu_R$, $\nu_2/2\nu_R$, ν_R' and ν_R). However for D_2O clathrate mixtures the stretching band was studied in detail for $\text{CH}_3\text{I} \cdot 17\text{D}_2\text{O}$, $\text{CH}_3\text{Cl} \cdot 7.67\text{D}_2\text{O}$ and $\text{CH}_3\text{Br} \cdot 7.67\text{D}_2\text{O}$, and the (ν_R' , ν_R) band was studied only in $\text{CH}_3\text{Br} \cdot 7.67\text{D}_2\text{O}$. All mixtures except Cl_2 and Br_2 were studied between 4.2°K and 200°K, while Cl_2 and Br_2 were observed only above 77°K. Sample histories and spectrometer conditions were typical of the ice experiments.

(ii) Results of Warming Clathrate Mixtures Containing H_2O and D_2O

The temperature dependences of the H_2O and D_2O absorptions in the annealed clathrate mixtures were the same as for cubic ice I. Typical spectra for ν_3 and ν_1 of $\text{CH}_3\text{Br} \cdot 7.67\text{D}_2\text{O}$ are given in Figs. 5.10 and 5.11. The details of these samples were averaged for CH_3Cl , CH_3Br , CH_3I , CHCl_3 and $\text{C}_2\text{H}_5\text{Br}$ mixtures and are compiled in Table V.XI. The details of several $\text{Cl}_2 \cdot 7.67\text{H}_2\text{O}$ and $\text{Br}_2 \cdot 8.6\text{H}_2\text{O}$ mixtures above $83 \pm 3^\circ\text{K}$ are given in Table V.XII. The spectra and plots were treated in the same manner as for

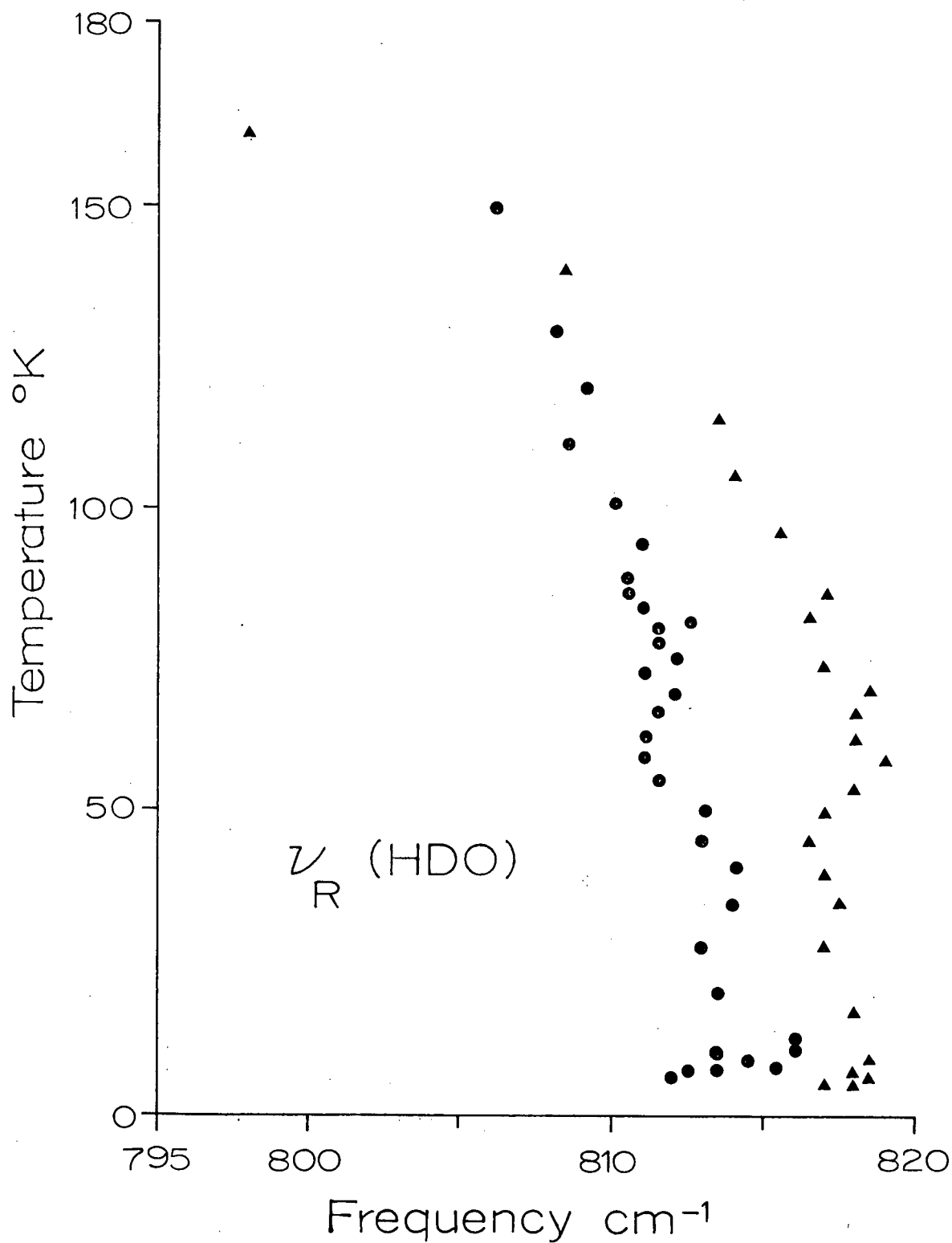


Fig. 5.9 The temperature dependence of $\nu_R(\text{HDO})$ for annealed $\text{CH}_3\text{Br} \cdot 7.67\text{D}_2\text{O}$ (4.00% HDO) clathrate mixture. This data is typical of other alkyl halide clathrate mixtures.

Table V.X The parameters for the HDO librations of three annealed clathrate mixtures.

		$\text{CH}_3\text{Br} \cdot 7.67\text{D}_2\text{O}$ (³ 4.00% HDO) ν_R (HDO)	$\text{CH}_3\text{Br} \cdot 7.67\text{D}_2\text{O}$ (³ 4.00% HDO) ν_R (HDO)	$\text{CH}_3\text{I} \cdot 17\text{D}_2\text{O}$ (³ 4.00% HDO) ν_R (HDO)	$\text{CH}_3\text{Br} \cdot 7.67\text{D}_2\text{O}$ (³ 4.00% HDO) ² ν_R (HDO) + ν_T
Low Temperature Limit	cm^{-1}	814.0±2.0	817.8±1.0	816.3±1.3	853.3±2.8
Low Temperature Dependence	$\frac{\text{cm}^{-1}}{^\circ\text{K}}$	< -0.03	< -0.03	--	< -0.09
High Temperature Dependence	$\frac{\text{cm}^{-1}}{^\circ\text{K}}$	-0.064±0.031	-0.135±0.055	-0.164±0.045	-0.125±0.028
"Freeze-in" Temperature	$^\circ\text{K}$	75±10	70±5	62±5	80±5
Irregularities in Frequency shifts	$^\circ\text{K}$	48-58	47-57	56-72	--

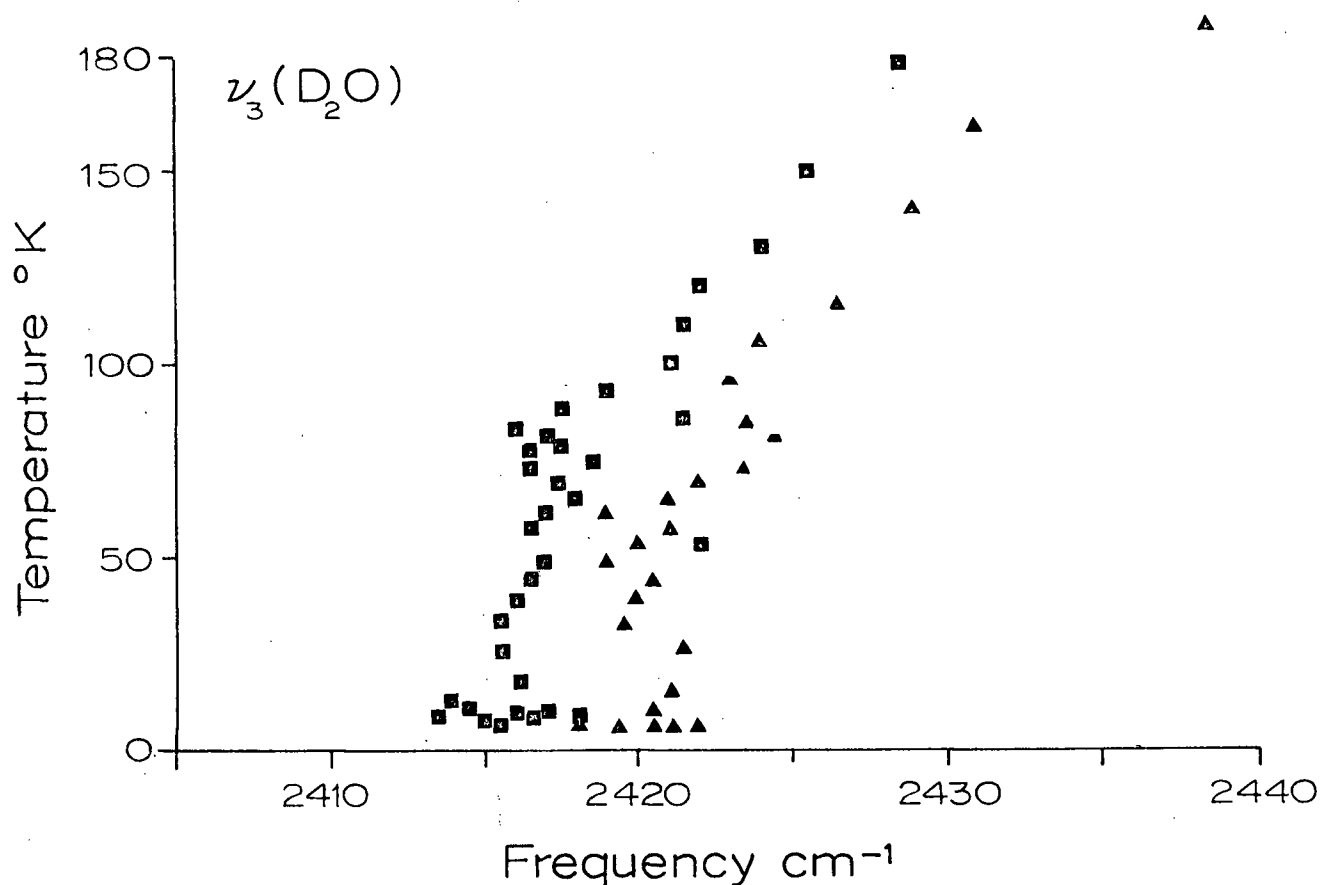


Fig. 5.10 The temperature dependence of $\nu_3(\text{D}_2\text{O})$ for annealed $\text{CH}_3\text{Br} \cdot 7.67\text{D}_2\text{O}$. Data from two specimens which had similar sample histories are given.

ice I to determine the details of the samples behaviours.

The liquid helium and liquid nitrogen cell frequency data did not always coincide within the errors of the two experiments. In general, the liquid helium cell data have been quoted in regions of doubt. However, the frequency-temperature dependences were equal for both sets of data.

For the $3\nu_{\text{R}}(\text{H}_2\text{O})$ region considerable error was introduced by atmospheric CO_2 absorption and the resulting instrument imbalance near 2300 cm^{-1} .

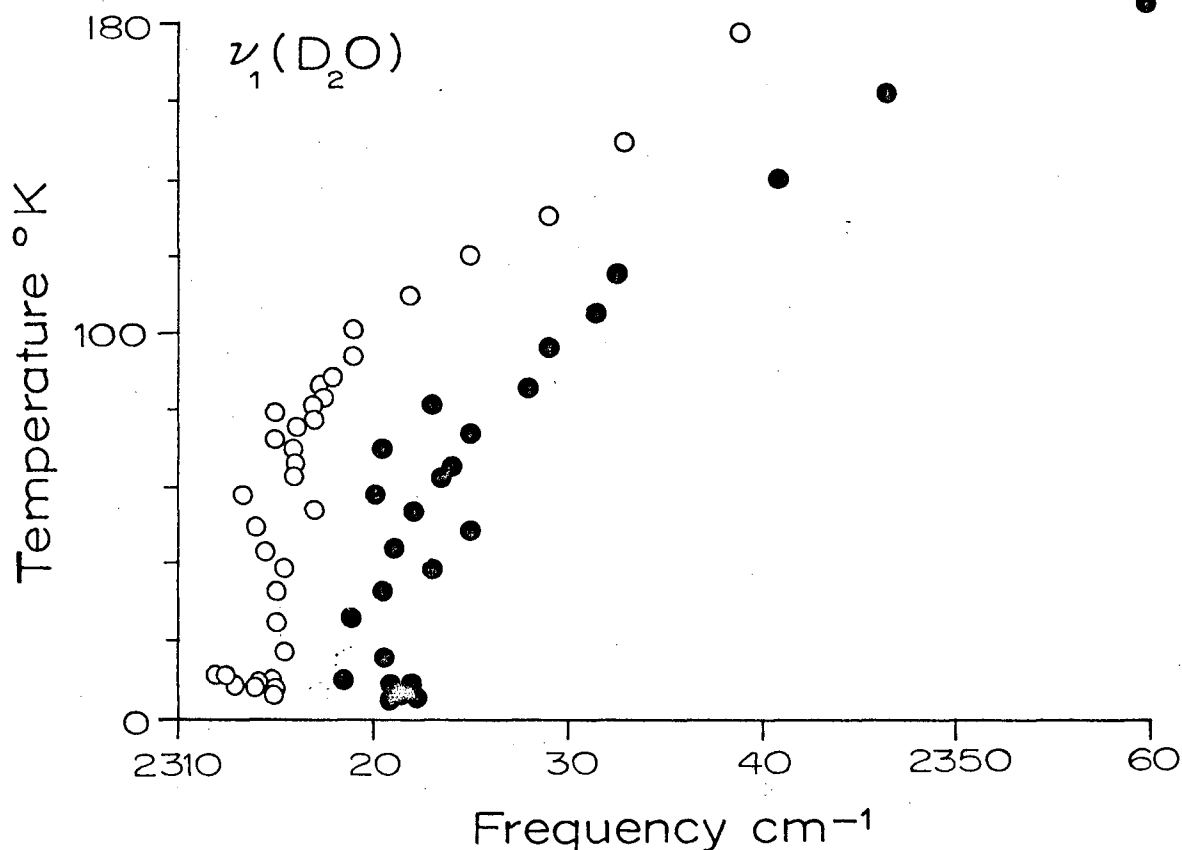


Fig. 5.11 The temperature dependence of $\nu_1(\text{D}_2\text{O})$ for annealed $\text{CH}_3\text{Br} \cdot 7.67\text{D}_2\text{O}$. Data from the same two experiments as in Fig. 5.10 are shown.

The best study of $3\nu_{\text{R}}(\text{H}_2\text{O})$ was made for a thick sample of $\text{Br}_2 \cdot 8.6\text{H}_2\text{O}$. The frequency-temperature dependence was distinctly negative.

Samples of $\text{Cl}_2 \cdot 7.67\text{H}_2\text{O}$ on CsI support windows gave anomalous behaviour after annealing to $190 \pm 5^\circ\text{K}$. The stretching band split into two peaks and three shoulders, Fig. 5.4(c). A sharp weak band and a very, very weak shoulder appeared on top of the general, broad ν_2 absorption: A peak at 1628 cm^{-1} and a shoulder near 1620 cm^{-1} . Samples of $\text{Cl}_2 \cdot 7.67\text{H}_2\text{O}$ on AgCl support windows did not exhibit such behaviour. The high frequency absorp-

Table V.XI The temperature dependences of H₂O (D₂O in brackets) modes averaged over the five alkyl halide annealed clathrate mixtures.

	Low Temperature Limit	Low Temperature Dependence	High Temperature Dependence	Freeze-in Temperature
H ₂ O (D ₂ O)	cm ⁻¹	cm ⁻¹ /°K	cm ⁻¹ /°K	°K
$\nu_1 + \nu_T$	3331±5 (sh) (2440±5)	<0.06 (0.06±0.03)	0.17±0.05 (0.14±0.06)	82±10 (93±15)
ν_3	3208±3 (vs) (2416±2)	<0.06 (0.05±0.03)	0.19±0.05 (0.12±0.04)	81±15 (88±10)
ν_1	3127±5 (sh) (2316±2)	<0.15 (<0.08)	0.24±0.05 (0.24±0.05)	85±20 (86±10)
$\nu_2/2\nu_R$	1588±6 (m)	<0.2	0.36±0.15	80±15
ν_R'	896±5 (sh) (677±3)	-0.07±0.01 (<0.03)	-0.18±0.05 (-0.15±0.07)	83±15 (80±10)
ν_R	831±5 (s) (646±3)	-0.05 ±0.01 (<-0.02)	-0.14±0.06 (-0.15±0.07)	85±17 (90±10)

Table V.XII The frequencies at 80°K and the high temperature dependences of $\text{Cl}_2 \cdot 7.67\text{H}_2\text{O}$ on AgCl and CsI and of $\text{Br}_2 \cdot 8.6\text{H}_2\text{O}$ on CsI.

Host Lattice		H_2O				
Guest Species		Cl_2	Cl_2	Cl_2	Br_2	Br_2
Sample Support Window		CsI	CsI	AgCl	AgCl	CsI
Frequency	$\nu_1 + \nu_T$	3368	3365	3338	3333	3332
at 80°K from	ν_3	3218	3215	3221	3222	3216
	ν_1	3145	3119	3147	3147	3147
Extrapolated	$3\nu_R$	2220±10	--	2225	2226	2214
	ν_2	1628±2	1624±5	1609	1622	1579
Linear	ν_R'	894	895	886	887	898
	ν_R	839	834	841	842	831
Dependence	cm^{-1}					
Frequency	$\nu_1 + \nu_T$	-0.12	-0.20	0.32	0.26	0.28
Dependence on	ν_3	0.13	0.12	0.22	0.16	0.17
	ν_1	0.19	0.54	0.24	0.18	0.21
Temperature	$3\nu_R$	--	--	-0.18	-0.12	-0.04
	ν_2	-0.06	<±0.06	0.46	0.19	0.40
	ν_R'	-0.09	-0.18	-0.10	-0.20	-0.05
	ν_R	-0.17	-0.15	-0.20	-0.16	-0.13

tion attributed to $(\nu_1 + \nu_T)$ was a peak near 3365 cm^{-1} for $\text{Cl}_2 \cdot 7.67\text{H}_2\text{O}$ on CsI. That was about 30 cm^{-1} higher than the shoulder observed in other samples and for $\text{Cl}_2 \cdot 7.67\text{H}_2\text{O}$ on AgCl. Also, the frequency-temperature dependence of $(\nu_1 + \nu_T) (\text{H}_2\text{O})$ from samples of $\text{Cl}_2 \cdot 7.67\text{H}_2\text{O}$ on CsI was negative. In other samples $(\nu_1 + \nu_T) (\text{H}_2\text{O})$ had a positive temperature dependence. The H_2O features from $\text{Cl}_2 \cdot 7.67\text{H}_2\text{O}$ on CsI and AgCl windows at 83°K were:

CsI Window	AgCl Window
3412 (sh) cm^{-1}	--
3368 (s)	3338 (sh) cm^{-1}
3285 (sh)	--
3218 (vs)	3221 (vs)
3145 (sh)	3147 (sh)
2220 (w)	2225 (w)
1883 (w)	--
1628 (sharp, weak)	--
<u>c.a.</u> 1600 (broad, m.)	1609 (broad, m.)
894 (sh)	886 (sh)
839 (m)	841 (m)

The sharp peak at 1628 cm^{-1} from the CsI window experiment exhibited no temperature dependence.

CHAPTER SIX

DISCUSSION OF THE CLATHRATE MIXTURES

6.1 The Clathrate Mixture Vitreous-Crystalline Phase Transformation

A. General Discussion

The nature of the samples formed by rapid condensation of clathrate mixtures was probably much the same as for vitreous ice I. Thus much of the discussion on annealing ice I applies here also, i.e. the onset of crystallization, the effects on the ir spectra and the processes involved in reorientation. As before the H₂O lattice modes shifted to higher frequency and the molecular modes shifted to lower frequency. The H₂O bands sharpened and had better defined features after annealing. The transformation temperature range began at $115 \pm 5^\circ\text{K}$ (uncorrected for source beam heating) and took about 18 minutes at 125°K . However, the range for the clathrate mixtures seemed to be extended to higher temperatures by about 10°K . The vitreous samples shifted irreversibly below 150°K and reversibly once warmed above 150°K . It was not clear that annealing vitreous clathrate mixtures produced the desired cubic 12 \AA or 17 \AA unit cell structures. We suspect that not a clathrate structure, but cubic ice I was probably formed. The longer transition temperature range suggested the vitreous clathrate mixtures were more stable than the vitreous H₂O or D₂O ice samples.

While the mechanism for H₂O or D₂O frequency shift was the same as in ice I (the formation of a fully hydrogen bonded network of each oxygen to four nearest-neighbour oxygen atoms at about the same distance as in ice I) there should be a fundamental difference for the ir spectra of clathrate-hydrates. X-ray crystallography had shown that the alkyl halide

and halogen clathrates had varying cage sizes and varying O····O distances (Table 0.2). Peak positions of annealed clathrate samples should have varied regularly as a function of unit cell size. The annealing results did not support this concept, but results on H₂O and D₂O were subject to large errors. HDO results were better and are discussed in section 6.3A.

B. Annealing Cl₂·7.67H₂O on CsI

Samples of Cl₂·7.67H₂O which were deposited on CsI and annealed to 190 or 200°K for 10 to 15 minutes gave unique H₂O spectra (Figs. 5.4(c) and 5.5), while the same samples annealed to only 180 ± 3°K gave typical H₂O spectra (Fig. 5.5). As well, the spectra from samples of Cl₂·7.67H₂O annealed on AgCl windows to 190 or 200°K for long times were typical of ice, as were the spectra of CH₃Cl, CH₃Br, CHCl₃ and C₂H₅Br clathrate mixtures annealed on CsI at 195°K for more than 10 minutes.

The Cl₂·7.67H₂O on CsI samples had five stretching band features (three shoulders at 3412, 3285 and 3145 cm⁻¹ and two peaks at 3368 and 3218 cm⁻¹) compared to three features in ice I and other annealed clathrate mixtures (two shoulders at 3338 and 3147 cm⁻¹ and a peak at 3221 cm⁻¹ for Cl₂·7.67H₂O on AgCl). As well there appeared a weak, sharp peak and an adjacent shoulder (1628 and 1607 cm⁻¹) on top of the broad ν_2 (H₂O) absorption. The weak peak and shoulder frequencies were independent of temperature. Other absorption features which arose were a peak at 1883 cm⁻¹, a distinct shoulder at 1100 cm⁻¹ and pronounced absorption between 2300 cm⁻¹ and 3000 cm⁻¹ (Fig. 5.4(c)). The last effect may have been due to increased scattering losses if the substrate surface became pitted by the sample, while

the shoulder at 1100 cm^{-1} may have been due to a Christiansen filter effect.

Mecke et al. (103) observed four well defined bands in their "ice I_h " spectra on NaCl windows (Table VI.I). However, Schiffer (104) studied a number of dihydrated sodium halides and showed that Mecke's "ice" was $\text{NaCl} \cdot 2\text{H}_2\text{O}$. The data of Table VI.I suggest that the $\text{Cl}_2 \cdot 7.67\text{H}_2\text{O}$ condensed and annealed on CsI may have formed a hydrated cesium halide layer on the substrate, i.e. $\text{CsI} \cdot x\text{H}_2\text{O}$, $\text{CsCl} \cdot x\text{H}_2\text{O}$ or $\text{CsICl}_2 \cdot x\text{H}_2\text{O}$.

The presence of hydrated cesium halide substrate was supported by the appearance of the sharp, weak peak at 1628 cm^{-1} and a shoulder at 1607 cm^{-1} in the spectra of $\text{Cl}_2 \cdot 7.67\text{H}_2\text{O}$ on CsI. These were similar to peaks observed by Mecke et al. (103) and Schiffer (104), Table VI.I.

That substrate hydration did not occur for $\text{Cl}_2 \cdot 7.67\text{H}_2\text{O}$ on AgCl nor for CH_3Cl , CH_3Br , CH_3I , CHCl_3 and $\text{C}_2\text{H}_5\text{Br}$ clathrate mixtures is not surprising. For AgCl and $\text{Cl}_2 \cdot 7.67\text{H}_2\text{O}$ it is probable that the Cl_2 does not oxidize AgCl, whereas it may oxidize CsI. As well, AgCl is chemically more resistant to hydration.

It is possible that Cl_2 reacted with CsI to form CsCl and ICl or else CsICl_2 . Intermediate steps may have allowed the formation of hydrated halide salts. Although hydrates of CsCl, CsI and CsICl_2 are not stable at 20°C , they may be stable at 200°K and lower.

We have already estimated that our samples were about 1μ ($10,000\text{ \AA}$) thick. From the relative intensities of the ice I and hydrated salt absorptions one might expect 10% or more of the H_2O in the original sample to be attached as water of hydration. Thus the formation of several hundred monolayers of CsICl_2 is unlikely since ICl_2^- is too long to fit

Table VI.I The ir absorptions due to H_2O stretches in dihydrated salts, "Mecke's ice", and annealed $Cl_2 \cdot 7.67H_2O$ on CsI(all at $83 \pm 3^\circ K$).

$Cl_2 \cdot 7.67H_2O$ on CsI	Ice on NaCl (a)	$NaCl \cdot 2H_2O$ (b)	$NaBr \cdot 2H_2O$ (b)	$NaI \cdot 2H_2O$ (b)	$CaSO_4 \cdot 2H_2O$ (c)
cm^{-1}	cm^{-1}				
3412 (sh)	3555 (m)	3538 (s)	3539 (s)	3568 (sh)	3549 (vs)
3368 (ms)	3471 (s)	3468 (vs)	3469 (vs)	3506 (s)	3496 (s)
3285 (sh)	3407 (s)	3405 (vs)	3406 (vs)	3461 (s)	3404 (vs)
3218 (s)	3245 (w)	3310 (vvw)	3360 (sh)	3437 (sh)	3242 (m)
3145 (sh)		3265 (mw)		3421 (vs)	
		3242 (mw)			
1628 (vw)	1645 (m)	1643 (s)	1635 (s)	1626 (sh)	
1607 (sh)	1616 (m)	1615 (s)	1614 (s)	1613 (s)	

(a) Ref. 103

(b) Ref. 104

(c) Ref. 127

into an interior I^- lattice site: It may however occupy an I^- surface lattice site. As well it seems unlikely that a solid-solid reaction would lead to deep penetration of Cl_2 or Cl^- into CsI since Harrison et al. (128) found some alkali halide single crystals were very resistive to exchange with Cl_2 even at room temperature.

The origin of the new absorption at 1883 cm^{-1} is not known. It lies well above the calculated $\nu_2(H_2O)$ position of Hornig et al. (105), 1780 cm^{-1} . It may be due to $(\nu_2 + \nu_T)$ for the hydrated salt $\nu_2(H_2O)$ and the H_2O lattice ν_T .

C. Oligomeric H₂O Absorptions

All the unannealed clathrate mixtures exhibited very weak peaks or shoulders in the region 3500-3700 cm⁻¹, Table VI.II. Similar absorptions were found for H₂O and D₂O ice I_v and the clathrate mixture peaks were also assigned to oligomeric H₂O and D₂O units. As was shown for CH₃Br·7.67H₂O (Table V.III) in three different specimens the positions, intensity and number of oligomeric features were dependent on the rate of sample deposition. The 3690 cm⁻¹ peak was obtained from a CH₃Br·7.67H₂O sample deposited in 11 minutes, while the 3620 cm⁻¹ peak was obtained from a sample deposited in 1.5 minutes and the peaks at 3645 and 3605 cm⁻¹ were obtained from samples deposited in 4.5 minutes. Fast deposition produced more localized heating and H₂O polymerization than slow deposition. Van Thiel *et al.* (117) suggested monomeric, dimeric and trimeric H₂O absorbed at (3725 and 3625), (3691 and 3546), and (3510 and 3355) cm⁻¹ respectively. On that basis we appear to have formed residual dimeric H₂O in the unannealed clathrate mixtures.

The presence of oligomeric H₂O and D₂O suggests a low mobility of molecules during condensation. However, low mobility of guest molecules does not necessarily follow. Finally, it may be possible to follow the rate of crystallization in ice I and clathrate mixtures by following the peak heights of oligomeric H₂O.

D. Unannealed Sample Guest Absorptions

Guest absorptions in unannealed clathrate mixtures due to alkylhalides were observed for all specimens. During annealing the general experience was

Table VI.II The weak peaks and shoulders attributed to oligomeric H₂O and D₂O ν_1 and ν_3 stretching modes in some clathrate mixtures and in some inert matrices.

M	CH ₃ Cl	CH ₃ Br	CH ₃ I	CHCl ₃	C ₂ H ₅ Br	Cl ₂	Br ₂	Ar(a)	Kr(a)	N ₂ (a)	CCl ₄ (a)
Moles M	1	1	1	1	1	1	1	300	380	240	1000
Moles R	7.67	7.67	17	17	17	7.67	8.6	1	1	1	1
	cm ⁻¹										
R is H ₂ O		3690*	3687	3689		3690	3691	3708	3700	3725	
			3668			3670		3699	3687	3686	
	3654	3645	3648	3639	3643			3634		3634	
		3620 ^X	3625			3617					
		3605					3612				
	3683		3580		3565			3574	3570		
Moles M	1	1	1					210	210	240	1000
Moles R	7.67	7.67	17					1	1	1	1
R is D ₂ O	2648	2644	2647					2637	2635	2655	2643
								2635	2632	2650	
								2622	2625	2639	
			2626					2615	2614	2617	
								2614	2610	2614	

(a) Ref. 115

* Very slow deposit X fast deposit

that guest absorptions were observed with undiminished peak heights up to $120 \pm 5^\circ\text{K}$, but they were unobserved above $170 \pm 5^\circ\text{K}$ or after recooling the samples to $83 \pm 3^\circ\text{K}$. The peak heights of bands in different clathrate types decreased at different rates, while the peak heights of several specimens of one clathrate mixture (i.e. $\text{CH}_3\text{Br} \cdot 7.67\text{H}_2\text{O}$) decreased at about the same rate. As one might expect the drop in guest peak heights began at the same temperature as the oligomeric H_2O disappeared (near $130 \pm 10^\circ\text{K}$).

Frequencies of guest absorptions in the unannealed clathrate-hydrates and of pure, solid guest molecules (all at $83 \pm 3^\circ\text{K}$) are listed in Table VI.III. For unannealed clathrate mixtures of CH_3Cl , CHCl_3 and $\text{C}_2\text{H}_5\text{Br}$ all strong and medium intensity absorptions of the pure solid were observed. In contrast, for CH_3Br and CH_3I unannealed clathrate mixtures, only some of the pure solid absorptions were observed. Strong unannealed clathrate guest absorptions expected near 3050, 1420, 895 or 964, and 596 cm^{-1} were unobserved. Also in the $\text{CH}_3\text{Br} \cdot 7.67\text{H}_2\text{O}$ sample, peaks were observed in the clathrate (1218, 1200, and 750 cm^{-1}) which were unobserved in the pure solid. The clathrate guest peaks were shifted only slightly from the pure solid peaks. However, where the pure solid had multiplets of peaks the clathrate peaks were singlets.

We can offer no explanation for the missing CH_3I and CH_3Br peaks nor for the extra CH_3Br peaks. The loss of guest band splitting between the pure solid and clathrate was not unexpected, the splitting of degeneracies in pure crystals being lost due to the range of absorption frequencies arising from the inhomogeneity among the guest sites in the vitreous mixtures.

There are at least three explanations of the loss of the clathrate guest absorptions in the annealed samples. First, there was too much guest in

Table VI.III Alkyl halide ir absorptions in the pure solid state and in some unannealed clathrate mixtures at $83 \pm 3^\circ\text{K}$.

CH ₃ Cl		CH ₃ Br		CH ₃ I		CHCl ₃		C ₂ H ₅ Br	
Unann.		Unann.		Unann.		Unann.		Unann.	
Clath.	solid(a)	Clath.	Solid(a)	Clath.	Solid(b)	Clath.	Solid(c)	Clath.	Solid(a)
cm^{-1}									
		3020 sh	3036 m		3035 m	3016 sh	3012	2985 vw	2984 m
2957 m	2950 w	2965 sh	2954 s	2936 vvw	2935 s				2963 w
				2915 vvw					2921 m
			2846 m						2859 w
			2830 m		2803 m				
									1459 w
	1444 sh				1436 m				1448 sh
	1443 s				1426 ms				1446 m
1443 m	1441 sh		1432 vs		1420 s				1440 m
1437 sh	1436 m		1417 vs		1401 ms				1433 sh
					1396 s				1376 m
1347 w	1345 m		1293 sh	1244 sh	1241 vs	1238 vvw	1235		1371 m
1338 vw	1336 m	1292 vvw	1291 vs	1234 w	1236 vs	1214 vw	1220	1254 vw	1255 m
		1218 vvw					1218	1242 vw	1242 s
		1200 sh							1232 m
1021 vw	1020 m		962 vw		895 vs		767		
			955 vs		888 vs	752 m	748	955 w	960 s
									961 sh
700 s	700 vs	750 s	589 sh			663			
	697 sh								785 w
	692 s		585 vs					760 sh	762 s
			570 m						735 w

(a) This work (b) Ref. 129 (c) Ref. 130

the unannealed mixture formed on the window: The excess guest diffused out and sublimed off the window during annealing, while the remainder was too small to detect. Secondly, all of the guest molecules may have diffused out of the H_2O lattice and sublimed off the window. Thirdly, the guest molecules may have been present but inactive due to some cage effect. The third possibility is unlikely since cage perturbations are more likely to induce anharmonicities, peak shifts or even enhance the intensities. The first explanation also seems unlikely since H_2O condenses at a much higher temperature than most of the guests, if anything the samples may have been deficient in guest. The expulsion of all guest molecules from the H_2O lattice seems most probable.

Further work, to be described later, was done to check which of the above reasons was most probable. One further logical method to use (which we did not) is observing clathrate-hydrates in Raman spectroscopy. There the H_2O bands are sharp, while most alkyl halide bands are ir and Raman active and thus the bulk samples may be prepared and observed, in contrast to the thin films of our ir technique.

6.2 Guest Species Absorptions

It was suggested in section 6.1 that sample condensation and annealing in an open cell chamber leads to expulsion of the foreign guest molecules from the H_2O or D_2O lattice in the absence of the equilibrium dissociation pressure of the clathrate. Two further experiments tested the possibilities of sample fractionation between the sample deposition tube and the substrate surface, and simple sample dissociation.

A. Isolated Chamber Condensation

Gaseous clathrate mixtures condensed in an isolated chamber (Fig. 1.2) and unannealed exhibited guest absorptions with approximately the same intensities relative to H_2O bands as open chamber samples. Therefore we concluded that the open chamber samples did not fractionate during deposition. The design of the closed chamber cell ensured that all of the gaseous sample condensed on one window while for open chamber condensation the heated deposition tube ensured that no H_2O or guest molecules condensed on the deposition tube tip.

Clathrate mixtures condensed in a closed chamber, but annealed to $185 \pm 5^\circ\text{K}$ and recooled to 83°K , exhibited no guest absorptions: The same behaviour exhibited by open chamber samples. That was contrary to Shurvell's (57) results and probably arose from the differences in maximum annealing temperature: He annealed only to $145 \pm 5^\circ\text{K}$. The annealing process was not followed in detail (spectroscopically) for closed chamber samples, but the annealed sample spectra for 83°K appeared the same as those in section 6.1 and in ice I.

The same spectroscopic results were obtained for unannealed or annealed samples whether they were observed in open or closed sample chambers. The guest molecules must have been expelled from the H_2O or D_2O lattice in the closed chamber, due to the absence of a positive clathrate stabilizing pressure of guest vapour at $185 \pm 5^\circ\text{K}$.

B. Low Temperature Mulls

The obvious alternative was to form clathrate-hydrate samples in bulk and observe their spectra by low temperature mulling. It was difficult to grind the samples at 77°K to a very fine powder and considerable scattering was observed from the large particle size. Whalley (95) obtained much better spectra (of ice) apparently with finer powders. The indices of refraction of the mulling agents and ice agreed fairly well in the visible region, but the indices change very rapidly over absorption bands and this seems to induce considerable scattering between 1700 to 2000 cm^{-1} and 2300 to 3000 cm^{-1} .

It was of course unnecessary to anneal mulled samples since the crystalline samples were initially cooled from 273°K to 83°K at 1 atmosphere of $\text{N}_2(\text{g})$. However, no guest absorptions were observed for either the mull of $\text{CH}_3\text{I} \cdot 17\text{H}_2\text{O}$ or $\text{CCl}_3\text{F} \cdot 17\text{H}_2\text{O}$. Most of the CH_3I or CCl_3F guest absorptions should have been observed in either the C_3H_8 or CClF_3 mulling agent.

Two explanations are possible. First, during transferal of sample from the preparation tube to the mortar and pestle the sample was warmed to 273°K momentarily and it may have dissociated. However, the CH_3I and CCl_3F clathrates were chosen specifically for their guests liquid states and low vapour pressures at 273°K and their clathrates low dissociation pressures. Secondly, the CH_3I and CCl_3F molecules may have been very soluble in liquid C_3H_8 and liquid CClF_3 even at low temperature. However, the clathrate samples were not observed to dissolve in the mulling agents. If the guests did dissolve in the mulling agent then they should still have been observed in the spectra as a solid solution.

We could not establish with confidence that the clathrate samples had not decomposed during preparation of the mull. The samples may have dissociated either during transfer to the pestle or during evacuation of the cryostat (with the sample temperature between 100 and 150°K). No attempts were made to analyze the small quantities of vapour evolved after warm-up of the cell to room temperature.

The H₂O skeletal absorptions observed in mulls were much like previous cases: Scattering distorted the bands considerably. One difference did occur, however, the ν_2 absorption was well defined at 1570 cm⁻¹ at 83°K. In most spectra the region from 1600 to 3000 cm⁻¹ was just one broad band which steadily increased in intensity.

C. Summary

Infrared observations by Hexter and Goldfarb (53) on HCl, H₂S, CO₂ and SO₂ clathrated in hydroquinone demonstrated that for weakly absorbing guests the guest absorption was unobserved in the clathrate, but strong absorbers like CO₂ and SO₂ were easily observed. They pointed out that in the amount of HCl-quinone clathrate used for the ir observations, only about 5% of the HCl needed for a reasonable HCl(g) spectrum was present. Davies and Child (55) also observed ir absorption by guests in quinone clathrates. They suggested that the shifts in guest frequencies were no larger than for solutions of guests in CCl₄. Their conclusion was that the cage had perturbing influences no larger than a non-polar solvent. We deduce that in our annealed clathrate-hydrate mixtures the guests all could not have been present and ir inactive.

We concluded that for unannealed clathrate mixtures, since there was no fine structure associated with the guest absorptions, guest rotation and translation was hindered. If the binding in the unannealed samples was not physical, but chemical, then we expected new guest functional group frequencies. The evidence indicates our methods were insufficient to form clathrate-hydrates.

6.3 The Temperature Dependences of Crystalline Clathrate Mixture Absorptions

A. HDO in Clathrate Mixtures

Discussion of the results from annealed clathrate-hydrate mixtures collapses to a discussion of cubic ice I: We assume the guest was all dispersed and a cubic ice I lattice formed at $185 \pm 5^\circ\text{K}$. The clathrate studies became independent checks of the reproducibility of cubic ice I experiments.

Consider the $\nu_{\text{OH}}(\text{HDO})$ frequencies from CH_3Cl , CH_3Br and CH_3I mixtures with D_2O (4.00% HDO). Except for one set of CH_3Br results, the clathrate-mixture low temperature limits, low temperature dependences, high temperature dependences, "freeze-in" temperatures and irregularities in frequency-temperature shifts agreed, within error, with HDO cubic ice I data.

Clathrate mixture $\nu_{\text{OD}}(\text{HDO})$ frequency limit, temperature dependences, "freeze-in" temperatures, etc., agreed, within error, with $\nu_{\text{OD}}(\text{HDO})$ of cubic ice I.

Half-height width data from clathrate-mixtures did not agree with cubic ice I HDO data. Both $\Delta\nu_{\text{OH}}^{\frac{1}{2}}$ and $\Delta\nu_{\text{OD}}^{\frac{1}{2}}$ from clathrates were at least 25 percent larger than in cubic ice I. Contrary to cubic ice I, $\Delta\nu_{\text{OD}}^{\frac{1}{2}}$ was

30 percent larger than $\Delta\nu_{\text{OH}}^{\frac{1}{2}}$. One can understand the increased $\Delta\nu_{\text{OH}}^{\frac{1}{2}}$ over cubic ice I on the basis of further H_2O exchange into the $\text{D}_2\text{O}(\text{H}_2\text{O})$ mixture as the sample aged, in spite of precautions. One cannot rationalize increased $\Delta\nu_{\text{OD}}^{\frac{1}{2}}$ in that way.

Notice that if a true clathrate had been formed from the CH_3Br mixture, for example, then the $\nu_{\text{OH}}(\text{HDO})$ frequency would have been expected at a much higher frequency than observed. Since CH_3Br forms a cubic type I clathrate ($\text{CH}_3\text{Br} \cdot 7.67\text{H}_2\text{O}$ ideal stoichiometry) with a 12.09 \AA cell parameter (Table 0.2) then the average $\text{O} \cdots \text{O}$ distance must be 2.809 \AA at 273°K . For $\text{R}(\text{O} \cdots \text{O}) = 2.755 \text{ \AA}$ in cubic ice I we found $\nu_{\text{OH}}(\text{HDO}) = 3290 \text{ cm}^{-1}$ (Fig. 5.12) and $\Delta\nu/\Delta R = 1921 \text{ cm}^{-1}/\text{\AA}$. Since the $\text{O} \cdots \text{O}$ distances differed by 0.054 \AA we expected a $\Delta\nu$ of 104 cm^{-1} . Thus $\text{CH}_3\text{Br} \cdot 7.67\text{D}_2\text{O}(\text{H}_2\text{O})$ clathrate should have had $\nu_{\text{OH}}(\text{HDO})$ absorbing near 3394 cm^{-1} (273°K). Assuming the same frequency-temperature dependence as in ice then at 83°K $\nu_{\text{OH}}(\text{HDO})$ should have absorbed at $3394 \text{ cm}^{-1} - 190^\circ\text{K} (0.200 \text{ cm}^{-1}/^\circ\text{K}) = 3356 \text{ cm}^{-1}$. The absence of such absorption also supported the conclusion that clathrates did not form. The same principles could be applied to $\text{CH}_3\text{I} \cdot 17\text{D}_2\text{O}(\text{HDO})$ and $\text{CH}_3\text{Br} \cdot 7.67\text{H}_2\text{O}(\text{HDO})$ mixtures.

The distribution of $\text{O} \cdots \text{O}$ distances is much greater in clathrates than in ice I due to four unique distances, each of which must have an ice-like distribution. One would expect considerably broader HDO bands in clathrates.

Librations of HDO in clathrate mixtures and cubic ice I also agreed within error with respect to high temperature frequency dependence, "freeze-in" temperature and frequency shift irregularities. The low temperature limits did not agree within our stated errors. The disagreement was not

sufficient to suggest clathrate had formed, i.e. increased $R(0\cdots0)$ in clathrates suggested a shift of $(15 - 20) \text{ cm}^{-1}$ from cubic ice I.

The irregularities observed in frequency shifts with increasing temperature were discontinuous shifts by $2 - 3 \text{ cm}^{-1}$, generally to higher frequency in the case of stretches and to lower frequency in the case of librations. Another break in the curves appeared near 80°K . These breaks may have been related to partial ordering, as was suggested before.

B. H_2O and D_2O in Clathrate Mixtures

Discussion of H_2O and D_2O absorptions in annealed clathrate-hydrate mixtures also reduces to a discussion of cubic ice I. The behaviour of H_2O and D_2O clathrate mixture absorption frequencies, half-height widths and temperature dependences were the same as in cubic ice I.

If true clathrate hydrates had formed on annealing then low temperature limits and half-height widths should have been significantly different from ice: They were not. The low temperature limits of each individual H_2O or D_2O absorption agreed within error, Table V.XI, for the set of clathrate mixture data. The average for each band, over all clathrate mixtures, agreed with the observed H_2O and D_2O ice I data. The only exceptions were for $\nu_1 + \nu_T(\text{D}_2\text{O})$, $\nu_R'(\text{D}_2\text{O})$ and $\nu_R(\text{D}_2\text{O})$. Those three sets of data were obtained from broad shoulders or ill-defined peaks, both of which were hard to define consistently. High temperature frequency dependences for each clathrate-mixture band agreed within error, Table V.XI, over

the set of clathrate mixtures. The "freeze-in" temperature data were also compatible.

There were two special points to consider, the negative temperature dependence of $\nu_1 + \nu_T$ from $\text{Cl}_2 \cdot 7.67\text{H}_2\text{O}$ on CsI and zero temperature dependence of the weak 1628 cm^{-1} ($\text{CsI} \cdot 2\text{H}_2\text{O}$?) band. Negative temperature dependence was characteristic of lattice modes. Since such an intense lattice overtone was unlikely, the 3368 cm^{-1} band may have been a combination of ν_1 with an overtone of a low frequency lattice mode (say $2\nu_T'$). The shift of $\nu_1 + \nu_T$ to higher frequency by 30 cm^{-1} was understood in terms of the smaller overlap with ν_3 than in ice I. Insensitivity of the weak, sharp 1628 cm^{-1} absorption to temperature is characteristic of non-hydrogen-bonded-lattice H_2O : That supports its assignment to ν_2 of, say, $\text{CsI} \cdot 2\text{H}_2\text{O}$.

Results of section 5.3 on H_2O and D_2O in annealed clathrate mixtures differed from those of McCourt (56) and Shurvell (57). We failed to detect their additional $3\nu_R$ absorption near 2400 cm^{-1} . However, we experienced problems from instrument imbalance through atmospheric CO_2 between 2280 and 2360 cm^{-1} . As well, attempts to duplicate their (56,57) SO_2 results failed. McCourt's samples do not appear to have been annealed, as suggested by the shape and positions of the H_2O absorptions. Inspection of McCourt's (56) and Shurvell's (57) original background spectra revealed slight, 0.02 abs. units, negative CO_2 absorptions from 2280 to 2360 cm^{-1} . For thick samples, requiring extensive reference beam attenuation and very small instrument source signals, the negative CO_2 absorption would be proportionally greater and could give the appearance of 2 ($3\nu_R$) bands instead of one. The position of the minimum between their 2 ($3\nu_R$) peaks corresponds closely to the CO_2 (gas) maximum. There was also evidence of oligomeric H_2O absorption in

their original spectra. We concluded their samples were unannealed and vitreous and that no extra $3\nu_R$ (H_2O) absorption appeared. Finally, the nearly identical spectra of the various ices suggests that similar spectra should be expected for the clathrates.

CHAPTER SEVEN

SUMMARY

7.1 Suggestions for Further Work

Extensions and new applications of this work are proposed under three headings: further work in the H_2O - HDO - D_2O ice systems, applications of isotopic substitution to other chemical systems, and further work on clathrate-hydrates.

A. Clathrate Mixtures

We recommend observation of bulk clathrate-hydrate samples in glass preparation tubes by laser Raman spectroscopy. Shifts of peak frequency, half-height width and intensity as a function of temperature should be easily followed. It is important to choose guest species which are strong Raman scatterers and whose frequencies are widely separated from the H_2O frequencies. In that case the guest frequencies would be perturbed the least by coupling to the H_2O lattice.

As an extension of the effect of the lattice, one could study clathrates whose guests frequencies are close to H_2O frequencies and would be expected to couple (to $\nu_3(\text{H}_2\text{O})$ say, which is weak in the Raman effect). One could also study the perturbing effect of the lattice on the guest by observing the D_2O clathrate analogues.

Finally, careful technique should permit one to grow clathrate-hydrate single crystals in glass tubes, simultaneously allowing one to confirm the clathrate structure by x-ray crystallography and to observe polarized Raman spectra.

We also recommend further attempts to observe low temperature mulls of clathrate-hydrates whose structures are confirmed by x-ray powder diffraction. Use of clathrate-hydrates which are more stable under ambient conditions (i.e. tetrahydrofuran hydrate) should facilitate mull preparation, but may make the spectroscopy more complicated.

B. Ice Systems

Some extensions of this work which should be completed are listed below.

1. Use dilute HDO frequencies to follow the annealing or vitreous-cubic ice I transformation in detail.
2. Determine the rates of transformation at various constant temperatures by following the shifts in HDO frequencies as a function of time.
3. Study ν_2 and $\Delta\nu_2^{1/2}$ in detail for liquid helium and liquid nitrogen experiments to resolve the $\nu_2 - 2\nu_R$ dilemma.
4. Check cubic ice I cooling and warming curves for hysteresis under slow and fast cooling (0.5 - 20 hours).
5. Investigate hydration of sample windows by Cl_2 and H_2O .

Some other projects related to this work are included below.

1. Carefully check the properties of cubic ice I in the temperature range 40 - 70°K by Raman scattering, infrared absorption and n.m.r. of HDO in D₂O considering the shift in stretching frequency in that range.
2. Investigate the behaviour of HDO frequencies below 10°K to check the extrapolation of our data.
3. Study HDO absorptions in the family of high pressure ices as a function of temperature over their stable ranges. This will permit the extension of hydrogen-bond force constants over a wider range of R(O····O) in similar electronic environments.
4. Obtain detailed linear expansion coefficients of cubic ice I down to 4°K.
5. Study the origin of ν_R as the H₂O triple point is approached from the three phases.
6. Use our HDO frequencies, ω_{OH} and X_{OH} to investigate various models of hydrogen-bonding as a function of R(O····O) and attempt to relate $\Delta\nu$ to changes in the covalent and electrostatic nature of the hydrogen-bond.
7. Study the anisotropy of hexagonal ice I single-crystals by observing differences in HDO frequencies and $\Delta\nu/\Delta R$ (as a function of temperature) along the a_0 and c_0 axes.
8. Determine the proton jump energy by observing at what temperature during warm-up a thin layer of D₂O embedded between thick layers of vitreous H₂O leads to the formation of characteristic HDO peaks. Deposition rates would have to

be extremely slow at 4.2°K. Heat of sublimation may be too large to permit isolation of a few mono-layers of D₂O on H₂O.

C. Other Chemical Systems

Several possible applications of the dilute isotopic substitution and temperature variation technique are listed below.

1. Study single-crystals of organic acids, whose crystal structures and linear expansion coefficients are known, as a function of temperature and relate $\nu_{OD}(\text{HDO})$ to $R(\text{O}\cdots\text{O})$ to better characterize the hydrogen-bond potential.
2. Study carbohydrates, hydrogen-bonding polymers and long chain molecules to determine the nature and variation of $\text{O}-\text{H}\cdots\text{O}$ hydrogen bonding.
3. Use dilute isotopic substitution in biological systems generally since the H₂O medium masks spectroscopic observations of H₂O.
4. Use dilute HDO and temperature variation to study the nature of hydrogen bonding in poly-water.

7.2 Conclusions

A. Annealing Ice I_v

Our infrared result for the transformation temperature range ($120 - 135 \pm 5^\circ\text{K}$ corrected for source beam heating) does not agree completely with the ranges of some other workers (Table 0.3). Our range seems to agree best with that of Dowell and Rinfret (74) and perhaps that of Sugisaki et al. (6). However, these ir results do not support Dowell's (74) conclusion that only 30% of the vitreous ice I was transformed to cubic ice I. However, their results may indicate that only 30% of their original sample was vitreous. The irreversible transformation frequency shifts (at 145°K) were: $\Delta\nu_1 = -42$, $\Delta\nu_3 = -36$, $\Delta\nu_2 = -56$, $\Delta\nu_R = +31$ and $\Delta\nu_T = +12 \text{ cm}^{-1}$. The transformation temperature range was independent of deposition rate, but transformation frequency shifts were not, faster depositions gave smaller shifts.

Oligomeric (probably dimeric and trimeric) H_2O and D_2O were present in considerable concentration in amorphous ice I: Slower depositions gave higher concentrations of oligomers. The oligomers were stable units up to $135 \pm 5^\circ\text{K}$. As much as 30% of the amorphous sample may have been in the form of oligomers.

B. HDO Studies

The assumption that dilute concentrations of HDO in H_2O or D_2O gave completely uncoupled HDO vibrators is invalid. At least one HDO frequency is coupled to a parent H_2O or D_2O frequency.

The low temperature limits of $\nu_{\text{OH}}(\text{HDO})$ and $\nu_{\text{OD}}(\text{HDO})$ were 3263.5 cm^{-1} and 2412.0 cm^{-1} respectively. The low temperature dependences of ν_{OH} and ν_{OD} were both $0.047 \text{ cm}^{-1}/^{\circ}\text{K}$ between 10°K and 80°K . The high temperature dependences of ν_{OH} and ν_{OD} were 0.200 and $0.123 \text{ cm}^{-1}/^{\circ}\text{K}$ between 80°K and 200°K .

Insofar as ω_{OH} and X_{OH} were a measure, the potential of HDO molecules in $\text{H}_2\text{O}/\text{D}_2\text{O}$ lattices changed its shape irregularly with temperature, i.e. the changes in ω_{OH} were not linear as temperature increased.

Hot bands and difference bands did not contribute significantly to the breadth of ν_{OH} and $\nu_{\text{OD}}(\text{HDO})$ and, by extension, not to stretches in H_2O or D_2O . Half-height width data supported the orientationally disordered proton theory of Whalley (88).

The temperature dependences of $\Delta\nu_{\text{OH}}(\text{HDO})$ and $\Delta\nu_{\text{OD}}(\text{HDO})$ from $100^{\circ} - 200^{\circ}\text{K}$ were 0.135 and $0.070 \text{ cm}^{-1}/^{\circ}\text{K}$. Within the limits of the infrared technique, $\nu_{\text{OH}}(\text{HDO})$ and $\nu_{\text{OD}}(\text{HDO})$ peak frequencies were sensitive to changes in $R(\text{O}\cdots\text{O})$ greater than 0.0001 \AA . HDO stretching absorptions were not linear functions of $R(\text{O}\cdots\text{O})$ over the whole temperature range $10^{\circ} - 200^{\circ}\text{K}$. The low temperature dependences $\Delta\nu_{\text{OH}}/\Delta R$ and $\Delta\nu_{\text{OD}}/\Delta R$ were $8.202 \times 10^3 \text{ cm}^{-1}/\text{\AA}$ and $6.629 \times 10^3 \text{ cm}^{-1}/\text{\AA}$ from $10^{\circ} - 100^{\circ}\text{K}$, while the high temperature dependences $\Delta\nu_{\text{OH}}/\Delta R$ and $\Delta\nu_{\text{OD}}/\Delta R$ were $1.921 \times 10^3 \text{ cm}^{-1}/\text{\AA}$ and $1.283 \times 10^3 \text{ cm}^{-1}/\text{\AA}$ from $150 - 200^{\circ}\text{K}$.

The calculated low temperature limit of $R(\text{O}\cdots\text{O})$ for cubic ice I was 2.753 \AA assuming $a_0 = 6.350 \text{ \AA}$ exactly at 143°K . The calculated changes in $R(\text{O}\cdots\text{O})$, with temperature were $\Delta R/\Delta T = 8.28 \times 10^{-6} \text{ \AA}/^{\circ}\text{K}$ from $0^{\circ} - 80^{\circ}\text{K}$ and $10.52 \times 10^{-6} \text{ \AA}/^{\circ}\text{K}$ from $130^{\circ} - 200^{\circ}\text{K}$.

Bellamy and Owen's (33) formula gave a good approximation to the relation between $R(0 \cdots 0)$ and $\nu_{OH}(HDO)$ in the temperature range 130°K to 200°K with the constant set at 57.77 cm^{-1} .

Anharmonicity correction, X_{OH} , had a low temperature limit of 105.6 cm^{-1} , a low temperature (0 - 60°K) dependence of $+0.032 \text{ cm}^{-1}/^{\circ}\text{K}$, a high temperature dependence (100° - 200°K) of $-0.038 \text{ cm}^{-1}/^{\circ}\text{K}$, and a maximum value of 108.7 cm^{-1} at 80°K.

The HDO harmonic stretching frequency had a low temperature limit at 3473.7 cm^{-1} , a temperature dependence (30°K - 200°K) of $+0.138 \text{ cm}^{-1}/^{\circ}\text{K}$ and a maximum displacement of 4 cm^{-1} from linearity at 80°K.

$\nu_R''(HDO)$ had a low temperature limit of 823 cm^{-1} and the shoulder (assigned to $(\nu_R'' + \nu_T)$) had a low temperature limit of 856 cm^{-1} . Various calculations indicated ν_{Rx} , ν_{Ry} and ν_{Rz} were degenerate for H_2O and D_2O and non-degenerate for HDO. The negative temperature dependence of lattice modes was understood in terms of a shallower potential and increasing excited state populations as temperature increased.

C. The H_2O and D_2O Studies

The order of ν_1 and ν_3 in the gas and cubic ice I phases was the same: Hydrogen bonding affected ν_1 and ν_3 of the gas phase equally, shifting them down proportionally. We conclude that the molecule-molecule coupling of ν_1 to ν_1 and ν_3 to ν_3 were similar in nature and that in cubic ice I, ν_1 and ν_3 were distinct transitions. The assignments of major H_2O and D_2O absorptions at 0°K were $\nu_1 + \nu_T = 3334$, $\nu_3 = 3204$, $\nu_1 = 3133$, $3\nu_R = 2239$, $\nu_2 = 1562$, $\nu_R + \nu_T = 881$, $\nu_R = 832$, and $\nu_T = 229.2 \text{ cm}^{-1}$ for

H_2O and $\nu_1 + \nu_T = 2464$, $\nu_3 = 2413$, $\nu_1 = 2320$, $3\nu_R = 1637$, $\nu_2 = 1189$, $\nu_R + \nu_T = 663$, and $\nu_R = 630 \text{ cm}^{-1}$ for D_2O , in basic agreement with previous authors. The absorption near 1600 cm^{-1} in H_2O definitely had a $2\nu_R$ underlying absorption.

Temperature dependence of ν_3 and ν_1 in absorptions for H_2O (above 100°K) confirmed the Raman temperature dependence of Val'kov (99). The data of HDO applied to H_2O and D_2O as well.

Blue's (85) formula led to anomalous results when applied to simple H_2O and D_2O molecules in ice. Assuming effective masses for two attached and two detached protons and also assuming that the three librations were degenerate or near-degenerate, then reasonable hydrogen bond bending force constants were calculated by Blue's method. From the $(\text{H}_2\text{O}, 3/4, 1/4)$ option we found $k(\text{O}-\text{H}\cdots\text{O}) = 0.60 \times 10^5 \text{ dynes/cm}$ and $k_{\text{H}}'(\text{O}\cdots\text{H}-\text{O}) = 0.21 \times 10^5 \text{ dynes/cm}$. These force constants predicted nearly degenerate D_2O librations ($586, 588$ and 591 cm^{-1}) about 6% below the observed value. The effective mass concept did not apply well to HDO.

An H_2O_3 model of ice gave a set of H_2O internal and lattice force constants in good agreement with those deduced by Trevino (93) and poorer agreement with Pimentel's results (97). That $k_{\phi\phi}(\nu_2)$ ($0.66 \times 10^5 \text{ dynes/cm}$) was smaller than the gas phase value was consistent with the lower ice frequency. H_2O_3 force constants were used to predict D_2O frequencies: Internal mode D_2O frequencies were 2 - 3% too low and lattice mode D_2O frequencies were 4 - 6% too high. The $\nu_R(\text{D}_2\text{O})$ calculated were about the same as from the effective mass model.

D. Clathrate Mixture Annealing

Condensation of a gaseous, stoichiometric mixture of H_2O or D_2O and guests, followed by annealing to $185 \pm 5^\circ\text{K}$, did not form crystalline clathrate-hydrate compounds. Guest species absorptions in amorphous H_2O masses were not subject to such large crystal field splittings as pure guest solids were.

REFERENCES

1. G.C. Pimentel and A.L. McClellan. The Hydrogen Bond. W.H. Freeman and Co., London, 1960.
2. N.D. Sokolov and V.M. Tschulanovski. Science, Moscow, 1964.
3. D. Hadzi and H.W. Thompson. Hydrogen Bonding. Pergamon Press, Paris, 1959.
4. W.C. Hamilton and J.A. Ibers. Hydrogen Bonding in Solids. W.A. Benjamin and Co., New York, 1968.
5. D. Eisenberg and W. Kauzmann. The Structure and Properties of Water. Clarendon Press, Oxford, 1969.
6. N. Riehl, B. Bullemer and H. Englehardt. Physics of Ice. Plenum Press, New York, 1969.
7. S. Bratoz. Advan. Quantum Chem., 3, pp. 209-37, 1967.
8. L. Pauling. The Nature of the Chemical Bond. Cornell University Press, Ithaca, 1940.
9. J.D. Bernal and R.H. Fowler. J. Chem. Phys., 1, pp. 515-48, 1933.
10. E. Bauer and M. Magat. J. Phys. Radium., 9, pp. 319-330, 1938.
11. J. Lennard-Jones and J.A. Pople. Proc. Roy. Soc., A205, pp. 155-162, 1951.
12. W.G. Schneider. J. Chem. Phys., 23, pp. 26-30, 1955.
13. R.F.W. Bader. Can. J. Chem., 42, pp. 1822-1834, 1964.
14. J.R. Platt. J. Chem. Phys., 18, pp. 932-35, 1950.
15. H.C. Longuet-Higgins and D.A. Brown. J. Inorg. Nucl. Chem., 1, pp. 60-67, 1955.
16. N.D. Sokolov. Dokladi Akad. Nauk. S.S.S.R., 58, pp. 611-614, 1947; Zh. Eksperim. i Teor. Fiz., 23, pp. 315-326, 1952.
17. C.A. Coulson and U. Danielsson. Arkiv. Fysik., 8, pp. 239-244, and pp. 245-255, 1954.
18. H. Tsubomura. Bull. Chem. Soc. Japan, 27, pp. 445-450, 1954.
19. F.B. van Duijneveldt and J.N. Murrell. J. Chem. Phys., 46, pp. 1759-67, 1967.

20. M. Hasegawa, K. Daiyasu and S. Yamosa. J. Phys. Soc. Japan, 27, pp. 999-1008, 1969.
21. P.G. Puranik and V. Kumar. Proced. Indian Acad. Sci., 58, pp. 29-37, 1963.
22. S. Bratoz. "Interactions Moleculaires Leur Classification Generale, Forces d'Exclusion de Pauli, Forces par Liason Hydrogene." Fondements Theoriques des Recherches sur les Actions Inter-moleculaires. Editions du Centre National de la Recherche Scientifique, Paris, 1966.
23. K. Szczepaniak and A. Tramer. Bull. Acad. Polon. Sci. Ser. Sci., Math., Astron. Phys., 13, pp. 79-83, 1965.
24. M. Weissmann and N.V. Cohan. J. Chem. Phys., 43, pp. 119-123, 1965.
25. E.R. Lippincott and R. Schroeder. J. Chem. Phys., 23, pp. 1099-1106, 1955.
26. R. Rein, G.C. Clarke and F.E. Harris. J. Mol. Struct., 2, pp. 103-109, 1968.
27. K. Nakamoto, M. Margoshes, and R.E. Rundle. J. Am. Chem. Soc., 77, pp. 6480-6486, 1955.
28. G.C. Pimentel and C.H. Sederholm. J. Chem. Phys., 24, pp. 639-641, 1956.
29. C.M. Huggins and G.C. Pimentel. J. Phys. Chem., 60, pp. 1615-1619, 1956.
30. S. Bratoz and D. Hadzi. J. Chem. Phys., 27, pp. 991-997, 1957.
31. C. Reid. J. Chem. Phys., 30, pp. 182-190, 1959.
32. L.J. Bellamy and R.J. Pace. Spectrochem. Acta., 25A, pp. 319-328, 1969.
33. L.J. Bellamy and A.J. Owen. Spectrochem. Acta., 25A, pp. 329-333, 1969.
34. K.B. Harvey, F.R. McCourt and H.F. Shurvell. Can. J. Chem., 42, 960-963, 1964.
35. M. Davies and W.C. Child. Spectrochem. Acta., 21, pp. 1195-1206, 1965.
36. D.F.R. Gilson. "Molecular Motion in Urea and Thiourea Adducts." Ph. D. Thesis, The University of British Columbia, Vancouver, 1959.

37. P. Raghunathan. "Nuclear Magnetic Resonance Studies on Clathrate-Hydrates." Ph.D. Thesis, The University of British Columbia, Vancouver, 1966.
38. M. von Stackelberg and H.R. Muller. Z. Elektrochem., 58, pp.25-39, 1954.
39. G.A. Jeffrey and R.K. McMullan. Prog. Inorgan. Chem., 8, pp. 43-108, 1967.
40. J.H. van der Waals and J.C. Platteeuw. Advances in Chemical Physics, 2, pp. 1-58. I. Prigogine, ed., Interscience Publishers, New York, 1959.
41. K.W. Allen and G.A. Jeffrey. J. Chem. Phys., 38, pp. 2304-5, 1963.
42. S. Sh. Byk and V.I. Fomina. Russian Chem. Revs., 37, pp. 469-90, 1968.
43. R.M. Barrer and D.J. Ruzicka. Trans. Faraday Soc., 58, pp. 2262-2271, 1962.
44. G.J. Wilson and D.W. Davidson. Can. J. Chem., 41, pp. 264-273, 1963.
45. D.W. Davidson and G.J. Wilson. Can. J. Chem., 41, pp. 1424-1434, 1963.
46. D.W. Davidson, M.M. Davies and K. Williams. J. Chem. Phys., 40, pp. 3449-3450, 1964.
47. R.K. McMullan and G.A. Jeffrey. J. Chem. Phys., 42, pp. 2725-2732, 1965.
48. Reference 37.
49. C.A. McDowell and P. Raghunathan. Molec. Phys., 15, pp. 259-270, 1968.
50. C.A. McDowell and P. Raghunathan. Molec. Phys., 13, pp. 331-431, 1967.
51. C.A. McDowell and P. Raghunathan. J. Molec. Struct., 2, pp. 359-368, 1968.
52. J.C. Burgiel, H. Meyer and P.L. Richards. J. Chem. Phys., 43, pp. 4291-99, 1965.
53. R.M. Hexter and T.D. Goldfarb. J. Inorg. Nucl. Chem., 4, pp. 171-178, 1957.

54. D.F. Ball and D.C. McKean. Spectroch. Acta., 18, pp. 933-938, 1962.
55. M. Davies and W.C. Child. Spectroch. Acta., 21, pp. 1195-1206, 1965.
56. F.R. McCourt. "An Infrared Study of Solid Gas Hydrates at 77°K." B.Sc. Thesis, Department of Chemistry, The University of British Columbia, Vancouver, 1962.
57. H.F. Shurvell. "An Infrared Study of Small Molecules in Inert Matrices." Ph.D. Thesis, The University of British Columbia, Vancouver, 1964.
58. K. Lonsdale. Proc. Roy. Soc., A247, pp. 424-434, 1958.
59. P.J. Owston. Adv. Phys., 7, pp. 171-188, 1958.
60. R. Brille and A. Tippe. Acta Cryst., 23, pp. 343-345, 1967.
61. G.P. Arnold, E.D. Finch, S.W. Rabideau and R.G. Wenzel. J. Chem. Phys., 49, pp. 4365-4369, 1968.
62. R.W.G. Wyckoff. Crystal Structures, vol. 1, 2nd edition, Interscience Publishers, New York, 1963.
63. S. LaPlaca and B. Post. Acta. Cryst., 13, pp. 503-505, 1960.
64. G. Dantl. Zeitsch. Phys., 166, p. 115, 1962.
65. R.H. Beaumont, H. Chihara and J.A. Morrison. J. Chem. Phys., 34, pp. 1456-57, 1961.
66. J.E. Bertie, L.D. Calvert and E. Whalley. J. Chem. Phys., 38, pp. 840-846, 1963.
67. Reference 5, page 109.
68. J.F. Nagle. J. Math. Phys., 7, pp. 1484-91, 1966.
69. G. Honjo and K. Shimaoka. Acta. Cryst., 10, pp. 710-11, 1957.
70. K.S. Pitzer and J. Polissar. J. Phys. Chem., 60, pp. 1140-42, 1956.
71. J.A. Pryde and G.O. Jones. Nature, 170, pp. 685-688, 1952.
72. H.J. De Nordwall and L.A.K. Stavely. Trans. Farad. Soc., 52, pp. 1061-1066, 1956.
73. M. Blackman and N.D. Lisgarten. Proc. Roy. Soc., A239, pp. 93-107, 1957.
74. L.G. Dowell and A.P. Rinfret. Nature, 188, pp. 1144-48, 1960.

75. J.A. McMillan and S.C. Los. Nature, 206, pp. 806-7, 1965.
76. J.A. Ghormley. J. Chem. Phys., 48, pp. 503-508, 1968.
77. G.J. Wilson, R.K. Chan, D.W. Davidson, and E. Whalley. J. Chem. Phys., 43, pp. 2384-91, 1965.
78. E. Whalley and J.B.R. Heath, J. Chem. Phys., 45, pp. 3976-82, 1966.
79. N. Bjerrum. Science, 115, pp. 385-90, 1952.
80. Reference 6, page 231.
81. Reference 6, page 344.
82. W.F. Giaugue and J.W. Stout. J. Am. Chem. Soc., 58, pp. 1144-50, 1936.
83. P. Flubacher, A.J. Leadbetter and J.A. Morrison. J. Chem. Phys., 33, pp. 1751-55, 1960.
84. A.J. Leadbetter. Proc. Roy. Soc., A287, pp. 403-425, 1965.
85. R.W. Blue. J. Chem. Phys., 22, pp. 280-83, 1954.
86. J.E. Bertie. Applied Spectros., 22, pp. 634-640, 1968.
87. E. Whalley and J.E. Bertie. J. Chem. Phys., 46, pp. 1264-70, 1967.
88. J.E. Bertie and E. Whalley. J. Chem. Phys., 46, pp. 1271-84, 1967.
89. P.A. Giguere and J.P. Arraudeau. Compte. Rend., 10, p. 1692, 1963.
90. V.I. Val'kov and G.L. Maslennikova. Optics and Spectroscopy, 1, pp. 881-884, 1956.
91. M.J. Taylor and E. Whalley. J. Chem. Phys., 40, pp. 1660-64, 1964.
92. H. Prask and H. Boutin. J. Chem. Phys., 48, pp. 3367-76, 1968.
93. S.F. Trevino. Appl. Spectros., 22, pp. 659-74, 1968.
94. Reference 6, pp. 287-304.
95. J.E. Bertie and E. Whalley. J. Chem. Phys., 40, pp. 1637-45, 1964.
96. J.E. Bertie and E. Whalley. J. Chem. Phys., 40, pp. 1646-59, 1964.
97. R. Zimmermann and G.C. Pimentel. Proced. 4th Biennial Meeting of the European Molecular Spectroscopy Group, Sept. 7-11, 1959, Pergamon Press, London, 1962.
98. P.A. Giguere and K.B. Harvey. Can. J. Chem., 34, pp. 798-808, 1956.

99. V.I. Val'kov and G.L. Maslenkova. Bull. Leningrad Univ., Phys. and Chem., 12, pp. 8-13, 1957.
100. T.A. Ford and M. Falk. Can. J. Chem., 46, pp. 3579-3586, 1968.
101. H.J. Hrostowski and G.C. Pimentel. J. Chem. Phys., 19, pp. 661-2, 1951.
102. G.L. Hiebert and D.F. Hornig. J. Chem. Phys., 20, pp. 918-19, 1952.
103. R. Mutter, R. Mecke and W. Luttke. Zeitsch. Physik. Chem., 19, pp. 83-88, 1959.
104. J. Schiffer. "Spectra of and Forces in Sodium Halide Dihydrates and Related Systems." Ph.D. Thesis, Princeton University, 1964.
105. D.F. Hornig, H.F. White and F.P. Reding. Spectroch. Acta., 12, pp. 338-49, 1958.
106. C. Haas and D.F. Hornig. J. Chem. Phys., 32, pp. 1763-69, 1960.
107. J.E. Bertie and E. Whalley. Spectroch. Acta., 20, pp. 1349-56, 1964.
108. N. Ockman. Adv. in Phys., 7, pp. 199-220, 1958.
109. E.H. Siegler. Engineering Reports, No. 563, Perkin-Elmer Corporation, Norwalk (1959).
110. J.M. Roche. Engineering Reports, No. 601, Perkin-Elmer Corporation, Norwalk (1959).
111. E.L. Wagner and D.F. Hornig. J. Chem. Phys., 18, pp. 296-304, 1950.
112. A.H. Hardin. "An I.R. Study of the Phosphine Solids." B.Sc. Thesis, Department of Chemistry, The University of British Columbia, 1963.
113. W.H. Duerig and I.L. Mador. Rev. Sci. Instr., 23, pp. 421-24, 1952.
114. K.W. Allen. J. Chem. Soc., 44, pp. 4131-32, 1959.
115. H.F. Shurvell. "An I.R. Study of D₂O and H₂O in Inert Matrices." M.Sc. Thesis, The University of British Columbia, 1962.
116. K. Nakamoto. "IR Spectra of Inorganic and Coordination Compounds." John Wiley and Sons, Inc., New York, 1963, p. 83.
117. M. Van Thiel, E.D. Becker, and G.C. Pimentel. J. Chem. Phys., 27, pp. 486-90, 1957.
118. S. Ikawa and S. Maeda. Spectrochim. Acta., 24, pp. 655-65, 1968.
119. C.C. Ferriso and C.B. Ludwig. J. Quant. Spect. Radiative Transfer, 4, p. 215, 1964.

120. M. Falk, private communication.
121. J.W. Nibler and G.C. Pimentel. J. Molec. Spectros., 26, pp.294-314, 1968.
122. J.C. Decius. J. Chem. Phys., 38, pp. 241-48, 1963.
123. Y. Morino, K. Kuchitsu, A. Takahashi and K. Maeda. J. Chem. Phys., 21, pp. 1927-1933, 1953.
124. G. Herzberg. Infrared and Raman Spectra of Polyatomic Molecules. Van Nostrand Company, Inc., New York, 1964.
125. R.W. Green. Ph.D. Thesis, The University of British Columbia, 1970, section 3.1.
126. G. Zerbi. Appl. Spectros. Revs., 2, pp. 193-261, 1969.
127. V. Seidl. J. Chem., 47, pp. 1361-8, 1969.
128. L.G. Harrison, M.D. Baijal, and D.J. Bird. Trans. Faraday Soc., 60, pp. 1099-1109, 1964.
129. D.D. Dows. J. Chem. Phys., 29, pp. 484-489, 1958.
130. M.P. Lisitsa and Y.P. Tsyashchenko. Optika i Spektroskopiya, 10, pp. 157-64, 1961.